



3-1987

Mathematical Modeling and Experimental Study of Dynamics and Structure Development during High Speed Melt Spinning of Nylon-6

Jayendra H. Bheda
University of Tennessee - Knoxville

Follow this and additional works at: https://trace.tennessee.edu/utk_graddiss



Part of the [Other Engineering Commons](#)

Recommended Citation

Bheda, Jayendra H., "Mathematical Modeling and Experimental Study of Dynamics and Structure Development during High Speed Melt Spinning of Nylon-6. " PhD diss., University of Tennessee, 1987. https://trace.tennessee.edu/utk_graddiss/2519

This Dissertation is brought to you for free and open access by the Graduate School at TRACE: Tennessee Research and Creative Exchange. It has been accepted for inclusion in Doctoral Dissertations by an authorized administrator of TRACE: Tennessee Research and Creative Exchange. For more information, please contact trace@utk.edu.

To the Graduate Council:

I am submitting herewith a dissertation written by Jayendra H. Bheda entitled "Mathematical Modeling and Experimental Study of Dynamics and Structure Development during High Speed Melt Spinning of Nylon-6." I have examined the final electronic copy of this dissertation for form and content and recommend that it be accepted in partial fulfillment of the requirements for the degree of Doctor of Philosophy, with a major in Polymer Engineering.

Joseph E. Spruiell, Major Professor

We have read this dissertation and recommend its acceptance:

Edward S. Clark, John F. Fellers, Larry C. Wadsworth, Donald C. Bogue

Accepted for the Council:

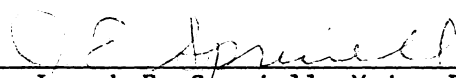
Carolyn R. Hodges

Vice Provost and Dean of the Graduate School

(Original signatures are on file with official student records.)

To the Graduate Council:

I am submitting herewith a dissertation written by Jayendra H. Bheda entitled "Mathematical Modeling and Experimental Study of Dynamics and Structure Development during High Speed Melt Spinning of Nylon-6." I have examined the final copy of this dissertation for form and content and recommend that it be accepted in partial fulfillment of the requirements for the degree of Doctor of Philosophy, with a major in Polymer Engineering.

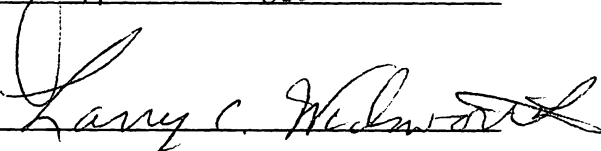


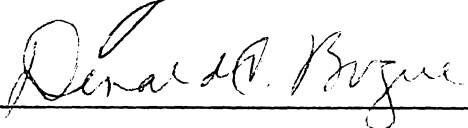
Joseph E. Spruiell, Major Professor

We have read this dissertation
and recommend its acceptance:









Accepted for the Council:



Vice Provost
and Dean of The Graduate School

MATHEMATICAL MODELING AND EXPERIMENTAL STUDY OF
DYNAMICS AND STRUCTURE DEVELOPMENT DURING
HIGH SPEED MELT SPINNING OF NYLON-6

A Dissertation

Presented for the

Doctor of Philosophy

Degree

The University of Tennessee, Knoxville

Jayendra H. Bheda

March 1987

To

Hansa, Poonam and Purvi

ACKNOWLEDGMENTS

The completion of this dissertation and the research work preceding it was possible due to assistance from many people. While it is not possible to mention everyone involved, there are several persons who deserve special mention for their efforts.

I am indebted to my advisor, Dr. J. E. Spruiell, for his guidance, patience and invaluable time which resulted in stimulating discussions throughout this work.

Appreciation is also extended to Professors D. C. Bogue, E. S. Clark, J. F. Fellers and other faculty members who received this work with encouraging discussions.

Financial assistance from and, more importantly, critical discussions with Dr. Kim, Dr. Wheeler and others of Allied Fibers and Plastics is acknowledged.

The capable assistance of Ted, Ron and Steve of the Electronics shop, Thompson, Doug and Jack of the Machine shop and Al and Mrs. Cagle of Stores is gratefully acknowledged.

I appreciate both past and present fellow graduate students who made my stay at the University an enjoyable and unforgettable experience.

This project would not have been completed, and I would not have been what I am now without the continuous support of my family members. To my wife Hansa and my daughters Poonam and Purvi, I express my greatest love and appreciation.

ABSTRACT

A mathematical model was developed to describe the high speed melt spinning behavior of nylon-6. This model is based on the equations of continuity, momentum and energy. These equations are combined with a Newtonian model for rheology to describe the process dynamics and models for the development of birefringence, molecular orientation and crystallization kinetics to describe the structure formation during high speed melt spinning of nylon-6. Physical property relationships from the literature are input and used together with the processing conditions to calculate velocity, diameter, temperature, stress, birefringence and crystallinity profiles along the spinline.

Online experimental techniques were used to obtain actual temperature, diameter and birefringence profiles. Two different molecular weight resins and two different mass throughputs were studied. Comparison of model predictions with experimental profiles showed that the trends predicted by the model were consistent qualitatively, but there were quantitative disagreements.

To obtain quantitative agreement, an analytical inversion procedure was developed in which online experimental data were utilized to generate key relationships for elongational viscosity and heat transfer coefficients. Utilization of these relationships in the model, provided a good agreement between experimental and predicted diameter and temperature profiles in the absence of crystallization. Subsequent adjustment in the parameter that controls the effect of orientation on crystallization rate provided good agreement between experimental and

predicted diameter, temperature and birefringence profiles, including the effects of crystallization with molecular orientation.

The model predictions and online experimental profiles indicate that high spinning speeds produced high spinline stresses and increased molecular orientation which induced crystallization in the spinline. Increasing the molecular weight of the resin produced higher spinline stresses (due to high melt viscosity) and induced online crystallization at a lower critical take-up velocity or at a higher temperature and smaller distance from the spinneret at chosen high take-up velocities. Under some spinning conditions (high speeds and lower throughput) the energy released by crystallization increased the local filament temperature which decreased the melt viscosity, allowing rapid local deformation or neck formation in the spinline.

TABLE OF CONTENTS

CHAPTER	PAGE
1 INTRODUCTION	1
Historical Perspective	1
State of the Art at Beginning of Present Research	3
Scope and Objectives of Present Research	6
2 LITERATURE REVIEW	9
Production and Basic Characteristics of Nylon-6	9
Physical Structure of Nylon-6	11
General	11
Structural Forms of Nylon-6	12
Relative Amounts of Various Phases	20
Crystallization Kinetics	23
Morphology and Orientation	25
Morphology	25
Orientation	27
Structure Development During Spinning	31
Low and Moderate Speeds	31
High Spinning Speeds	35
Theoretical Aspects of Melt Spinning	39
General	39
Force Balance	40
Rheology	46
Heat Transfer	50
Crystallization Kinetics	55
Isothermal Considerations	56
Non-isothermal and Orientation Considerations	61
Mathematical Modeling	69
3 EXPERIMENTAL DETAILS AND DATA ANALYSIS	76
Polymer and Process Details	76
Nylon-6 Resins	76
Melt Spinning Experiments	77

CHAPTER	PAGE
Online Measurements	81
Diameter	81
Birefringence	86
Temperature	87
Sinline Tension	89
Conditioned Fiber Characterization	89
Diameter and Birefringence	89
Density	91
Wide Angle X-ray Scattering	91
X-ray Diffractometer Scans	92
Differential Scanning Calorimetry	94
Mechanical Properties	95
4 EXPERIMENTAL RESULTS	97
Online Experimental Measurements	97
Diameter Profiles	97
Temperature Profiles	107
Birefringence Profiles	112
Sinline Tension	112
Effects of Post-Spinning Equilibration with the Environment	118
Structural Changes with Ambient Conditioning	118
Structure and Properties of Conditioned Fibers	123
Discussion of Experimental Results	141
Comparison with Previous Investigations	141
Analysis of Errors in Online Measurements	146
5 SIMULATION OF THE MELT SPINNING PROCESS	154
Mathematical Model	154
Continuity	155
Momentum Balance	155
Energy Balance	157
Rheological Model	158
Birefringence and Orientation	159
Crystallization Kinetics	160
Continuous System Modeling Program	162
Predictions of the Model	163
Discussions	202

CHAPTER	PAGE
6 IMPROVEMENT OF MODEL THROUGH EXPERIMENTAL RESULTS	213
Comparison of Model Predictions Based on Literature Parameters to online Experimental Profiles	213
Analytical Inversion Procedure	226
Inversion Procedure Results	230
Discussion of Inversion Procedure Results	249
Comparison of Experimental Online profiles and Predictions of Improved Model	259
7 CONCLUSIONS AND RECOMMENDATIONS	282
REFERENCES	287
APPENDIXES	303
A. Program for data acquisition from the Zimmer diameter monitor.	304
B. Program for statistical analysis of diameter data.	307
C. Program for tensiometer data acquisition and statistical calculation of average tension.	309
D. CSMP Program for model of nylon-6 melt spinning with literature property input.	310
E. CSMP Program for inversion procedure.	315
F. CSMP Program for improved model of nylon-6 melt spinning.	317
VITA	320

LIST OF TABLES

TABLE	PAGE
3.1 Viscosity average molecular weight results.	77
4.1 Results of relative amounts of phase - analysis for conditioned nylon-6 filaments for CN9984: (a) $W = 3.073$ g/min, (b) $W = 5.154$ g/min.	132
4.2 Results of relative amounts of phase - analysis for conditioned nylon-6 filaments for BHS: (a) $W = 2.993$ g/min, (b) $W = 5.069$ g/min.	133
4.3 Results of DSC analysis of conditioned nylon-6 filaments for CN9984: (a) $W = 3.073$ g/min, (b) $W = 5.154$ g/min. . . .	139
4.4 Results of DSC analysis of conditioned nylon-6 filaments for BHS: (a) $W = 2.993$ g/min, (b) $W = 5.069$ g/min. . . .	140
5.1 Summary of experimental processing conditions.	164

LIST OF FIGURES

FIGURE		PAGE
2.1	Structure of the α -form of nylon-6: (a) monoclinic shape and dimensions of the unit cell, (b) antiparallel chain arrangement of hydrogen bonded sheets, (c) the chain directions shown in the basal plane of the unit cell. . .	13
2.2	Hexagonal and pseudo-hexagonal symmetries. The dashed lines outline the basal plane of a hexagonal unit cell.	16
2.3	Structure of the γ -form of nylon-6: (a) parallel chain arrangement of hydrogen bonded sheets, (b) chain directions shown in the basal plane of the unit cell. . .	18
2.4	Schematic x-ray fiber diagrams of nylon-6: (a) α -form, (b) γ -form. The fiber axis is vertical.	19
2.5	Illustration of folded-chain lamella with idealized adjacent reentry of chains.	26
2.6	Model of (a) drawn and (b) drawn and annealed fiber. . . .	29
2.7	Schematic of forces in fiber spinline.	41
3.1	Schematic of the experimental apparatus.	78
3.2	Schematic of Zimmer diameter monitor.	82
3.3	Operating principle of Zimmer diameter monitor.	82
3.4	Schematic of the temperature measuring apparatus.	88
4.1	Diameter distribution at 20 cm from the spinneret for CN9984 with a mass throughput of 3.073 g/min and take-up velocity of 1960 m/min.	98
4.2	Diameter distribution at 90 cm from the spinneret for CN9984 with a mass throughput of 3.073 g/min and take-up velocity of 1960 m/min.	99
4.3	Diameter distribution at 150 cm from the spinneret for CN9984 with a mass throughput of 3.073 g/min and take-up velocity of 1960 m/min.	100
4.4	Diameter distribution at the indicated distances from the spinneret for CN9984 with a mass throughput of 3.073 g/min and take-up velocity of 7310 m/min.	101
4.5	Experimental diameter profiles for CN9984 with a mass throughput of 3.073 g/min.	103

FIGURE	PAGE
4.6 Experimental diameter profiles for BHS with a mass throughput of 2.993 g/min.	104
4.7 Experimental diameter profiles for CN9984 with a mass throughput of 5.154 g/min.	105
4.8 Experimental diameter profiles for BHS with a mass throughput of 5.069 g/min.	106
4.9 Experimental temperature profiles for CN9984 with a mass throughput of 3.073 g/min.	108
4.10 Experimental temperature profiles for BHS with a mass throughput of 2.993 g/min.	109
4.11 Experimental temperature profiles for CN9984 with a mass throughput of 5.154 g/min.	110
4.12 Experimental temperature profiles for BHS with a mass throughput of 5.069 g/min.	111
4.13 Experimental birefringence profiles for CN9984 with a mass throughput of 3.073 g/min.	113
4.14 Experimental birefringence profiles for BHS with a mass throughput of 2.993 g/min.	114
4.15 Experimental birefringence profiles for CN9984 with a mass throughput of 5.154 g/min.	115
4.16 Experimental birefringence profiles for BHS with a mass throughput of 5.069 g/min.	116
4.17 Experimental spinline tension at a position of 190 cm from the spinneret.	117
4.18 Change in birefringence with conditioning time for CN9984 with a mass throughput of 3.073 g/min.	119
4.19 Change in birefringence with conditioning time for BHS with a mass throughput of 2.993 g/min.	120
4.20 Change in birefringence with conditioning time for CN9984 with a mass throughput of 5.154 g/min.	121
4.21 Change in birefringence with conditioning time for BHS with a mass throughput of 5.069 g/min.	122
4.22 Density of conditioned nylon-6 filaments as a function of take-up velocity.	124

FIGURE	PAGE
4.23 Birefringence of conditioned nylon-6 filaments as a function of take-up velocity.	125
4.24 Chain axis crystalline orientation function of conditioned nylon-6 filaments versus take-up velocity. . .	126
4.25 Typical WAXS patterns of conditioned nylon-6 filaments for CN9984 with a mass throughput of 3.073 g/min: (a) 1960 m/min, (b) 4615 m/min, (c) 7310 m/min.	128
4.26 Typical WAXS patterns of conditioned nylon-6 filaments for BHS with a mass throughput of 2.993 g/min: (a) 1780 m/min, (b) 3880 m/min, (c) 6660 m/min.	129
4.27 Typical WAXS patterns of conditioned nylon-6 filaments for CN9984 with a mass throughput of 5.154 g/min: (a) 1570 m/min, (b) 3855 m/min, (c) 6455 m/min.	130
4.28 Typical WAXS patterns of conditioned nylon-6 filaments for BHS with a mass throughput of 5.069 g/min: (a) 1250 m/min, (b) 3170 m/min, (c) 5790 m/min.	131
4.29 Typical normalized DSC traces of conditioned nylon-6 filaments for CN9984 with a mass throughput of 3.073 g/min. .	135
4.30 Typical normalized DSC traces of conditioned nylon-6 filaments for BHS with a mass throughput of 2.993 g/min. .	136
4.31 Typical normalized DSC traces of conditioned nylon-6 filaments for CN9984 with a mass throughput of 5.154 g/min. .	137
4.32 Typical normalized DSC traces of conditioned nylon-6 filaments for BHS with a mass throughput of 5.069 g/min. .	138
4.33 Initial modulus of conditioned nylon-6 filaments as a function of take-up velocity.	142
4.34 Tenacity of conditioned nylon-6 filaments as a function of take-up velocity.	143
4.35 Elongation to break of conditioned nylon-6 filaments as a function of take-up velocity.	144
5.1 Predicted velocity profiles for CN9984 with a mass throughput of 3.073 g/min.	165
5.2 Predicted velocity profiles for BHS with a mass throughput of 2.993 g/min.	166
5.3 Predicted velocity profiles for CN9984 with a mass throughput of 5.154 g/min.	167

FIGURE		PAGE
5.4	Predicted velocity profiles for BHS with a mass throughput of 5.069 g/min.	168
5.5	Predicted temperature profiles for CN9984 with a mass throughput of 3.073 g/min.	170
5.6	Predicted temperature profiles for BHS with a mass throughput of 2.993 g/min.	171
5.7	Predicted temperature profiles for CN9984 with a mass throughput of 5.154 g/min.	172
5.8	Predicted temperature profiles for BHS with a mass throughput of 5.069 g/min.	173
5.9	Predicted diameter profiles for CN9984 with a mass throughput of 3.073 g/min.	176
5.10	Predicted diameter profiles for BHS with a mass throughput of 2.993 g/min.	177
5.11	Predicted diameter profiles for CN9984 with a mass throughput of 5.154 g/min.	178
5.12	Predicted diameter profiles for BHS with a mass throughput of 5.069 g/min.	179
5.13	Predicted velocity gradient profiles for CN9984 with a mass throughput of 3.073 g/min.	180
5.14	Predicted velocity gradient profiles for BHS with a mass throughput of 2.993 g/min.	181
5.15	Predicted velocity gradient profiles for CN9984 with a mass throughput of 5.154 g/min.	182
5.16	Predicted velocity gradient profiles for BHS with a mass throughput of 5.069 g/min.	183
5.17	Predicted rheological force profiles for CN9984 with a mass throughput of 3.073 g/min.	185
5.18	Predicted rheological force profiles for BHS with a mass throughput of 2.993 g/min.	186
5.19	Predicted rheological force profiles for CN9984 with a mass throughput of 5.154 g/min.	187
5.20	Predicted rheological force profiles for BHS with a mass throughput of 5.069 g/min.	188

FIGURE	PAGE
5.21 Predicted spinline stress profiles for CN9984 with a mass throughput of 3.073 g/min.	189
5.22 Predicted spinline stress profiles for BHS with a mass throughput of 2.993 g/min.	190
5.23 Predicted spinline stress profiles for CN9984 with a mass throughput of 5.154 g/min.	191
5.24 Predicted spinline stress profiles for BHS with a mass throughput of 5.069 g/min.	192
5.25 Predicted amorphous orientation factor profiles for CN9984 with a mass throughput of 3.073 g/min.	194
5.26 Predicted amorphous orientation factor profiles for BHS with a mass throughput of 2.993 g/min.	195
5.27 Predicted amorphous orientation factor profiles for CN9984 with a mass throughput of 5.154 g/min.	196
5.28 Predicted amorphous orientation factor profiles for BHS with a mass throughput of 5.069 g/min.	197
5.29 Predicted crystalline index profiles for CN9984 with a mass throughput of 3.073 g/min.	198
5.30 Predicted crystalline index profiles for BHS with a mass throughput of 2.993 g/min.	199
5.31 Predicted crystalline index profiles for CN9984 with a mass throughput of 5.154 g/min.	200
5.32 Predicted crystalline index profiles for BHS with a mass throughput of 5.069 g/min.	201
5.33 Predicted birefringence profiles for CN9984 with a mass throughput of 3.073 g/min.	203
5.34 Predicted birefringence profiles for BHS with a mass throughput of 2.993 g/min.	204
5.35 Predicted birefringence profiles for CN9984 with a mass throughput of 5.154 g/min.	205
5.36 Predicted birefringence profiles for BHS with a mass throughput of 5.069 g/min.	206
6.1 Comparison of predicted and experimental diameter profiles for CN9984 with a mass throughput of 3.073 g/min.	214

FIGURE		PAGE
6.2	Comparison of predicted and experimental diameter profiles for BHS with a mass throughput of 2.993 g/min.	215
6.3	Comparison of predicted and experimental diameter profiles for CN9984 with a mass throughput of 5.154 g/min.	216
6.4	Comparison of predicted and experimental diameter profiles for BHS with a mass throughput of 5.069 g/min.	217
6.5	Comparison of predicted and experimental temperature profiles for CN9984 with a mass throughput of 3.073 g/min.. .	218
6.6	Comparison of predicted and experimental temperature profiles for BHS with a mass throughput of 2.993 g/min.. .	219
6.7	Comparison of predicted and experimental temperature profiles for CN9984 with a mass throughput of 5.154 g/min.. .	220
6.8	Comparison of predicted and experimental temperature profiles for BHS with a mass throughput of 5.069 g/min.. .	221
6.9	Comparison of predicted and experimental birefringence profiles for CN9984 with a mass throughput of 3.073 g/min.. .	222
6.10	Comparison of predicted and experimental birefringence profiles for BHS with a mass throughput of 2.993 g/min.. .	223
6.11	Comparison of predicted and experimental birefringence profiles for CN9984 with a mass throughput of 5.154 g/min.. .	224
6.12	Comparison of predicted and experimental birefringence profiles for BHS with a mass throughput of 5.069 g/min.. .	225
6.13	Test comparison of inversion procedure for velocity profiles for CN9984 with a mass throughput of 3.073 g/min and take-up speed of 1960 m/min.	231
6.14	Test comparison of inversion procedure for diameter profiles for CN9984 with a mass throughput of 3.073 g/min and take-up speed of 1960 m/min.	232
6.15	Test comparison of inversion procedure for temperature profiles for CN9984 with a mass throughput of 3.073 g/min and take-up speed of 1960 m/min.	233
6.16	Test comparison of inversion procedure for velocity gradient profiles for CN9984 with a mass throughput of 3.073 g/min and take-up speed of 1960 m/min.	234

FIGURE	PAGE
6.17 Test comparison of inversion procedure for temperature gradient profiles for CN9984 with a mass throughput of 3.073 g/min and take-up speed of 1960 m/min.	235
6.18 Test comparison of inversion procedure for rheological force profiles for CN9984 with a mass throughput of 3.073 g/min and take-up speed of 1960 m/min.	236
6.19 Test comparison of inversion procedure for viscosity profiles for CN9984 with a mass throughput of 3.073 g/min and take-up speed of 1960 m/min.	237
6.20 Test comparison of inversion procedure for heat transfer coefficient profiles for CN9984 with a mass throughput of 3.073 g/min and take-up speed of 1960 m/min.	238
6.21 Calculated and regressed viscosity relation from inversion procedure for CN9984 with a mass throughput of 3.073 g/min and take-up speed of 1960 m/min.	250
6.22 Calculated and regressed viscosity relation from inversion procedure for BHS with a mass throughput of 2.993 g/min and take-up speed of 1780 m/min.	251
6.23 Calculated and regressed viscosity relation from inversion procedure for CN9984 with a mass throughput of 5.154 g/min and take-up speed of 1570 m/min.	252
6.24 Calculated and regressed viscosity relation from inversion procedure for BHS with a mass throughput of 5.069 g/min and take-up speed of 1250 m/min.	243
6.25 Calculated and regressed heat transfer coefficient relation from inversion procedure for CN9984 with a mass throughput of 3.073 g/min and take-up speed of 1960 m/min.	244
6.26 Calculated and regressed heat transfer coefficient relation from inversion procedure for BHS with a mass throughput of 2.993 g/min and take-up speed of 1780 m/min.	245
6.27 Calculated and regressed heat transfer coefficient relation from inversion procedure for CN9984 with a mass throughput of 5.154 g/min and take-up speed of 1570 m/min.	246
6.28 Calculated and regressed heat transfer coefficient relation from inversion procedure for BHS with a mass throughput of 5.069 g/min and take-up speed of 1250 m/min.	247
6.29 Comparison of elongational viscosities from inversion procedure of present experimental data, those from model and those from the literature.	255

FIGURE	PAGE
6.30 Comparison of elongational viscosities from inversion procedure for CN9984 with a mass throughput of 3.073 g/min and take-up speed of 1960 m/min using Sakiadis's and Hamana et al.'s air drag coefficients.	257
6.31 Comparison of heat transfer coefficients from inversion procedure of present experimental data and those from the literature.	260
6.32 Comparison of predicted and experimental birefringence profiles for CN9984 with a mass throughput of 3.073 g/min and $c = 100$	262
6.33 Comparison of predicted (from improved model) and experimental birefringence profiles for CN9984 with a mass throughput of 3.073 g/min and $c = 800$	264
6.34 Comparison of predicted (from improved model) and experimental birefringence profiles for CN9984 with a mass throughput of 5.154 g/min and $c = 800$	266
6.35 Rate constant versus temperature for CN9984 with a mass throughput of 3.073 g/min and $c = 1.25 \times 10^5 / (T_m - T)$	267
6.36 Comparison of predicted (from improved model) and experimental diameter profiles for CN9984 with a mass throughput of 3.073 g/min.	269
6.37 Comparison of predicted (from improved model) and experimental diameter profiles for BHS with a mass throughput of 2.993 g/min.	270
6.38 Comparison of predicted (from improved model) and experimental diameter profiles for CN9984 with a mass throughput of 5.154 g/min.	271
6.39 Comparison of predicted (from improved model) and experimental diameter profiles for BHS with a mass throughput of 5.069 g/min.	272
6.40 Comparison of predicted (from improved model) and experimental temperature profiles for CN9984 with a mass throughput of 3.073 g/min.	273
6.41 Comparison of predicted (from improved model) and experimental temperature profiles for BHS with a mass throughput of 2.993 g/min.	274
6.42 Comparison of predicted (from improved model) and experimental temperature profiles for CN9984 with a mass throughput of 5.154 g/min.	275

6.43	Comparison of predicted (from improved model) and experimental temperature profiles for BHS with a mass throughput of 5.069 g/min.	276
6.44	Comparison of predicted (from improved model) and experimental birefringence profiles for CN9984 with a mass throughput of 3.073 g/min.	277
6.45	Comparison of predicted (from improved model) and experimental birefringence profiles for BHS with a mass throughput of 2.993 g/min.	278
6.46	Comparison of predicted (from improved model) and experimental birefringence profiles for CN9984 with a mass throughput of 5.154 g/min.	279
6.47	Comparison of predicted (from improved model) and experimental birefringence profiles for BHS with a mass throughput of 5.069 g/min.	280

CHAPTER 1

INTRODUCTION

Historical Perspective

① The basis of the man-made fiber industry is the formation of fibers from polymer melts and solutions. The incentive for development of man-made fibers was their technological and economic advantages over naturally occurring cotton, silk and wool fibers. The first synthetic fibers were based on modification of naturally occurring cellulose e.g. cellulose nitrate, cellulose xanthate and cellulose acetate (1-5). The fiber formation processes involved in these cases, known as ²dry and wet spinning, were patented as early as the 1880's (2-5). In these processes the polymer is dissolved in a solvent to form a spinning dope and this dope is extruded either into a chamber containing heated gases to evaporate the solvent (dry spinning) or into a bath containing a coagulant (wet spinning). These fiber formation processes based on polymer solutions were necessary for cellulose and cellulose derivatives or (for any polymer), (natural or synthetic, which degrades before melting.)

② The commercial development of synthetic thermoplastic polymers in the 1920's and 1930's created the opportunity for direct fiber formation from the melt, i.e., melt spinning. The first commercial melt spun fiber was produced from polyvinyl chloride by I. G. Farbenindustrie in the early 1930's but did not prove very successful (6). The first truly successful melt spun fiber was nylon-66 which was developed by Carothers (7-10) and which was commercialized by E. I. duPont in 1939. Soon afterwards, during 1942, nylon-6 fiber was commercialized by I. G.

Farbenindustrie) followed by polyethylene terephthalate (PET) fiber by Imperial Chemical Industries in 1946. The last of the major melt spun fibers to be developed was isotactic polypropylene (PP). Its development required the preparation of the stereoregular polymer through use of special catalysts (now called Ziegler-Natta catalysts). Polypropylene fiber was developed by Natta and his coworkers and commercialized by Montecatini in 1954. Numerous other thermoplastic polymers, including various other polyolefins, polyamides and polyesters, have been melt spun over the years. Most of these have found application in specialty applications such as ropes, cords and filtration fabrics from low, high and linear low density polyethylenes; flameproof, resilient and high temperature gas filtration fabrics from modified nylons; snap-back fibers from modified thermoplastic elastomer type polyesters.

9) In the melt spinning process, polymer chips are melted into a viscous fluid, usually in a screw extruder, and then the molten polymer is pumped through a spinneret (die) forming continuous filaments. The filaments are drawn down to a smaller diameter, solidified and taken-up by a winding device. Melt spun fibers, sometimes called "as-spun", generally have high extensibility. Orientation and other physical properties vary to a great extent, depending on spinning conditions. Historically these properties have not been sufficient for direct application and the as-spun fibers are generally "hot drawn" in order to further develop desirable properties. In the drawing process the as-spun filaments are delivered from a set of feed rollers to a second set of rollers through a hot zone. The linear speed of the second set of rollers is about two to six times that of the feed rollers. The drawing

process modifies both the structure, including molecular orientation and crystallinity, and the mechanical properties of the filaments; e.g., modulus, tenacity and elongation to break.) In recent years a major commercial trend has been toward (increased spinning speed and reduction in the draw ratio in the hot drawing step). A long term goal of research in this area is to (eliminate the drawing step and produce finished fiber in a one step process). However, to date this goal has not been achieved. In spite of this the increased production rates associated with higher spinning speeds has provided incentives to increase commercial spinning speeds. (Current industrial practice involves spinning speeds in the range up to 5000 meters per minute, while spinning speeds in excess of 10,000 meters per minute have been studied at the laboratory scale.)

State of the Art at Beginning of Present Research

⑥ (The melt spinning process for different polymers was successfully developed for many years on the basis of empiricism without a deep insight into the physical nature of the processes involved. However, there has now been a considerable effort made to understand both the dynamics of the melt spinning process and the relationship between spinning conditions and fiber structure.) Ziabicki in the late 1960's (11) and in the mid 1970's (12) summarized the literature dealing with the experimental and theoretical framework for kinematics and dynamics of deformation of the spinline, heat transfer aspects, molecular orientation accompanying fiber spinning and kinetics of polymer crystallization. Following Ziabicki several experimental studies of melt spinning of various polymers at low and intermediate speeds (up to 2500

m/min) appeared. In our department alone Spruiell and/or White and their coworkers (13-34) studied melt spinning of PP, PE, PET, nylon-66, nylon-6, and others. Other authors included Keller and Machin (35), Fung and Carr (36), Samuels (37), Simpson et al. (38), Chappel et al. (39), Ziabicki and Kedzierska (40), Hamana et al. (41,42), Ishibashi et al. (43), and many others. These studies were mostly to elucidate the structure development of as-spun fibers and/or treated the structure and properties of as-spun fibers. ⁽¹⁾ The structure development involved characterization of molecular orientation, level of crystallinity and morphology through the use of the techniques of x-ray diffraction (wide and small angle), density, birefringence, electron microscopy, etc. Attempts were also made to relate mechanical properties of fibers to their structure formation. In addition to developing an understanding of the structural details of fiber, an indirect advantage of these studies was the establishment of fiber characterization techniques.

Various other authors studied the dynamic, rheological and heat transfer processes occurring in melt spinning. Dynamic studies made by Ziabicki (12), Matowich and Pearson (44), Bankar et al. (25), among others, emphasized the momentum balance in terms of various force contributions to development of the rheological force within the filament. Sano and Orii (45), Hamana et al. (42), Sakiadis (46), and others attempted theoretical and experimental analyses of the air drag force contribution in the momentum balance. Rheological studies by Cogswell (47), Ishizuka and Koyama (48,49) and in our laboratory (50-55) tried elongational viscosity measurements. But the technique was limited to LDPE, HDPE, and PP, as the viscosities of nylons and polyesters were

generally too low to be characterized by available techniques for independent elongational viscosity measurement. Han and Lamonte (56), Hill and Cuculo (57), Acierno et al. (13), Minoshima et al. (52), on the other hand have tried to obtain elongational viscosity through isothermal melt spinning. Denn (58) and White (59) have attempted critical reviews of dynamics and rheological aspects of melt spinning.

Shimizu and his coworkers (60-71) were first to report experimental study of high speed spinning of various polymers including PP, PET, nylon-6, nylon-66, etc. These studies concluded that increased take-up speeds influence fiber structure formation and so also mechanical properties of as-spun fibers. In some cases beyond about 7000 m/min either there was leveling off of enhanced molecular orientation and mechanical properties or decrease of orientation and mechanical properties. They also reported a "necking" phenomenon, an apparent sudden drawdown of fiber diameter to its final value on the spinline, beyond about 3000 m/min in the case of PET. Amongst other groups Heuvel et al. (72,73), Hamidi et al. (74), Yasuda (75), Bragato and Gianotti (76,77), and others have also studied high speed spun nylons and PET. {In our department also {Koyama et al. (34)}, Bai (32) and Zieminski (33) have {studied high speed melt spun nylon-6}, PET and nylon-66, respectively. While {Koyama et al. emphasized the effect of molecular weight in the structure development of as-spun nylon-6 fibers}, Bai and Zieminski emphasized the development and use of online experimental measurements as a tool to develop an understanding of high speed melt spinning of PET and nylon-66, respectively.

Since theoretical developments were made by different contributors only recently were attempts made to combine all ideas to formulate an approximate solution of a system of mathematical equations describing the whole process and its variants. Initial attempts were made by Kase and Matsuo (78,79), Hamana et al. (41), Lamonte and Han (80), Fisher and Denn (81), Matsui and Bogue (82) and others. These studies tried to provide a consistent treatment of non-isothermal modeling of melt spinning at low speeds with emphasis on rheological constitutive equation. These studies considered rheological model variations such as Newtonian, non-Newtonian, viscoelastic differential and integral models. Prastaro and Parini (83), Gagon and Denn (84), George (85), Dutta and Nadkarni (86) and others attempted modeling of the spinline at intermediate spinning speeds (up to 3,500 m/min). With the increasing spinning speeds these studies showed that the spinline dynamics were more affected by aerodynamics and acceleration effects rather than viscosity controlled processes. Kikutani (87), Bai (32), Zieminski (33) and others attempted to extend modeling efforts into the range of high speed spinning. They considered an essentially empirical crystallization kinetics model along with descriptions of dynamics, heat transfer, constitutive equation, etc. in order to develop non-isothermal modeling at such high spinning speeds.

Scope and Objectives of Present Research

The present research work is a continuation of the research on the melt spinning of nylon-6 in which an improved understanding at high

speeds is attempted through combination of experimentation and theoretical mathematical modeling.

(Experimentation involving measurements of diameter and temperature profiles of the filament, tension developed within the filament and birefringence development in the threadline) are described. These data are key to unlocking the mysteries of the dynamics and (structure development during high speed melt spinning.) In prior studies diameter profiles were measured by a microscope, either on the spinline or after cutting and freezing a small portion of the threadline. The former technique necessitated use of a guide to prevent filament movement during measurement and hence could be used only on a limited portion of spinline for which the guide did not stick. The cutting technique involved shrinkage due to cooling and relaxation of the filament before the diameter measurement could be made. There is a great need for accurate non-contact measurement of online diameter over the whole spinline and the present study provides these results for two nylon-6 resins. Accurate online diameter measurement also adds to the accuracy of birefringence measurement since birefringence is the ratio of optical retardation to diameter of the filament. (Important variables which influence the dynamics and structure development during melt spinning are polymer molecular weight, mass throughput, take-up speeds, etc. The present research examined each of these variables for nylon-6.)

It has been said that we truly understand a subject only when we can describe it quantitatively. Consequently, a major goal of the present research was to develop a mathematical description of the high speed melt spinning of nylon-6. The mathematical model is an extension

of the earlier work of Zieminski (33); it is a combination of kinematics and dynamics of deformation of the spinline including rheology of the polymer melt, heat transfer and most importantly polymer crystallization kinetics accompanying molecular orientation. The latter is an important aspect of modeling particularly for high speed spinning of nylon-6 and other crystallizable fiber forming polymers such as polypropylene (PP), nylon-66, polyethylene terephthalate (PET), etc. The validity and quantitative success of the model is examined through comparisons between the online experimental measurements of the diameter, birefringence and temperature profiles and model predictions. Discrepancy between model predictions and online experimental results were examined in an effort to understand inadequacies in the model or to improve the model parameters.

It is believed that the experimental and theoretical efforts described in this dissertation led to a realistic mathematical model of high speed melt spinning of nylon-6. It is hoped that these efforts will ultimately lead to a much improved analysis and understanding of fiber science and technology.

CHAPTER 2

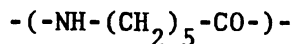
LITERATURE REVIEW

Production and Basic Characteristics of Nylon-6

Nylons belong to a general class of polyamides which are condensation products containing recurring amide groups as an integral part of the main polymer chain. ⁽⁸⁾ The first rational synthesis of nylon-6 was due to Carothers and Berchet (7) in 1930, but molecular weight only of order of 1000 was achieved. This was part of a research program which led to Carothers and Hill's (8,9) development of melt spinning of synthetic polycondensate fibers. ⁽⁸⁾ However, high molecular weight nylon-6 was not developed until the work of Schlack (88) in 1938, and commercialization as a melt spun synthetic fiber was due to the I.G. Farbenindustrie (89). The polymerization involved ring opening of ϵ -caprolactam in the presence of water. A stabilizer such as acetic acid is added to control the average chain lengths of the polymer and consequently the molecular weight. The polycaprolactam is extruded into a water bath and then cut into small pellets. These pellets contain about 10% monomer and other oligomers. These are removed by leaching the pellets in boiling water, and are then dried to less than 0.1% moisture content by weight before spinning. The continuous process of polymerizing ϵ -caprolactam is described in the literature (90-92).

{ The name "nylon" was coined by E. I. duPont Company for polyamides, which included the carbonamide group -CONH- as a recurring unit of the main chain. Several nylons emerged depending on initial diamine and diacid monomers and they were named according to number of carbon atoms

in the monomers. Thus nylon-6 is polycaprolactam having 6 carbon atoms in the repeat unit



Nylon-6 has a melting point of about 215 - 220°C, which is about 40°C lower than that of nylon-66. The glass transition temperature of nylon-6 is in the range of 45 - 50°C. It contains about 10% extractable material (including water) which acts as a plasticizer and has important implications on its processing and final physical properties.

Caprolactam is the major component (about 70%) of the extractable portion; the remaining 30% consists of roughly equal portions of cyclic dimers, trimers, tetramers, pentamers, hexamers, highly cyclic oligomers and water (93). }

The ability to absorb moisture is an important factor in the ability of a fiber to absorb dyes and to be dyed at normal pressures; moisture absorption also affects the comfort in wearing of textile apparel made from synthetic filaments. The electrostatic properties of nylons are considerably altered by the extent of moisture absorption, being highest under conditions of low humidity and low moisture absorption. {All nylons absorb moisture readily from air, and will hold it firmly through hydrogen bonding with the amide groups. The higher the amide content, the greater is the affinity toward moisture. }

{ The important factors in the establishment of an equilibrium between a polyamide and water containing environment are: the relative humidity (RH), the amide content and the amount of crystallinity. Nylon-6, having quite high amide content among the common commercial nylons, exhibits a high moisture absorption (94); the moisture content

reaches to about 10% at RH of 100% (95). Significant decrease in moisture absorption is observed with increase in crystallinity (96). Absorbed moisture serves as a plasticizer, reducing modulus and tensile strength, while increasing elongation with increase in moisture content (97). }

① { The effect of crystallinity on the properties of nylons is substantially the same as it is for other semicrystalline polymers. }
Modulus, tensile strength and related properties such as hardness and yield point increases with increasing crystallinity while measures of toughness such as impact strength decrease. However, the effect of crystallinity in nylons can hardly be discussed independent of that of water content. Not only can water have an effect on crystallinity but it also changes physical properties independently. Once a sample has absorbed a given amount of water at any temperature, this water can be removed and replaced at this temperature without noticeable effect on crystallinity, but the effect on properties will be substantial. Water lowers T_g and the characteristic temperature of mechanical relaxation. }

/ Physical Structure of Nylon-6

General

Nylons are different from many other crystalline polymers such as high density polyethylene in that { the degree of crystallinity can be controlled over a wide range. For nylons high crystallinity requires both parallel alignment of the chain and uniformity in the manner in which hydrogen bonds are formed. This question of uniformity with respect to hydrogen bond formation accounts for the wide range of

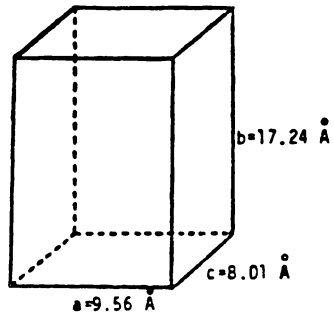
crystallinity.) The (simplest concept) of (morphology) treats the molecular aggregations as (two distinct phases) - (crystalline phase embedded in an amorphous entanglement of chains.) (However, the morphology of nylons is complicated because of the presence of several crystalline phases. The molecules fold to form thin ribbon or wafer shaped crystals termed "lamellae" and these in turn can aggregate into spherical clusters called "spherulites". Orientation results when molecular orientation in the melt induces oriented nucleation and growth of lamellae, or operations such as drawing or rolling induce the partial break up of lamellae and spherulites and form new structures.)

Structural Forms of Nylon-6

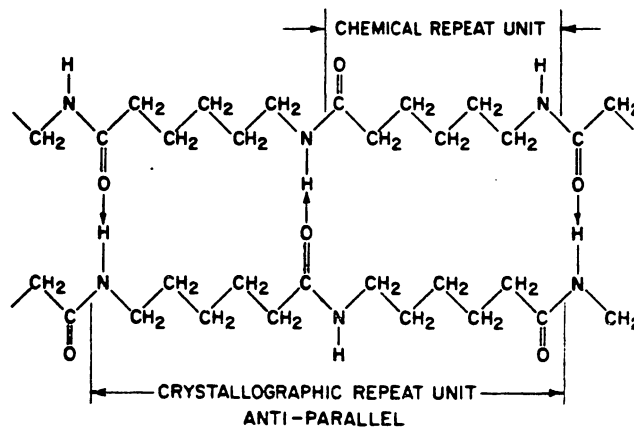
The earliest investigations on the crystal structure of nylon-6 were carried out by Brill (98) in 1943, and later by Wallner (99). This was followed by a more complete crystal structure study by Holmes, Bunn and Smith (100). A monoclinic unit cell was proposed for nylon-6 containing 8 monomeric units with the dimensions

$$a = 9.56 \text{ \AA}, \quad b = 17.24 \text{ \AA}, \quad c = 8.01 \text{ \AA}, \quad \beta = 67.5^\circ$$

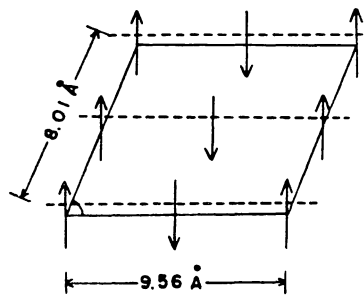
The shape and dimensions of the unit cell are shown in Figure 2.1a. The b axis of the monoclinic unit cell is considered to be the axis of symmetry and it is also the chain axis for nylon-6. This structure is called α form (101) and has the planar zigzag extended chain structure as shown in Figure 2.1b. Hydrogen bonding between the amide and carbonyl groups of adjacent nylon-6 chains results in the formation of hydrogen bonded sheets. Figure 2.1c shows the basal plane of monoclinic unit cell and the chain directions in the unit cell. Nylon-6 is not centrosymmetric and is characterized by a directionality to the molecule



(a)



(b)



(c)

Figure 2.1 Structure of the α -form of nylon-6: (a) monoclinic shape and dimensions of the unit cell, (b) antiparallel chain arrangement of hydrogen bonded sheets, (c) the chain directions shown in the basal plane of the unit cell.

(NH-CO or CO-NH) such that if a molecule is reversed end-for-end, it cannot be superimposed upon itself (Figure 2.1b). The hydrogen bonded sheets of the α form of nylon-6 involve adjacent molecules which have opposite directionality and are said to be antiparallel. Arranged in this manner, all the H-bonds can be formed without strain. If adjacent molecules were of the same direction (parallel), only half of the H-bonds could be formed, and infrared studies (94,101,102) show that this is not the case for the α form. The H-bonded sheets are also staggered up and down instead of always being displaced in same direction. The resulting structure is monoclinic instead of triclinic and there are four molecular segments in a unit cell, where the crystallographic repeat unit consists of two chemical repeat units. Because of crystallographic convention for monoclinic structures, the direction along the molecular chain (chain axis) is labeled the b-axis rather than the c-axis as is the case for the triclinic nylon-66. Because there are four molecular segments rather than one in a unit cell, the Miller indices are doubled for the non-fiber axes. Thus, the intense equatorial reflections of nylon-66 are indexed as (100) and (010,110) doublet, the equivalent reflections for nylon-6 α form are (200) and (002,202) doublet.

Several authors have recognized the existence of more than one crystalline form of nylon-6. A second crystalline form of nylon-6, referred to as the γ form, was first detected by Holmes et al. (100). They suggested that it is due to a parallel relative shifting of alternate chains in the H-bonded sheets by about one atom. This leads to a modified unit cell with poorer H-bonding. Infrared studies (94) show

that the H-bonds are essentially complete, and as a consequence the polymer chain accommodates to this situation by rotation about single bonds into a puckered or pleated conformation. This results in a molecular repeat distance which is shorter than that of the fully extended chains and a molecular packing which is pseudo-hexagonal (101). Pseudo-hexagonal means that the packing of the molecules is such that the location of the molecules can be described by a lattice of hexagonal dimensions but that the structure lacks true hexagonal symmetry. True hexagonal symmetry requires that each element of the structure be exactly duplicated when rotated through 60 or 120° (Figure 2.2). A structure such as that on the right of Figure 2.2 is also described as metrically hexagonal; however, the molecule does not possess the required symmetry to exist in a true hexagonal cell of the observed dimensions.)

{ The pseudo-hexagonal (γ form), was also studied by Slichter (103) who proposed that it was due to parallel rather than antiparallel chains. Ziabicki (104) reported that a pseudo-hexagonal form can be obtained by melt spinning of nylon-6. He also discussed the conversion of this phase to normal monoclinic α phase (105). Tsuruta et al. (106) produced highly oriented γ form fibers using iodine-potassium iodide treatment, which made more detailed studies possible. Other studies (107-110) were published describing the transition between the α and γ crystals by iodine-potassium iodide treatment. Kinoshita (101) and later Vogelsong (111) proposed a hexagonal or pseudo-hexagonal unit cell for the γ form, composed of extended parallel chains with kinks. Vogelsong gave the unit cell dimensions as }

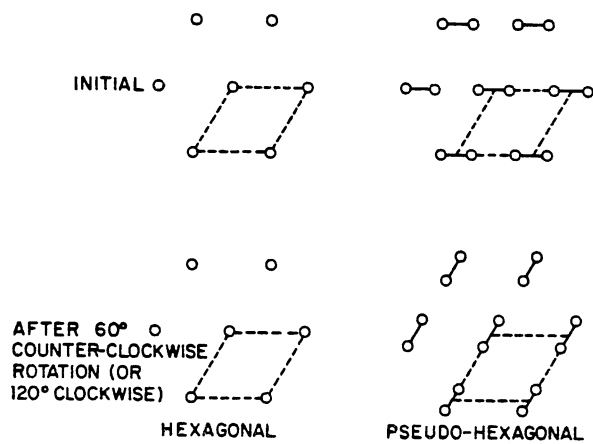


Figure 2.2 Hexagonal and pseudo-hexagonal symmetries. The dashed lines outline the basal plane of a hexagonal unit cell.

Source: Kinoshita, Y., Makromol. Chem., 33, 1 (1959).

$$a = c = 4.79 \text{ \AA}, \quad b = 16.7 \text{ \AA}, \quad \gamma = 60^\circ$$

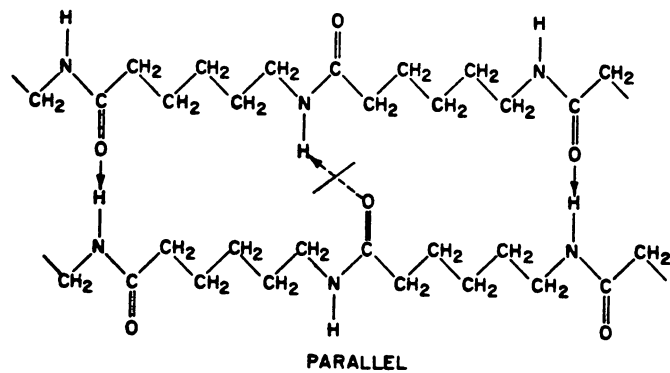
This unit cell would contain only two monomeric units. Later Arimoto (112) proposed a monoclinic unit cell for the γ form with

$$a = 9.33 \text{ \AA}, \quad b = 16.88 \text{ \AA}, \quad c = 4.78 \text{ \AA}, \quad \beta = 121^\circ$$

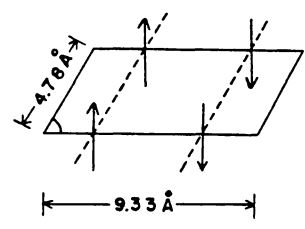
This unit cell nearly exhibits pseudo-hexagonal symmetry and contains four monomeric units. This structure is illustrated in Figure 2.3 and should be compared to the structure of the α -phase shown in Figure 2.1.)

There is a marked difference between the diffraction patterns from the two crystalline forms of nylon-6, α (monoclinic) and γ (monoclinic or pseudo-hexagonal) (100,113-115). As shown in Figure 2.4, two equatorial peaks are present in the α pattern in the 2θ range of $18 - 28^\circ$, against only one present in the γ pattern. Also a strong meridional peak is present in the γ pattern as opposed to a very weak one in the α pattern. A major difference is the reduced repeat distance in the γ form compared to the α form, which results in a change in layer line spacing.)

(Besides these major crystal structures of nylon-6, Roldan and Kaufman (115) summarized a series of studies by proposing that nylon-6 can exist in an " α " form (Holmes et al.), an " α paracrystalline form" (Brill) with variable unit cell parameters, a stable " β " structure and an unstable pseudo-hexagonal structure similar to a nematic liquid crystal which they called the " γ " crystal (Ziabicki and Kedzierska). Several other authors (109,113,116-118) have proposed different crystal structures. Parker and Lindenmeyer (119) have summarized the unit cell data (converted to monoclinic form) for nylon-6; they conclude that there are two crystal forms α and γ , and each may have variable lattice constants. Gianchandani et al. (29,30) have attempted an overall



(a)



(b)

Figure 2.3 Structure of the γ -form of nylon-6: (a) parallel chain arrangement of hydrogen bonded sheets, (b) chain directions shown in the basal plane of the unit cell.

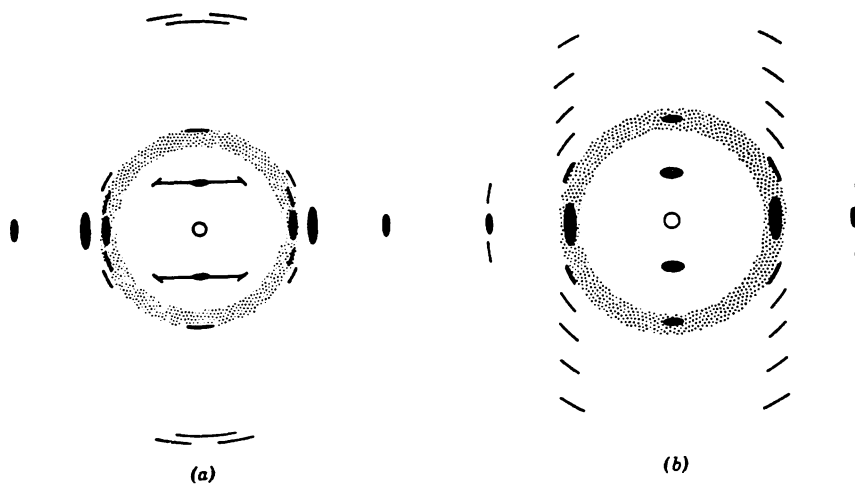


Figure 2.4 Schematic of x-ray fiber diagrams of nylon-6: (a) α -form, (b) γ -form. The fiber axis is vertical.

Source: Miyake, A., J. Polym. Sci., 44, 223 (1960).

classification of structure based on the existence of the two major crystalline forms, α and γ , and the presence of structural defects in most nylon-6 samples. Recent work of Murthy, Ahroni and Szollosi (120) also suggests that the structure of nylon-6 fibers can be discussed in terms of α and γ forms only. }

Gianchandani et al. describe {the phase formed in filaments spun at low speeds after conditioning}. They concluded that this phase {is a poorly developed paracrystalline phase based on the α -crystal form} This " α^* " form corresponds to the γ^* form of Illers et al. (118) and to the pleated α form of Stepaniak et al. (121,122). They further conclude that {the γ phase is obtained by the strain induced crystallization occurring from the oriented melt under dry conditions. This conclusion was based on the fact that an increase in spin draw ratio tends to increase the amount of γ phase. Both α and γ phases in spun filaments exhibit a poorly developed pseudo-hexagonal structure. }

Relative Amounts of Various Phases

Although numerous investigators have studied the structure and properties of nylon-6, only a few have described the methods of obtaining the relative amounts of phases present. All such methods are approximate and depend on the nature of various approximations made in the analysis.

Authors who attempted to separate the relative amounts of phases include Roldan et al. (123), who assumed the existence of a β phase in developing their method of determination. This assumption of separate β and γ phases makes their method obsolete in view of {the more recent conclusions that only α and γ phases need be considered.} Dismore and

Statton (124) employed the crystallization perfection index for nylon-6 and involved a calculation of the separation of the (200) and (002, 202) peaks. This method does not give any indication of the relative amounts of α and γ phases and it is limited to samples for which peaks can be easily resolved, e.g., in a fairly well developed α form structure.

Kyotani and Mitsuhashi (125) use peak heights instead of the areas under curves to determine the relative amounts of phases. Consequently, their method is influenced by the crystallite size and perfection, and will be subject to errors if the peak widths differ in different samples.

Stepaniak et al. (121,122) used a method which involves the separation of intensity distribution from a random sample in the range of $2\theta = 15 - 30^\circ$ into α , γ and amorphous contributions. They obtained an amorphous "template" by scanning the radial intensity distribution of a highly oriented sample. Hence, a total crystalline contribution of the sample was obtained by then subtracting the amorphous intensity from the overall intensity. They assume that the (200) and (002, 202) reflections of the α form occur at $2\theta = 20^\circ$ and 24° respectively. Hence all the crystalline scatter in the range of $2\theta = 18 - 20^\circ$ and above 24° results from the α form. The rest of the scattering is part α and part γ . This approach seems somewhat arbitrary at best.

An extensive literature review was done by Gianchandani et al. (29,30) regarding the approaches made by various researchers in trying to get the relative amounts of α , γ and amorphous phases. They have also determined quantitatively the relative amounts of phases by their own method which uses a combination of X-ray and density data. The same method was later used by Suryadevara (31). Their technique utilizes two

standard samples, the α standard which is mostly α form, and the other, the γ standard which is mostly γ form. They use the integrated intensities of the equatorial scan in the 2θ range $14 - 28^\circ$ and that of the (020) meridional reflection at 2θ of about 11° .)

A mathematical model was used by Heuvel et al. (126) for the separation of the scattering from the two crystalline forms. Three curves, assumed to represent two α reflections and γ and amorphous equatorial diffraction, are fitted by the computer to the equatorial diffraction scans. However, an apparent limitation of this method is that the γ and amorphous contributions are treated as one of the three curves. Later Heuvel et al. (127) developed a five line model that allowed the separation of the diffraction profile into an amorphous peak, two γ and two α peaks. This allows the computation of α , γ and amorphous fractions, but is rather complicated. (By far, the simplest method for separating the relative amounts of phases seems to be that of Gianchandani et al. (29,30) using the (020) reflection. Their results were found to be consistent qualitatively with those of Heuvel et al. (126). The method does not involve complicated analytical procedures to separate overlapping peaks.) Stepaniak et al. (122) cautioned against using the (020) reflection due to possible effect of the slippage of the H-bonded sheets in the γ structure, however, Gianchandani et al. (29,30) argue that this effect is less troublesome compared to the problems associated with separating the equatorial scan into its components. A recent study by Salem et al. (128) argues that quantitative results are best obtained using the five-line model of Heuvel et al. (127). However, this conclusion can also be criticized.

Crystallization Kinetics

{ Experimental observations of the rate of development of crystallinity in polymers are of many types. Sometimes specific volume variation as a function of time at constant temperature is observed or the rate of formation and growth of spherulites is observed directly with a polarizing microscope. Crystallization rates have also been measured using X-ray, infrared and density techniques. }

The overall crystallization rate is frequently analyzed by the well known Avrami equation which gives rate constant and Avrami exponent. However, many experiments show that the equation does not describe the entire crystallization process of polymers, especially the perfection of crystals and a {slow growth of crystallite size which follows the initial crystallization process. The latter process is referred to as secondary crystallization. } (Nylons exhibit primary and secondary crystallization.)

The rate of crystallization of a nylon is dependent upon the chemical structure, molecular weight, thermal history and the presence of nucleating agents or other additives. For a given class of nylons, the rate of crystallization will typically rise with increasing amide concentration. Once a certain molecular weight is attained, the rate of crystallization at a given temperature is an inverse function of molecular weight, because the increase of viscosity with molecular weight decreases the mobility of the polymer chains. Temperature is the most important parameter for control of the rate of crystallization and resultant level of crystallinity. For any semicrystalline polymer there is a particular temperature or degree of supercooling at which the rate of crystallization is maximum. Above T_m and sufficiently below T_g the

rate of crystallization is zero. } Polyethylenes crystallize so rapidly over a broad temperature range that they cannot be quenched to a fully amorphous state, whereas PET can be quenched to fully amorphous state easily. Nylons are the intermediate between the two extremes and encompass a considerable range depending upon chemical structure. }

{ After initial (primary) crystallization, a typical nylon is metastable and will undergo further crystallization. In this secondary crystallization, the plasticizing effect of water is quite important. For any nylon, the lower the level of crystallinity and the higher the level of absorbed water, the higher will be the rate of secondary crystallization at a given temperature. A prime difference between primary and secondary crystallization is that the latter usually does not involve morphological change to any great extent. }

{ Many workers have measured the rate of growth of spherulites of nylon-6 and 66 (129-132). Some authors have reported the crystallization kinetics of nylon-6 as a function of temperature during the crystallization process. The rate constants are calculated by use of the Avrami equation:

$$\theta = \theta_{\infty} \{1 - \exp(-Kt^n)\} \quad (2-1)$$

where θ and θ_{∞} are crystallinity level at time t and infinite time (time to achieve equilibrium crystallinity) respectively. K is a rate constant and n is a constant called the Avrami exponent whose value depends on the mechanism of nucleation and growth of crystals. }

{ Burnett and McDevit (130) have studied the growth of nylon-6 spherulites in a temperature range of 102 to 182°C. They plotted the rate of growth versus temperature and obtained a typical bell shaped

curve. They observed that, at constant temperature, growth rate was constant. Inoue (132) obtained crystallization isotherms of nylon-6 at temperatures from 205 to 215°C using a dilatometric technique. The Avrami equation was used to calculate the half time of crystallization, $t_{\frac{1}{2}}$, which was 18 minutes or higher depending on the crystallization temperature. Later Inoue (133) studied the effects of various nucleating agents on the rates of crystallization. The use of nucleating agents resulted in decrease of induction time and increase in the rate of crystallization.)

{ Magill (134) studied the effects of melt history, moisture content and relative viscosity on induction time during isothermal crystallization. He also measured the kinetics of isothermal crystallization over a wide range of temperatures using an online camera and unpolarized light (135). He observed the maximum rate of crystallization to occur at about 140°C and the half time of crystallization was ten seconds. The half time increased for higher crystallization temperatures.)

/ Morphology and Orientation

{ Morphology

Polymers capable of crystallization from solution generally precipitate as thin layer crystals termed "lamellae" (136). These lamellar crystals are a result of chain folding with the idealized conformation being that of "adjacent reentry" as illustrated in Figure 2.5. Realistically, depending on the condition of crystallization, the folds may project with varying degrees of looseness above the surface.

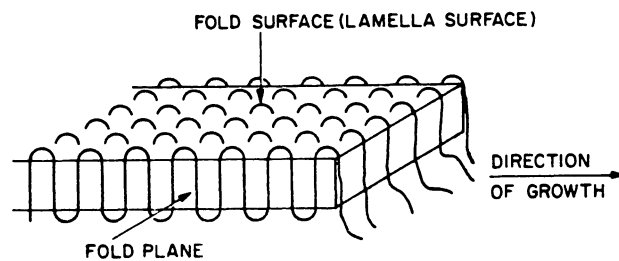


Figure 2.5 Illustration of folded-chain lamellae with idealized adjacent reentry of chains.

Source: Geil, P. H., *Polymer Single Crystals*, Interscience, New York (1963).

A somewhat different chain folding mechanism, not detailed yet, is needed for nylon-6 (137-139) where the molecular segments are normal to the surface of the lamellae. The fold surface in nylon-6 appears to be parallel to the (120) plane (140). Geil (137) obtained single crystals of nylon-6 by precipitating from a glycerin solution; he found lamellae thicknesses of about 60 Å. Ogawa et al. (139) reported that the diffraction pattern of such nylon-6 crystals correspond to the γ pseudo-hexagonal form. In commercial processing such as extrusion, considerable mechanical and thermal stresses give rise to a variety of non-spherulite oriented structures (141). The nylons differ from most other crystalline polymers in that under the usual conditions of processing, the resulting morphology is much more spherulitic. This appears to result from the relatively large supercooling and slow crystallization.)

Orientation

The crystallinity is influenced by the orientation of hydrogen bonds with respect to the chain molecules. Spherulites and row structures result from various orientation of lamellae. The tensile strength and modulus increase greatly as the molecules are oriented so that they become parallel to the fiber axis. As chains become aligned parallel to the fiber axis, more covalent bonds come into position for load bearing. However, the sensitivity of physical properties of nylon fibers to the spinning conditions and post treatments show that more complex types of morphology are involved. It has been proposed (124) that the initial drawing step produces a structure in which the chains are highly extended and essentially parallel to the axis with relatively

few chain folds. The degree of uniformity of the hydrogen bond direction is low, resulting in low crystallinity. Subsequent heat treatments result in breaking of hydrogen bonds. Enough mobility is thus provided to allow the chains to fold into small folded chain aggregates similar to lamellae but with a high portion of chains connecting one fold-chain to another (Figures 2.6a and 2.6b).

Quantitative analysis of orientation in fibers was started by Hermans (142) defining orientation factor as a ratio of the resultant polarization anisotropy of a given fibrous system to the maximum theoretical polarization anisotropy in the principal directions of the polarizability tensor. Hence

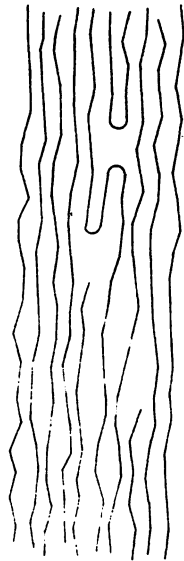
$$f_H = \frac{\alpha_{\parallel} - \alpha_{\perp}}{\alpha_1 - \alpha_2} \quad (2-2)$$

where α_{\parallel} and α_{\perp} are polarizabilities in directions parallel and perpendicular to the fiber axis, respectively, and α_1 and α_2 are polarizabilities, parallel and perpendicular to the polymer chain. For rigid crystallites Hermans showed that

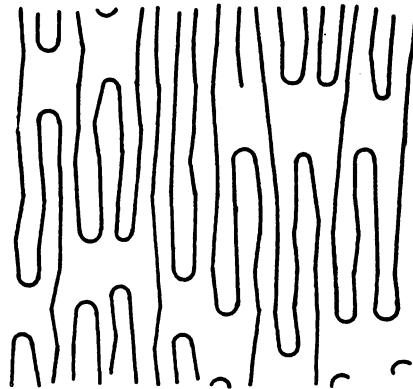
$$f_H = \frac{3 \langle \cos^2 \phi_{c,z} \rangle - 1}{2} \quad (2-3)$$

where $\phi_{c,z}$ is the angle between the chains and a reference axis z.

Stein et al. (144,145) have extended the above equation to calculate the orientation factors of all three crystallographic axes in crystal systems with orthogonal axes. Wilchinsky (146) has generalized the analysis to allow computation of orientation factors for non-orthogonal unit cells. His analysis can be used to determine the



(a)



(b)

Figure 2.6 Model of (a) drawn and (b) drawn and annealed fiber.

Source: Dismore, P. F. and W. O. Statton, J. Polym. Sci.,
13, 133 (1966).

orientation factors of a certain crystallographic axis even when reflection from a set of planes which are normal to the axis are not available.} Among other applications this analysis has been used by Wilchinsky (147), Hoshino et al. (148) and Samuels (149) to obtain the orientation factors of PP films.

{ A number of papers have been published on the quantitative determination of crystalline orientation factors of nylon-6. Sakoaku, Morosoff and Peterlin (150) reported data on chain axis orientation of nylon-6 bristles. They made use of Wilchinsky's analysis using the (200), (002) and (202) reflections of monoclinic nylon-6 crystals. They reported an increase in the chain axis orientation factor when nylon-6 fibers are drawn. Bankar et al. (23,26) calculated the orientation factors of spun filaments assuming a hexagonal symmetry. Their results show that the chain axis crystalline orientation factor, f_c , increases with take-up velocity and spinline stress, but f_a decreases. This implies that as the take-up velocity increases the c-axis tends to become more aligned to the fiber axis while the a-axis tends to become more perpendicular to the fiber axis. Gianchandani et al. (29,30) also reported an increase in the orientation factors of nylon-6 with draw down. The increase was from 0.07 to 0.71 for an increase in spin draw ratio from 15 to 240. They found that orientation was little affected by subsequent annealing. They also followed the change in chain axis crystalline orientation of nylon-6 when the spun filaments were drawn at 90°C. Several other authors (122,133,151-153) have also calculated the orientation factors of nylon-6. The general trend in these studies was

that the chain axis orientation factor increased with take-up velocity and also when the fibers were drawn.)

Structure Development During Spinning

Low and Moderate Speeds

Properties of melt spun fibers depend largely upon their structure formation. By this is meant their molecular orientation, crystallinity and morphology. The structure, in turn depends on the spinning process variables. Carothers and Hill (9) showed the importance of the effects of spinning variables like fiber tension on the X-ray diffraction patterns and explained the observed effects in terms of the molecular orientation. Hearle (154) reviewed the early studies of the fine structure in fibers but did not consider any process variables. Keller (155) presented X-ray data to support his qualitative discussion on "Shish-Kebab" or "row" structures which were considered to be complex structures formed from lamellar crystals and fibrils due to deformation imposed during crystallization. Ziabicki and Kedzierska (40,104,156) were the first to publish X-ray patterns and birefringence data of melt spun fibers and showed that orientation of molecules increased with take-up stresses. Furukawa et al. (157) and Kitao et al. (158) emphasized study of crystallinity development in the spinline. Spruiell and White (9) correlated the interaction of stress, temperature and cooling rate through the continuous cooling transformation (CCT) curve concept, a well known concept for dealing with phase transformation kinetics in metallurgy. The stress and cooling rate were shown to influence the temperature at which crystallization begins. They

suggested that stress and orientation decreased the free energy of formation of the crystal nuclei which would lead to an observably higher crystallization rate.)

Abbott and White (15) examined the variation of orientation and crystallinity with spinning speed, with melt flow rate and melt temperature in melt spun HDPE and LDPE fibers. The modulus and tensile strength were found to increase with increasing crystalline orientation. Online X-ray measurements were made by Katayama et al. (159) on PE, PP and polybutene-1. They found that increased molecular orientation caused increased crystallization rate. They also investigated the interaction of the heat of fusion and the rate of heat transfer from the spinline. Aggarwal et al. (160) found that stretching PE initially involved alignment of the a axis with the stretch direction with the b and c axes randomly distributed. Upon further deformation the c axis tended to align with stretch direction. Ishikawa (161) using compression and stretching techniques coupled with X-ray diffraction on PE fibers found a difference in morphology with spinning conditions. Southern et al. (162) interpreted the high orientation and unusual properties of PE fibers in terms of an extended chain morphology. Keller and Machin (35) and later Fung and Carr (36), using electron microscopy on melt spun PE fibers concluded the presence of row nucleated structures caused by orientation of melt during draw down. These structures were explained on the basis of the skin-core effect caused by a stress effect in the solidifying fiber producing higher degree of orientation at the fiber surface and chain tilting with respect to fiber axis at an angle that varied with the radius. Dees and Spruiell (16) also concluded that the

morphology of the as spun PE fibers is row nucleated and having twisted lamellar folded chain overgrowth; the quantity of each depended on the spinning conditions. This morphology was explained by the combination of increased crystallization rate, caused by the spinline stresses, and a change in variable that affected the rate of heat transfer.

Henson and Spruiell (163) and Nadella et al. (28) studied spinline stresses for PP fibers and found that the morphology developed was determined primarily by spinline stresses. SAXS studies (20,24,164,165) on PP fibers showed a continuous ring at low take-up velocities, interpreted by Samuels (37) as being due to unoriented lamellar superstructure which could be due to a spherulitic growth. Binsbergen (166) studied orientation induced nucleation in PP and found that crystalline structures oriented along the lines of strain. Garber and Clark (167) concluded that crystallization under a high stress produced a highly oriented row nucleated morphology in polyoxymethylene.

Simpson et al. (38), Chappel et al. (39), Slichter et al. (168,169), Starkweather (153,170) and Danford et al. (27) have studied the crystallinity and orientation of nylon-66 fibers by performing online X-ray experiments and/or birefringence measurements. Nakamura et al. (171), Dumbleton (172) and Benaim (173) have studied spinline stresses for PET fibers and again showed that crystallization was due to enhanced crystallization kinetics at large spinline stresses.

(Ziabicki and Kedzierska (40,104) were among the earliest to make basic studies of structure development during melt spinning of nylon-6. They obtained the WAXS patterns and measured birefringence of spun fibers which was found to be an increasing function of spinline

stresses. Hamana et al. (41,42) and Ishibashi et al. (43) made online birefringence measurements as a function of spinline position. Ishibashi and Ishii (174) and Ishibashi and Furukawa (175) studied the effect of heating chambers placed around the spinline on birefringence of the running filament and found that the increase in birefringence is due to crystallization of the filament.)

Studies of melt spun nylon-6 have also been published by Pasika et al. (176), Sakoaku et al. (150), Wasiak and Ziabicki (177), Slichter (103) and Ruland (178). Bankar et al. (26) and Hiramani and Tanimura (179) made online WAXS and birefringence measurements. (Bankar et al. concluded that as spun fiber is amorphous and that the crystallization of nylon-6 takes place on the bobbin. They also report a gradual increase in birefringence with increasing take-up velocity.)

(Gianchandani et al. (29,30), from WAXS and birefringence measurements, concluded that nylon-6 filaments undergo both primary and secondary crystallization. They predicted strain-induced crystallization on the running threadline. They have made a quantitative analysis of the α and γ fractions present in nylon-6, using a combination of X-ray and density data. They concluded that the relative amounts of phases in nylon-6 filaments depend upon the molecular orientation developed during spinning. Higher amorphous and α -phase fractions and lower γ -phase fractions were obtained for low orientation samples than for higher orientation samples.)

Structure development in the wet spinning of nylon-6 has been studied by Kiyotosukuri et al. (180) and by Hancock et al. (181). They

report that in most cases, wet spun fibers exhibited the α -monoclinic crystal structure.

✓ High Spinning Speeds

(High speed spinning was aimed at eliminating the drawing step. Higher molecular orientation and better mechanical properties were expected for high speed spun fibers when compared to fibers spun at lower speeds. Early studies of Ziabicki and Kedzierska (40) and Nakamura et al. (171) on the structure of fibers spun at 3,000-4,000 m/min showed this and also that the mechanical properties of high speed spun fibers were inferior to those of drawn fibers spun at lower speeds. Studies by Shimizu et al. (182) and Heuvel and Huisman (72) revealed that high speed spun fibers exhibited a high degree of crystallinity, comparable to that in drawn fibers, but inferior mechanical properties. High speed spinning also gives higher per spindle productivity, but this would be only of secondary importance, if the properties can match those of the drawn fibers, which would be of great importance. There has been, however, relatively little information in the literature to date on commercial high speed spinning. This could be attributed to the complications that arise in devising the take-up equipment to wind fibers at high speeds and also the proprietary nature of such research. Hasegawa (183) discusses the mechanics of high speed take-up machines and the problems associated with them. A great difficulty with high speed spinning is the filament breakage during winding.)

(In spite of the difficulties, fibers have been spun at speeds up to 10,000 m/min using an air jet nozzle and a godet at the laboratory scale by Shimizu and coworkers (60-71,182).) Study on PP (182) indicated that

fiber diameter depends on spinline distance and air pressure in the nozzle. They found (60) that beyond 3000 m/min, the yield point in the stress-strain curve had disappeared. The birefringence was independent of extrusion temperature but the density remained a function of the temperature and cooling rate. They also found (61) a drastic increase in the initial Young's modulus, the thermal contraction and a decrease in SAXS intensity, in addition to a shoulder in the melting peak in DSC traces. These findings were interpreted in terms of constrained amorphous chains trapped between crystallites when the polymer crystallized under stress. Furthermore, the elastic recovery of the fiber was affected by spinning conditions (62).

Study on PET (63) indicated that below 4000-5000 m/min the fiber structure formation takes place at lower take-up velocities with increasing molecular weight due to increasing elongational viscosity. Also, the degree of crystallinity and the molecular orientation reached limiting values at take-up speeds above 5000 m/min. Beyond some critical spinning condition, a decrease in density and birefringence, crimping of the fiber and the appearance of a shoulder in melting peak in DSC traces resulting from sliding or scission of the molecules or increased void content was noted. A subsequent study on PET (64) showed that take-up speed primarily influenced fiber structure formation whereas the effect of changing the mass flow rate was minor in comparison. A later study (65) indicated that beyond 7000 m/min the density and birefringence decreased and degree of crystallinity achieved a limiting value and SAXS patterns changed from a four spot X pattern to a two spot meridional pattern. The crystallites were almost completely oriented while the

orientation of the amorphous regions remained low and exhibited a maximum at 6000 m/min. At very high take-up speeds, the skin-core effect was noted, the skin having increased number of voids, degree of crystallinity and molecular orientation being higher than in the core. This effect presumably resulted from large radial stress and temperature gradients within the fiber.

Beyond 3000 m/min, PET (67) was observed to exhibit an online "necking" phenomenon, an apparent drawdown of the fiber diameter to its final value in a very short distance. Shimizu postulated the existence of an oriented mesophase in the neck region prior to crystallization. The neck region appeared closer to the spinneret with increasing take-up velocity or decreasing mass throughput. WAXS patterns (70) revealed that the crystallite size increased in both the chain and lateral dimensions while the imperfection parameter decreased with take-up speed. This interpretation of WAXS patterns was based on the existence of an oriented mesophase, an intermediate between the crystalline and amorphous phases (71).

Amongst other groups, Heuvel and Huisman (72,73), Hamidi et al. (74), Yasuda (75), George et al. (184), Bragato and Gianotti (76,77) have also studied high speed spun PET fibers. (Nylon-66 studies have been reported by Shimizu (67), Lecluse (185) and Colcough and Baker (186). Shimizu et al.) (68) reported polymorphic response of poly(ethylene - 1,2 - diphenoxyethane - p,p - dicarboxylate) (PEET) to spinning conditions. (In a later study Shimizu et al. (70) compared several polymers such as PET, PP, nylon-6 and nylon-66.)

{ Studies on high speed melt spun nylon-6 fibers were carried out by Heuvel and Huisman (187) and Shimizu et al. (66). These studies were made at higher speeds than those reported by Ziabicki and Kedzierska (40) and Nakamura et al. (171). High crystallinity and orientation were observed with increased take up speeds which were similar to the results from high speed spinning of PET (72). Heuvel and Huisman's results (187) show that nylon-6 yarns spun at speeds below 3,000 m/min are not completely crystallized and that the crystallization also takes place after moisture pick up during conditioning. Yarns spun at speeds higher than 3,000 m/min, however, produce a stable crystal structure and there is little further crystallization occurring. Birefringence data collected by Shimizu et al. (66) as a function of time after spinning support Heuvel and Huisman's results. Both studies report an increase in γ -phase with an increase in take-up speed, and the increase becomes lesser at higher speeds. Drawing the filaments resulted in the transition from γ to α -form. Heuvel and Huisman (187), who emphasized the characterization of the crystalline phase, used a five-line model to computer fit the equatorial profile in order to separate the X-ray scattering from the γ -phase from that from the amorphous phase (63). They propose that at take-up speeds greater than 2,500 m/min, γ -crystals are mainly generated from orientation induced nuclei and α -crystals grow slowly after moisture pick up. They obtained better oriented γ -crystals which were larger in dimensions compared to the α -crystals. Mechanical properties study of nylon-6 filaments spun at high speeds by Shimizu et al. (66) indicates the increase in tensile strength and decrease in elongation to break.)

{ A more recent study by Suryadevara (31) emphasized the effect of molecular weight in the structure development of nylon-6 filaments spun at high speeds. He reported that the spinline stresses increased rapidly with take-up velocity and molecular weight. The increase with molecular weight was more rapid at higher take-up velocities than at lower ones. The WAXS patterns indicated a significant level of crystallinity, and a high γ -phase content at high take-up velocities in low molecular weight samples. The total crystalline fraction and the γ -phase content decreased with increase in molecular weight. This was attributed to the slower crystallization rates and lower ultimate crystallinities for high molecular weight samples. Increased molecular weights resulted in increased crystalline orientation factors. Birefringence and densities increased with take-up velocity and molecular weight. }

Theoretical Aspects of Melt Spinning

General

Complex interrelations between momentum transfer and heat transfer and rheological properties of the fiber forming material determine the shape of the spinline, the regularity and uniformity of resulting fibers, and their resulting structure and mechanical properties. Transition from low to high spinning speeds is associated with transition from a viscosity controlled process to one controlled by inertia and air drag. At very high speeds air drag becomes especially important and a dynamic problem that excites many researchers is the appearance of abrupt deformation of the spinline resembling the necking in cold drawing of solid polymers. The occurrence of this phenomenon at

high speeds has been confirmed in several independent studies using both online and offline measurements. The deformation profile of the spinline and the appearance of neck-like deformation play an important role in the development of internal structure and in the stability of the process. Elucidation of cooling, rheological properties of the polymer (molecular weight and temperature dependent elongational viscosity) and crystallization provides a critical information for optimization of the melt spinning process.

Although the initial studies of melt spun fibers began in 1932 by Carothers and Hill (9), the first detailed series of studies of both theoretical and experimental aspects of the process to appear in the open literature were performed by Ziabicki and Kedzierska (40,104,156,188,189) in the late 1950's and early 1960's. They used the framework of continuum mechanics to formulate the governing equations of mass, momentum and energy balances in the spinline. The continuity equation was expressed as (189)

$$W = AV\rho = \text{constant} \quad (2-4)$$

where W is mass flow rate, A is cross-sectional area, V is the spinning speed and ρ is the density of the fiber. This equation applies at any point along the threadline provided a steady state condition has been achieved.

Force Balance

Ziabicki (188) first reported a force balance for a fiber spinline schematically shown in Figure 2.7. The forces acting on the spinline include the applied tension F_L , the vertical drawdown force of gravity,

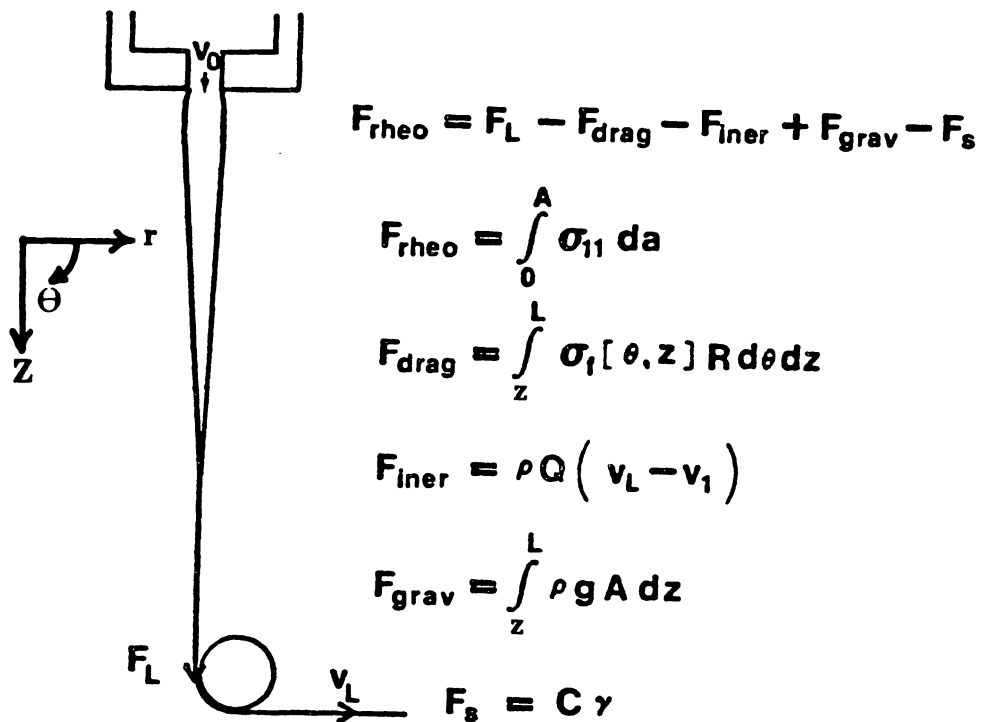


Figure 2.7 Schematic of forces in fiber spinline.

F_{grav} , the forces due to frictional air drag, F_{drag} , the inertial forces due to reaction to acceleration of the fiber, F_{iner} , and the force due to surface tension on the exposed fiber-air interface, F_{surf} . The rheological force, F_{rheo} , acting to deform the descending fiber is the resultant of the applied forces and other contributing components listed above. The force balance was expressed as

$$F_{rheo} = F_L + F_{grav} - F_{drag} - F_{iner} - F_{surf} \quad (2-5)$$

At any position z on the spinline these forces may be expressed as

$$F_{grav} = \int_z^L \rho g A dz \quad (2-6)$$

$$F_{drag} = \int_z^L \sigma_d(\theta, z) R d\theta dz \quad (2-7)$$

$$F_{iner} = W(V_L - V) \quad (2-8)$$

$$F_{surf} = C \gamma \quad (2-9)$$

$$F_{rheo} = \int_0^A \sigma_{11} dA \quad (2-10)$$

where A is the cross-sectional area, σ_d is the air drag shear stress, σ_{11} is the tensile stress within the filament, ρ is the density, W is the mass flow rate and C is a constant determined by the filament shape.

The relative magnitudes of the different force components vary considerably with the spinning conditions. If no tension is applied to the spinline then gravitational force F_{grav} alone acts to develop the spinline dynamics. If tension is applied then both F_L and F_{grav} must be considered. As the drawdown is increased, F_L will come to dominate F_{grav} . The higher spinning speeds involve increased drawdown rates to give rise to increased frictional drag and inertial forces. Surface

tension force, F_{surf} , is generally considered negligible compared to the magnitude of the other force components. Thus, depending upon drawdown velocity, several regimes have been identified by Bankar et al. (25) for nylon-6 and are summarized below

Gravitational spinning - Trouton asymptote (190)

$$F_{rheo} \simeq F_{grav} \quad (2-11)$$

Low drawdown

$$F_{rheo} \simeq F_L + F_{grav} \quad (2-12)$$

Moderate drawdown - Ziabicki-Kedzierska asymptote

$$F_{rheo} \simeq F_L \quad (2-13)$$

High drawdown or high speed spinning

$$F_{rheo} \simeq F_L + F_{grav} - F_{drag} - F_{iner} \quad (2-14)$$

If filament diameter and temperature profiles along the spinline are known, F_{grav} and F_{iner} can be evaluated using the available experimental data. The main unknown in the force balance of the fiber spinline is the air drag force, F_{drag} . In the case of high speed spinning this component of the force balance becomes increasingly important.

There have been a number of experimental and theoretical investigations to estimate F_{drag} . The F_{drag} is represented, as is traditional in engineering Newtonian fluid mechanics, through a friction factor C_d commonly known as the drag coefficient and is given as

$$\sigma_d = C_d \left(\frac{\rho V^2}{2} \right) \quad (2-15)$$

The F_{drag} is in general expressed as

$$F_{drag} = \rho C_d V^2 A \quad (2-16)$$

To evaluate C_d for melt spinning, Sakiadis (46) performed a laminar and turbulent boundary analysis to calculate the drag on a constant diameter cylinder passing through a stationary fluid at a constant velocity. He considered the drag force as a function of parameter ξ defined by

$$\xi = 8 \left(\frac{Re_x}{Re} \right) \quad (2-17)$$

where Re_x and Re are the Reynolds numbers based on the length and diameter of the cylinder, respectively. Andrews (191) studied experimentally the air drag on a stationary filament in a wind tunnel and expressed drag coefficient as

$$C_d = 1.30 Re^{-0.61} \quad (2-18)$$

Similar experiments by Aoki et al. (192) obtained

$$C_d = 0.18 Re^{-0.44} \quad (2-19)$$

Sano and Orii (45) measured tensions at various positions along the moving threadline and determined that

$$C_d = 0.68 Re^{-0.8} \quad (2-20)$$

Hamana et al. (42) performed similar experiments as that of Sano and Orii and found

$$C_d = 0.37 Re^{-0.61} \quad (2-21)$$

The latter two correlations involved fiber diameters in the 30 - 100 μm range and spinning speeds in the range of 200 - 1200 m/min and involved Reynolds numbers in the 10 - 100 range.

Kwon and Prevorsek (193) performed experimental studies on air drag forces using a technique which involved the air boundary layer

surrounding the fiber being spun. Their results indicate that the air drag values obtained from available correlations underestimated the actual drag force. A possible cause was the swaying of the fiber which gave an apparent diameter larger than the actual diameter of the fiber.

Gould and Smith (194) also experimentally measured the drag on filaments and yarns hanging from a sensitive strain gauge. The Reynolds number range was between 20 and 200 for speeds approaching 6000 m/min and yarn diameter less than 300 μm . They also found that the drag force increased significantly when the fiber was allowed to vibrate freely. Gould and Smith also analyzed the data of Sano and Orii (45) and Hamana et al. (42) and found that these earlier correlations as well as their own data could be represented by

$$C_d = 0.27 Re^{-0.61} \quad (2-22)$$

Under these conditions compact yarns behaved as a thick fiber of the same surface area. They also found that drag forces on fibers of 10 - 100 μm in diameter are not affected by the presence of other filaments unless the spacing is less than 100 μm .

Kubo (195) describes an extended theory of the boundary layer on the surface of the running filament, including the effects of inertia and heat flux which causes considerable variation in kinematics of air surrounding the hot filament. Matsui (196) considers the boundary layer on the filament to be turbulent at high speeds because of the large value of the length based Reynolds numbers and formulated a simple expression for C_d using turbulent theory. This results in

$$C_d = 0.37 Re^{-0.61} \quad (2-23)$$

Shimizu and Okui (197) indicate the limited importance of air drag for structure formation as compared to inertial forces. They discuss two sections of the spinline; the deformation section and the downstream section after solidification. In the deformation section air drag plays secondary role in the balance of forces. Most of the structure formation takes place in the deformation section while skin friction is well developed in the downstream section of the spinline.

Thus numerous investigations have been carried out to evaluate the air drag coefficient. Unfortunately, there does not exist a general consensus on the actual numerical value of the coefficients in the drag coefficient expression, but there is agreement that the expression has the form

$$C_d = \text{const } Re^{-n} \quad (2-24)$$

where the exponent n is probably about 0.61.

Rheology

Two different flow geometries are involved in fiber spinning - shear and uniaxial extension. The respective material characteristics in these two geometries affect the fiber formation process. Flow within the spinneret channel, die swell and melt fracture phenomena are controlled by shear flow characteristics of the spinning melt under extrusion conditions (shear rates range up to $10^2 - 10^4 \text{ sec}^{-1}$; extrusion temperatures generally range from 150 to 300°C). On the other hand, the kinematics and dynamics of deformation occurring well below the spinneret are affected by extensional characteristics (elongational viscosity) over a wide range of temperatures from the extrusion

temperature to the ambient medium temperature and at rather small elongation rates not exceeding 80 sec^{-1} except at high spinning speeds.

The rheological behavior of polycondensate polymer melts such as nylons and polyesters is nearly Newtonian up to shear rates of 10^2 sec^{-1} whereas PP and other polyolefin melts exhibit viscoelasticity involving pronounced normal stresses and relaxation effects.

The temperature dependence of shear viscosities can be described by the Arrhenius equation

$$\eta(T) = \text{const} \exp\left(\frac{E_\eta}{RT}\right) \quad (2-25)$$

where E_η is the activation energy for flow. In the extrusion temperature range E_η can often be considered constant, usually of the order of 8 - 15 Kcal/mole, but it increases considerably at lower temperatures. In such a case viscosity can be approximated by the empirical formula of Williams, Landel and Ferry (198) (known as WLF equation)

$$\log_{10} \left[\frac{\eta(T)}{\eta(T_g)} \right] = \frac{-17.44(T - T_g)}{(51.6 + T - T_g)} \quad (2-26)$$

where T_g is the glass transition temperature. Newtonian viscosity of polymer melts is strongly affected by the weight average molecular weight of the polymer, M . The most popular empirical equation has the form

$$\eta = \text{const} M^n \quad (2-27)$$

where exponent n ranges from 1 to 3.5, the lower values are for low M and values up to 3.5 are for high M .

Much less is known about the rheological characteristics of extensional flow. Unlike shear viscosity, steady state elongational

viscosity of polymer melts is a nearly constant or slowly increasing function of the elongation rate. The pioneering study of elongational flow was reported by Trouton (190) who set out to determine the 'coefficient of viscous traction' of pitch. The "Trouton law" states that at the limit of infinitely small elongation rates, elongational viscosity η_{el} is three times the shear viscosity

$$\lim_{q \rightarrow 0} \eta_{el} = 3\eta \quad (2-28)$$

Since 1960 studies of elongational flow have been reported for various polymer melts including polystyrene by Ballman (199), polyethylenes by Cogswell (200), Meissner (201,202) and White and his coworkers (50-55) and PP by Ishizuka and Koyama (48,49). Of these only PP is a major commercial melt spun fiber forming material. Other important fiber forming polymers such as nylons and PET have too low a viscosity to be easily characterized by the independent rheometer technique used for the polyolefins. The low rigidity of these filaments at high temperature involved in such measurements also makes them to be easily disturbed from the constant deformation rate or tension stress flows, required with such measurements.

There have been attempts to use the spinline as an elongational rheometer to arrive at elongational viscosities rather than through an independent rheometer. Han and coworkers (56,80,203) examined the rheological aspects of isothermal spinning by considering elongational viscosity, deformation and heat transfer effects. They arrived at a semi-empirical generalized equation for the elongational viscosity as a function of the elongation rate and temperature. The mathematical model developed for elongational viscosity was similar to that of Kase and

Matsuo (78,79,204) and required a numerical solution but satisfied the mass, momentum and energy balances. The apparent elongational viscosity was computed for PP (79) and nylon-6 (43) from experimental melt spinning data. Hill and Cuculo (205) performed an experimental study on the melt spinning of PET which included the effects of molecular weight, temperature and elongation rate on the elongational viscosity. Chen et al. (14) and Spearot and Metzner (206) considered the influence of viscoelasticity and the deformation history on the process and Acierno et al. (13) performed an investigation on non-Newtonian melt behavior in isothermal spinning. Matowich and Pearson (207) and White (208) have attempted a theoretical analysis of melt spinning taking a non-Newtonian approach toward the rheology of the melt involved. Larson (209) compared the isothermal spinline velocity profiles predicted by Doi-Edwards and co-rotational Maxwell constitutive equations. Both models predicted limited spinnability (short spinline and low draw ratios) which contrasted with the unlimited spinnability found using an upper convected Maxwell constitutive equation. The spinning behavior of the Doi-Edwards formulation was dominated by the elongational strain measure rather than the distribution of relaxation times. Investigations discussed so far were limited to low spinning speeds.

Ziabicki (210) has recently tried to introduce the effect of high spinning speeds on the rheology of the polymer melt. High speed spinning involving high deformation rates may lead to the appearance of viscoelastic effects that are absent (or negligibly small) at lower speeds. He points out that according to the similarity principle characterized by the Deborah number (the product of relaxation time and

deformation rate), there should be a rheological correspondence between slow spinning of highly viscoelastic polymers (narrow MWD PP and branched PE) and ultra high speed spinning of nearly inelastic PET and nylons. He also explains "necking" behavior of the spinline in terms of elongation rate dependence of elongational viscosity in addition to strong temperature dependence. Other workers have so far only introduced ideas on the effect of high speeds on rheological behavior and have suggested empirical modifications to elongational viscosity; however, everyone seems to agree that there is a need for experimental studies of the effect of crystallization on elongational viscosity.

Heat Transfer

Heat transfer from the melt spinline to the ambient medium involves several mechanisms: radiation, free convection and forced convection. The effect of radiation is strongly dependent on the temperature of the fiber. Consequently it is greater in the initial period of the cooling process, where the temperature is greatest. Because the melt temperature of polymers is generally less than 300°C, the radiation contribution is usually negligible compared to the convective heat transfer.

Neglecting viscous heat dissipation and heat released by crystallization, the temperature profile within the descending fiber is determined by the steady state energy equation

$$\rho C_p \left(V_r \frac{\partial T}{\partial r} + V_z \frac{\partial T}{\partial z} \right) = -\frac{1}{r} \frac{\partial}{\partial r} (r q_r) - \frac{\partial q_z}{\partial z} \quad (2-29)$$

where ρ is the melt density, C_p is specific heat capacity, q_r and q_z are the r and z components of heat flux, respectively, and V_r and V_z are r and z components of velocity and T is the melt temperature. When

simplifying assumptions are made that V_z and T depend on z only, q_z is negligibly small and C_p is independent of T , equation (2-29) becomes

$$\rho C_p V_z \frac{dT}{dz} = -\frac{1}{r} \frac{\partial}{\partial r} (r q_r) \quad (2-30)$$

Further, the following boundary condition describes the physical situation under consideration

$$\text{at } r = R(z), q_r(R(z)) = h(T - T_a) + \lambda \varepsilon (T^4 - T_a^4) \quad (2-31)$$

in which λ is the Stefan-Boltzman constant, h is the heat transfer coefficient, T_a is the ambient medium temperature and ε is the emissivity. Multiplying both sides of equation (2-30) by $r dr$ and integrating the result from $r = 0$ to $r = R$ and using the boundary condition of equation (2-31)

$$\frac{1}{2} \rho C_p R^2 \frac{dT}{dz} = -R [h(T - T_a) + \lambda \varepsilon (T^4 - T_a^4)] \quad (2-32)$$

Further using continuity

$$W = \rho \pi R^2 V_z \quad (2-33)$$

we finally get

$$\frac{dT}{dz} = -\frac{2}{C_p} \left(\frac{\pi}{\rho W V_z} \right)^{\frac{1}{2}} [h(T - T_a) + \lambda \varepsilon (T^4 - T_a^4)] \quad (2-34)$$

On the right side of equation (2-34) the first term is convective heat transfer and the second term is for radiation. Such an expression was first developed by Kase and Matsuo (78) in their analysis of spinline heat transfer and dynamics. Nakamura et al. (171,211) included the heat generated due to crystallization and neglected the radiation term; this resulted in the expression

$$\frac{dT}{dz} = -\frac{2}{C_p} \left(\frac{\pi}{\rho W V_z} \right)^{\frac{1}{2}} h(T - T_a) + \frac{\Delta H_f}{C_p} \frac{d\theta}{dt} \quad (2-35)$$

where ΔH_f is the heat of fusion and θ is the degree of crystallinity.

Andrews (212) used a two dimensional approach to the problem, including the radial temperature gradient in addition to the axial temperature gradient. Wilhelm (213) applied Andrews' energy balance to his experimental data and found some agreement. Ziabicki and Kedzierska (214) attempted to model this phenomenon by considering a hot cylinder immersed in an isothermal cooling fluid. Their analysis included simplifying assumptions to yield a tractable problem, however, the results did not agree with experimental data. Barnett (215) used numerical analysis to compute the temperature profile using forced and free convection. Copley et al. (216) investigated the effect of fiber attenuation on the axial temperature gradient of the fiber. Morrison (217) also performed numerical analysis on the cooling and solidification process including heat of fusion as well as convective and radiative heat transfer.

The key parameter in calculating the temperature profile of the spinline is the heat transfer coefficient, h . There have been many attempts to provide theoretical and empirical relationships describing h as a function of spinning conditions through use of dimensionless groups such as Nusselt (Nu), Reynolds (Re), Prandtl (Pr) and Grashof (Gr) numbers. These groups are given as

$$Nu = \left(\frac{h D}{k_{air}} \right) \quad (2-36)$$

$$Re = \left(\frac{D V \rho_{air}}{\eta_{air}} \right) \quad (2-37)$$

$$Pr = \left(\frac{C_{p_{air}} \eta_{air}}{k_{air}} \right) \quad (2-38)$$

$$Gr = \left(\frac{D^3 \rho_{air} \beta_{air} g \Delta T}{\eta_{air}} \right) \quad (2-39)$$

where D is filament diameter, V is velocity, g is acceleration due to gravity, k_{air} , ρ_{air} , $C_{p_{air}}$, η_{air} , β_{air} are thermal conductivity, density, specific heat, viscosity and coefficient of thermal expansion of air (cooling medium), respectively, and ΔT is the temperature difference between the filament and air.

Free convection, associated with the motion of the ambient medium in the temperature field around the cooling filament, is the typical heat transfer mechanism for a stationary system, and it may prevail in melt spinning at very low take-up speeds. In this case

$$Nu = (Gr, Pr) \quad (2-40)$$

when the spinline moves in a stationary air with high take-up speeds and/or a parallel or transverse air flow is applied, heat transfer is due to forced convection and in this case

$$Nu = \left(Gr, Pr, \frac{z}{D} \right) \quad (2-41)$$

where z is the exposed length of the filament for parallel or transverse air flow.

Vasudevan and Middleman (218) and Acierno et al. (13) considered the laminar boundary layer over a continuous cylinder moving axially; however, their solution did not fit well with experimentally measured Nu values for the spinline. Glicksman (219) considered laminar and

turbulent boundary layers in axial air flow over a stationary cylinder and found that

$$Nu = 0.325 Re^{0.3} \quad (2-42)$$

Kase and Matsuo (78) developed an empirical relation for heat transfer coefficient given by

$$Nu = 0.42 Re^{0.34} \quad (2-43)$$

This result was extended to heat transfer in the presence of transverse air flow. In this case

$$Nu = Nu_o \left[1 + \left(\frac{8 V_a}{V} \right)^2 \right]^{0.167} \quad (2-44)$$

where Nu_o is the Nusselt number in absence of transverse air flow and V_a and V are the transverse air and fiber velocities, respectively.

Sano and Nishikawa (220) based on axial air flow over heated wires found

$$Nu = 0.32 + 0.155 Re^{0.5} \quad (2-45)$$

Sano and Yamada (221) extended this relation to transverse air flow and expressed it as

$$Nu = 0.35 + 0.5 Re^{0.5} \quad (2-46)$$

where

$$Re = Re_{ef} + (0.3 Re_o^{0.36} - 0.2)^2 + (1.26 Gr^{0.07} - 0.7)^2 \quad (2-47)$$

Here Re_{ef} and Re_o are Reynolds numbers with and without transverse air flow, respectively. Measurements for a stationary cylinder in an axial

air stream by Mueller (222) and Roberts (223) resulted in the empirical relations

$$Nu = 0.516 Pr^{0.3} Re^{0.43} \quad (2-48)$$

and

$$Nu = 0.746 Re^{0.38} \quad (2-49)$$

These two relations predict too-rapid cooling along the spinline. So far the relations developed by Kase and Matsuo (78), Glicksman (219) and Sano and Nishikawa (220) provide the better results for spinline temperature profiles.

Crystallization Kinetics

The transformation of a spinning melt into a solid polymer (solidification) is one of the most important elements of fiber formation. Solidification involves irreversible changes of many structural and macroscopic characteristics of the material such as molecular orientation, crystallinity, viscosity, mechanical properties, etc. Phase transitions seldom occur in a true thermodynamic equilibrium and the physical behavior of spinline is determined by instantaneous, time dependent degree of transformation. In melt spinning of polymers crystallization is the most important phase transition. The time dependent changes in degree of crystallinity affects heat transfer, rheological properties of the polymer and, consequently, the kinematics and dynamics of spinning. Of particular significance is its effect on fiber structure. Crystallization in the course of fiber formation proceeds in unsteady, non-isothermal and, frequently, in oriented systems.

The theory of crystallization kinetics in fiber formation is far from being complete; even empirical description is scanty. Some attempts have been made to proceed from the simplified isothermal situation and then to include non-isothermal and orientation effects. The crystallization of polymers has been characterized as a two step process. The initial step involves formation of a nucleus of sufficient size to form the basis of a crystal, followed by a growth process whereby material is incorporated into the nucleated crystal.

Isothermal considerations. Nucleation under isothermal condition can occur by either homogeneous or heterogeneous mechanism. In the former case the rate of nucleation is constant in time whereas in the latter case nucleation occurs on existing crystalline heterogeneities. Fisher et al. (224) proposed polymer crystallization theory as an extension of theories for non-polymeric materials. The nucleation step was based on the theory of Becker and Doring (225) for condensed systems. Devoy and Mandelkern (226) used Turnbull's heterogeneous nucleation model (227) and showed that the free energy barrier to nucleation was lower for heterogeneous nucleation than that for homogeneous nucleation. Cormia et al. (228) reviewed early experimental studies and concluded that nucleation in polymers was almost entirely heterogeneous.

Avrami (229-231), Johnson and Mehl (232), Evans (233) and Kolmogoroff (234) independently developed mathematical expressions for the time dependence of degree of crystallinity, θ . These relationships were of the form

$$\theta(t) = 1 - \exp\{-E(t)\} \quad (2-50)$$

where $E(t)$ is a function whose form depends on the assumptions used with respect to the nucleation and growth mechanisms. For growth of N_0 predetermined nuclei

$$E(t) = N_0 v(0,t) \quad (2-51)$$

where $v(0,t)$ is the volume of nucleus as a function of time. For growth accompanied by sporadic nucleation with nucleation rate $\dot{N}(t)$

$$E(t) = \int_0^t \dot{N}(s) v(s,t) ds \quad (2-52)$$

where $v(s,t)$ is the volume of a growing nucleus nucleated at the instant s and growing until time t where $t > s$.

Equations (2-50) through (2-52) do not involve any restrictions on the time dependencies of nucleation and growth rates. Contributions $E(t)$ coming from various types of nuclei and various modes of growth can be superposed yielding the overall rate of transformation. Usually only special cases of these equations are considered. For example, if nucleation and growth rates are constant (linear or interface growth) or if growth rates are inversely proportional to the square root of time (diffusion controlled growth), then

$$E(t) = K t^n \quad (2-53)$$

or

$$E(t) = \ln 2 \left(\frac{t}{t_{\frac{1}{2}}} \right)^n \quad (2-54)$$

where $t_{\frac{1}{2}} = t(\theta = \frac{1}{2})$ is the crystallization half period, n is the Avrami exponent and K is the rate constant. When dealing with experimental data for isothermal crystallization the parameters K and n can be evaluated by fitting the crystallization isotherm (235). In general, higher values

of n represent greater dimensionality in the growth process (from rod shapes to discs to spheres).

The asymptotic degree of transformation as predicted by equation (2-50) is $\theta_\infty = 1$, since $E(t)$ tends to infinity. For polymers which do not crystallize completely it can be modified by replacing the absolute degree of transformation, θ , by its relative value expressed as

$$\frac{\theta(t)}{\theta_\infty} = 1 - \exp\{-E(t)\} \quad (2-55)$$

The nucleation rate, $\dot{N}(t)$, in equation (2-52) consists of two different contributions (12)

$$\dot{N}(t) = \dot{N}_{th} + \dot{N}_{ath} \quad (2-56)$$

The first one, \dot{N}_{th} , is related to thermal fluctuations leading to formation of nuclei and the other, \dot{N}_{ath} , appears only when the thermodynamic state variables (temperature, pressure, etc.) of the system are changed. \dot{N}_{ath} is generally proportional to the rate at which the system changes its state i.e. the cooling rate, pressure drop, etc. Turnbull and Fisher (236) have proposed an isothermal steady state solution for thermal nucleation rate. They assume spherical nuclei and consider the distribution function of cluster sizes for a single variable (radius). They find that

$$\dot{N}(t) = \text{const} \left(\frac{ckT}{h} \right) \exp\left(-\frac{E_a}{kT}\right) \exp\left(-\frac{\Delta F}{kT}\right) \quad (2-57)$$

where E_a is the activation energy for molecular motion across the crystal/melt interface and ΔF is the free energy of formation of a cluster having a critical radius; the latter is given by

$$\Delta F_{sph} = \frac{16 \pi \alpha^3 T_m^2}{3(\Delta H \Delta T)^2} \quad (2-58)$$

where α is the surface tension, ΔH is the heat of fusion, T_m is melting temperature and ΔT is the supercooling. Polymer nucleation is usually assumed to involve the formation of cylindrical rather than spherical nuclei. The distribution function for cylindrical clusters involves two variables and this problem has been approached by keeping the same form for \dot{N}_{th} as for spherical cluster but replacing ΔF with an expression derived for cylinders (237,238):

$$\Delta F_{cyl} = \frac{8 \pi \alpha_e \alpha_s^2 T_m^2}{(\Delta H \Delta T)^2} \quad (2-59)$$

where α_e and α_s are the surface tensions on the head and side of the cylinder, respectively. Another approximate approach to cylindrical nucleation was proposed by Hoffman et al. (239).

Growth processes are usually described in terms of two dimensional nucleation on the crystal surface. Thus Hoffman and Lauritzen (240) proposed a theory based on equation (2-57) for the isothermal, steady state, linear growth rate with appropriate critical free energies ΔF .

Since existing theories of nucleation and growth are limited in practice to steady, isothermal conditions and can not be treated effectively in more complex crystallization regimes in terms of equations (2-50) to (2-52), some simpler theories based on empirical data with simplified assumptions were developed. Ziabicki (241) considered a quasistatic model in terms a of first order kinetic equation:

$$\frac{d\theta}{dt} = K[\phi(t)]\{\theta_\infty[\phi(t)] - \theta\} \quad (2-60)$$

where ϕ is a time dependent parameter such as temperature, orientation factor, etc. Assuming that the equilibrium value, θ_{∞} , is constant, the rate function $K(\phi)$, was expressed through crystallization half time, $t_{\frac{1}{2}}$, a direct result of experiments made at $\phi = \text{constant}$. The relative degree of crystallinity was then expressed as

$$\ln \left(1 - \frac{\theta}{\theta_{\infty}} \right) = - \ln 2 \int_0^t \frac{ds}{t_{\frac{1}{2}}[\phi(s)]} \quad (2-61)$$

Nakamura et al. (171,211) introduced the isokinetic assumption where the time dependence of all growth rates, $G_i(t)$, were considered to be equal to the time dependence of the nucleation rate, $\dot{N}(t)$,

$$\dot{N}(t) = aU(t) \quad (2-62)$$

$$G_i(t) = b_i U(t) \text{ for all } i \quad (2-63)$$

where a and b_i are constants and $U(t)$ was an arbitrary function of time. The crystallization function $E(t)$ from equation (2-51) becomes

$$E(t) = c \left[\int U(s) ds \right] = c' \left[\int G_i(s) ds \right]^n \quad (2-64)$$

In addition it was assumed that the time dependence of \dot{N} and G_i results only from the variation of some parameter of state ϕ as

$$U(t) = U[\phi(t)] \quad (2-65)$$

and crystallization half periods for constant ϕ were defined as follows

$$t_{\frac{1}{2}}(\phi) = \text{const} (\dot{N} G_1 G_2 \dots G_{n-1})^{-\frac{1}{n}} = \text{const} [U(\phi)]^{-1} \quad (2-66)$$

then finally from equation (2-64)

$$E(t) = \ln 2 \left[\int_0^t \frac{ds}{t_{\frac{1}{2}}[\phi(s)]} \right]^n \quad (2-67)$$

Note that the equation (2-61) is a special case of equation (2-67) with $n = 1$.

Non-isothermal and orientation considerations. Isokinetic and quasistatic conditions can not be justified for non-isothermal processes as nucleation and growth rates and the resulting crystallization rates are very sensitive to temperature. Steady state nucleation or growth rates depend on temperature mainly through the activation energy and free energy terms, the linear pre-exponential factor (ckT/h) being negligible; equation (2-57) was rewritten as

$$\ln \dot{N}_{th}(T) \simeq \text{const} - [E_a(t) + \Delta F_{nuc}(T)]/kT \quad (2-68)$$

$$\ln G_i(T) \simeq \text{const} - [E_a(t) + \Delta F_{gr}(T)]/kT \quad (2-69)$$

At higher temperatures, activation energy, E_a , being small compared to critical free energy, ΔF , the temperature dependence was considered to be determined by the ΔF term. Mandelkern (235) found that the logarithm of nucleation and growth rate was a linear function of $(T_m/T\Delta T)$ or $(T_m^2/T\Delta T^2)$, depending on two or three dimensional nucleation for $(\Delta F/kT)$ term, respectively. At lower temperatures the activation energy term becomes important and nucleation (or growth) rates pass through a maximum at some temperature T_{max} . The effects of non-isothermal conditions are not confined to the variation of \dot{N}_{th} and G_i with temperature, but they also involve the athermal nucleation rate, \dot{N}_{ath} , as

$$\dot{N}_{ath} = - \left(\frac{\partial R}{\partial T} \right) \left(\frac{dT}{dt} \right) \iint F ds \quad (2-70)$$

where R is a vector characteristic of the cluster having critical dimensions (for example, the critical radius for spherical clusters), F is a distribution function of cluster size and shape, S is the critical boundary and $(-dT/dt)$ is cooling rate. Development of this approach has not lead to significant results. On the other hand, experimentally observed crystallization half time, $t_{\frac{1}{2}}$, or its reciprocal, rate constant (K), was reproduced by empirical relation (241)

$$K(T) = K_{max} \exp \left[-4 \ln 2 \left(\frac{T - T_{max}}{D} \right)^2 \right] \quad (2-71)$$

where K_{max} is the maximum in the rate-temperature curve, T_{max} is the temperature at K_{max} and D is the half width of the rate-temperature curve. This equation represents K as Gaussian function of temperature in the range of $T_g < T < T_m$ and it was found to fit Wood and Bekkedahl's (242) data for natural rubber very well. The resulting degree of crystallinity can be expressed in terms of the integral

$$\int_{T_g}^{T_m} K(T) dT \simeq K_{max} (4 \ln 2)^{-\frac{1}{2}} D \int_{-\infty}^{+\infty} \exp(-u^2) du \simeq 1.064 K_{max} D \equiv G \quad (2-72)$$

Here, G (area under rate-temperature curve in the range of $T_g < T < T_m$) is known as the kinetic crystallizability and has been used for qualitative comparison of the crystallization behavior of various polymers. Thus, at low degrees of transformation ($\theta < \theta_{\infty}$) and identical, constant cooling rates, the crystallization rate for nylon-66 ($G \simeq 139$) will be 125 times higher than that for PET ($G \simeq 1.1$) and about 20 times higher than that for nylon-6 ($G \simeq 6.8$). With this empirical relationship equation (2-67) becomes

$$E[t(T)] = -\ln(1 - \theta) = \text{const} K_{max} \left[\frac{\int_{T_0}^T \exp[-4 \ln 2 \left(\frac{T' - T_{max}}{D}\right)^2] dT'}{\left(\frac{dT'}{dt}\right)} \right]^n \quad (2-73)$$

Takayanagi and Kusumoto (243) combined an expression for thermal nucleation rate (equations (2-68) and (2-69)) with the WLF expression for the activation energy and proposed

$$K(T) = A \exp \left[\frac{BT}{(T - T_g + 51.6)^2} - \frac{CT_m}{T(T_m - T)} \right] \quad (2-74)$$

with three adjustable constants A, B and C. This expression was restricted to temperatures close to T_m with small supercooling and can lead to errors in the range of T_{max} which is approximately 0.8 times T_m .

Experimental information about non-isothermal crystallization is scanty. Some qualitative investigations were made by Inoue (244), Schultz (245), and Boon (246). Ozawa (247) studied the effect of cooling rates on crystallization kinetics of PET using DSC. Crystallization kinetics of HDPE were studied by Nakamura et al. (248) and they found the results to be reasonably consistent with their isokinetic model, however, the temperature range involved was very narrow and cooling rate did not exceed 0.5 °C/min.

Polymer crystallization is very sensitive to molecular orientation in the amorphous regions in addition to the thermal conditions. The most reliable data on the kinetics of oriented crystallization concern cross-linked rubbers. Isothermal crystallization of elongated samples held in isometric conditions yield crystallization rates and Avrami exponent as a function of deformation. On the other hand crystallization experiments in shear flow, stirred systems or in elongational flow only yield indirect or qualitative information about crystallization rates and morphology of oriented crystallized material.

Katz (249) found that amorphous natural rubber would crystallize when stretched. Treloar (250) and Gent (251) observed a rapid increase in crystallization rate and decrease in Avrami exponent, reaching $n=1$ for vulcanized rubbers with increasing deformation. Kim and Mandelkern (252) found decreased value of n from 3.6 for isotropic rubber (stretch ratio $\lambda = 1$) to 1.3 for $\lambda = 6$ based on stress relaxation experiments. Observations have been made in shear flow or in the stirred polymer solutions confirming the increase in incipient crystallization temperatures and rates (253-256) while induction times were found to decrease with shear rate or stirring velocity (257,258).

Wasiak (259) studied crystallization and changes in amorphous and crystal orientation of amorphous PET with various degrees of initial orientation. The observed crystallization half periods were reduced in the ratio of 1:45 and the value of n was markedly reduced when an initially isotropic sample was replaced with one having an amorphous orientation factor of 0.6. Similar results were reported by Smith and Steward (260) on PET. Many observations concerning polymer crystallization in elongational flow are indicative of the great importance of orientation effects in fiber formation. Nakamura et al. (171) and Bai (32) observed that melt spun PET fibers are usually amorphous due to very low kinetic crystallizability, however, high speed spinning accompanied by strong molecular orientation, despite an increased cooling rate, produces partially crystalline fibers. Similar experimental observations were made by Ziemiński (33) for high speed spun nylon-66, the only difference being that crystallization appeared at lower speeds than that in case of PET. Dees and Spruiell (16)

observed an 8 fold reduction in the crystallization half time for PE fibers melt spun at higher take-up velocity.

Theoretical study (261,262) of simultaneous crystallization and change in molecular orientation was attempted through a parameter δ defined by

$$\delta = \frac{t_{or}}{t_{\frac{1}{2}}} \quad (2-75)$$

where t_{or} is the characteristic time of orientation related to relaxation of orientation in the absence of stress. When δ is smaller than unity, the changes in orientation proceed rapidly before any progress in crystallization takes place. If, on the other hand, δ is much larger than unity, then crystallization proceeds rapidly before the initial degree of orientation is reached. When δ is close to unity, orientation and crystallinity changes are strongly linked. For PET it was found that temperature corresponding to $\delta = 1$ is 150°C and shows strong coupling between transient molecular orientation in amorphous regions and crystallization.

Abbott and White (15) presented a general theory of non-isothermal crystallization including oriented conditions. A two dimensional energy balance was considered with a crystal growth front advancing through the solidifying fiber. Both homo- and heterogeneous nucleation mechanisms were involved and nucleation rate, N_{kj} , was obtained as a function of temperature and deformation rate. Their result was

$$\theta = 1 - \exp[-\Sigma \int K_{kj}(T, \tau) d\tau] \quad (2-76)$$

where

$$K_{kj} = \frac{N_{kj} C_j}{\rho L} \beta^{j+\alpha} \xi^{j+\alpha} \quad (2-77)$$

Ishizuka and Koyama (263-266) studied the crystallization kinetics of PP on a running spinline using the following relation for a heterogeneously nucleated system

$$-\ln \left[1 - \frac{\theta}{\theta_{\infty}} \right] = \rho_a k_f \Sigma [\Sigma G_j [T(u), \Delta n_a(u)] \Delta t] N_i [T(\tau), \Delta n_a(\tau)] / \rho_c \theta_{\infty} \quad (2-78)$$

where θ_{∞} is the maximum crystallinity, ρ_c and ρ_a are the density of the crystalline and amorphous phases respectively, G_j is the time, temperature and orientation dependent linear growth rate and N_i is the temperature and orientation dependent nucleation rate. Δn_a is the orientation factor of the amorphous phase and k_f is a shape factor which depends on the dimensionality of the growth. They found that a two-dimensional growth model provided the best fit of the experimental data. The crystallization of PP during melt spinning was dictated by the initial local molecular orientation of the supercooled melt and only highly oriented molecules would be successively incorporated into the growing crystal.

Abhiraman (267) analyzed the crystallization process in terms of the orientation distributions of the crystalline and amorphous phases. It was assumed that the orientation of the crystals was the same as that of the nuclei from which they were initiated. Krigbaum and Roe's (268) hypothesis was used to relate the nuclei orientation distribution to that of the amorphous precursor. He concluded that the crystallization of an oriented precursor would lead to a higher degree of anisotropy than that of the precursor. The depletion of the oriented precursor would lead to an amorphous orientation normal to the initial preferred direction. The overall orientation increases with crystallization.

To develop more fundamental theory, the effect of molecular orientation on the melting temperature, T_m , has been attempted. Generally a thermodynamic approach is adopted by which the effect of deformation on the entropy and enthalpy of the system is evaluated. The entropy contribution for both Gaussian (253,254,268) and non-Gaussian (269,270) chains always leads to an increased T_m whereas the enthalpy contribution may lead to a higher or lower T_m . Jarecki (271) included rotational isomerism in the enthalpy and found a higher T_m than for Krigbaum and Roe's (268) result for Gaussian chains.

Ziabicki (272) adopted a kinetic approach to analyze thermal nucleation expression (equation (2-57)) for spherical clusters. He proposed that activation energy of molecular transport, E_a , and/or free energy of nucleus formation, ΔF , can be affected by stress or orientation. If the molecules (segments) of the amorphous phase are not spherical but elongated, their translation from the surrounding amorphous matrix to the surface of the cluster will depend on the orientation of the segment with respect to the surface of the cluster. The activation energy for a given pair (cluster,segment) will depend on the orientations of cluster (angle ϕ_{cr}) and the segment (angle ϕ_s) with respect to some stationary coordinate system. The average activation energy will depend on the orientation distributions of clusters, $W_1(\phi_{cr})$ and segments, $W_2(\phi_s)$ both controlled by the applied molecular orientation parameter, λ and given by

$$\bar{E}_a(\lambda) = \iint E_a(\phi_{cr}, \phi_s) W_1(\phi_{cr}) W_2(\phi_s) d\phi_{cr} d\phi_s \quad (2-79)$$

The effect on critical free energy of nucleus formation, a function of equilibrium T_m , expressed as

$$\Delta F(T_m) = \text{const} \left(\frac{T_m}{\Delta T} \right)^p \quad (2-80)$$

with $p = 1$ and 2 for primary and secondary nucleation respectively, Ziabicki found that

$$\frac{d\Delta F}{d\lambda} = -p\Delta FT \left(\frac{dT_m}{d\lambda} \right) / (T_m\Delta T) \quad (2-81)$$

Thus when T_m increases with λ , the critical free energy for nucleation and growth decreases and the resulting effect on \dot{N}_{th} will be increase of nucleation rate with increasing λ as given by

$$\frac{d\dot{N}_{th}}{d\lambda} = - \left(\frac{\dot{N}_{th}}{kT} \right) \left(\frac{dF}{d\lambda} \right) \quad (2-82)$$

The effect of orientation on the activation energy was considered to be less important than the effect of T_m .

Ziabicki (272) also proposed the effect of orientation to the formation of nuclei according to athermal mechanism. He postulated that with increasing orientation of some structural elements some clusters become thermodynamically stable and capable of spontaneous growth; the athermal nucleation rate becomes

$$\dot{N}_{ath} = - \left(\frac{\partial R}{\partial \lambda} \right) \left(\frac{d\lambda}{dt} \right) \iint F ds \quad (2-83)$$

where the characteristic vector R and the distribution function, F , depend on the molecular deformation λ . Restriction of the effect of orientation to T_m led to

$$\frac{dR}{d\lambda} = \frac{\partial R}{\partial T_m} \frac{\partial T_m}{\partial \lambda} \quad (2-84)$$

and an increased nucleation rate was predicted.

Apart from more fundamental studies, Ziabicki (262) also attempted simpler and more tractable formulas for orientation dependent crystallization rates which can be directly used in the interpretation of polymer processing. He proposed that any sufficiently smooth function of molecular orientation (f), X , can be expressed as

$$X(f) = X(0) + a_1 f + a_2 f^2 + a_3 f^3 + \dots \quad (2-85)$$

where X can be T_m or free energy or crystallization rate, K , etc. which are scalar valued functions of f . The linear term $a_1 f$ drops out for

$$\left(\frac{\partial X}{\partial f}\right)_{f=0} = a_1 + 2a_2 f + 3a_3 f^2 + \dots = 0 \quad (2-86)$$

leading to $a_1 = 0$ and higher than square terms are neglected for small values of f . Thus

$$\ln \left[\frac{K(f)}{K(0)} \right] \simeq A(T) f^2 \quad (2-87)$$

Combination of non-isothermal and orientation effects produced

$$K = K_{max} \exp \left[-4 \ln 2 \left(\frac{T - T_{max}^0}{D^0} \right)^2 + A(T) f^2 \right] \quad (2-88)$$

where the superscripted zeros refer to the unoriented state.

Mathematical Modeling

Melt spinning being a non-isothermal, variable property, uniaxial elongational flow situation, it is readily amenable to mathematical analysis, provided some simplifying assumptions are made. Initial attempts were made for low take-up speeds followed by moderate and high speeds and almost all studies have utilized numerical solution using

computer simulation. Most of moderate and high speed modeling involved PET melt spinning.

The first attempt to model the melt spinning process was made by Kase and Matsuo (78,79). They combined a one dimensional Newtonian fluid model for the spinline with only applied take-up forces acting with a one dimensional energy balance with forced convection heat transfer. They predicted that increasing spinneret diameter with the same take-up speed slows drawdown and cooling and increases the drawdown force. Increasing take-up speed while maintaining fiber diameter again has similar effect but drawdown force does not change. They also studied the effect of extrusion temperature and transverse air flow.

Hamana et al. (41) extended Kase and Matsuo's model by including air drag, gravitation and momentum flux forces while treating the melt as a Newtonian fluid. They presented comparisons between theory and experiment for various cases. Lamonte and Han (80) considered non-Newtonian effects on the elongational viscosity. Fisher and Denn (81) used a special form of the convected Maxwell model (a differential viscoelastic model) developed by Marrucci (273) from considerations of the rheological behavior of systems of dumbbell model molecules while keeping Kase and Matsuo's force and energy balances. They described detailed calculations for the spinline velocity and temperature profiles by varying heat transfer coefficients. Matsui and Bogue (82) used a viscoelastic integral model by considering the force balance and measured temperature profiles for HDPE. This investigation was unique in that it considered both flow in the spinneret and in the spinline as

well as accounting for temperature variations in polymer properties. The studies described so far involved low take-up speeds.

Prastaro and Parrini (83) attempted to define critical spinning parameters for PET through equations of motion, energy and Newtonian rheological model. They assumed temperature independent specific heat and density and neglected inertia, gravity and air drag force components to the force balance. Under these restrictions, they presented a correlation of the critical conditions where fiber breakage would occur. Gagon and Denn (84) extended Fisher and Denn's (81) approach for PET with Newtonian and Phan-Thein constitutive equation. Their model was extremely sensitive to the choice of heat transfer expression and did not discriminate between the Newtonian and viscoelastic model when compared to the experimental data of George (85). The air drag caused an increase in the stress with the Newtonian model as against a decrease with viscoelastic model. They concluded that this was due to the coupling between the stress and velocity in the viscoelastic model. Since several boundary conditions were specified rather than as the solution of the simulation, it became more of a descriptive model rather than a predictive model. George (85,274) attempted a comparison of constant and variable tension spinning for PET and concluded that there was no effect on the velocity and temperature profiles, but stress at the freeze point increased almost 2-fold for the variable tension model. He also attempted to show structure development through a correlation between birefringence and mechanical properties.

Yasuda et al. (275-277) attempted modified heat transfer and air drag expressions to model radial variations (275) and multifilament

spinning (276,277). Radial temperature gradient was claimed to be the source of the radial orientation distribution and to account for it a partial differential heat transfer expression was used. The solution indicated a temperature difference of 2 to 12°C between the center and the surface of the fiber. Using computed stress at the freeze point (where the velocity reached 95% of the take-up velocity), a relation between birefringence and stress was developed which led to radial orientation distribution. They concluded that radial orientation distribution increased with velocity, presumably from an increase in the temperature gradient, and that it decreased with increasing cooling air temperature. For multifilament spinning of PET they (276,277) proposed heat and mass balances for the quench air over small individual filament segments in a given row within the fiber bundle. They used an empirical correlation based on the details of the air drag phenomenon for determining the quantity of air being "pumped" due to the "chimney effect". In a later study (277) they indicated that the denier variation was related to the position of maximum in the velocity gradient for individual filaments in the bundle.

Dutta and Nadkarni (86) used Gagon and Denn's (84) approach with a temperature and intrinsic solution viscosity (IV) dependent Newtonian viscosity. They attempted to establish the sensitivity of the model with respect to several variables and concluded that the extrusion temperature, IV, mass throughput and take-up velocity were the most significant variables. Shenoy and Nadkarni (278) extended Dutta and Nadkarni's approach for PET to obtain insight into structure development through computation of birefringence. They verified the stress optical

law for PET using data from several different industrial plants. The utility of these simulations was demonstrated by a case study of factors affecting a constant denier product.

The models described so far were not applicable to the melt spinning process where crystallization takes place on the spinline. Kikutani (87) proposed orientation induced crystallization kinetics for high speed spinning of PET and included an empirical crystallinity factor in the elongational viscosity equation. This formulation predicted online crystallization at take-up speeds greater than 3000 m/min and appearance of "necking" phenomenon experimentally observed at high speeds for PET. Bai (32) compared online experimental diameter, temperature and birefringence profiles to those predicted from Kikutani's model. he found that a reasonable quantitative agreement between the experimental data and the model predictions could be obtained by adjusting various parameters so that the appearance of the necking region coincided. This, however, led to a discrepancy in the predicted and experimentally observed take-up speeds.

Zieminski (33) recently attempted to develop a generalized model describing the high speed spinning behavior of crystallizable polymers. It included the effects of acceleration, gravity and air drag on the kinematics of the process, the effects of temperature and molecular orientation on the crystallization kinetics of the polymer, and the effects of temperature, molecular weight and crystallinity on the elongational viscosity of the polymer melt. He found a good agreement between his online experimental measurements (diameter, temperature and birefringence profiles) for nylon-66 and that of Lu and Spruiell's (279)

experimental work on PP with model predictions. However, in both cases online diameter data were restricted to the mostly solidified region of the spinline. He concluded that orientation induced crystallization occurred in nylon-66 for spinning speeds greater than 4000 m/min and it was relatively insensitive to variation in Avrami exponent in the range of 1 to 3 and to the variation of exponent of crystallinity in elongational viscosity expression in the range from 2 to 12.

George and Deeg (280) have proposed an interesting "inversion procedure" for extracting important information needed in modeling melt spinning. They point out that historically, models have been used to calculate velocity, temperature and stress profile from the process conditions with "assumed" extensional viscosity and heat transfer coefficient relations. In their "inversion procedure" experimentally measured velocity and temperature profiles and a single tension measurement at the freeze point are used to calculate a rheological spinning function (RSF) and a thermal spinning function (TSF). RSF is essentially the extensional viscosity restricted in the region of temperature-deformation rate plane covered by the spinning process. Also, TSF is basically a heat transfer expression, again restricted to the measured spinline temperature range. They presented the results from such a procedure using error free calculated data and for induced normal, random errors in temperature and velocity data. They argue that the value of induced errors are typically in the range encountered in actual experimental measurements. They concluded that their procedure worked very well for calculated data with and without induced error

except in bottom portion of the spinline; however, they have not reported so far the results on actual experimental data.

CHAPTER 3

EXPERIMENTAL DETAILS AND DATA ANALYSIS

Polymer and Process Details

Nylon-6 Resins

Two nylon-6 samples with different molecular weight were used in this study. The lower molecular weight sample, CN9984, was supplied by the American Enka Company and the higher molecular weight sample, BHS, was supplied by Allied Fibers and Plastics Company. Detailed characterization of viscosity average molecular weight of these samples through dilute solution viscosity measurements was reported by Suryadevara (31). The viscosity average molecular weights of the two resins differed by approximately a factor of two as shown by Suryadevara's results summarized in Table 3.1. Koyama et al. (34) reported shear viscosities of these samples measured at 260°C using an Instron Capillary rheometer.

Since nylon-6 absorbs moisture from the atmosphere, these samples were dried in a vacuum oven (model 5831) supplied by National Appliance Company, Portland, Oregon. The drying was carried out in 600 gram batches of the polymer placed in an aluminum tray under an absolute pressure of 0.5 inches mercury and at a temperature of 110°C for sixteen hours. The dried pellets were then stored in Teflon-sealed glass jars purged with prepurified nitrogen. The drying procedure was established by Bankar (23) and was later used by Gianchandani (29) and Suryadevara (31) and was found to be satisfactory in bringing the moisture content down to 0.03 - 0.04 percent.

Suryadevara (31) also reported the degradation characteristics of these samples in terms of variation in viscosity average molecular weight before and after drying and before and after extrusion. His extrusion conditions and experiment were the same as those used in the present research. His findings are summarized in Table 3.1.

Table 3.1 Viscosity average molecular weight results.

Resin	Viscosity Average Molecular Weight
CN9984 As received	23,550
CN9984 Dried	25,250
BHS Dried	53,210
BHS After Extrusion	47,190

Melt Spinning Experiments

Fourne extruder-spinning equipment (shown schematically in Figure 3.1) supplied by Fourne Associates, West Germany was used to melt spin the nylon-6 filaments. The extruder consisted of a screw (diameter = 13 millimeters, length = 300 millimeters), connected to a variable speed electric motor through a gear box, enclosed in a barrel which had two independently controlled band type heaters along its length. The screw and barrel received polymer pellets by gravity feed from a 7 liter capacity, nitrogen purged hopper. Just underneath the hopper, the barrel throat was fitted with a cooling water sleeve to facilitate feeding of the polymer pellets from the hopper and prevent the polymer from

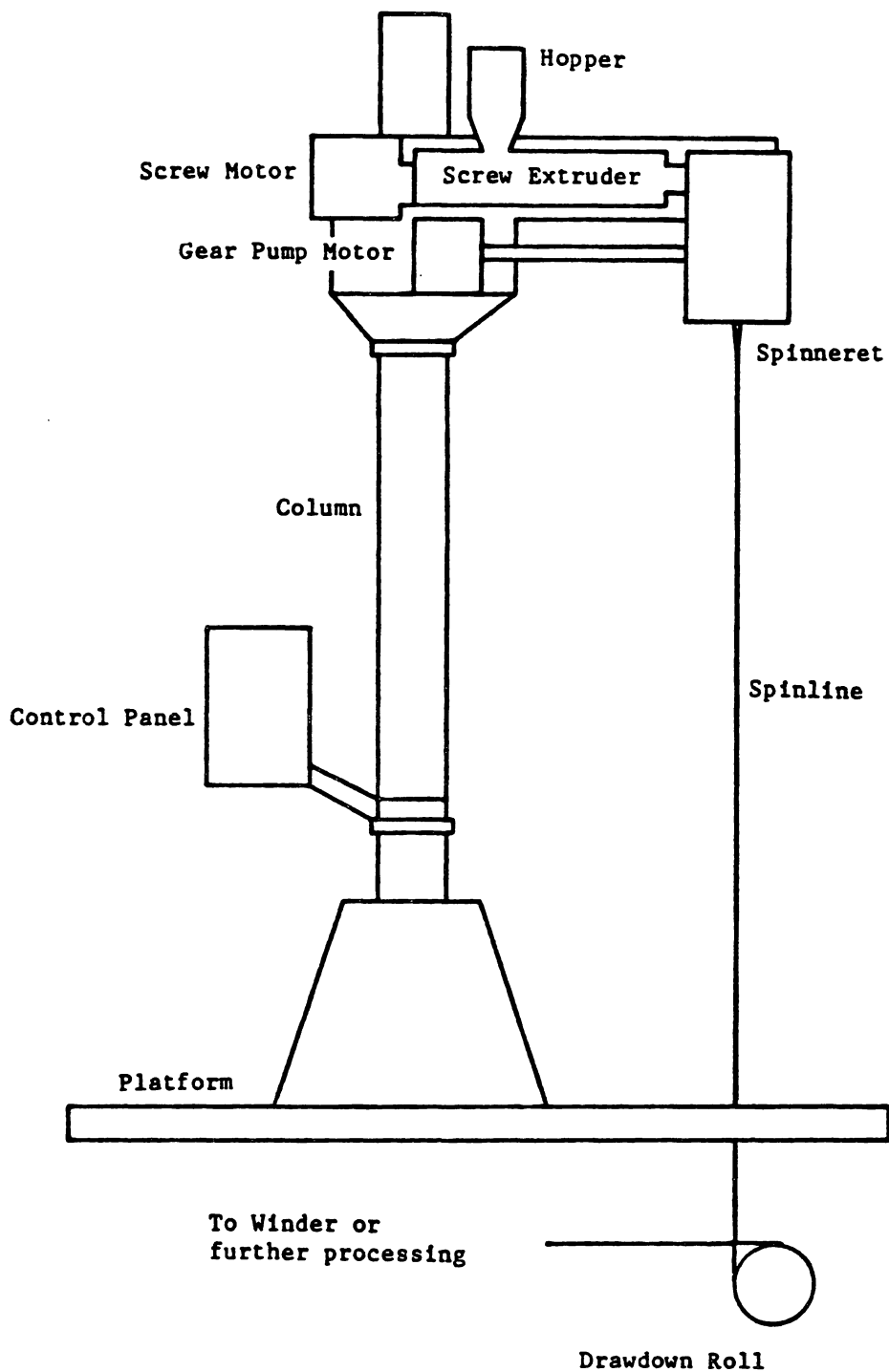


Figure 3.1 Schematic of the experimental apparatus.

immediate contact with the hot barrel. Two zones on the screw and barrel served to meter, melt and pump the molten polymer to the spinning head. The spinning head also had two independently controlled cylindrical mica filled heaters. In addition to the thermocouples associated with the cylindrical heaters, two resistance temperature detectors were placed in the spinning head which indicated actual melt temperature. At the top end of the spinning head a Dynisco pressure transducer (model PT441AE - 10M - 6/30) was mounted to indicate melt pressure when sufficient molten polymer was being pumped from screw and barrel. At the bottom end of the spinning head was a slot for a Zenith gear pump (Type HPB - 4647) which had two counter-rotating intermeshing gears which delivered a constant mass throughput of molten polymer to the spinneret pack. The gear pump was connected to a variable speed motor through a removable shaft. The actual mass throughput was determined by the density of the material, size of the gears and the rotational speed of the gears. A typical spinneret pack had a disc type of spinneret with a single capillary orifice (diameter = 0.0762 centimeters, length/diameter = 5), a breaker plate and metal screens.

The entire assembly of the extruder, spinning head, gear pump and spinneret pack was mounted on a movable carriage so that the assembly could be either swung around or moved up and down along the vertical column. A control panel had temperature controllers for barrel and spinning head heaters along with melt temperature indicator for resistance temperature detectors placed in the spinning head. It also had an ammeter and a voltmeter indicating current and voltage supplied to the screw motor.

An air jet drawdown device supplied by Rhone - Poulenc Fibers, France was used to drawdown and take-up the nylon-6 filaments. This drawdown device, operating on the principle of the air aspirator, used pressurized air to produce a suction force at the filament entrance. As there was no rotating drum, it was not possible to set a precise predetermined take-up velocity directly. The take-up velocity was varied by control of the air pressure and the actual take-up velocity achieved was calculated subsequently from the measurements of diameter and density of the filament through the continuity equation.

Several initial runs were made to determine the optimum operating parameters such as temperature on different barrel and spinning head zones, screw speed, gear pump speed, and approximate aspirator air pressure required to produce a chosen spinning velocity. A typical run began with the loading of the dried nylon-6 pellets into the nitrogen purged hopper. The cooling water on the barrel throat was turned on, followed by heater controllers on different zones. About one to two hours of time was allowed to attain the set temperature for each zone and to ensure complete melting of any material left in the extruder and spinning head from previous runs. An appropriate gear pump speed was selected to produce the desired mass throughput followed by extruder screw speed so that the melt pressure between the barrel end of the spinning head and gear pump indicated by the Dynisco pressure transducer was in the range of 500 - 1500 psi. The exiting filament from the spinneret was taken to the aspirator entrance and appropriate air pressure was applied. The filaments from the aspirator were allowed to fall into a card board box through a plastic pipe. Samples of nylon-6

fibers were collected and taken to the conditioning room in the Department of Textiles, Merchandising and Design. This room was maintained at constant temperature of 70°F and a relative humidity of 65%. The samples were allowed to equilibrate with the conditioning environment before any subsequent characterization.

Online Measurements

Diameter

Bai (32) and Zieminski (33) used an Olympus microscope to measure online diameter. In their technique they employed an aluminum guide to keep the filament in the field of view of the microscope. Even with the guide the diameter measurement was tedious, time consuming and subject to human error. Major difficulty was encountered, particularly when the filament was quite hot and tacky (close to the spinneret). Therefore it was felt necessary to develop a non-contact online diameter measurement technique.

A Zimmer diameter monitor (model 460/2) with digital display (model 466/2) supplied by Zimmer OHG, West Germany (schematically shown in Figure 3.2) was acquired. Its operation was based on a non-contact electro-optic back illumination principle permitting measurements on both opaque and semitransparent materials. Details of the principle of operation (shown schematically in Figure 3.3) are explained as follows. A light emitting diode (LED) generated a continuous light output at 930 nm of which the light flux was monitored by a Reference photodiode. This photodiode controlled the current through the LED with the help of a suitable amplifier. This way the light flux emitted from the LED could

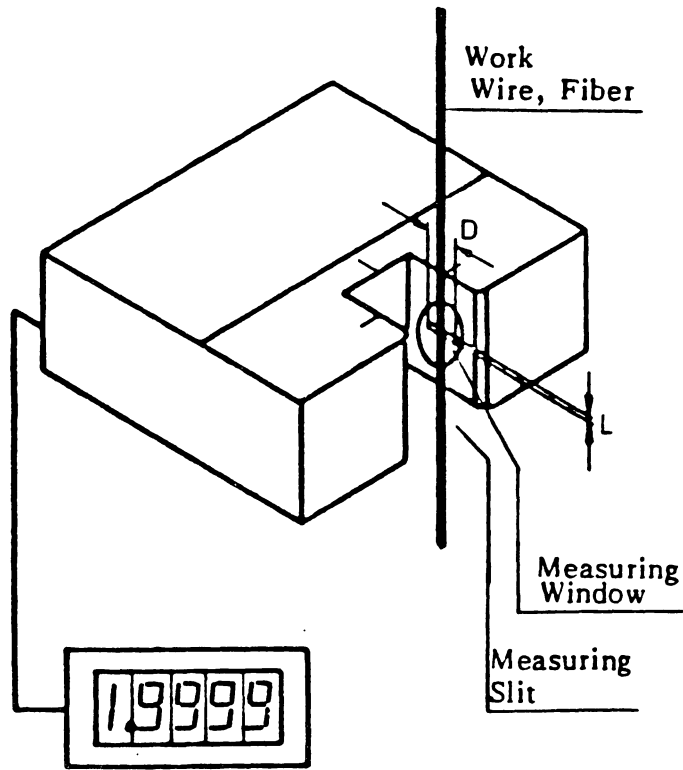


Figure 3.2 Schematic of Zimmer diameter monitor.

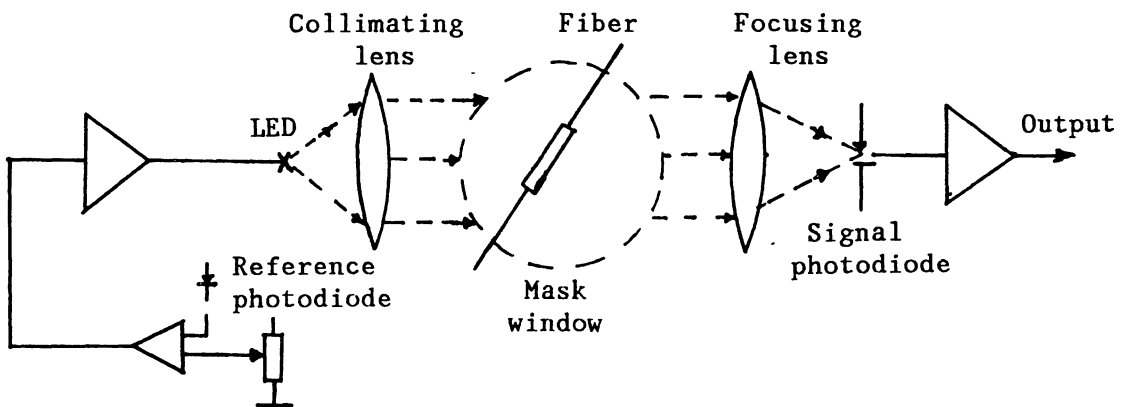


Figure 3.3 Operating principle of Zimmer diameter monitor.

be kept constant and independent of temperature and aging of the LED. The light beam was collimated by a collimating lens and this collimated beam was focused onto a signal photodiode by a focusing lens. A mask of dimension 2.5X11 millimeters was placed into the collimated beam in front of the focusing lens. The output signal of the photodiode increased with an increased diameter (obstruction placed within the window of the mask) and the diameter was digitally displayed in millimeters on the display unit.

The Zimmer diameter monitor had a range of 0 to 2 millimeters for diameter measurement with a resolution of 0.5 micrometer. It is to be noted that the displayed diameter was a reading averaged over 11 millimeters of filament length. It also had a gain control knob which allowed the gain to vary from 0.9 to 1.9. Variation in gain was useful in using the instrument over wide range of diameter (lower gain for smaller diameter and higher gain for larger diameter) and in correcting for transparency of fiber, particularly in the melt region. A zero knob allowed the user to set the zero and a set of calibration standards, opaque metal wires ranging in diameter from 50 micrometer to 1.6 millimeter, allowed accurate calibration of the instrument. The monitor also had a fitting for blowing a small stream of prepurified nitrogen to keep dirt or flying particles away from the sensor area as these influence the reading to a great extent, particularly when they are within the mask region. The top cover of the instrument was shielded by a thick phenolic insulating plate whose purpose was to prevent the instrument from heat up when measurements were made near the spinneret region.

After proper zeroing and calibration of the instrument, the initial trials were carried out on the spinline. The displayed diameter values showed substantial variation and difficulty arose in choosing the correct value of diameter. The variation in diameter values was due to movement of the fiber in and out of focus field of the sensor and to variations in throughput rate, take-up tension due to air suction force, temperature of extrusion, etc. Due to this difficulty it was decided to convert the analog output of the Zimmer sensor to a digital output through an analog-to-digital converter and store the digital output using a microcomputer capable of recording and storing the data at time intervals of a millisecond. For this purpose an Applied Micro Technology microcomputer was used with CP/M operating system. A Preston amplifier was used to amplify the output signal of the Zimmer monitor through its variable gain control. This was useful in amplifying smaller diameter output to a higher value to collect all possible variations and the larger diameter output was collected essentially without any amplification. The amplifier also provided a zero adjustment for the entire data acquisition system. This was needed because it was found to be difficult to zero the analog-to-digital converter which was the most important unit of the data acquisition system. A computer code written to acquire data from the Zimmer sensor is included in Appendix A. These data were then processed to arrive at statistically calculated diameter.

A statistical calculation computer code (included in Appendix B) was used for 2000 data points collected at a particular position on the threadline. This program first divides the data by the preamplification factor used on the Preston amplifier; then it lists all the diameter

values with number of occurrences of a particular diameter value. Then the diameter values are corrected for transparency according to a linear calibration equation developed separately. To develop this equation three standard fibers were used. The first one was a 500 micrometer diameter, transparent polystyrene standard. It was assumed that it has almost the same transparency as the nylon-6 melt near the spinneret region. The second and third fibers were about 150 micrometer and about 50 micrometer nylon-6 translucent fibers. The true diameters of these standards were measured using an Olympus microscope and then the diameter value was determined using the Zimmer monitor. A linear regression line was obtained through the three diameter values and the resulting equation was rearranged such that the independent variable was Zimmer reading and dependent variable was the true diameter. Thus this rearranged equation could directly be used in the statistical program to correct for transparency and to generate a statistical distribution of corrected diameter variation with number of occurrences of that value. The peak of the distribution was taken as the most probable diameter at a particular position in the spinline.

In actual experiments the Zimmer monitor was mounted on a movable carriage so that the sensor could be moved up and down the spinline. Before inserting the spinning filament into the sensor area, the zero of the instrument and of the amplifier were checked. Usually the measurement was started at a position close to the take-up device, taking 2000 data points at time intervals of 10 milliseconds. Then the monitor was moved 10 centimeters up on the spinline, zero was checked and again 2000 data points were collected at that position. The whole

procedure was repeated until about 10 centimeters from the spinneret. Up near the spinneret the time interval between data points was reduced so that the sensor area of the monitor was kept for the least feasible amount of time in the vicinity of the hot filament and hot spinneret.

Birefringence

The online birefringence measurements were made using an Olympus polarizing microscope (model 206080) equipped with a bifilar eyepiece and an Olympus 4 order Berek compensator (model CTP1-200105). The microscope was mounted transversely to the spinline and an aluminum guide was used to keep the filament in the field of view. The measurement was made with crossed polars on the microscope. At the "zero" reading on the compensator a black band was observed across the field of view, when a birefringent fiber was brought into view the black band was shifted and the optical crystal of the compensator was tilted until the black band was brought back to the "zero" reference position. Since the crystal could tilt in either direction two readings were possible, one on the left of reference zero and other on the right of reference zero depending on which way the crystal was tilting. The smaller reading was subtracted from the larger reading and the difference was used to perform an interpolation from the table of values supplied with the compensator manual. The interpolated value was multiplied by 2.065 (a constant associated with the Olympus Berek 4 order compensator). This produced the optical retardation in meters. The online birefringence was then the ratio of optical retardation to online diameter. The compensator readings were taken as close to the take-up device as possible and then at 10 centimeter intervals toward the

spinneret. This was continued until the point was reached where the fiber temperature was such that it would begin to stick to the guide and the spinline would break.

Temperature

The online surface temperature of the filament was measured using a Barnes Infrared microscope (model RM-2B). The set-up for these measurements is shown schematically in Figure 3.4. A black body radiator was used so that the temperature of the filament could be determined without the need of an extensive calibration procedure in absolute temperature measurement. The radiator consisted of a small electrically controlled heater placed in intimate contact with a copper block which was coated with high temperature optically black paint. This radiator then provided a means of exhibiting a constant background radiation at any temperature in the range of 30 - 280°C. The radiator, along with the microscope, was mounted on an adjustable carriage so that the whole assembly could be moved up and down along the spinline. A null deflection method was employed in that the black body radiator was set at a predetermined temperature and the pointer on the potentiometer was brought on the scale at some arbitrary value. Then the filament was brought in focus between the radiator and microscope eye piece. This would cause a steady deflection on the potentiometer. The direction of deflection indicated whether the surface temperature of the filament was higher or lower than that of the radiator. The filament temperature was determined by finding the position on the spinline for null deflection.

The procedure used in this study was to select an initial temperature near the extrusion temperature for the radiator and then

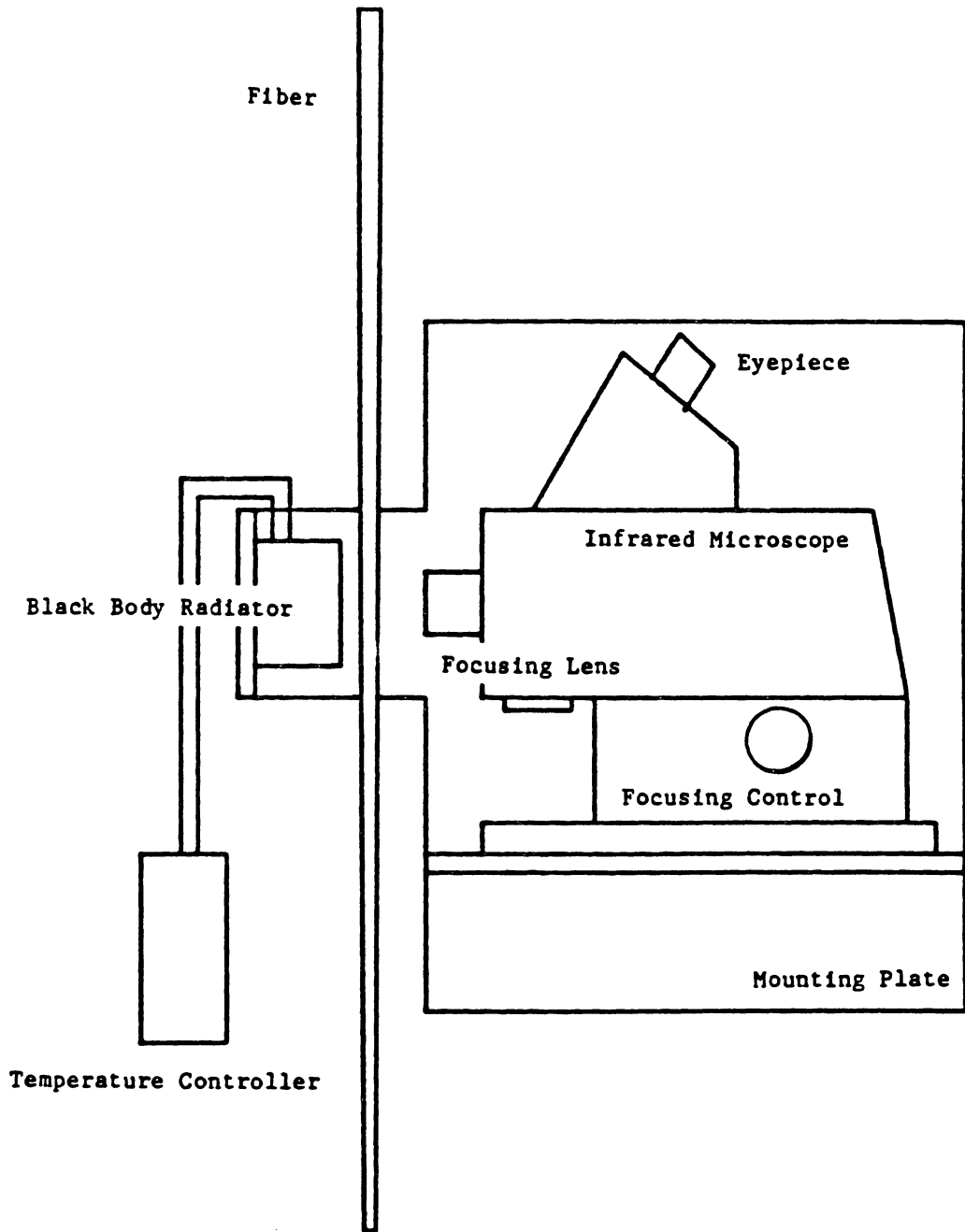


Figure 3.4 Schematic of the temperature measuring apparatus.

locate the position on the spinline where the surface temperature of the filament was the same as the radiator temperature. The temperature of the radiator was then reduced by 10°C and sufficient time was allowed for the radiator to reach steady state; then again the position on the spinline corresponding to this temperature was determined. This procedure was repeated down the length of the spinline.

Spinline Tension

The tension in the spinline was measured using a Rothschild Tensiometer with a model INTEG R-1198 measuring head. This instrument was connected to an Applied Micro Technology microcomputer with an analog to digital converter. Before actual spinline measurements began, the instrument was zeroed and, then calibrated using a 5 gram dead weight attached to a nylon-6 filament. The filament was pulled slowly through the tensiometer head by a variable speed electric motor. The full scale adjustment on the tensiometer was done while the weight was moving slowly downwards.

The tension on the running threadline was measured by carefully inserting the measuring head into the spinline at a position just above the take-up device. A computer code, given in Appendix C, was used to collect 300 digitized tension values and an average value was calculated for tension directly in gram-force units.

Conditioned Fiber Characterization

Diameter and Birefringence

The diameter and birefringence of the conditioned nylon-6 fibers were determined using an Olympus Polarizing microscope and a Leitz 30

order tilting plane compensator (model 553096). The bifilar eye piece was calibrated with a standard scale at the same magnification that was to be used in the collection of the diameter data. Samples of the fiber were mounted on a glass slide with double stick tape and then the glass slide was placed in the microscope translator. Precautions were taken to avoid stretching the fiber during the mounting procedure. The translator was used to bring the fiber into the microscope's field of view and the position of the eye piece cross-hairs at the left and right edges of the fiber were recorded. The diameter was calculated by subtracting the eye piece scale readings and multiplying the result by a scale factor which was determined by calibration with an optical standard (1 division = 8.7×10^{-5} meters).

After the diameter readings were taken the polars on the microscope were crossed and the compensator was inserted into the microscope for optical retardation measurement. The procedure described for online retardation measurement was carried out with the slight difference due to use of a 30 order compensator instead of the 4 order compensator. In the case of the 30 order compensator, one reading was on the red, or forward, scale and the other on the black, or backward, scale. The optical retardation for birefringence calculation was determined by adding the red and black scale readings of the compensator and again performing a table interpolation using values supplied with the compensator manual. The interpolated value was multiplied by 6.07 (a constant associated with the Leitz 30 order compensator). This produced the optical retardation in meters. The birefringence was then the ratio of optical retardation to diameter of conditioned fiber. At least ten

sets of measurements on the final fibers were taken at each different spinning condition and the results were averaged. These averaged final fiber diameters were also used to calculate the take-up speeds from the continuity equation.

Density

The densities of the conditioned filaments were determined in a toluene - carbon tetrachloride density gradient column at 23°C. The gradient column was prepared and calibrated according to ASTM standard D1505 - 68 with density ranging from 1.10 to 1.15 gm/cm³. The fiber samples were soaked in toluene - carbon tetrachloride solution and then carefully introduced into the column. A twenty - four hour period was allowed for fibers to reach the equilibrium position in the column; then their position was recorded. The density of the samples was calculated from a calibration plot in terms of density of standard glass beads versus position of glass beads in the column.

Wide Angle X-ray Scattering

A Philips Norelco x-ray generator with nickel filtered CuK α radiation of wavelength 1.542 Å (0.1542 nm) was used to obtain wide angle x-ray scattering (WAXS) patterns of the conditioned fibers. The fibers were wound on a sample holder taking care that the fibers were not stretched while winding. The sample holder was then mounted on the WAXS unit so that the fiber axis was normal to the x-ray beam. The unit was operated at 40 kilovolts and 15 milliamperes using pinhole collimation. The WAXS patterns were recorded on Kodak Blue Brand x-ray film using a sample to film distance of about 3 centimeters. After

exposure time of about 4 hours the films were developed in Kodak Industrex developer for 5 minutes, fixed in Kodak Rapidfix for 5 minutes and then given a 10 minute water wash.

X-ray Diffractometer Scans

For determining relative amounts of phases and the crystalline orientation function of conditioned fiber samples, x-ray diffractometer scans were performed by a Rigaku Geigerflex x-ray diffractometer which was interfaced with a microprocessor and a Digital Equipment Corporation PDP 11/34 computer. The microprocessor and computer controlled all sample manipulation and data collection procedures.

In order to determine the relative amounts of α and γ phases present in the nylon-6 filaments the integrated intensities from the meridional scan of the 020 reflection (corresponding to 2θ value of about 11°) for 2θ range of $7 - 15^\circ$ and from the equatorial scan for 2θ range of $14 - 28^\circ$ were measured. These integrated intensities were corrected for background intensity for the above specified 2θ range for each scan.

The relative amounts of α , γ and amorphous phases were determined from the integrated intensity data acquired from the Rigaku x-ray diffractometer by the method of Gianchandani et al. (30). The amount of γ -phase in a given sample was calculated by

$$X_\gamma = \frac{R - R_\alpha^s}{R_\gamma^s - R_\alpha^s} X_\gamma^s \quad (3-1)$$

where X_γ and X_γ^s are the mass fractions of γ -phase in the sample and in the standard γ sample, respectively. R is the intensity ratio of the sample given by

$$R = \frac{\int_7^{15} I_{020} d(2\theta)}{\int_{14}^{28} I_{eq} d(2\theta)} \quad (3-2)$$

where I_{020} is the intensity obtained from the meridional scan containing (020) peak at about 2θ value of 11° and I_{eq} is the intensity obtained from the equatorial scan. R_α^S and R_γ^S in equation (3-1) are the intensity ratios of the standard α and γ samples, respectively. The values for R_α^S , R_γ^S and X_γ^S reported by Gianchandani et al. (30) were 1.11×10^{-2} , 128.0×10^{-2} and 0.75, respectively. The α -phase fraction was calculated from

$$X_\alpha = \frac{(\bar{v} - \bar{v}_{am}) - X_\gamma(\bar{v}_\gamma - \bar{v}_{am})}{\bar{v}_\alpha - \bar{v}_{am}} \quad (3-3)$$

which resulted from

$$X_\gamma + X_\alpha + X_{am} = 1.0 \quad (3-4)$$

and

$$\bar{v} = X_\gamma \bar{v}_\gamma + X_\alpha \bar{v}_\alpha + X_{am} \bar{v}_{am} \quad (3-5)$$

where X_α , X_γ and X_{am} are the mass fractions of α -phase, γ -phase and amorphous phase in the sample, and v , v_α , v_γ , and v_{am} are the specific volumes of sample, α -phase, γ -phase and amorphous phase, respectively. The specific volumes of the crystalline phases were calculated from the unit cell dimensions and the amorphous density was taken from the literature. The values reported by Gianchandani et al. (30): $\rho_\gamma = 1.17 \text{ gm/cm}^3$, $\rho_\alpha = 1.23 \text{ gm/cm}^3$ and $\rho_{am} = 1.08 \text{ gm/cm}^3$.

Crystalline orientation function was measured using the 020 reflection occurring at a 2θ value of about 11° . After setting the 2θ at the intensity maximum for this reflection, azimuthal step scans were

carried out with intensities measured at β values (the azimuthal angle) ranging from 0 to 90° in one degree steps. Background corrections were applied by making similar step scans performed at 2θ values of 7° and 15°. The data were collected by the Rigaku x-ray diffractometer and PDP 11/34 computer system. These data were processed using a program written by Galen Richeson to calculate the $\langle \cos^2 \phi_{hkl,z} \rangle$ for the 2θ value corresponding to 020 reflection from

$$\langle \cos^2 \phi_{020} \rangle = \frac{\int_0^{\frac{\pi}{2}} I_{020} \cos^2 \phi \sin \phi \, d\phi}{\int_0^{\frac{\pi}{2}} I_{020} \sin \phi \, d\phi} \quad (3-6)$$

The chain axis crystalline orientation factors (considering the b axis to be the chain axis) were then calculated from

$$f_b = \frac{3 \langle \cos^2 \phi_{020} \rangle - 1}{2} \quad (3-7)$$

Differential Scanning Calorimetry

A Perkin - Elmer Series 7 Thermal Analysis Differential Scanning Calorimeter (DSC) was used to obtain thermal traces of the conditioned fibers. Fiber samples were cut and sealed in aluminum pans supplied by Perkin - Elmer. The samples were weighed on a Mettler analytical balance (model 760) in the range of 2 to 10 milligrams. Before using actual fiber samples the instrument was calibrated using a standard Indium sample according to Perkin - Elmer specified procedure. DSC traces for all samples were made from 40 to 270°C at a heating rate of 20°C per minute.

Mechanical Properties

The mechanical properties (initial modulus, tenacity and elongation to break) of the conditioned fibers were determined by using an Instron Universal Testing Instrument (Table model 1122) in the tensile mode. A two thousand gram load cell (model 2511-102) and pneumatic grips were used in all the experiments. Before actual property measurements the procedures for zeroing, balancing and calibration of the instrument were performed according to the manufacturer's instructions. The testing conditions were crosshead speed of 20 millimeters per minute, chart speed of 100 millimeters per minute, chart full scale of 100 grams. All tests were performed at room temperature. The diameter of each fiber was determined prior to each test using the Olympus microscope as described previously under diameter measurement.

For actual tests the grips were set three centimeters apart and a single fiber was placed securely in the grips with minimum initial tension using a pneumatic pedal. The chart and crosshead were started and the force, as measured by the load cell, was recorded as a function of time. The initial modulus, tenacity and elongation to break for conditioned fibers were calculated from the force versus time chart. The initial modulus was calculated from the slope of the initial linear portion of chart as follows:

$$\begin{aligned} \text{Initial Modulus} &= \text{Stress/Strain} \\ &= \frac{\text{Force for initial portion/Area of cross section}}{\text{strain}} \end{aligned} \quad (3-8)$$

where

$$\text{Strain} = \frac{\text{Distance on chart corresponding to force} \times \text{Crosshead speed}}{\text{gauge length} \times \text{chart speed}} \quad (3-9)$$

Tenacity was calculated from

$$\text{Tenacity} = \frac{\text{Force corresponding to break point}}{\text{Initial area of cross section}} \quad (3-10)$$

And elongation to break was calculated from

$$\% \text{ Elong. to break} = \frac{\text{Dist. on chart up to break pt.} \times \text{Crosshead speed}}{\text{gauge length} \times \text{chart speed}} \quad (3-11)$$

Area of cross section was calculated from the diameter measurement. For each sample about ten experiments were performed to calculate averages of all the mechanical properties.

CHAPTER 4

EXPERIMENTAL RESULTS

Online Experimental Measurements

Diameter Profiles

The measured diameter at a particular position on the spinline was the result of statistical analysis of 2000 data points collected by using the Zimmer diameter monitor and Applied Micro Technology microcomputer. The variation in diameter values is due to filament movement in and out of focus in the field of the Zimmer diameter monitor and variations in mass throughput, extrusion temperature, air suction force causing drawdown of filament, etc. A typical distribution of diameter values at 20 cm, 90 cm and 150 cm from the spinneret for CN9984 at 3 g/min throughput and at take-up speed of 1960 m/min is shown in Figures 4.1 to 4.3. It is seen that closer to spinneret (20 cm) the distribution is quite broad and becomes relatively narrower at positions farther from the spinneret (90 and 150 cm). The peak of the distribution was taken as the most probable diameter at that particular position on the spinline.

An interesting feature of this technique is that it can quickly determine whether necking is occurring and accurately locate the necking position as shown in the diameter distributions at 7300 m/min at various positions from 130 cm to 150 cm in Figure 4.4. At 130 and 150 cm the distribution is unimodal (exhibiting only one peak) while at 135 and 140 cm it becomes bimodal, indicating the occurrence of two possible diameter values which are quite different from each other. This result

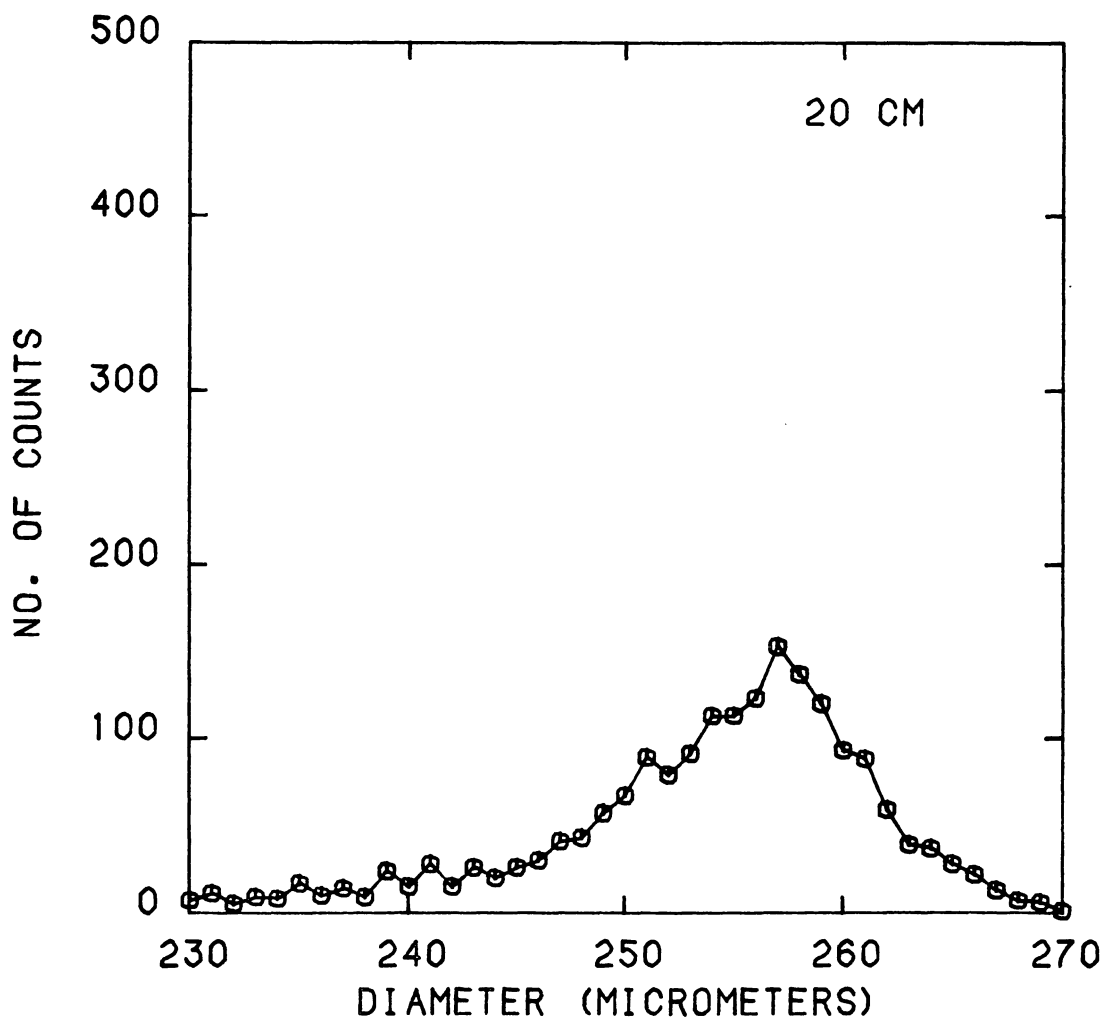


Figure 4.1 Diameter distribution at 20 cm from the spinneret for CN9984 with a mass throughput of 3.073 g/min and take-up velocity of 1960 m/min.

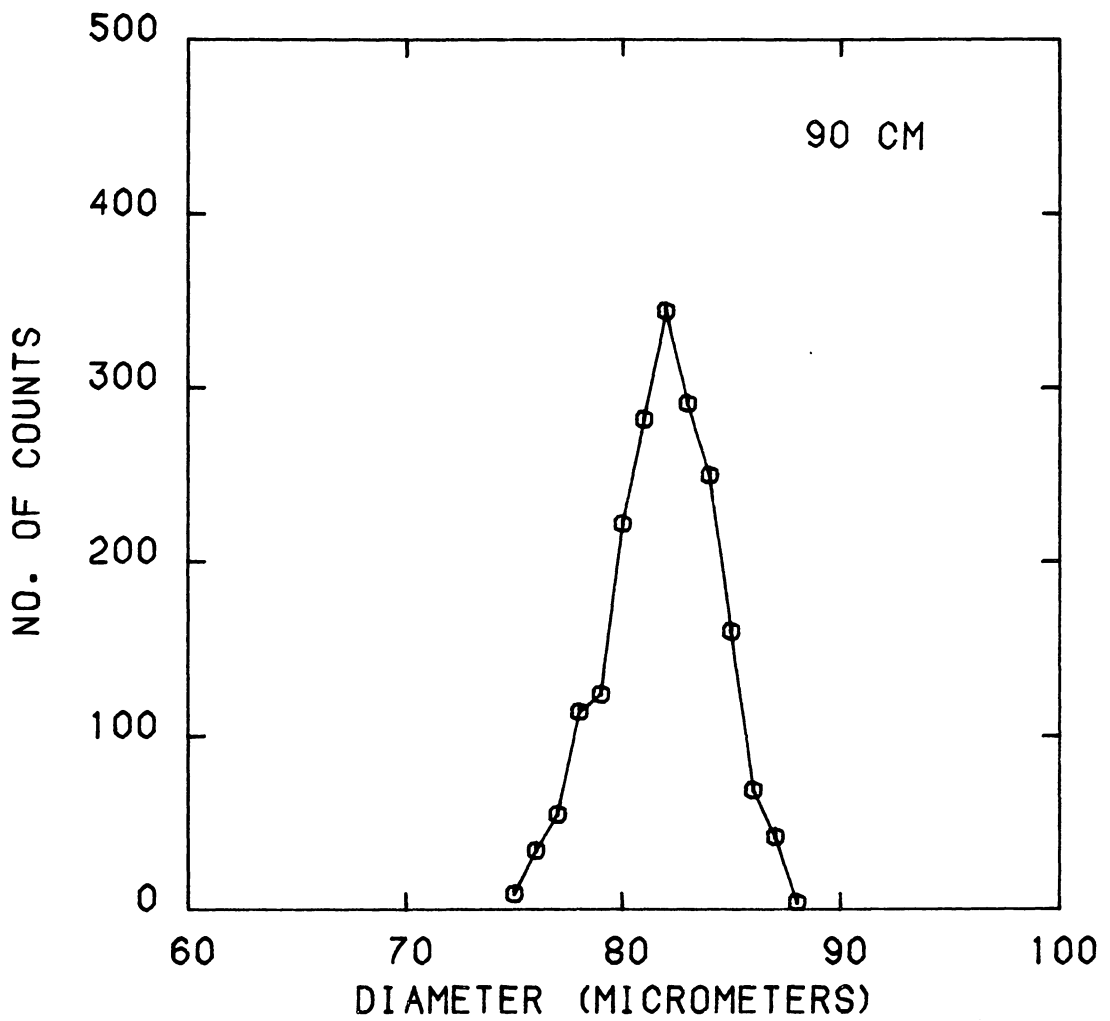


Figure 4.2 Diameter distribution at 90 cm from the spinneret for CN9984 with a mass throughput of 3.073 g/min and take-up velocity of 1960 m/min.

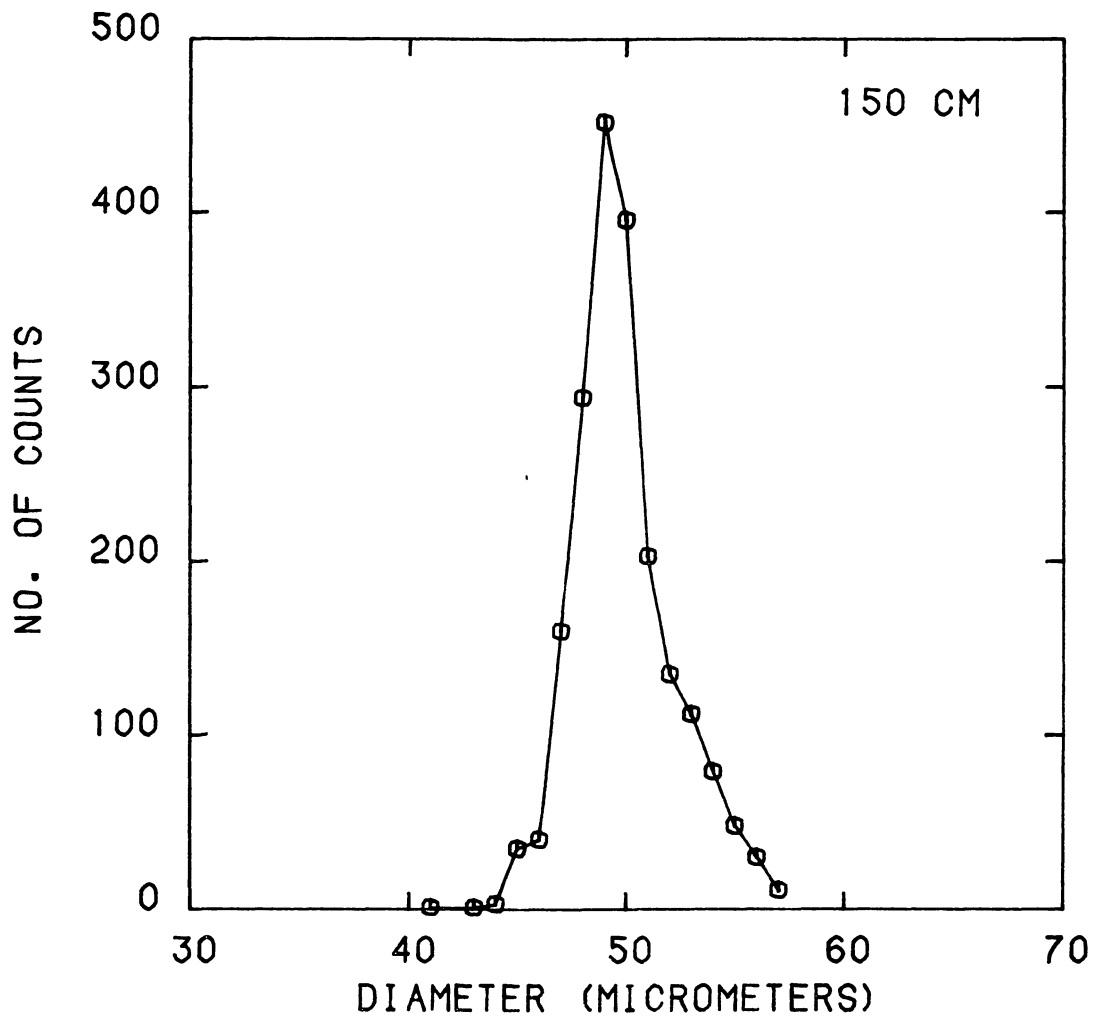


Figure 4.3 Diameter distribution at 150 cm from the spinneret for CN9984 with a mass throughput of 3.073 g/min and take-up velocity of 1960 m/min.

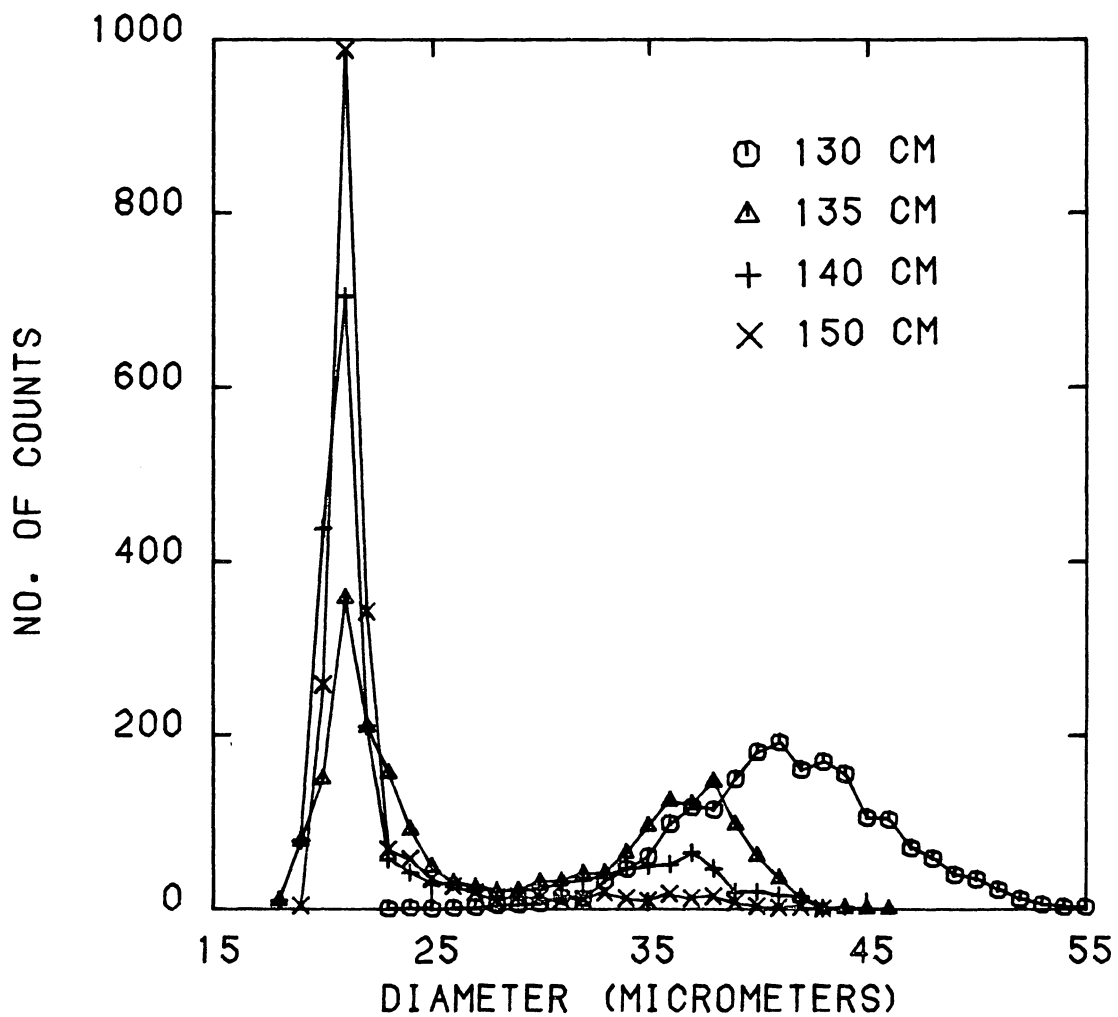


Figure 4.4 Diameter distribution at the indicated distances from the spinneret for CN9984 with a mass throughput of 3.073 g/min and take-up velocity of 7310 m/min.

is due to the fact that the neck oscillates up and down over a few centimeters (about 5 cm in this case).

The experimental online diameter profiles for both CN9984 and BHS resins at mass throughputs of about 3 and 5 g/min were obtained by statistical analysis described above and the results are shown in Figures 4.5 to 4.8. The rightmost points shown on these figures give the final (offline) values. At lower take-up speeds the drawdown of the spinline takes place over a larger distance compared to that at higher take-up speeds, as the final diameter on the spinline is close to take-up device at lower speeds while the final value of diameter is approached well before the take-up device at high speeds. The effect of mass throughput for each resin is quite appreciable in that the diameter drawdown is substantially faster for 3 g/min than for 5 g/min at similar speeds. As far as the effect of molecular weight is concerned, the diameter drawdown is faster for BHS than for CN9984 when compared at similar take-up speeds and mass throughput. These comparisons indicate that the higher melt viscosity of the BHS resin tends to shift the drawdown toward the higher temperature regime nearer the spinneret where the filament is more easily deformed. In the case of lower mass throughput the effective heat transfer leads to lower temperature of spinline at any given distance from the spinneret (temperature profiles will be discussed in the following section) which results in higher melt viscosity at any given position. This tends to shift the regime of easy deformation to positions closer to the spinneret.

Necks in the diameter profiles were observed for 3 g/min mass throughput for both CN9984 and BHS, whereas no necking was observed for

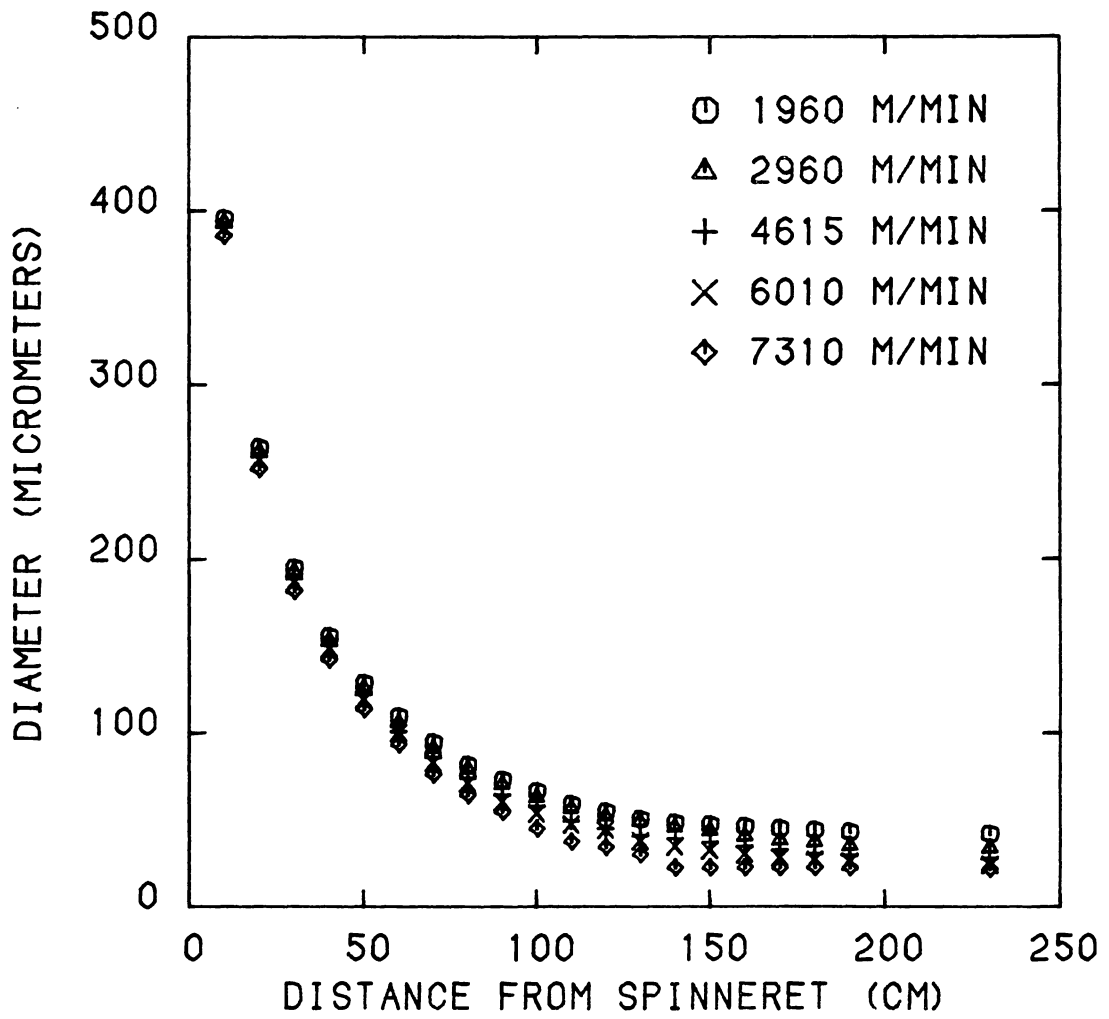


Figure 4.5 Experimental diameter profiles for CN9984 with a mass throughput of 3.073 g/min.

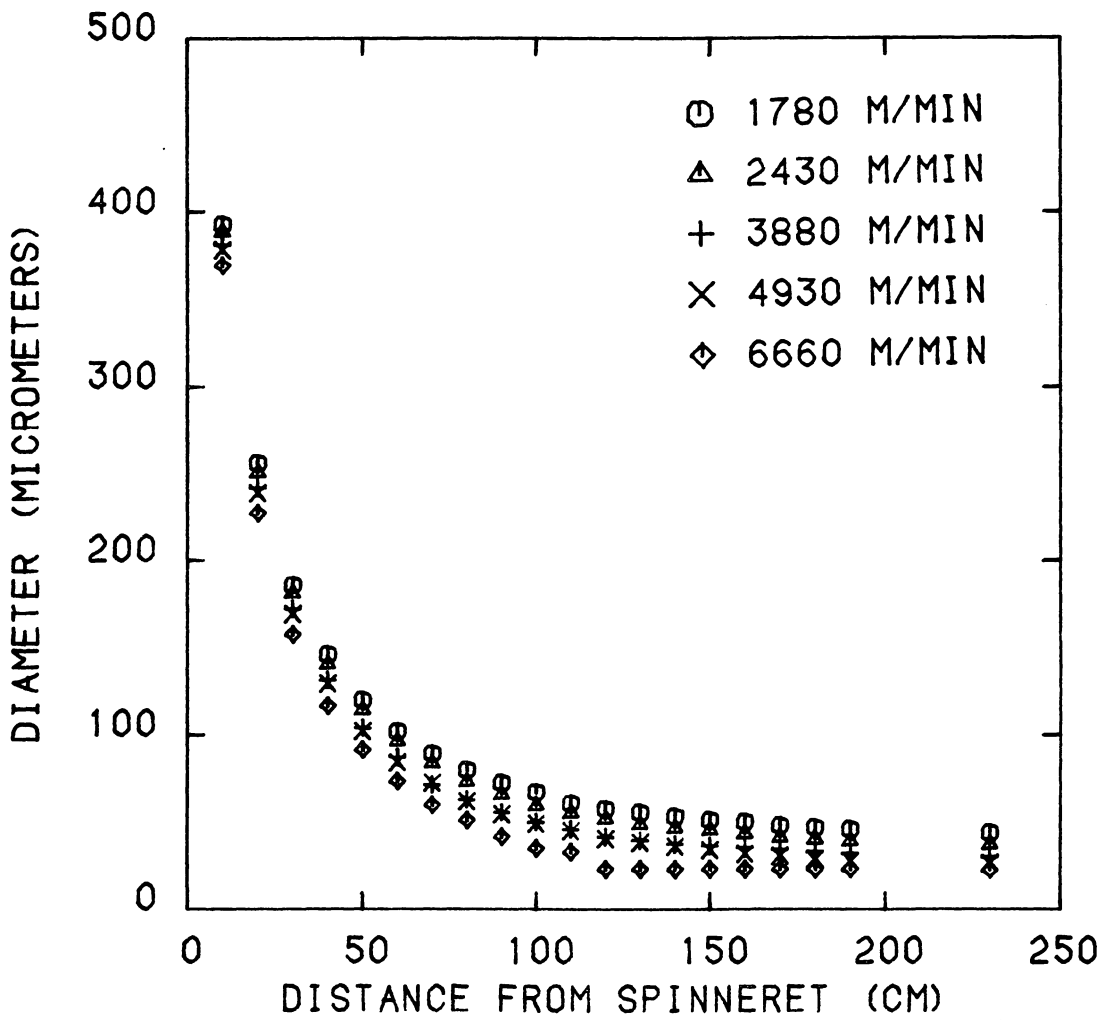


Figure 4.6 Experimental diameter profiles for BHS with a mass throughput of 2.993 g/min.

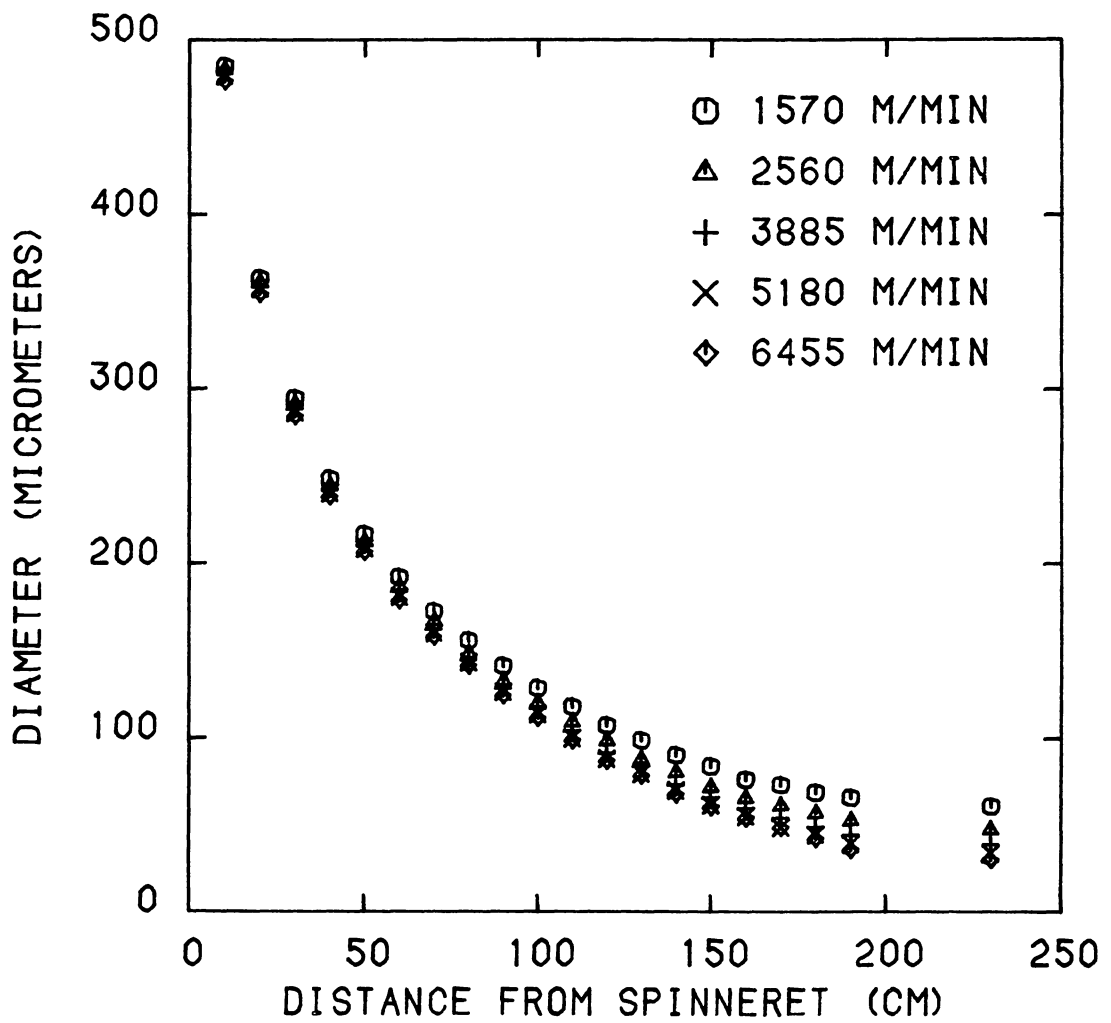


Figure 4.7 Experimental diameter profiles for CN9984 with a mass throughput of 5.154 g/min.

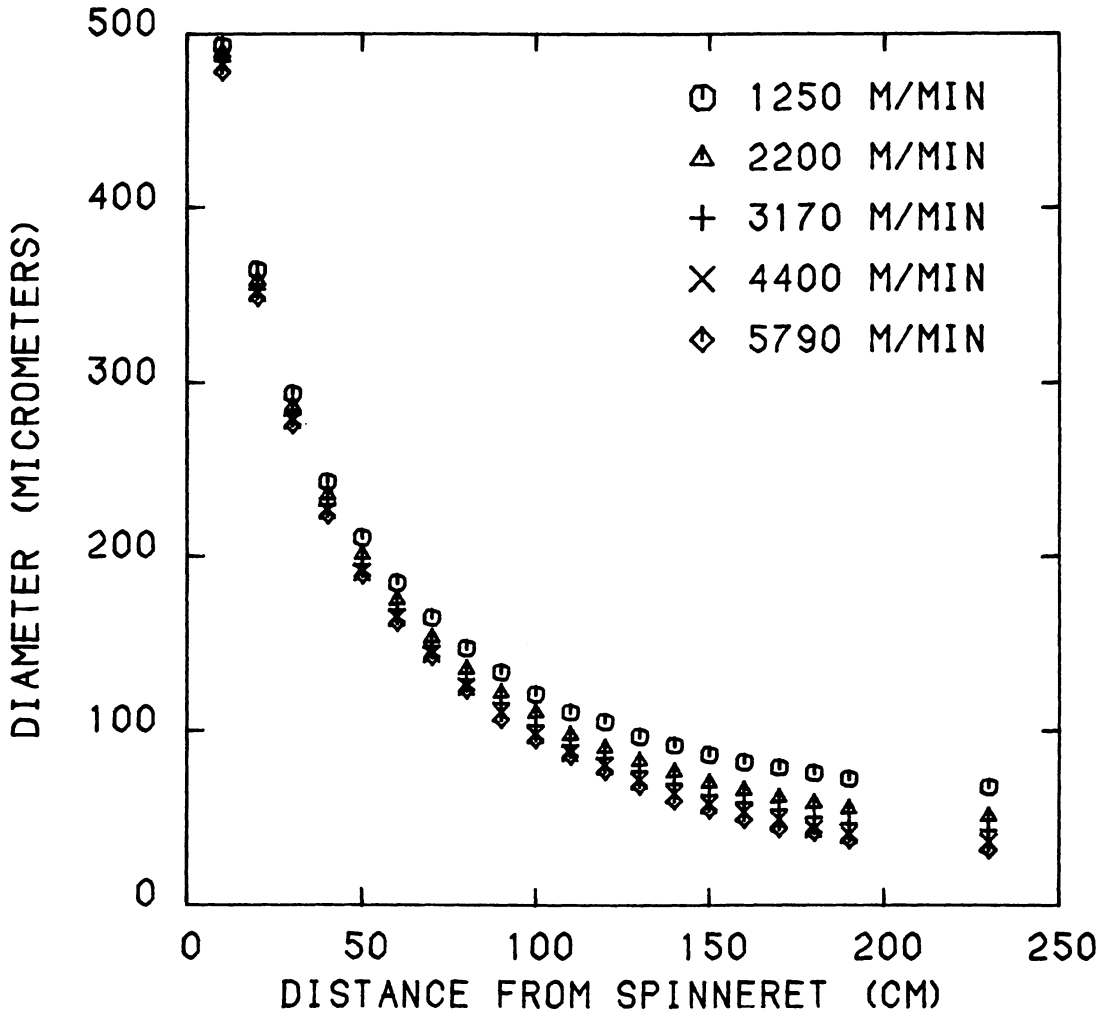


Figure 4.8 Experimental diameter profiles for BHS with a mass throughput of 5.069 g/min.

either resin at 5 g/min throughput for the range of take-up speeds studied. The necking in diameter occurs at lower spinning speed and closer to the spinneret for BHS (6660 m/min and 115 cm) than that for CN9984 (7310 m/min and 135 cm).

Temperature Profiles

Figures 4.9 to 4.12 show the corresponding experimental online temperature profiles. The temperature profiles seem to be relatively independent of the take-up speeds except that at high speeds a plateau was observed at 3 g/min throughput for CN9984 at about 140 cm and for BHS at about 120 cm from the spinneret. These plateau positions are very close to the positions in each case where necking in the corresponding diameter profiles was observed. Relative independence of temperature profile with increasing take-up speed for a particular mass throughput seems to be the result of a competition between increased heat transfer rate due to increased surface to volume ratio of a volume element and the reduced time required for that volume element to reach a particular position. Thus at lower take-up speeds the specific surface (surface to volume ratio) of a volume element is lower allowing less cooling but the time required for that volume element to reach a particular position is higher allowing higher cooling and vice a versa. The effect of mass throughput on temperature profiles is quite substantial in that the cooling rate for 3 g/min throughput is considerably higher than that for 5 g/min due to larger filament diameter. Consequently, lower temperature is observed at any position on the spinline for 3 g/min condition compared to that for 5 g/min for a given take-up speed.

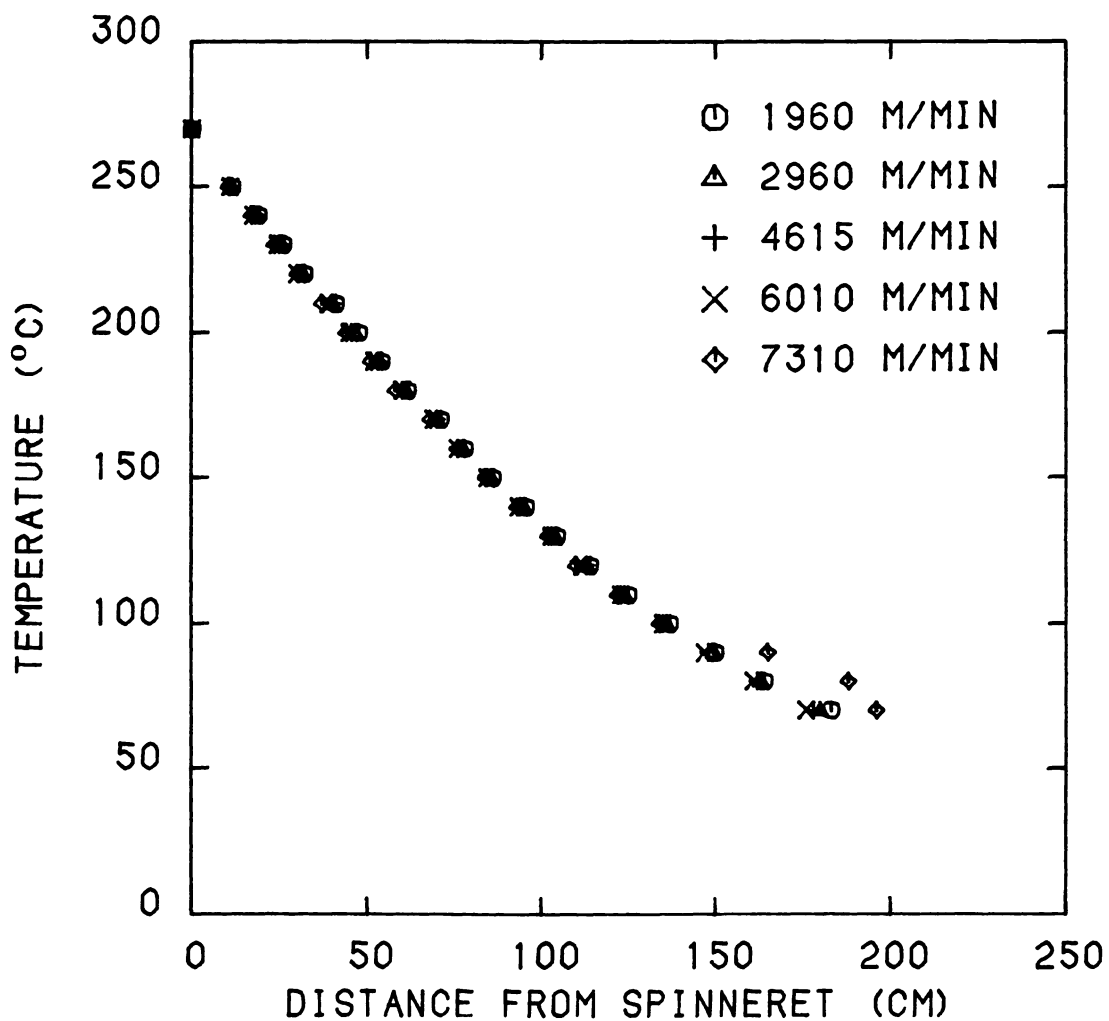


Figure 4.9 Experimental temperature profiles for CN9984 with a mass throughput of 3.073 g/min.

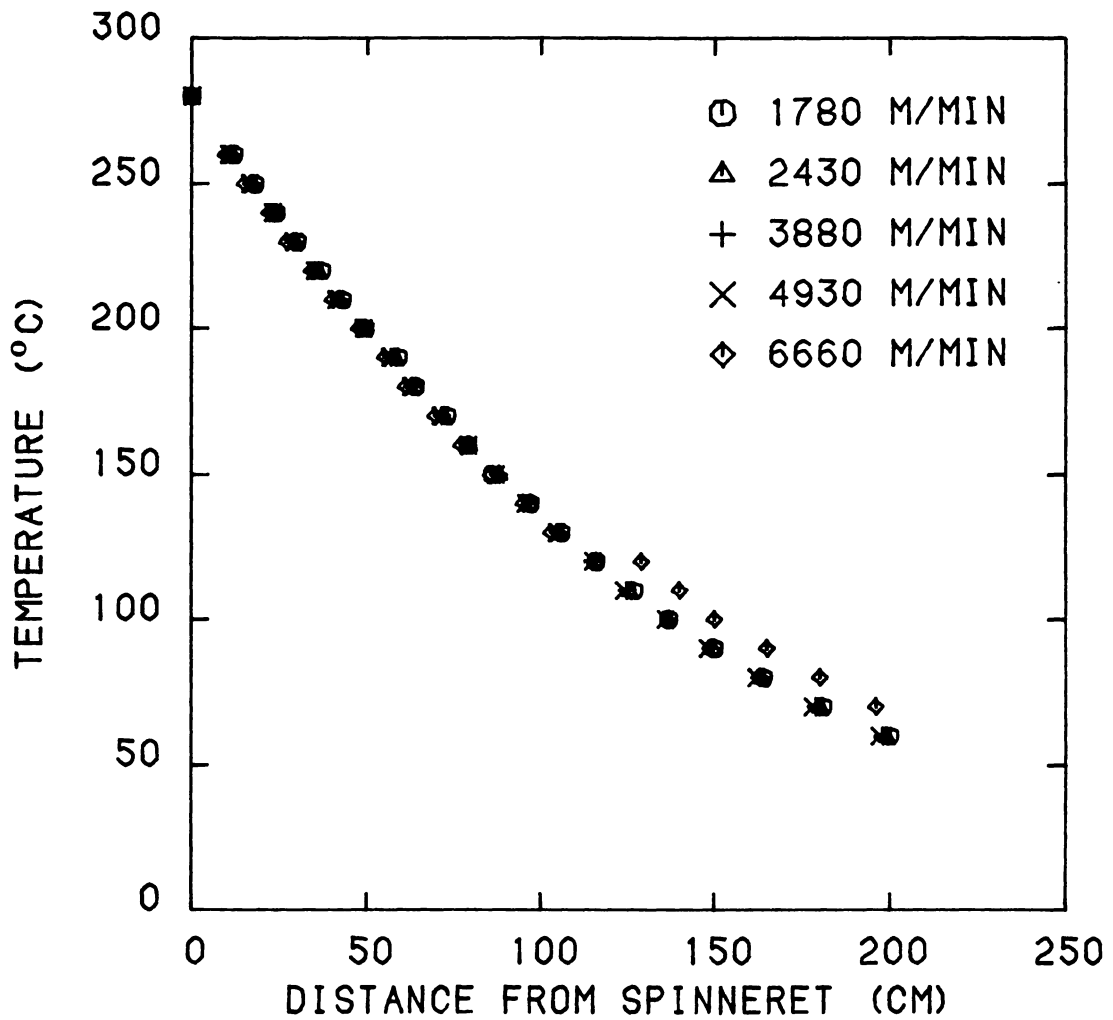


Figure 4.10 Experimental temperature profiles for BHS with a mass throughput of 2.993 g/min.

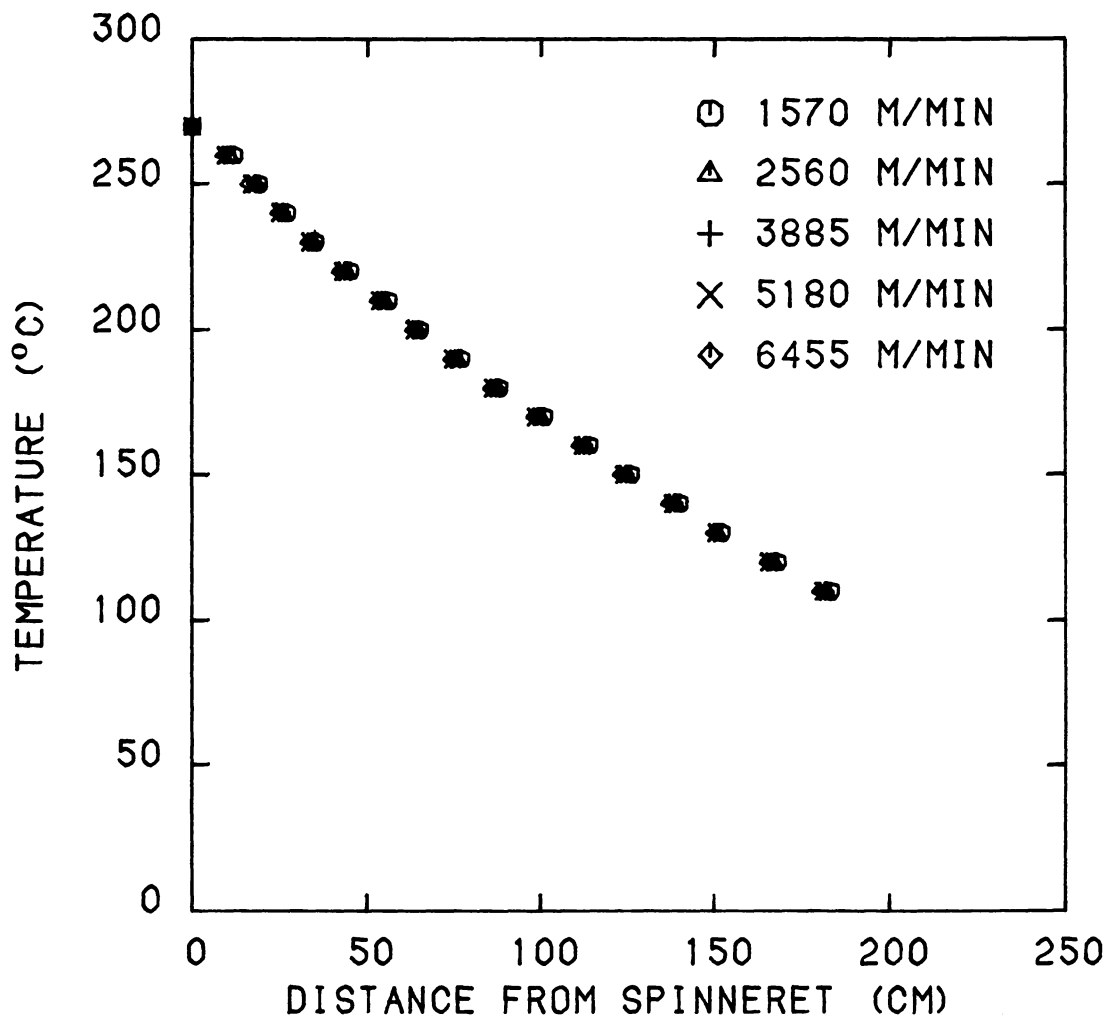


Figure 4.11 Experimental temperature profiles for CN9984 with a mass throughput of 5.154 g/min.

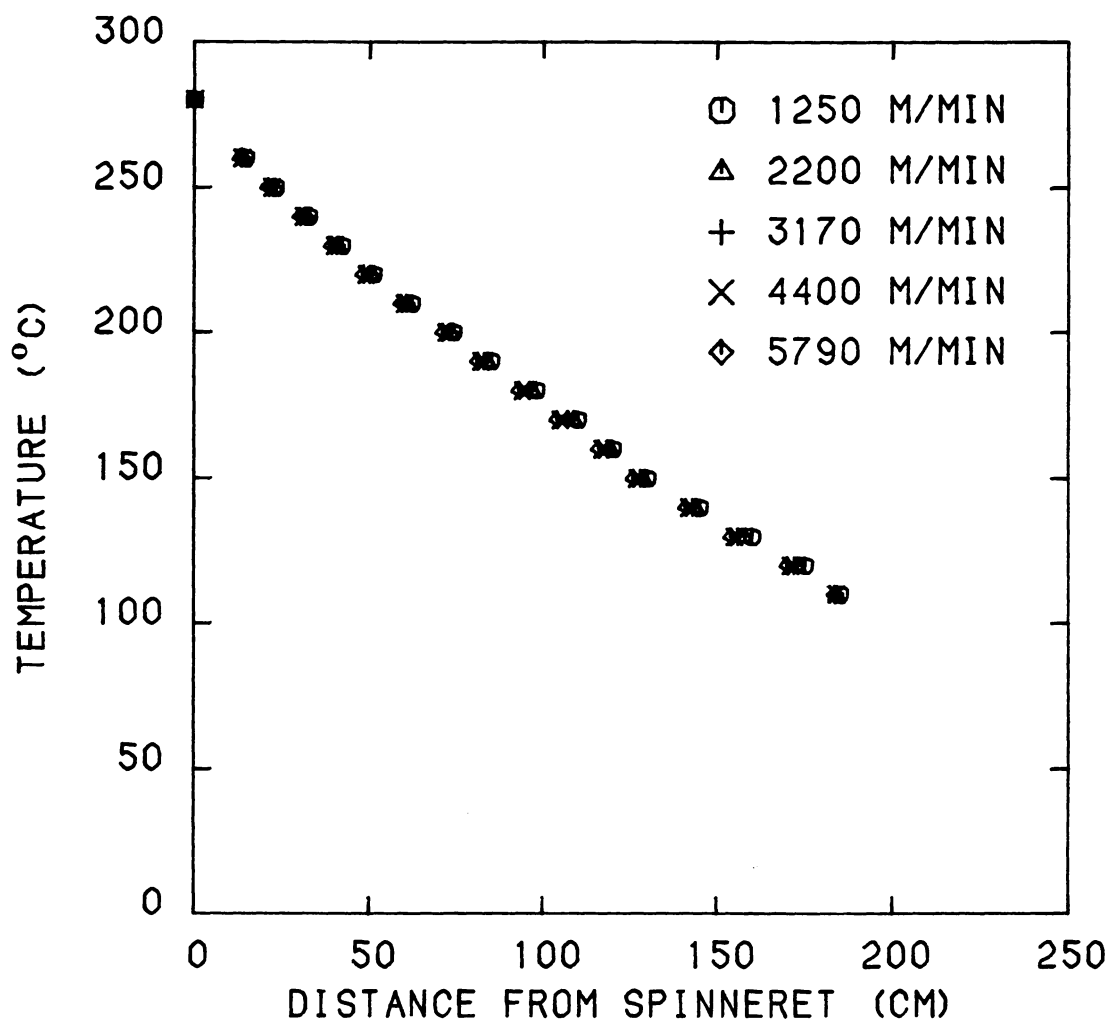


Figure 4.12 Experimental temperature profiles for BHS with a mass throughput of 5.069 g/min.

Birefringence Profiles

Figures 4.13 to 4.16 show the corresponding experimental online birefringence profiles. The rightmost points on these figures give the value of offline birefringence as soon as it can be measured (it took approximately 2 minutes after the sample was collected in the receiving container). These profiles, for both resins, show a steady increase up to the offline value at lower take-up speeds for a throughput of 3 g/min and at all speeds studied for a throughput of 5 g/min. At high speeds for a throughput of 3 g/min the steady initial increase is followed by a sudden jump in birefringence and a subsequent leveling out at a much higher value than that for lower take-up speeds. The jump in birefringence for BHS occurred at lower speeds and closer to the spinneret than that for CN9984. The position of the jump in birefringence corresponds to the appearance of necking in the respective diameter profile and the plateau in the respective temperature profile for both the resins, indicating the appearance of online crystallization.

Spinline Tension

Figure 4.17 shows the experimental spinline tension measured at a distance of 190 cm from the spinneret for both resins and for throughputs of 3 and 5 g/min as a function of take-up speed. The spinline tension increases with take-up speed at all conditions but the rate of increase is higher at high speeds for throughput of 3 g/min than for 5 g/min. The increase in tension at high speeds is due to the higher air drag and inertial force contributions. Generally, spinline tension is higher for a throughput of 5 g/min than for 3 g/min, and a similar

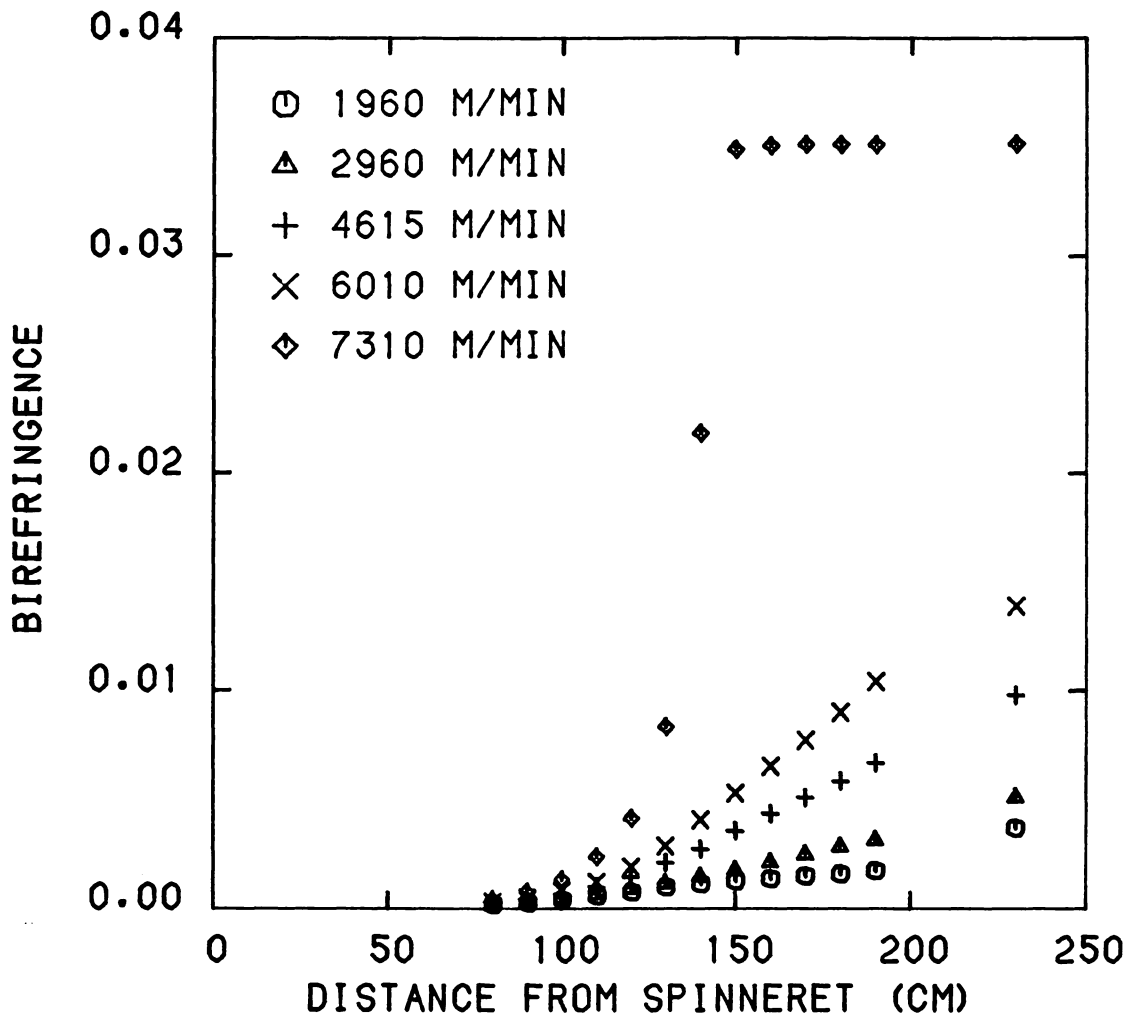


Figure 4.13 Experimental birefringence profiles for CN9984 with a mass throughput of 3.073 g/min.

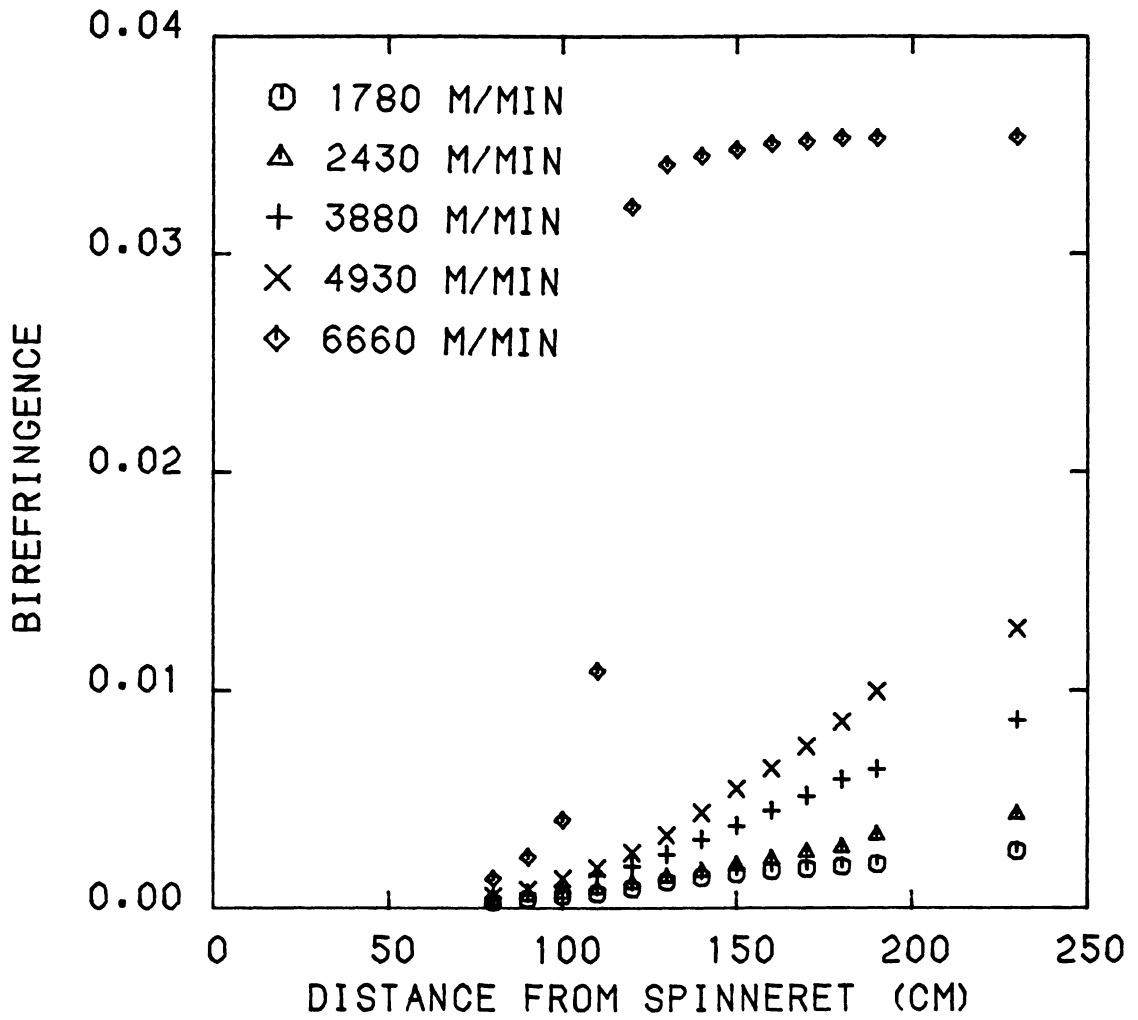


Figure 4.14 Experimental birefringence profiles for BHS with a mass throughput of 2.993 g/min.

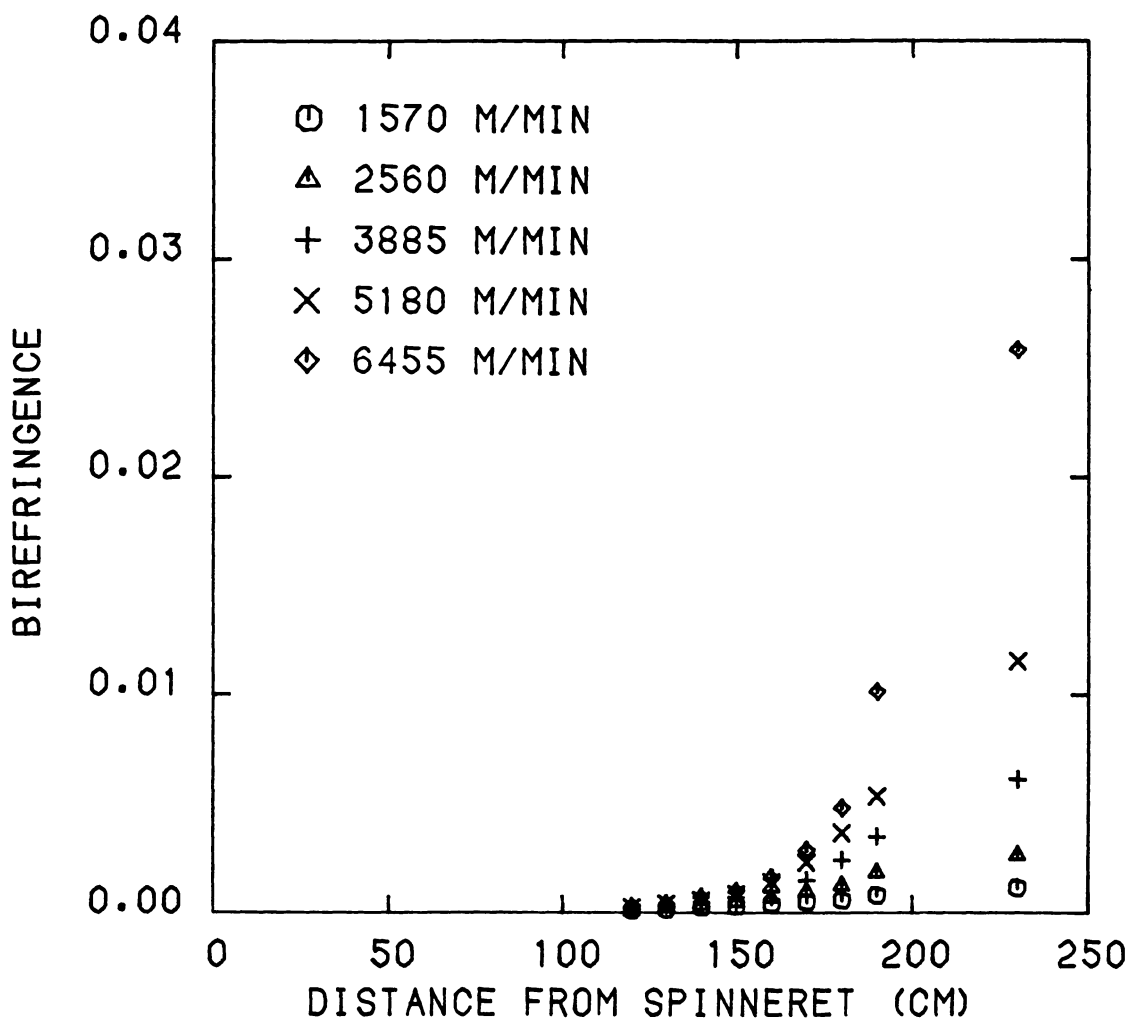


Figure 4.15 Experimental birefringence profiles for CN9984 with a mass throughput of 5.154 g/min.

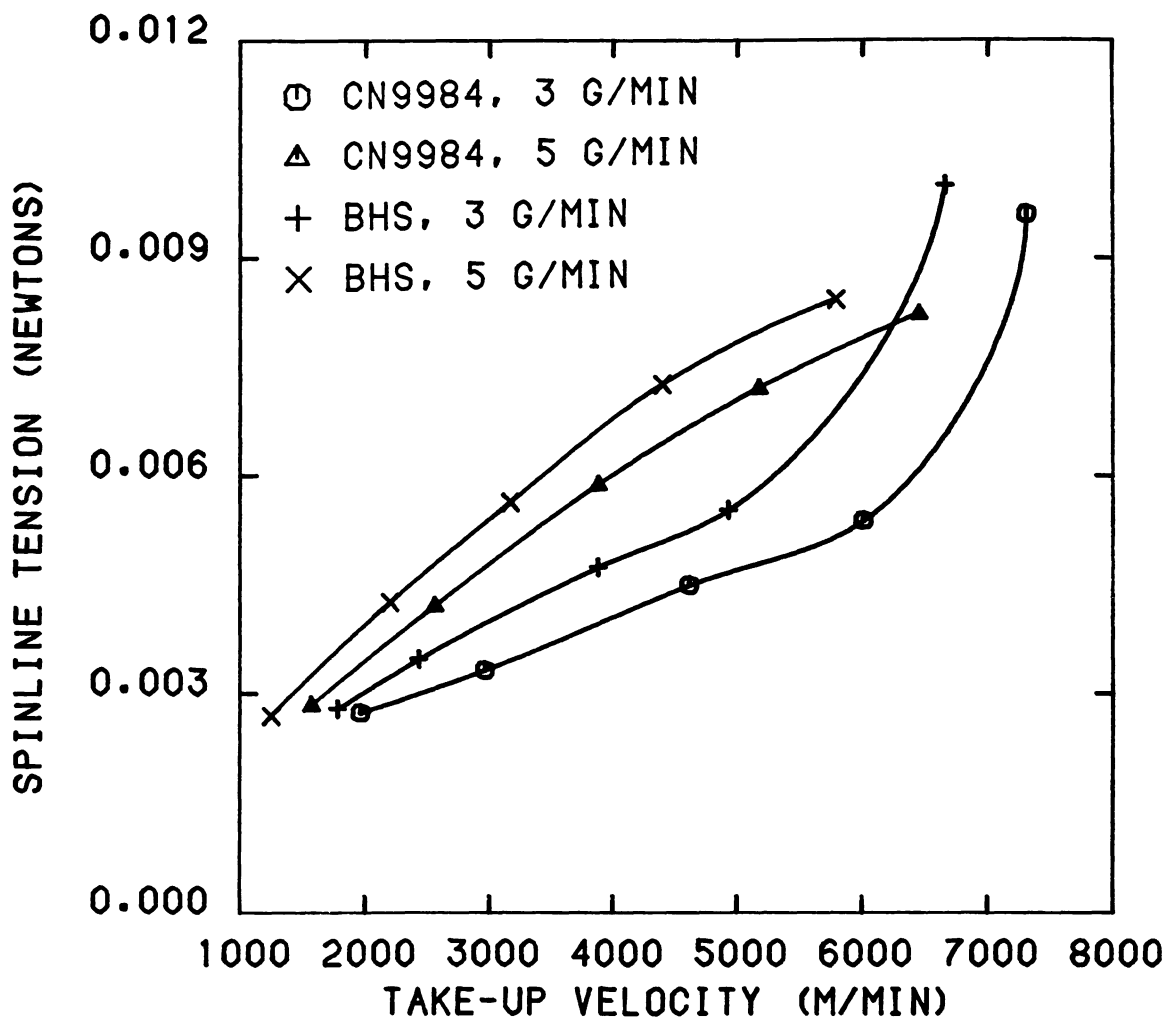


Figure 4.17 Experimental spinline tension at a position of 190 cm from the spinneret.

trend is observed for BHS compared to CN9984. The observed trend with variation of throughput is due to substantially higher inertial and air drag force contributions at higher throughput. The inertial force is a product of throughput and difference in velocity and consequently the higher inertial force contribution at higher throughput. The higher throughput results in larger diameter and air drag contribution is higher for larger diameter filament for similar speeds. The observed trend with variation of molecular weight of resin is due to the fact that higher melt viscosity of higher molecular weight develops higher tension for similar drawdown.

Effects of Post-Spinning Equilibration with the Environment

Structural Changes with Ambient Conditioning

We also studied the effect of conditioning time on the birefringence of the melt spun filaments. Figures 4.18 to 4.21 show the effect of conditioning time under ambient conditions on birefringence change. For fibers spun at low to intermediate take-up speeds these figures show a jump in birefringence at about 5 minutes of conditioning time followed by leveling out at a final value which varied with spinning speed. This effect is apparently caused by crystallization due to water absorption from the atmosphere. The jump in birefringence was relatively shorter (also note the initial value of birefringence is higher) for BHS resin than that for CN9984 and at high speeds there was no significant change in birefringence for either resin, particularly after the necking occurred at throughput of 3 g/min.

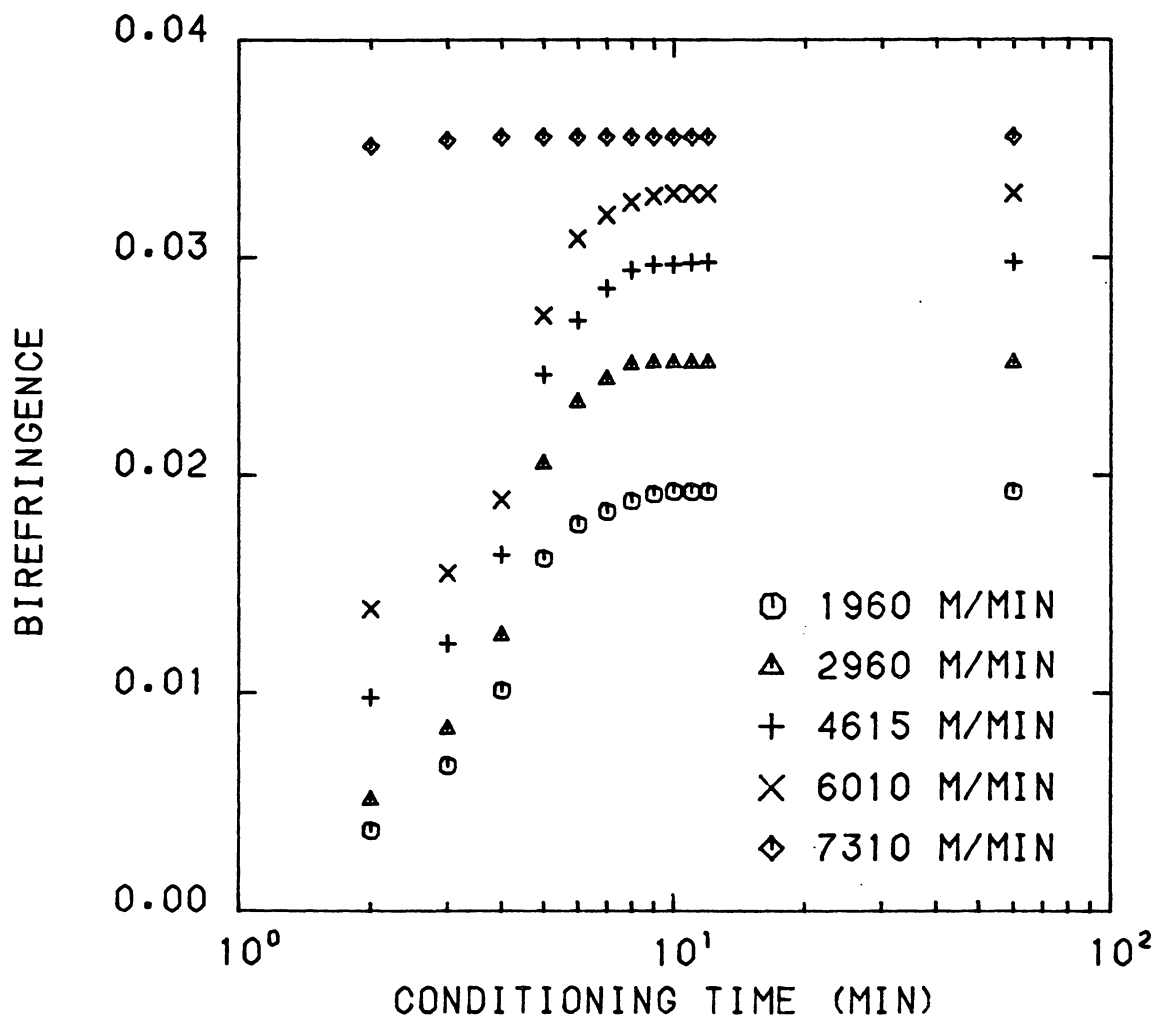


Figure 4.18 Change in birefringence with conditioning time for CN9984 with a mass throughput of 3.073 g/min.

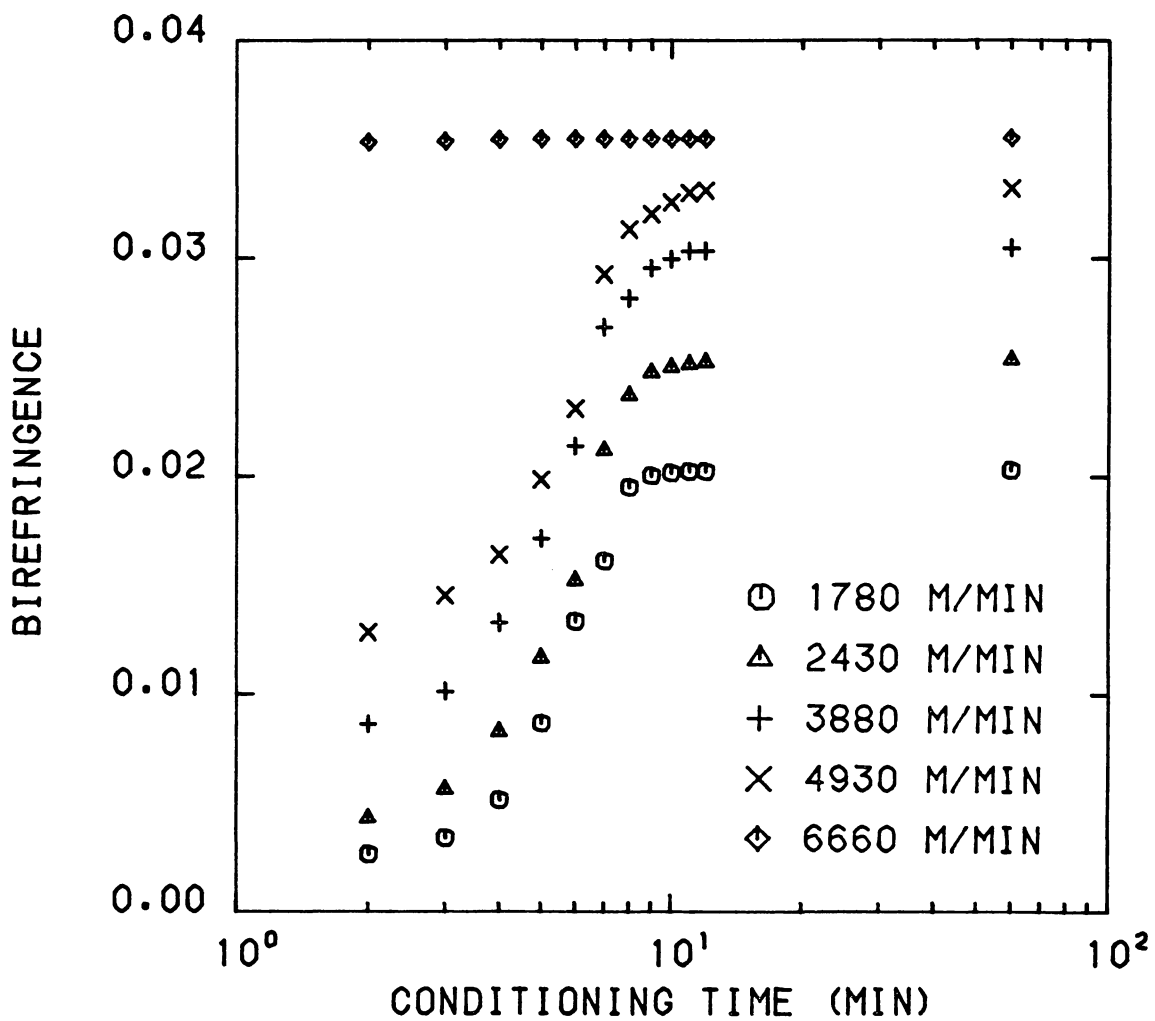


Figure 4.19 Change in birefringence with conditioning time for BHS with a mass throughput of 2.993 g/min.

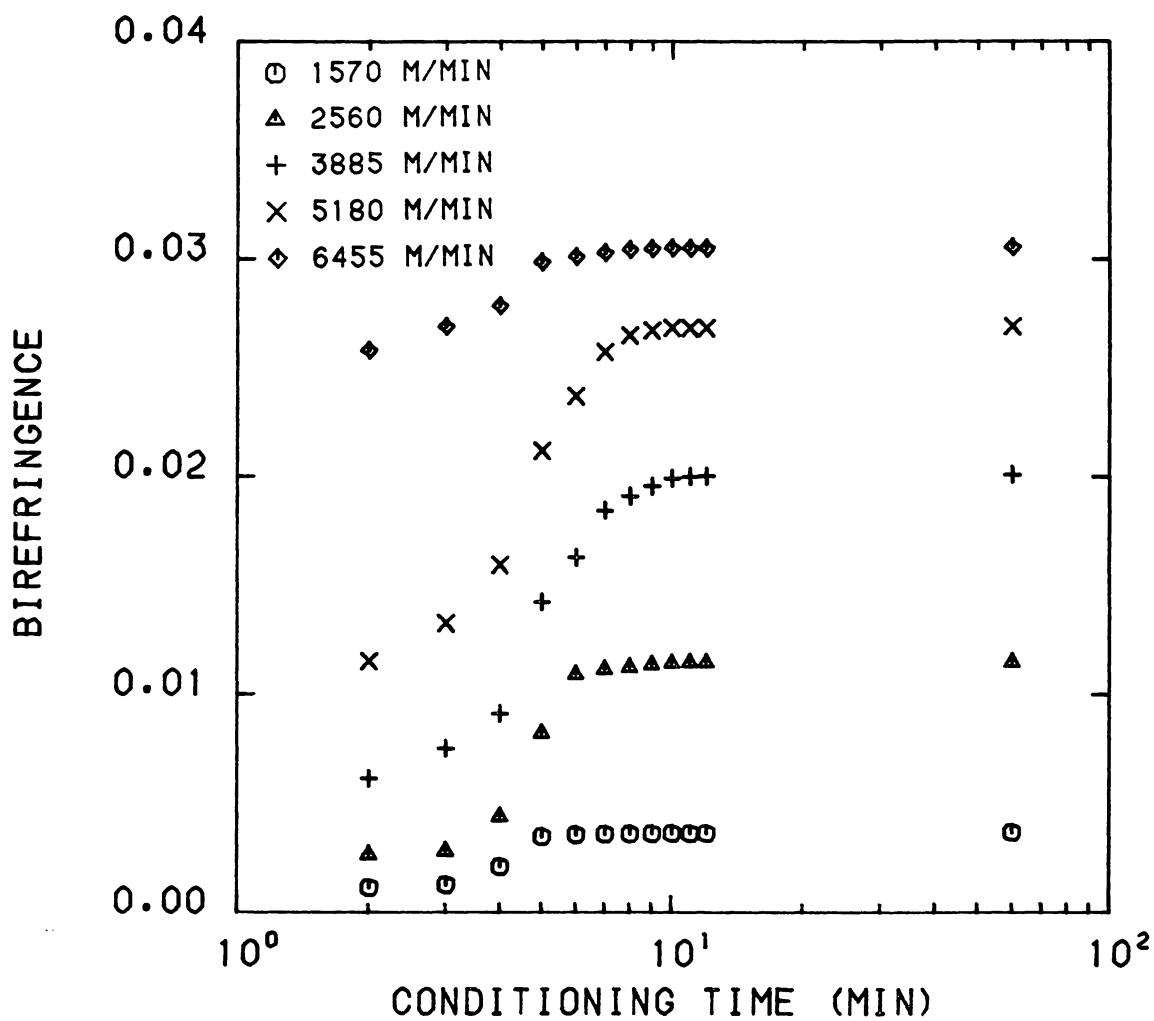


Figure 4.20 Change in birefringence with conditioning time for CN9984 with a mass throughput of 5.154 g/min.

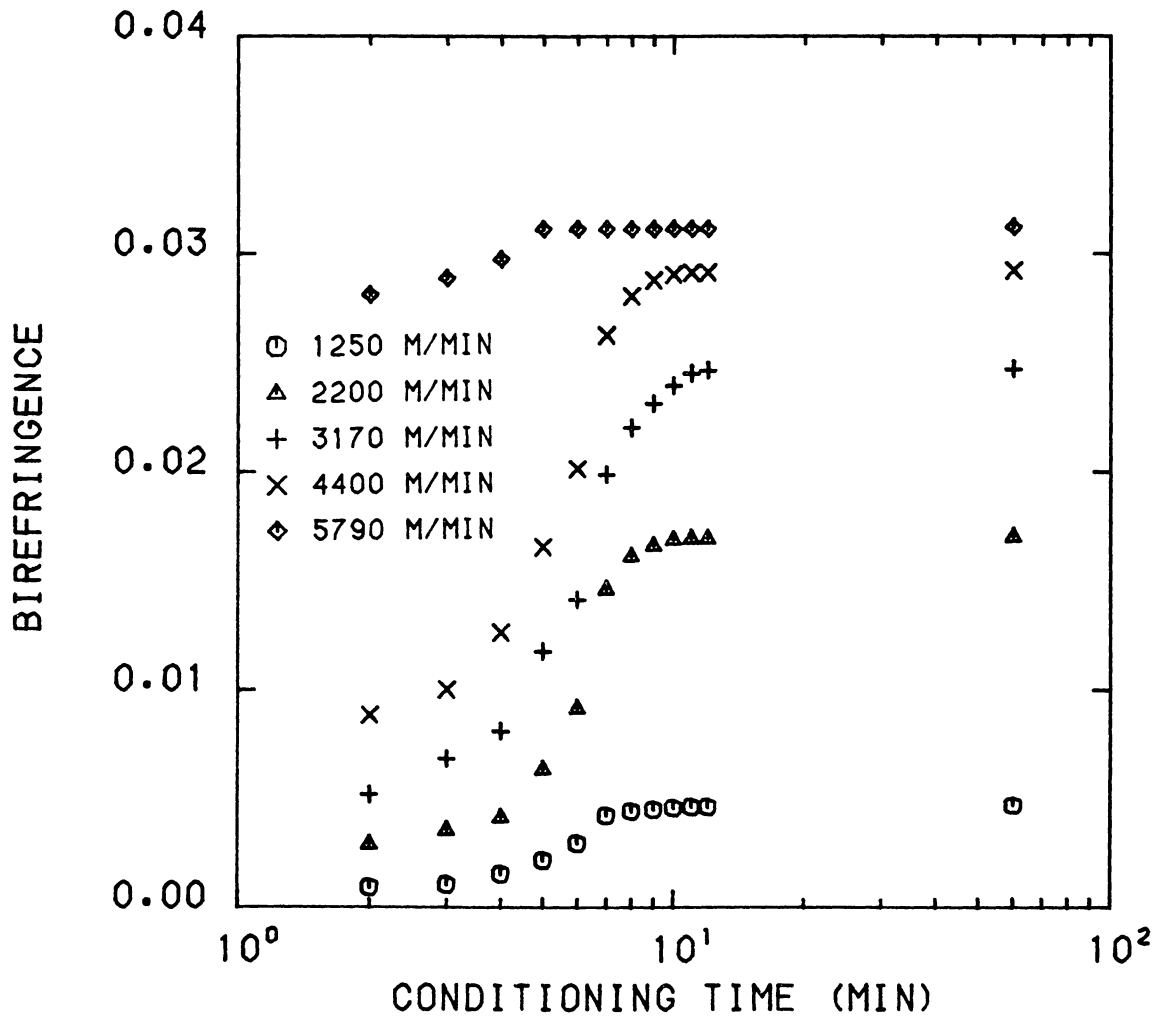


Figure 4.21 Change in birefringence with conditioning time for BHS with a mass throughput of 5.069 g/min.

Structure and Properties of Conditioned Fibers

Samples from various spinning conditions (various take-up speeds and two mass throughputs of 3 and 5 g/min) for both CN9984 and BHS resins were conditioned and characterized according to test procedures described in Chapter 3. The results of characterization have been compared with Suryadevara's (31) results who previously studied structure development in high speed melt spun nylon-6 resins of various molecular weight including the two studied here.

Figure 4.22 shows the density of the conditioned filaments as a function of take-up velocity for both the resins and two mass throughputs. The general trend seems to be an initial increase and then a leveling off of density at high velocities. BHS samples generally show higher density at a given take-up velocity compared to that for CN9984 samples. Samples at mass throughput of 5 g/min exhibited higher densities than that at 3 g/min. The higher density trend could be due to either higher overall crystallinities or due to higher α -phase content with similar overall crystallinity.

Figure 4.23 shows the final birefringence of conditioned samples as a function of take-up velocity for both the resins and at the two mass throughputs. The birefringence increases with increasing take-up velocity, increasing molecular weight, and decreasing mass throughput. With increasing take-up velocity, there is an initial rapid increase in birefringence followed by leveling off.

The measured birefringence is a measure of the average molecular orientation in the samples including both amorphous and crystalline phases. Figure 4.24 shows the corresponding crystalline chain axis

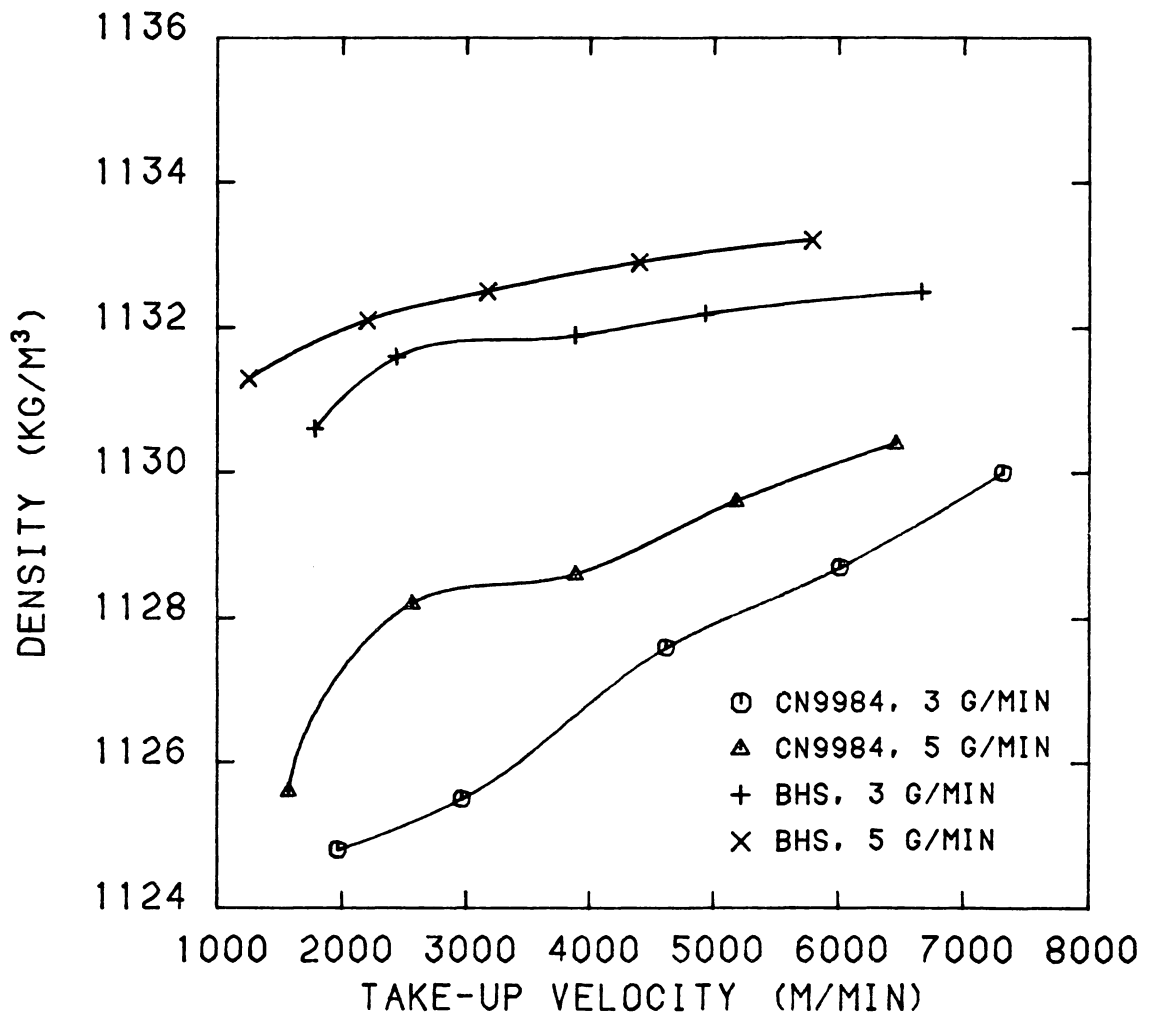


Figure 4.22 Density of conditioned nylon-6 filaments as a function of take-up velocity.

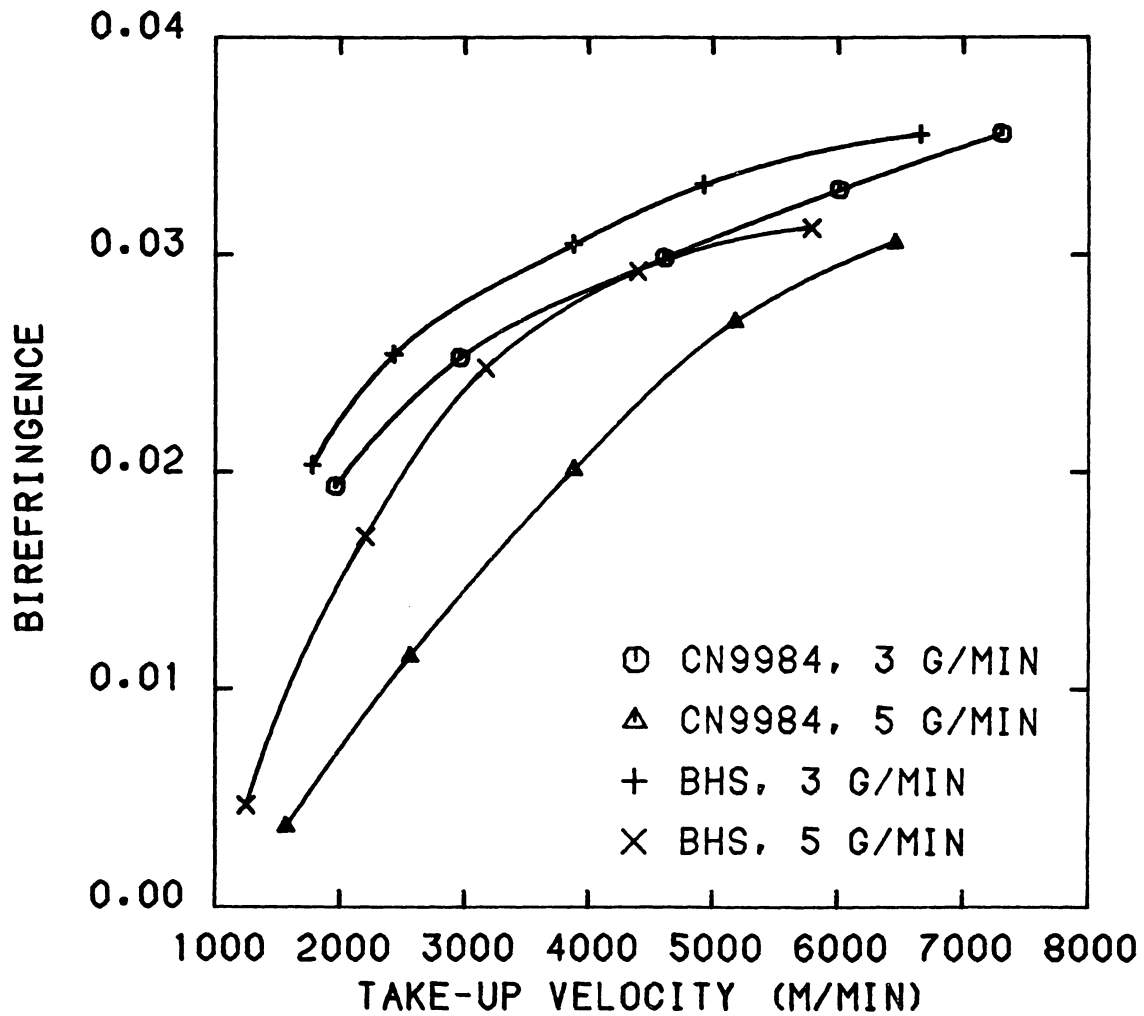


Figure 4.23 Birefringence of conditioned nylon-6 filaments as a function of take-up velocity.

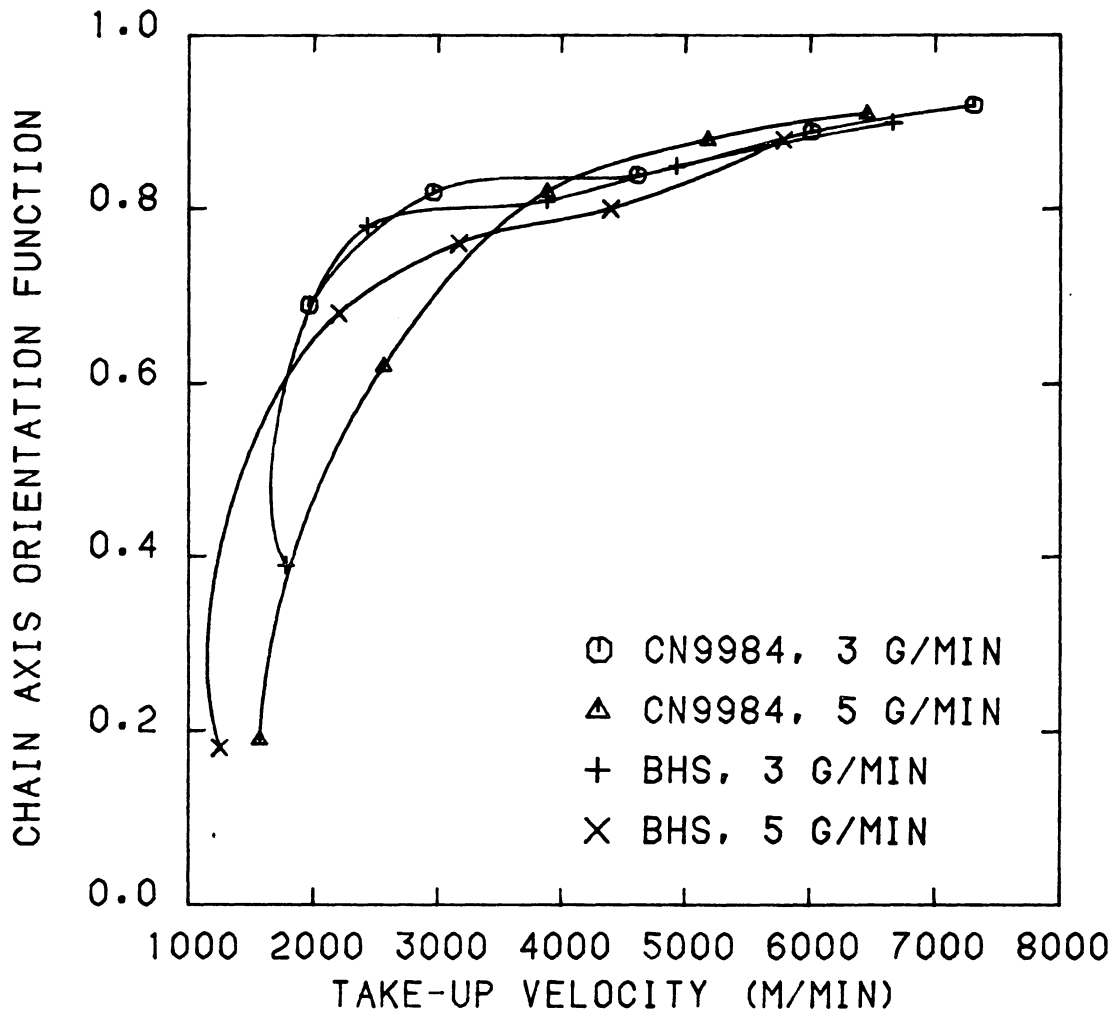
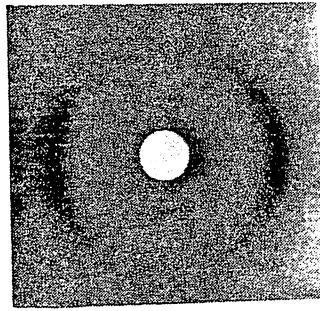


Figure 4.24 Chain axis crystalline orientation function of conditioned nylon-6 filaments versus take-up velocity.

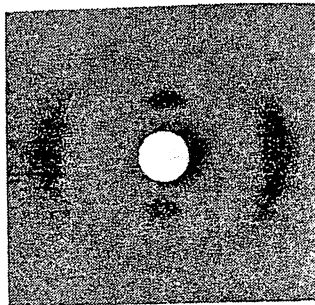
orientation function versus take-up velocity. At low take-up velocities the value of the crystalline orientation function is quite low (about 0.2) and increases rapidly, followed by a leveling off at quite high value (about 0.9) at high take-up velocities. The differences in the orientation function with changes in molecular weight and mass throughput are not as clear-cut as in the case of the birefringence, though they seem to be similar in nature.

Figures 4.25 to 4.28 show typical WAXS patterns for conditioned filaments. These patterns indicate qualitatively a significant amount of crystallinity. At lower spinning speeds, the patterns exhibit a broad equatorial peak (corresponding to (200,202) doublet) and a relatively weak meridional peak (corresponding to (020) plane). With increasing take-up speeds, both the equatorial and meridional peaks become sharper and particularly the meridional peak becomes more intense and exhibits lower azimuthal spread indicating a high γ -phase content and higher orientation of the γ -phase.

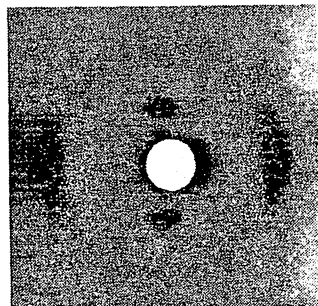
The determination of relative amounts of α , γ and amorphous phases were attempted by the method of Gianchandani et al. (30) described in Chapter 3. The results of this analysis are summarized in Tables 4.1 and 4.2 for both resins and each of the two mass throughputs. With increasing take-up speeds γ -phase fraction increases, α -phase fraction decreases and total sum of α and γ -phase fractions increases. The total crystalline fraction is higher for lower molecular weight resin than that for higher molecular weight resin samples and similar trend was observed for lower mass throughput compared to higher mass throughput results. At high speeds γ -phase fraction calculated was so high that it



(a)

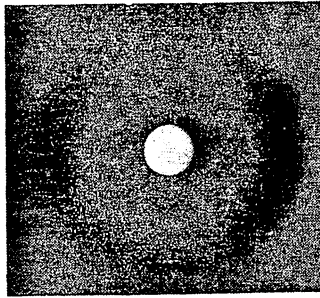


(b)

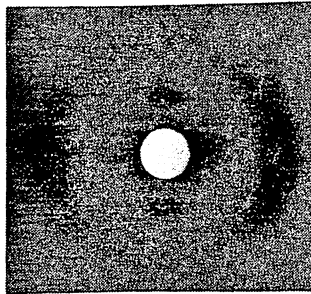


(c)

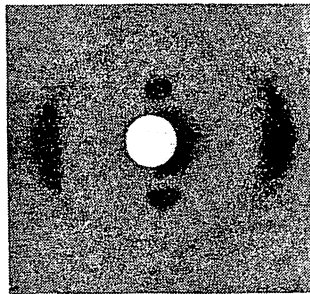
Figure 4.25 Typical WAXS patterns of conditioned nylon-6 filaments for CN9984 with a mass throughput of 3.073 g/min: (a) 1960 m/min, (b) 4615 m/min, (c) 7310 m/min.



(a)

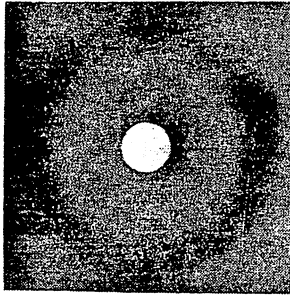


(b)

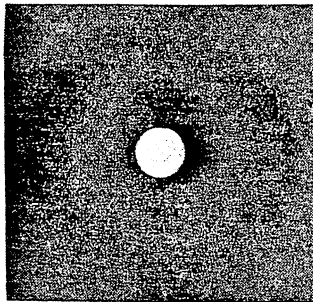


(c)

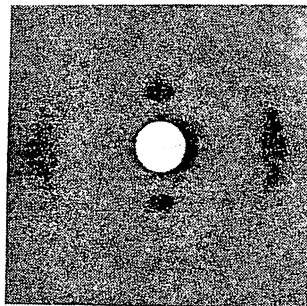
Figure 4.26 Typical WAXS patterns of conditioned nylon-6 filaments for BHS with a mass throughput of 2.993 g/min: (a) 1780 m/min, (b) 3880 m/min, (c) 6660 m/min.



(a)

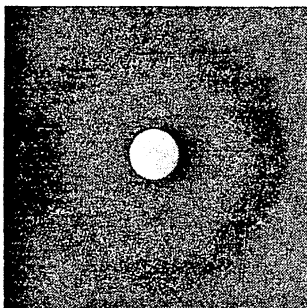


(b)

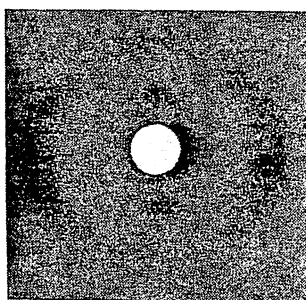


(c)

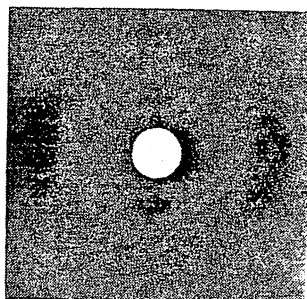
Figure 4.27 Typical WAXS patterns of conditioned nylon-6 filaments for CN9984 with a mass throughput of 5.154 g/min: (a) 1570 m/min, (b) 3855 m/min, (c) 6455 m/min.



(a)



(b)



(c)

Figure 4.28 Typical WAXS patterns of conditioned nylon-6 filaments for BHS with a mass throughput of 5.069 g/min: (a) 1250 m/min, (b) 3170 m/min, (c) 5790 m/min.

Table 4.1 Results of relative amounts of phase - analysis for conditioned nylon-6 filaments for CN9984: (a) $W = 3.073$ g/min, (b) $W = 5.154$ g/min.

Take-up speed (m/min)	Phase Fractions			Total Crystalline ($X_\gamma + X_\alpha$)
	γ -phase X_γ	α -phase X_α	Amorphous X	
(a) Mass throughput: 3.073 g/min				
1960	0.107	0.259	0.634	0.366
2960	0.242	0.179	0.579	0.421
4615	0.596	-	0.404	0.596
6010	0.740	-	0.260	0.740
7310	0.816	-	0.184	0.816
(b) Mass throughput: 5.154 g/min				
1570	0.014	0.323	0.662	0.338
2560	0.102	0.286	0.612	0.388
3885	0.318	0.152	0.530	0.470
5180	0.715	-	0.285	0.715
6455	0.980	-	0.020	0.980

Table 4.2 Results of relative amounts of phase - analysis for conditioned nylon-6 filaments for BHS: (a) $\dot{W} = 2.993$ g/min, (b) $\dot{W} = 5.069$ g/min.

Take-up speed (m/min)	Phase Fractions			Total Crystalline ($X_\gamma + X_\alpha$)
	γ -phase X_γ	α -phase X_α	Amorphous X	
(a) Mass throughput: 2.993 g/min				
1780	0.028	0.349	0.623	0.377
2430	0.194	0.252	0.554	0.446
3880	0.384	0.134	0.482	0.518
4930	0.505	0.060	0.435	0.565
6660	0.681	-	0.319	0.681
(b) Mass throughput: 5.069 g/min				
1250	0.017	0.361	0.622	0.378
2200	0.103	0.313	0.584	0.416
3170	0.187	0.262	0.551	0.449
4400	0.400	0.131	0.469	0.531
5790	0.529	0.051	0.420	0.580

led to negative values for α -phase fraction indicating that the simplified method of Gianchandani et al. (30) is not suitable for high γ -phase content samples. This seems to be due to the fact that the standard γ sample itself had γ -phase fraction of 0.75. Further, at high take-up speed the meridional peak is so sharp and narrow that the articular slice for which integrated intensity is measured is no longer equivalent to the slice on equatorial peak for integrated intensity. This effect leads to quite high value of integrated intensity ratio. Since the primary purpose of this study was not to develop a method for relative amounts of phases, further treatment of this problem was not attempted. However, Gianchandani et al.'s method provided values of relative amounts of phases that could be used to indicate trends with spinning variables and provide relative comparison for a considerable range of take-up speeds studied. The observed trends were quite similar to those previously reported by Suryadevara (31) and Koyama et al. (34).

The comparison of typical DSC curves for some of the conditioned samples are shown in Figures 4.29 to 4.32. At lower speeds only one endothermal peak is present which splits into two peaks, presumably, corresponding to α and γ -phases with increasing take-up speeds. The quantitative information obtained from DSC curves is summarized in Tables 4.3 and 4.4. Melting peak temperature increases with increasing take-up speeds and also it is relatively higher for 3 g/min throughput samples compared to that for 5 g/min samples. Similar trends are observed for heat of fusion (ΔH) values. Lower molecular weight resin samples have higher values of ΔH than that for higher molecular weight

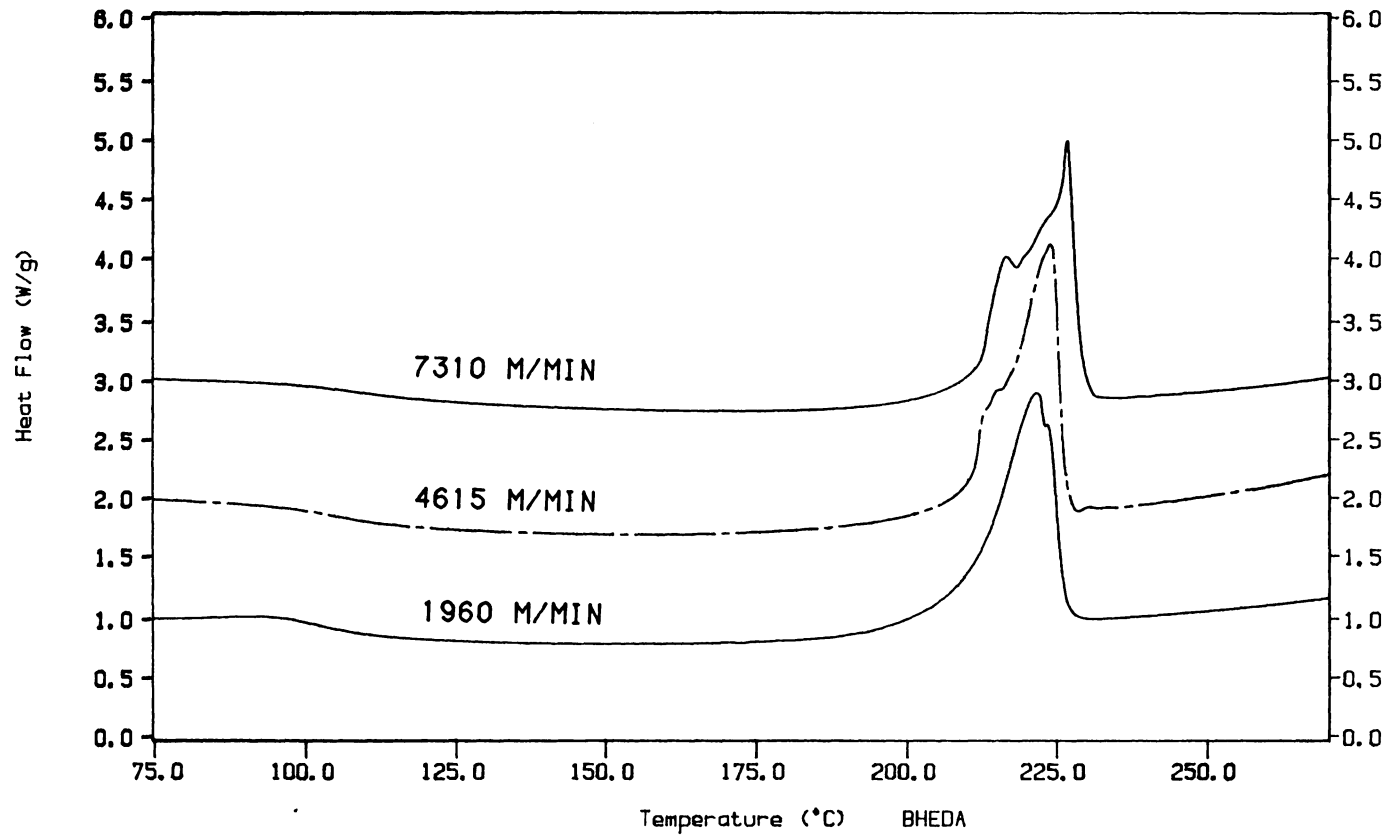


Figure 4.29 Typical normalized DSC traces of conditioned nylon-6 filaments for CN9984 with a mass throughput of 3.073 g/min.

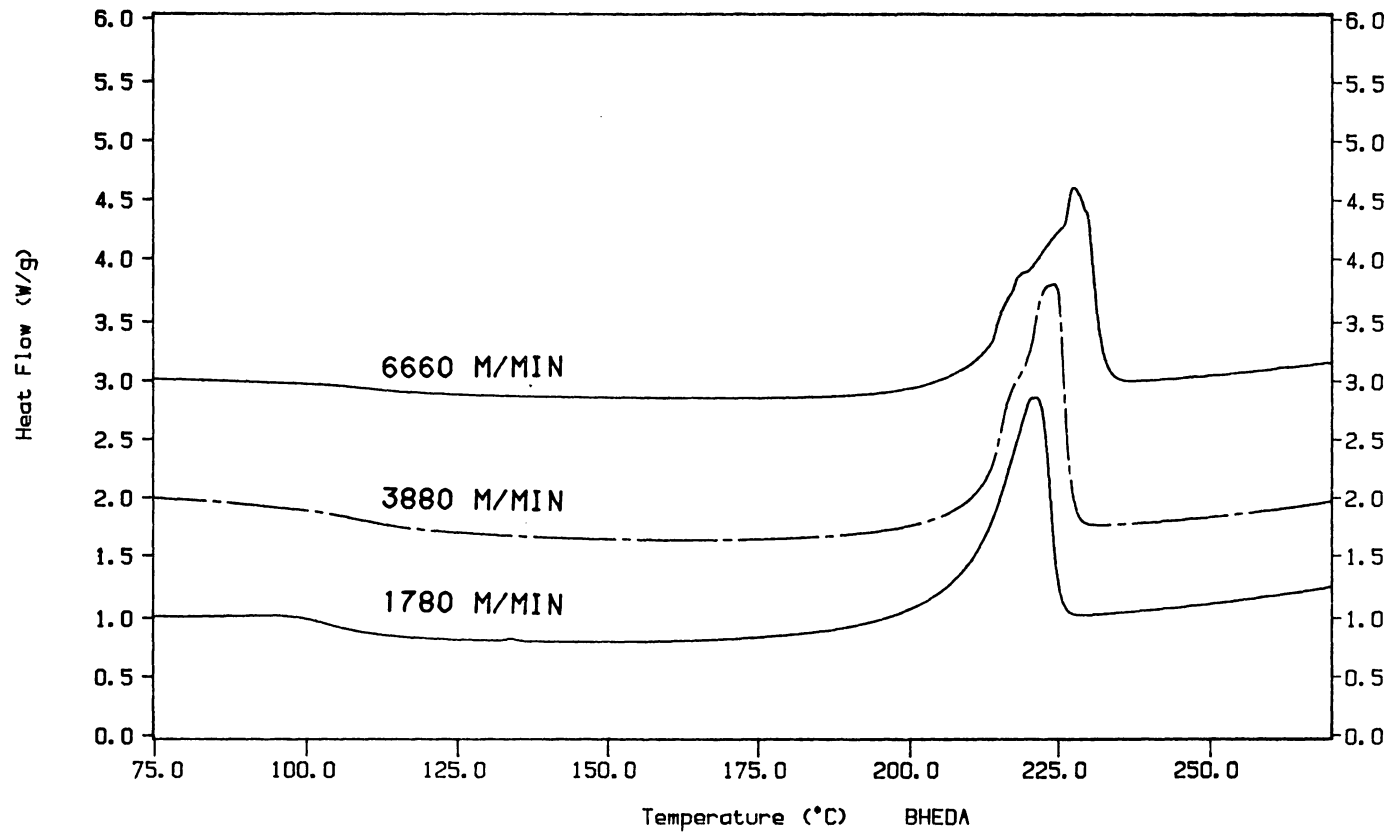


Figure 4.30 Typical normalized DSC traces of conditioned nylon-6 filaments for BHS with a mass throughput of 2.993 g/min.

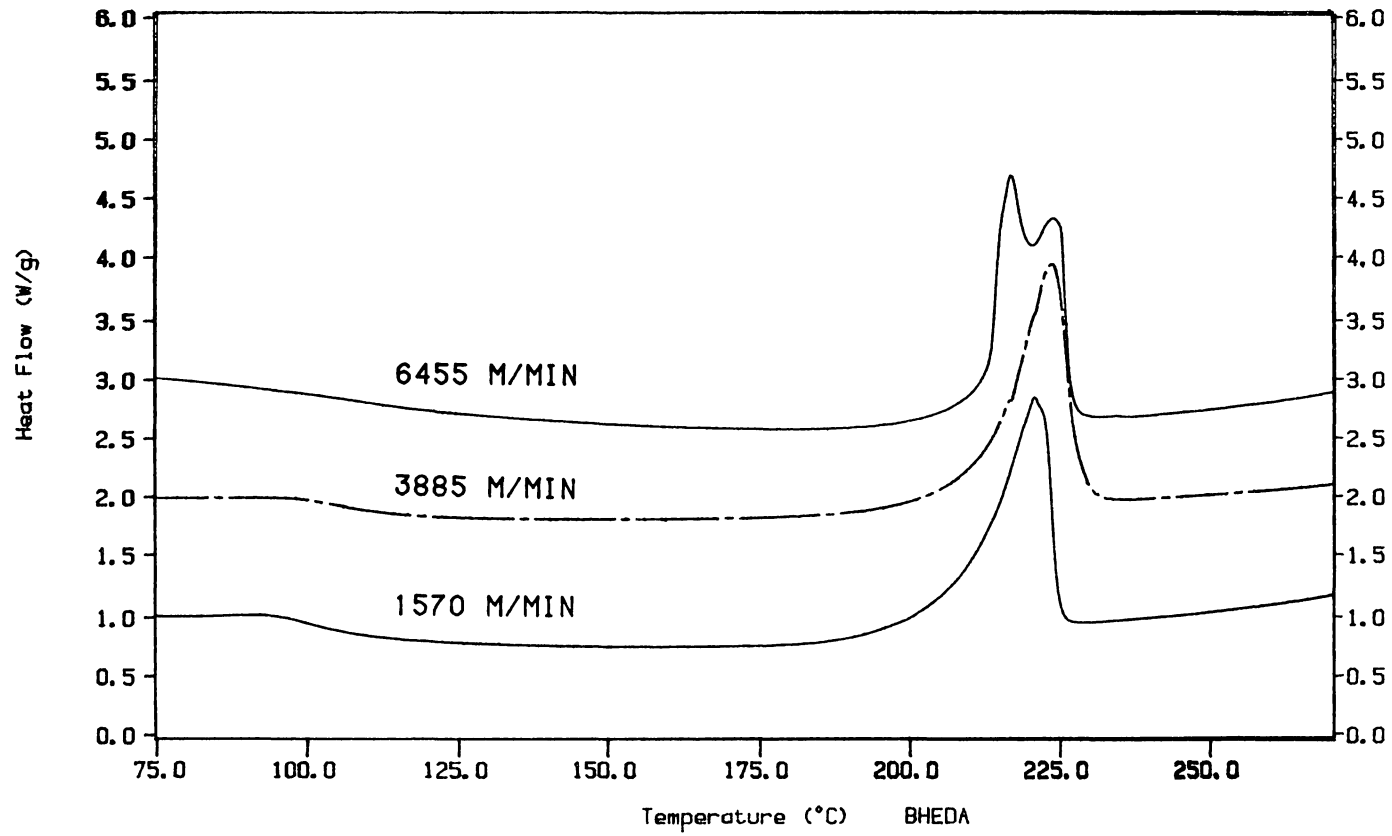


Figure 4.31 Typical normalized DSC traces of conditioned nylon-6 filaments for CN9984 with a mass throughput of 5.154 g/min.

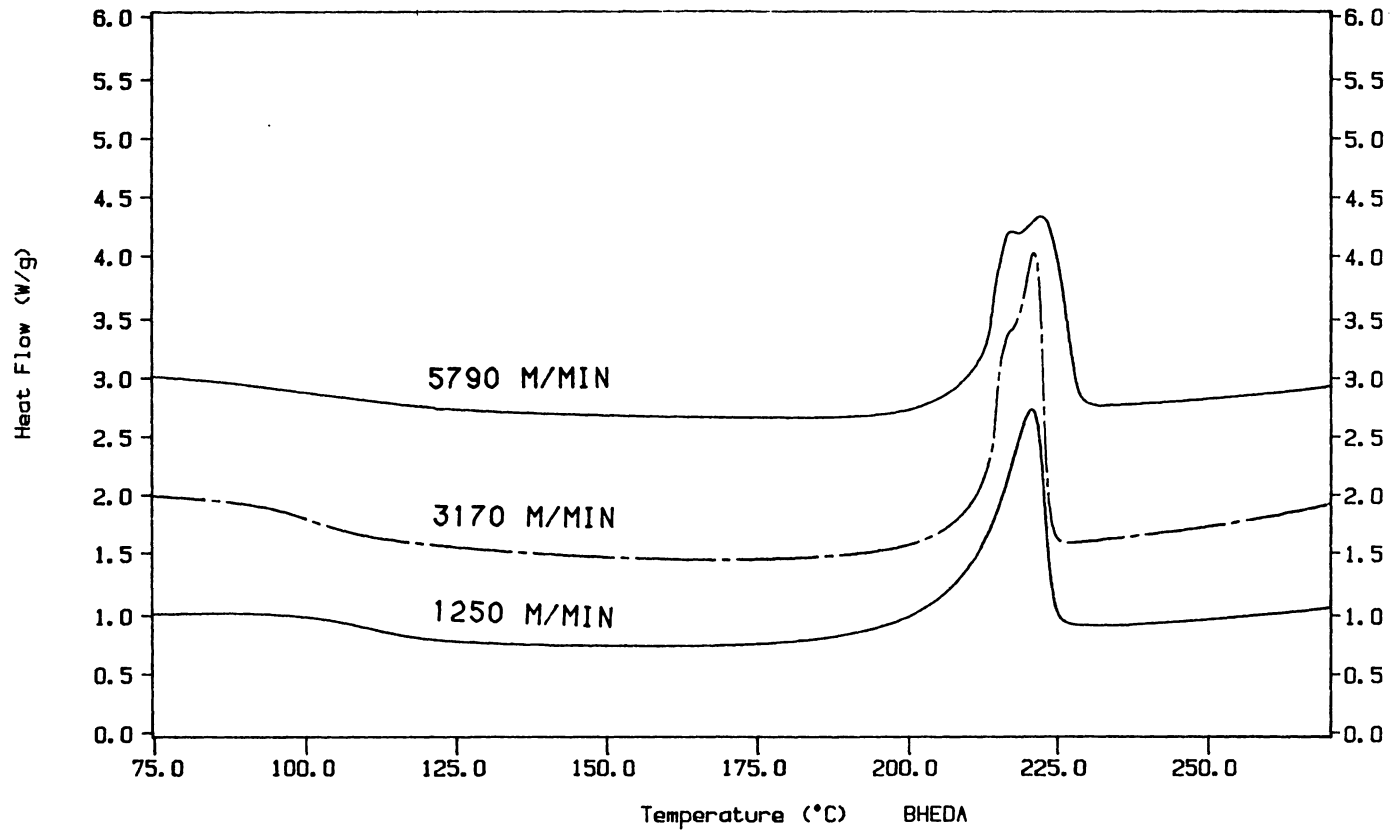


Figure 4.32 Typical normalized DSC traces of conditioned nylon-6 filaments for BHS with a mass throughput of 5.069 g/min.

Table 4.3 Results of DSC analysis of conditioned nylon-6 filaments for CN9984: (a) W = 3.073 g/min, (b) W = 5.154 g/min.

Take-up speed (m/min)	Melting peak temperature (°C)	Heat of fusion (J/g)
(a) Mass throughput: 3.073 g/min		
1960	221.51	66.83
4615	223.73	66.70
7310	226.52	68.47
(b) Mass throughput: 5.154 g/min		
1570	220.64	65.89
3885	223.44	67.17
6455	224.13	67.74

Table 4.4 Results of DSC analysis of conditioned nylon-6 filaments for BHS: (a) $\dot{W} = 2.993$ g/min, (b) $\dot{W} = 5.069$ g/min.

Take-up speed (m/min)	Melting peak temperature (°C)	Heat of fusion (J/g)
(a) Mass throughput: 2.993 g/min		
1780	222.02	64.85
3880	223.97	64.96
6660	227.43	65.18
(b) Mass throughput: 5.069 g/min		
1250	220.67	61.86
3170	220.90	61.32
5790	221.95	63.53

samples whereas melting peak temperature was relatively independent of the molecular weight.

Figures 4.33 to 4.35 show the mechanical properties results for conditioned fiber samples. Initial modulus and tenacity increases while elongation to break decreases with increasing take-up velocities. Initial moduli and tenacities are higher while elongation to break is lower for BHS and 3 g/min throughput samples than that for corresponding CN9984 and 5 g/min samples, respectively.

Discussion of Experimental Results

Comparison with Previous Investigations

Bankar et al. (26), Gianchandani et al. (30) and Nakamura et al. (171) previously have made detailed experimental studies of nylon-6 filaments melt spun at low to intermediate spinning speeds (100 to 1500 m/min). They attempted to describe structural variations of as-spun filaments in terms of crystallinity level, relative amounts of α and γ phases, molecular orientation, etc. They concluded that at low to intermediate spinning speeds, nylon-6 crystallizes on the bobbin rather than in the spinline. Heuvel and Huisman (187), Shimizu et al. (66) and Koyama et al. (34) made similar attempts at high spinning speeds. Heuvel and Huisman emphasized the effect of increasing spinning speeds on relative amounts of α and γ phases while Koyama et al. studied effects of molecular weight of resin on structure and properties of conditioned nylon-6 filaments. They concluded that both molecular weight and take-up speeds greatly influence the structure formation and mechanical properties of high speed melt spun filaments. Our results on conditioned

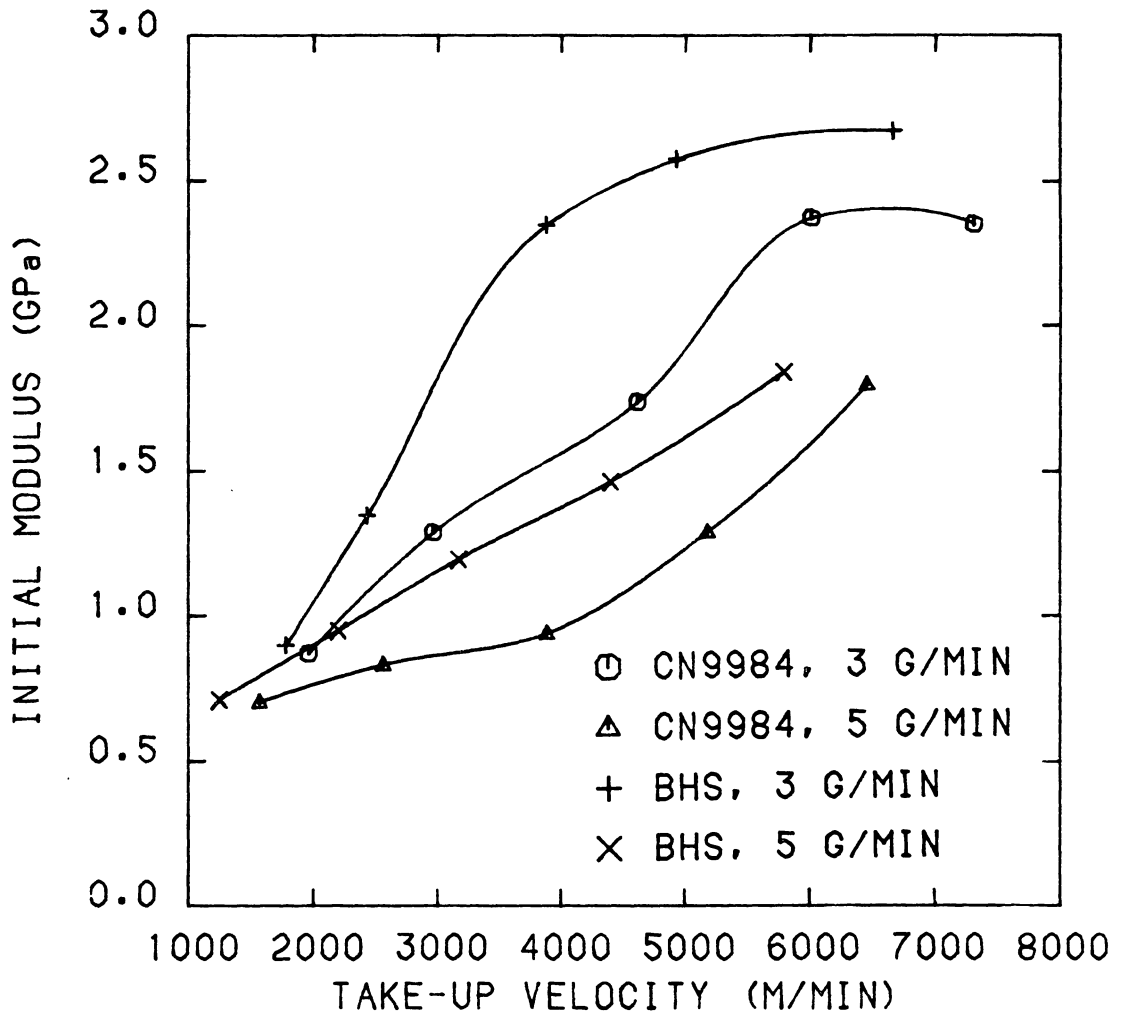


Figure 4.33 Initial modulus of conditioned nylon-6 filaments as a function of take-up velocity.

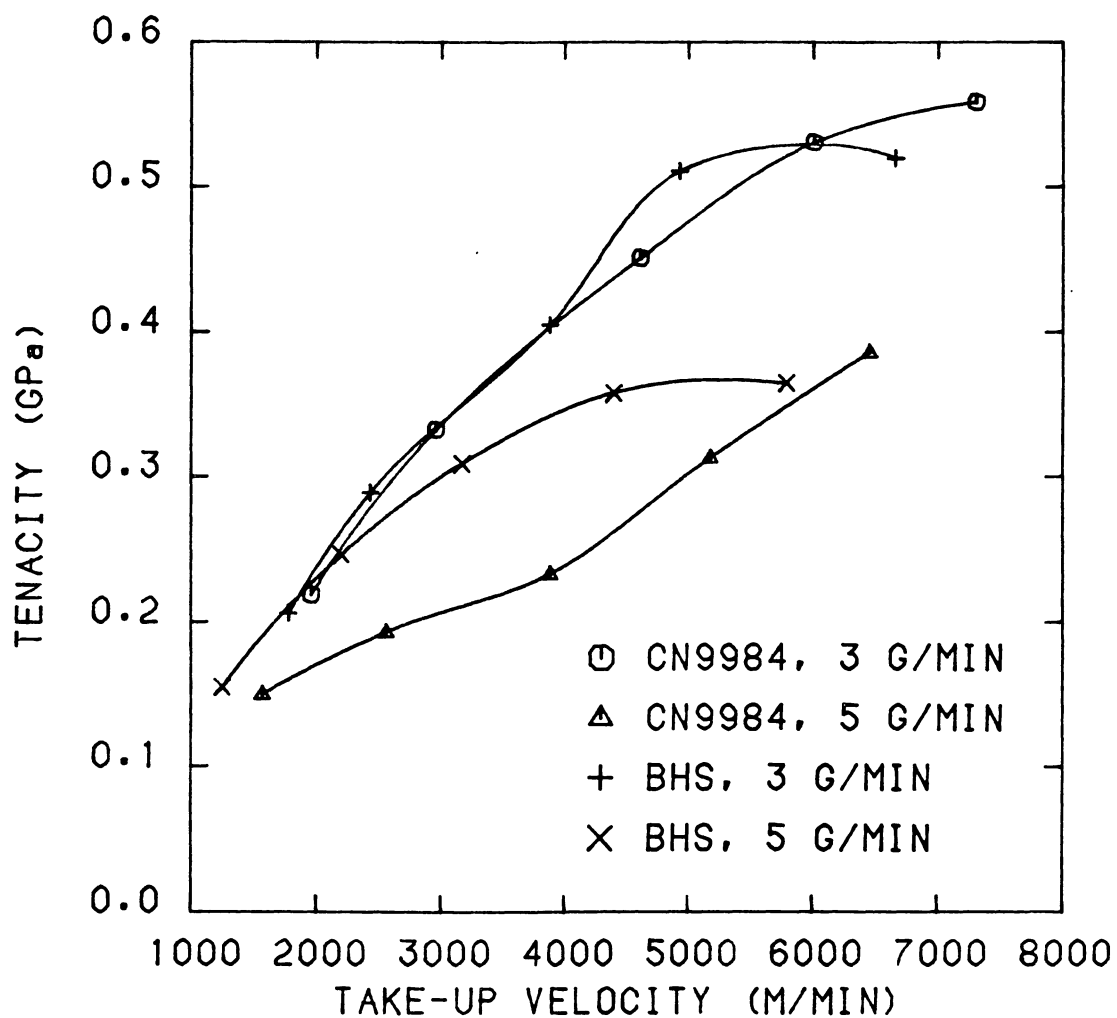


Figure 4.34 Tenacity of conditioned nylon-6 filaments as a function of take-up velocity.

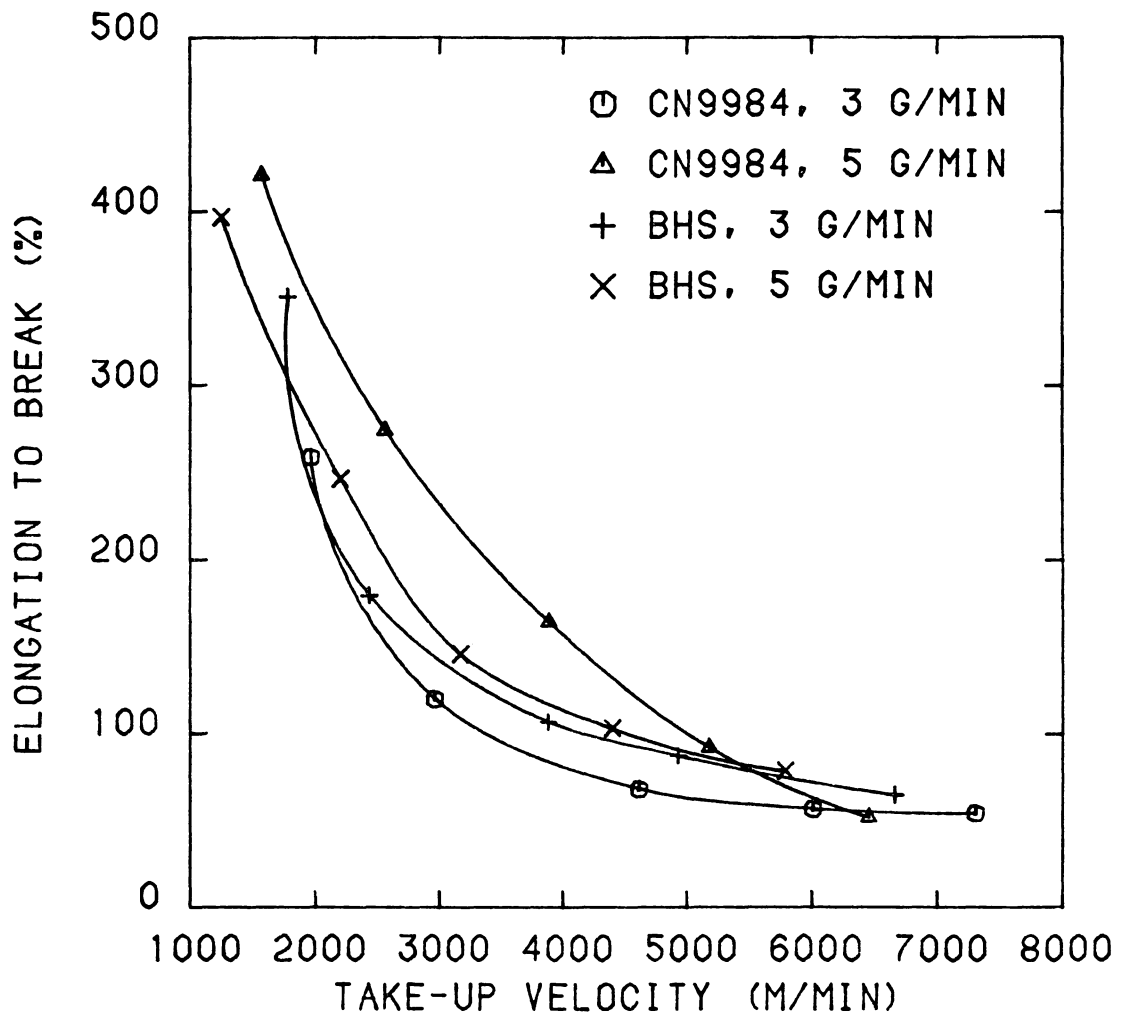


Figure 4.35 Elongation to break of conditioned nylon-6 filaments as a function of take-up velocity.

filaments described in the section on structure and properties of conditioned filaments were qualitatively quite similar to these earlier investigations. Some minor quantitative differences can be traced to the use of different techniques for characterizing the structure and the relatively higher spinning speeds involved in this study.

In addition to mechanical properties of conditioned filaments, Shimizu et al. (66) studied the effect of conditioning time on birefringence change in a broad range of take-up speeds in order to understand mechanism of crystallization of nylon-6 filaments. They showed that from 500 to 4000 m/min the birefringence change with time exhibited S-shape dependence with a rapid increase in birefringence occurring after about 8 minutes of conditioning time in ambient environment. Filaments spun at speeds higher than 4000 m/min had relatively high initial birefringence (just after spinning), and their birefringence did not increase much with aging time. Our results for birefringence showed quantitatively similar variation with aging time, confirming that at higher take-up speeds high molecular orientation develops on the spinline and this enhanced orientation leads to crystallization on the spinline.

Our results also point out that both molecular weight of the resin and mass throughput greatly influence the quantitative changes in the birefringence versus conditioning time curve. It seems that conditions under which large spinline stresses are generated lead to high molecular orientation and consequently online crystallization. Thus the structure formation of conditioned filaments is a manifestation of the structure developed in the spinline plus the effect of equilibration with the

environment. There seems to be general agreement among previous investigators that moisture absorption during this equilibration process facilitates molecular mobility by interrupting the interchain hydrogen bonds in the amorphous nylon. This allows rearrangement and crystallization with aging time. Further insight into what processes are occurring during spinning of nylon-6 can be obtained from the measurements made on the running spinline.

Analysis of Errors in Online Measurements

The main goal of this research was to provide insight into spinline dynamics and structure formation in the spinline through online measurements. This is to be accomplished through detailed comparison of the online results with calculation from a mathematical model. An important consideration before using these measurements for such comparisons is to know the reliability and accuracy of the measurements. Ideal condition for these measurements would be that the melt spinline is in steady state. In reality, however, there are variations in process parameters such as extrusion temperature, mass throughput, ambient temperature, take-up force, etc. The non-contact measurement would be ideal because the spinline is not perturbed by the measuring devices due to contact with the instrument. Precision and accuracy of the instrument itself is also important in determining the quality of the data. Finally the ease of measurement and possibility of collecting the data with all variations facilitates obtaining the average values through statistical analysis.

In prior studies online diameter measurements were made using an Olympus microscope. This technique necessitated use of a guide to

prevent the filament movement out of the focus field of microscope. Even with the guide the diameter measurement was tedious, time consuming and subject to the human error. Major difficulty was encountered, particularly when the filament was hot and tacky making diameter measurement almost impossible. Online diameter measurement with the Zimmer diameter monitor in this study provided non-contact measurements and thus the measurement was possible over the whole spinline. Use of a microcomputer with the Zimmer monitor facilitated quick collection of 2000 data points at a particular position on the spinline; this made it possible to obtain a most probable diameter value statistically.

The manufacturer of the Zimmer diameter monitor provided the information that the instrument has a resolution of 0.5 μm within its diameter measurement range of 0 - 2 millimeters. Further, the instrument has high enough signal bandwidth, permitting error free measurements even at speed of 10,000 m/min and at the lateral movement speed of up to 500 m/sec of running filament. The precision and accuracy of the whole data acquisition system (Zimmer monitor connected to Applied Micro Technology microcomputer and Preston Amplifier) was checked by obtaining the diameter distribution of various calibration wires in the diameter range of 50 - 1600 μm . The distributions were very sharp with the maximum width of about 2 μm for diameters up to 200 μm and about 4 μm for diameters from 400 to 1600 μm . Thus, it appears that the maximum error introduced in diameter measurement due to the instrument and computer system is of the order of about $\pm 1\%$.

An attempt was made to understand the observed diameter variations and the source of the differences in the online diameter distribution

curves at various positions on the spinline (20 cm, 90 cm and 150 cm from the spinneret shown in Figures 4.1 to 4.3, respectively). It was pointed out earlier that the variation in diameter values is due to filament movement in and out of the focus field of the Zimmer diameter monitor and variations in mass throughput (W), extrusion temperature, air suction force, etc. The former variation is due to the measuring instrument whereas the latter ones are due to the process itself. Ignoring the measurement error, we can get an understanding of the relationship of the variation of processing variables to the measurements through the following analysis.

According to the principle of continuity we may write

$$\bar{W} = \bar{\rho} \bar{V} \left(\frac{\pi \bar{D}^2}{4} \right) \quad (4-1)$$

where the overbars mean averages. If equation (4-1) is differentiated and it is assumed that ρ and V are constant and only D varies with variation in W , then

$$\Delta W = \bar{\rho} \bar{V} (\pi/4) 2D \Delta D \quad (4-2)$$

Dividing equation (4-2) by equation (4-1)

$$\pm \frac{\Delta W}{W} \simeq \pm 2 \frac{\Delta D}{D} \quad (4-3)$$

or

$$\Delta D \simeq \pm \left(\frac{\Delta W}{W} \right) \frac{D}{2} \quad (4-4)$$

For the data shown in Figures 4.1 to 4.3, $W \simeq 3.0$ g/min and peak diameter values are about 258 μm , 82 μm and 50 μm for Figure 4.1, Figure 4.2 and Figure 4.3, respectively. Further assuming that W might vary by as much as $\pm 10\%$, we find $\Delta W \simeq \pm 0.3$ and from equation (4-4)

$$\Delta D \simeq \pm 0.1(D/2) \quad (4-5)$$

Thus for $D \simeq 258 \mu\text{m}$; $\Delta D \simeq \pm 12.9 \mu\text{m}$

for $D \simeq 82 \mu\text{m}$; $\Delta D \simeq \pm 4.1 \mu\text{m}$

and for $D \simeq 50 \mu\text{m}$; $\Delta D \simeq \pm 2.5 \mu\text{m}$

Careful examination of Figures 4.1 to 4.3 shows that in all cases the significant variation in diameter values about the peak diameter values follows these estimated trends which is close to $\pm 5\%$. This result clearly explains why the diameter variation is much greater for the measurements of the larger diameters than for the smaller diameters.

If we assume that the variation occurs in V rather than in W then differentiating equation (4-1) we get

$$0 = (\pi/4)\bar{\rho}V2D\Delta D + (\pi/4)\bar{\rho}\bar{D}^2\Delta V \quad (4-6)$$

and therefore

$$\pm \frac{\Delta V}{V} \simeq \pm 2 \frac{\Delta D}{D} \quad (4-7)$$

This shows that a variation in V of 10%, i.e. $\Delta V/V \simeq 0.1$ will cause the same variation in D as a 10% variation in W .

It seems probable that the variation in extrusion temperature and gear pump speeds cause a variation in W . Variation in air pressure and in the effect it has within the drawdown device lead to variation in take-up velocities. Thus, diameter variation would seem to result from both these sources. If we assume that they may be treated independently, we may write

$$2 \frac{\Delta D}{D} \simeq \frac{\Delta V}{V} + \frac{\Delta W}{W} \quad (4-8)$$

or

$$\pm \Delta D \simeq \pm \left(\frac{\Delta V}{V} + \frac{\Delta W}{W} \right) \frac{D}{2} \quad (4-9)$$

The diameter distribution data indicate that the total error, $(\Delta V/V) + (\Delta W/W)$, is of the order of 10%. To obtain an independent estimate of $(\Delta V/V)$ we need to make measurements using a positive take-up device with known variation in $(\Delta V/V)$. All of our data were taken with an air aspirator which did not have positive control over take-up speed.

Prior studies of measuring online birefringence basically involved measurement of optical retardation by the birefringent filament. The two most common optical systems used are transmission systems and compensation systems. The former system was used by Ishibashi et al. (43) on running threadline. It involved the photoelectric measurement of the intensity of the light passed through birefringent filament placed between a pair of polarized plates. The compensation system was used by Katayama (159), Bai (32) and Zieminski (33) and in the present study. A Berek compensator introduced between crossed polars of the microscope provides directly the optical retardation.

The birefringence is calculated from the ratio of optical retardation to filament diameter; its accuracy is thus dependent on accuracies in measurements of optical retardation and in diameter. The variation of diameter values, as described above, is of the order of about $\pm 5\%$. The precision of compensator used was about $\pm 2\%$ on an average retardation value of 1×10^{-6} meters. An estimate of total variation in optical retardation was about 5 to 6%. This estimate was obtained through taking about five sets of readings at a particular position in the spinline and then arriving at standard variation in measurement.

Note that this estimated variation includes both due to measurement and due to process variations.

The above discussed estimated errors in diameter and retardation measurement can provide further insight into the errors associated with calculated birefringence values. The birefringence (Δn) is given by

$$\Delta n = \frac{R}{D} \quad (4-10)$$

where R is the optical retardation and D is the diameter.

Differentiating equation (4-10) gives

$$d(\Delta n) = \frac{D dR - R dD}{D^2} \quad (4-11)$$

Dividing equation (4-11) by equation (4-10) we get

$$\frac{d(\Delta n)}{\Delta n} = \frac{dR}{R} - \frac{dD}{D} \quad (4-12)$$

and therefore

$$\frac{\Delta(\Delta n)}{\Delta n} \simeq \pm \left(\frac{\Delta R}{R} + \frac{\Delta D}{D} \right) \quad (4-13)$$

As discussed in a previous paragraph ($\Delta R/R$) $\simeq \pm 0.06$ and ($\Delta D/D$) $\simeq \pm 0.05$ and therefore $\Delta(\Delta n)/\Delta n \simeq \pm 0.11$. Thus, the error in birefringence values will be of the order of about $\pm 11\%$.

Various instruments used for measuring online temperature are either based on principle of contact thermocouple or interferometric method or based on the heat radiation from the filament. Contact thermocouple instrument has been used by Kase and Matsuo (78), Acierno et al. (13), Dees and Spruiell (16) and others in their fiber spinning studies. The most important limitation of this instrument was the fact that measurements could only be made on solidified parts of the spinline. It also involves generation of frictional heat because of the

contact required between moving spinline and the stationary thermocouple. This perturbs the filament by the contact which may cause a change in the filament behavior. The interferometric method was applied by Barnett (215) and Shimizu et al. (66) which involved the schlieren patterns in the air surrounding the spinline. Both the calibration and measurements are very sensitive to temperature of air surrounding the spinline. The most natural basis of non-contact temperature measurement is provided by either direct recording of heat radiation from the filament or by compensating the radiation from the filament by a background body maintained at known temperature. Barnes infrared microscope is based on this principle and was used by Bai (32), Zieminski (33) and in this study to measure the temperature of the running threadline.

The accuracy in temperature measurement also will depend on possible variations due to measurement itself and due to process variations. The variation due to measurement includes precision of infrared microscope which involves sensitivity scale of potentiometer to indicate the deflection of pointer with some minimum temperature difference and the accuracy of temperature control of black body radiator. The precision of the infrared microscope and that of temperature controller for radiator is of the order of $\pm 1^{\circ}\text{C}$. The estimated total variation of temperature measurement including variation due to process was about ± 2 to 3°C over the most critical part of the spinline. This estimate was arrived by the observation that movement of instrument over 1 to 1.5 cm of spinline instantaneously showed

deflection in potentiometer for fixed radiator temperature. The average cooling rate in terms of spinline length was about $2^{\circ}\text{C}/\text{cm}$.

It should be noted that the variation in either optical retardation or temperature measurement could not be analyzed in detail either due to measurement variation or due to process variation as in case of diameter measurement. The difficulty was due to the fact that data taking for retardation and temperature measurement was wholly manual and it took approximately three to five minutes to take a single data at a particular position in the spinline. A better estimate is possible when a rapid computer acquisition procedure is available for data taking so that some reasonable statistical analysis can be applied.

The accurate measurement of online diameter, birefringence and temperature profiles not only provide basic understanding of dynamics and structure development during melt spinning but are key to check the validity of results of simulations of melt spinning, details of which are developed in the next chapter.

CHAPTER 5

SIMULATION OF THE MELT SPINNING PROCESS

Mathematical Model

A mathematical model for the high speed melt spinning of nylon-6 was developed using theoretical developments of mass, momentum and energy balances and a crystallization kinetics model including temperature and orientation effects. These developments along with previous attempts at modeling were reviewed in Chapter 2. Zieminski (33) has presented a rigorous development of the fundamental equations of continuity, momentum and energy, including boundary conditions involved, and appropriate assumptions based on the physics of the melt spinning process. We have used Zieminski's mathematical formulation which results in a series of eight highly coupled ordinary differential equations which are numerically solved by the Continuous System Modeling Program (CSMP) developed by the IBM Company and available on the University of Tennessee Computer Center's (UTCC) IBM-370 computer system.

This model is a set of highly coupled ordinary differential equations with appropriate initial and/or boundary conditions specified. The model requires physical property correlations and empiricisms derived from the literature for a particular polymer (nylon-6 in our case) as inputs. A great deal of the effort required to apply the model is associated with establishing these inputs.

Continuity

The spinning operation is assumed to be a steady state process and the mass balance is given as

$$W = AV\rho \quad (5-1)$$

where A is cross sectional area of the descending fiber, V is velocity and ρ is the polymer density. Further assuming that V and ρ are functions of z only (no radial variations)

$$\frac{d}{dz}(AV\rho) = 0 \quad (5-2)$$

Assuming the cross section to be a cylinder of diameter D then we may write

$$A = \frac{\pi D^2}{4} \quad (5-3)$$

The density ρ is considered to be temperature and crystallinity dependent for nylon-6 (133) as follows

For temperature above T_m

$$\rho = (0.8816 + 5.64 \times 10^{-4}T)^{-1} \quad (5-4)$$

and below T_m

$$\rho = [(0.8816 + 5.64 \times 10^{-4}T) - (2.92 \times 10^{-2} + 3.26 \times 10^{-4}T)\theta]^{-1} \quad (5-5)$$

The initial condition for equation (5-2) is $V(0) = V_0$ with $D = D_{\text{spinneret}}$

Momentum Balance

Combination of mass and force balances produced a differential force balance

$$dF_{rheo} = dF_{iner} + dF_{drag} - dF_{grav} \quad (5-6)$$

where

$$dF_{iner} = W dV \quad (5-7)$$

$$dF_{drag} = \pi \rho_a V^2 D dz \quad (5-8)$$

$$dF_{grav} = \left(\frac{Wg}{V} \right) dz \quad (5-9)$$

Since the drag force was considered as a differential quantity, the local drag coefficient derived by Sakiadis (46) from boundary layer theory rather than the integral drag coefficients described by others was used according to

$$C_d = \frac{2}{(\beta Re)} \quad (5-10)$$

where the parameter β is evaluated from a z dependent parameter ξ given by

$$\xi^2 = 8 \int_0^\beta \frac{(z-1) \exp(2z) + z^2 + 1}{z^2} dz \quad (5-11)$$

and also

$$\xi^2 = 64 Re \frac{z}{D} \quad (5-12)$$

where Re is the Reynolds number based on the fiber diameter and velocity

$$Re = \frac{\rho_a V D}{\mu_a} \quad (5-13)$$

The stress along the spinline is given by

$$\sigma = \frac{F_{rheo}}{(\pi D^2/4)} \quad (5-14)$$

A table of β and ξ was used as input in the model and the integral in equation (5-11) was evaluated numerically using CSMP. During execution ξ was evaluated for a particular value of z and the value of β was

evaluated through $\beta - \xi$ table interpolation; this β value was then used to calculate the local drag coefficient. The density (ρ_a) and viscosity (μ_a) of air were considered to be constant with values $\rho_a = 6.62 \times 10^{-5}$ gm/cm³ and $\mu_a = 2.8 \times 10^{-4}$ poise (281). The initial condition for equations (5-7) to (5-9) were $F_{iner}(0) = 0$, $F_{drag}(0) = 0$ and $F_{grav}(0) = 0$, considering the die to be the origin of the co-ordinate system and integration is performed from the die to the take-up unit with suitable increment in z . Since $F_{rheo}(0)$ is not known a suitable value is evaluated by iteration. The procedure involves an initial guess for $F_{rheo}(0)$ and comparison of the final take-up velocity with the known value of this boundary condition. Based on this comparison the value of $F_{rheo}(0)$ is changed until the calculated take-up velocity matches the given boundary condition.

Energy Balance

Assuming no radial variations of temperature, T , in the filament and that heat conduction, radiation and viscous heat generation is negligible compared to heat transfer due to convection and heat generated by crystallization the energy balance becomes

$$\frac{dT}{dz} = -\frac{\pi h(T - T_a)}{WCp} + \frac{\Delta H}{Cp} \frac{d\theta}{dz} \quad (5-15)$$

ΔH is heat of fusion and was taken to be 45 cal/gm for nylon-6 (12). The quantity $d\theta/dz$ is crystallinity gradient. For equation (5-15) the initial condition is $T(0) = T_{spinneret}$. The heat transfer coefficient h given by Kase and Matsuo (78) was taken as

$$h = 6.85 \times 10^{-5} \left(\frac{\rho V^2}{W} \right)^{0.259} \quad (5-16)$$

which was modified for transverse air flow as

$$h = h_o \left[1 + \left(\frac{8V_a}{V} \right)^2 \right]^{0.167} \quad (5-17)$$

C_p was considered to be temperature dependent for nylon-6 (282). This quantity is given as follows

From melt to 160°C

$$Cp(fluid) = 0.577 + 3.36 \times 10^{-4} T \quad (5-18)$$

and below 160°C

$$Cp(solid) = 0.325 + 1.50 \times 10^{-3} T \quad (5-19)$$

Rheological Model

Nylon-6 melt was considered to be a Newtonian fluid. Accordingly

$$\frac{dV}{dz} = \frac{\sigma}{\eta} \quad (5-20)$$

where σ is spinline stress given by equation (5-14) and η is extensional viscosity which was considered to be molecular weight and temperature dependent for nylon-6 (283).

Above T_m an Arrhenius type temperature dependence was assumed

$$\eta = 3 * 2.2956 \times 10^{-19} (M_w)^{3.4} \exp \left(\frac{6855}{T + 273} \right) \quad (5-21)$$

Below T_m the temperature dependence was taken to be of the WLF form

$$\eta = \text{const} \exp \left[\frac{(-8.86(T - T_m))}{(T + 101.6 - T_m)} \right] \quad (5-22)$$

The constant in equation (5-22) was calculated by using the viscosity calculated by equation (5-21) at T_m (where the change in temperature dependence was made) for equation (5-22). An empirical relation of

Kikutani (87) which was further established by Zieminski (33) was used to introduce crystallinity dependence;

$$\eta = \eta_o \left[4.605 \left(\frac{\theta}{\theta_\infty} \right)^{12} \right] \quad (5-23)$$

The initial condition for equation (5-20) is $\sigma = \sigma_{die}$ which is computed from the guessed value of $F_{rheo}(0)$. Integration of equation (5-20) leads to velocity as a function of z which then could be used to calculate diameter through continuity.

Birefringence and Orientation

The amorphous birefringence and orientation factor were modeled by a combination of the stress optical law with a Maxwell fluid element.

The stress optical law

$$\Delta n_a = C_{op} \sigma \quad (5-24)$$

was differentiated with respect to time (assuming that stress optical coefficient, C_{op} , is independent of time) to yield

$$\frac{\partial \Delta n_a}{\partial t} = C_{op} \frac{\partial \sigma}{\partial t} \quad (5-25)$$

The Maxwell element produced for $(\partial\sigma/\partial t)$ the relation

$$\frac{\partial \sigma}{\partial t} = E \frac{dV}{dt} - \frac{E\sigma}{\eta} \quad (5-26)$$

Substituting for $(\partial\sigma/\partial t)$ in equation (5-25) leads to

$$\frac{\partial \Delta n_a}{\partial t} = C_{op} E \frac{dV}{dt} - C_{op} \frac{E\sigma}{\eta} \quad (5-27)$$

Converting the partial derivative with respect to time to the total derivative with respect to position z through $(\partial/\partial t) = (1/V)(d/dz)$ and substituting for $\Delta n_a = C_{op} \sigma$ in equation (5-27)

$$\frac{d\Delta n_a}{dz} = \frac{C_{op}E}{V} \frac{dV}{dz} - \frac{E\Delta n_a}{V\eta} \quad (5-28)$$

Integration of this equation gives Δn_a from which the total birefringence was calculated from

$$\Delta n = (1 - \theta)\Delta n_a + \theta f_c \Delta_c^\circ \quad (5-29)$$

Since high speed spinning involves high crystalline orientation factor (f_c), it was assumed that $f_c = 0.9$ and was constant. The amorphous orientation factor (f_a) was calculated from

$$f_a = \frac{\Delta n_a}{\Delta_a^\circ} \quad (5-30)$$

For nylon-6 the stress optical coefficient, C_{op} , intrinsic amorphous birefringence, Δ_a° , and intrinsic crystalline birefringence, Δ_c° , were considered to be constant at the values of $C_{op} = 1.8 \times 10^{-10} \text{ cm}^2/\text{dyne}$ (69), $\Delta_a^\circ = 0.0825$ and $\Delta_c^\circ = 0.0963$ (284); Young's modulus, E , was considered to be a function of temperature and was evaluated by linear interpolation of the experimental data of Greco et al. (285). The initial condition for equation (5-28) was $\Delta n_a(0) = \Delta n_{a0}$ which was evaluated from the stress optical law for $\sigma = \sigma_{\text{spinneret}}$.

Crystallization Kinetics

An empirical model for crystallization kinetics with temperature and orientation dependence was used. The basis for this model was the generalized Avrami analysis (229-231)

$$\theta(t) = \theta_{\infty} [1 - \exp(-[\int_0^t K d\tau]^n)] \quad (5-31)$$

The temperature and orientation dependence of the rate constant, K, was assumed similar to that proposed by Ziabicki (12);

$$K = K_{max} \exp \left[-4 \ln 2 \left(\frac{T - T_{max}^0}{D^0} \right)^2 + cf_a^2 \right] \quad (5-32)$$

In order to evaluate the crystallization rate, equation (5-31) was differentiated with respect to time

$$\frac{\partial \theta}{\partial t} = \theta_{\infty} n K \left(\int_0^t K d\tau \right)^{n-1} \exp \left[- \left(\int_0^t K d\tau \right)^n \right] \quad (5-33)$$

Converting time derivative to position derivative through $(\partial/\partial t) = (1/V)(d/dz)$,

$$\frac{d\theta}{dz} = \frac{\theta_{\infty} n K}{V} \left(\int_0^z \frac{K}{V} dz' \right)^{n-1} \exp \left[- \left(\int_0^z \frac{K}{V} dz \right)^n \right] \quad (5-34)$$

For nylon-6, Ziabicki (12) has also provided values for various parameters. The maximum rate constant is $K_{max} = 0.14 \text{ sec}^{-1}$; the temperature corresponding to K_{max} , $T_{max} = 146^{\circ}\text{C}$; the half width of the rate-temperature distribution curve, $D_0 = 46^{\circ}\text{C}$. Based on the results of Ziemiński (33), the value of Avrami exponent was taken to be $n = 3$. Ziemiński compared results for different values of n and found that there was insufficient difference between predictions to justify use of any other value than 3. For lack of any information about the value of the parameter c for nylon-6, this parameter was considered to be constant with a value corresponding to its estimated value for PET. This value was $c = 200$ (76). Initial condition for equation (5-34) was $\theta(0) = 0$ since at the spinneret the melt temperature was well above T_m .

Continuous System Modeling Program

CSMP is a Fortran based package developed by IBM which allows simulation of physical systems with minimum programming of complex numerical schemes such as integration and differentiation. A CSMP code for any physical process consists of three segments called initial, dynamic and terminal segments. In the initial segment constants and initial conditions are specified along with tabulated data requiring interpolation. In the dynamic segment the mathematical expressions used to simulate the physical system are described. These mathematical expressions could be ordinary differential equations to be integrated or functions that must be differentiated. These statements can be sorted or non-sorted depending on coupling between them. In the terminal segment any simple calculations subsequent to the dynamic calculations are performed and more importantly statements to print and/or to plot the output, to specify the end of calculations and method of calculations are included.

Numerical solution of the mathematical model included solving simultaneously differential equations (5-6) to (5-9), (5-15), (5-20), (5-28) and (5-34). Since this system of mathematical expressions described several physical processes whose solutions were expected to occur at much different time scales, a numerical integration scheme designed for stiff equations was employed. A detailed description of this and other integration and differentiation techniques along with instructions for using CSMP is included in a guide book authored by Speckhart and Green (286). The computer code used for the present mathematical model for melt spinning is given in Appendix D.

Predictions of the Model

The mathematical model, developed for high speed melt spinning and described in the preceding section was numerically solved using various physical properties and relationships for nylon-6 from the literature. Processing conditions for the solutions were chosen to correspond to those used in the experimental online measurements. These processing conditions are summarized in Table 5.1

The predictions of the model are in the form of profiles along the spinline, from spinneret to drawdown device. Although all equations are solved simultaneously in the model, the equations based primarily on dynamics and heat transfer result in profiles for velocity, temperature, diameter, velocity gradient, rheological force and spinline stress profiles. Equations including structure development concepts provide birefringence, amorphous orientation factor and crystalline index profiles. Predictions of all these quantities were made for a series of take-up speeds for each of two different molecular weight resins (CN9984 - 23,500 and BHS - 53,200) and two different mass flow rates (about 3 and 5 g/min). The precise take-up speeds for these different conditions were different because of the fact that, in the experimental studies, the air aspirator take-up device did not have positive control on take-up speed. Instead, the air suction pressure was varied and final take-up speed was calculated from the continuity equation.

Figures 5.1 to 5.4 show the predicted velocity profiles for each resin and two mass throughputs, each of which involved five different take-up speeds. These profiles show initially a gradual deformation region followed by a leveling out at the final velocity. Above a certain

Table 5.1 Summary of experimental processing conditions.

Extrusion temperature	- 270°C for CN9984 - 280°C for BHS
Mass throughput	- 3.073 and 5.154 g/min for CN9984 - 2.993 and 5.069 g/min for BHS
Spinneret	- Circular cross section diameter = 762 micrometer length/diameter ratio = 5
Spinline length	- 2.0 meters
Cooling conditions	- Stationary air, temperature = 25°C
Take-up Speeds	- 1200 - 7300 meters/min (corresponding to air pressure of 2, 10, 20, 45 and 80 psi on the aspirator)

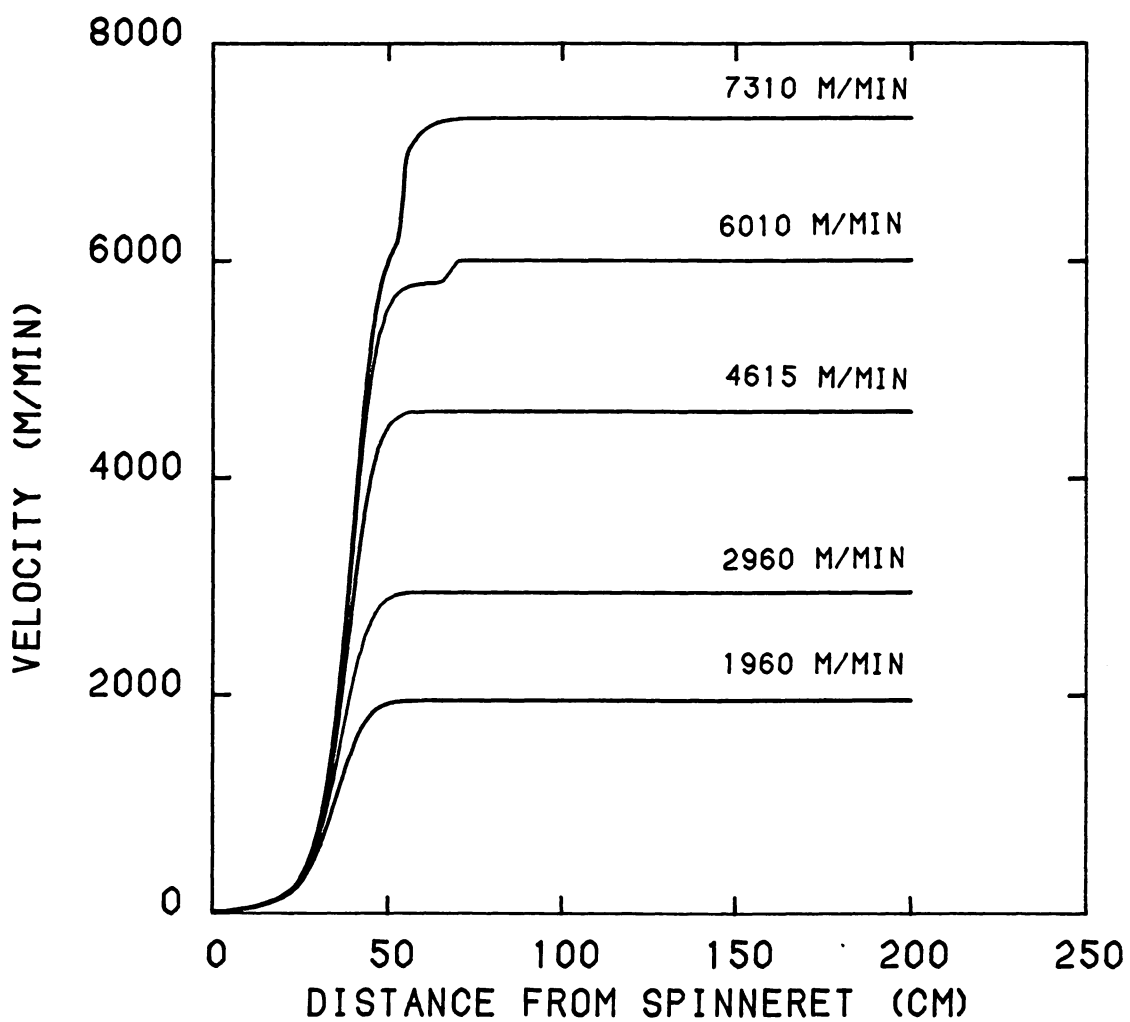


Figure 5.1 Predicted velocity profiles for CN9984 with a mass throughput of 3.073 g/min.

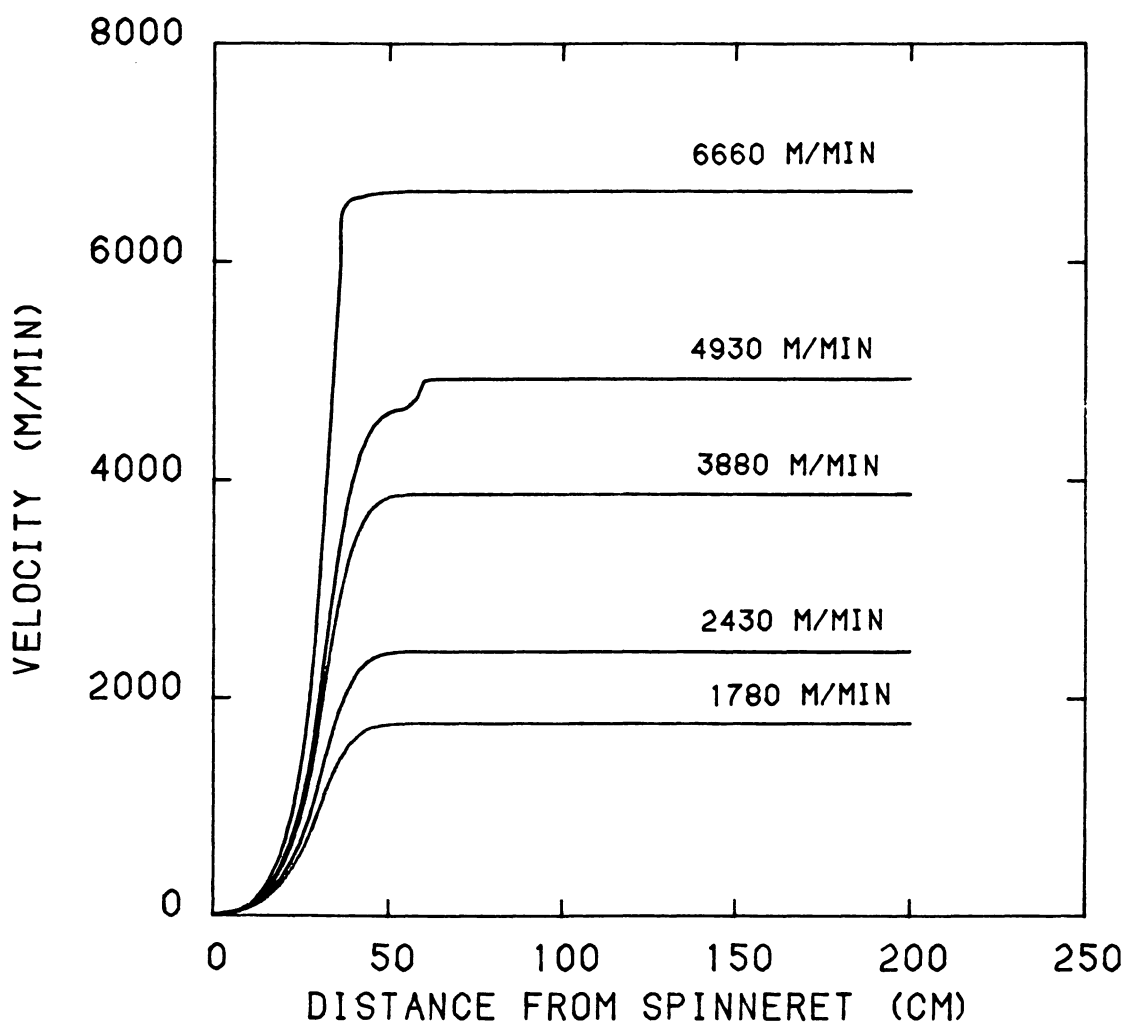


Figure 5.2 Predicted velocity profiles for BHS with a mass throughput of 2.993 g/min.

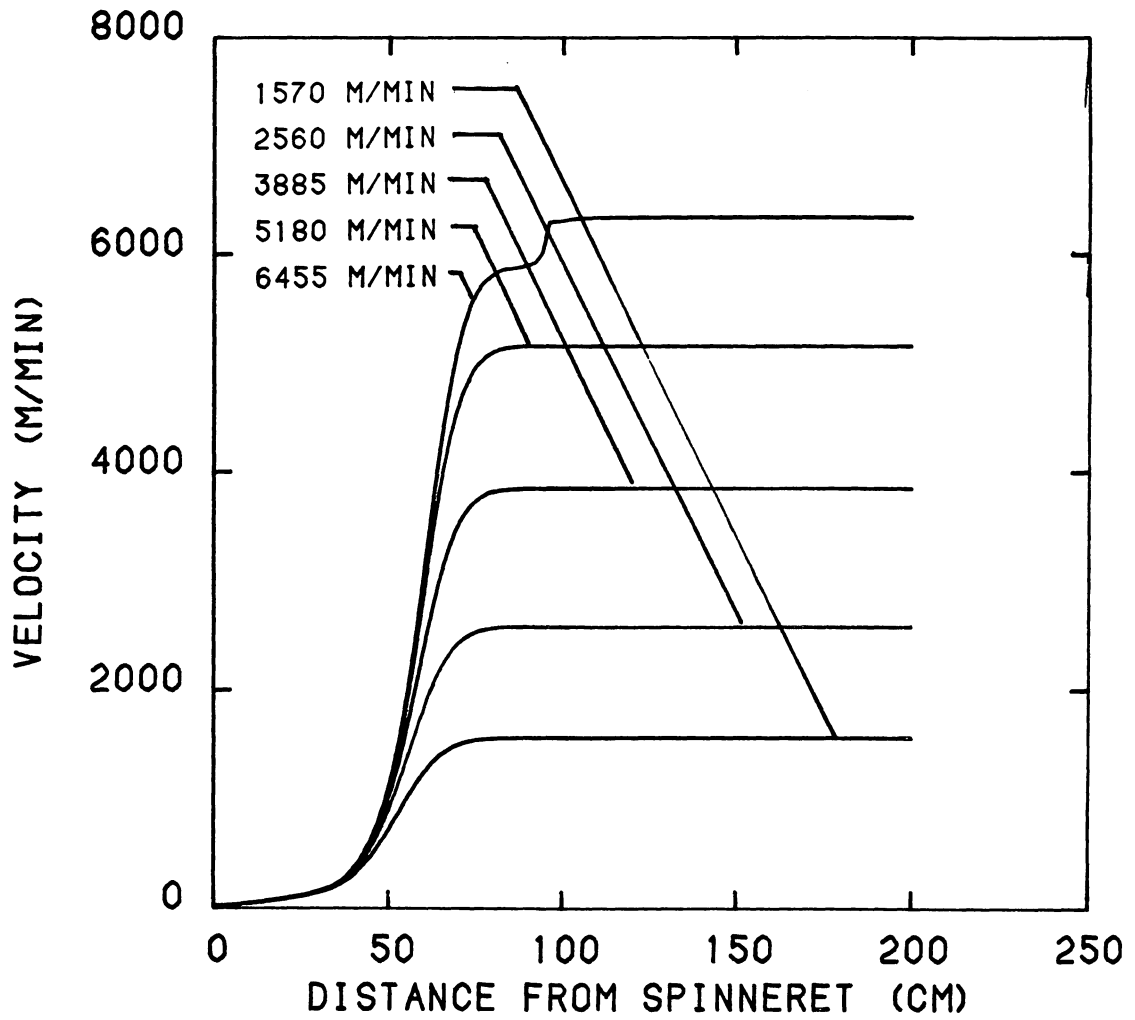


Figure 5.3 Predicted velocity profiles for CN9984 with a mass throughput of 5.154 g/min.

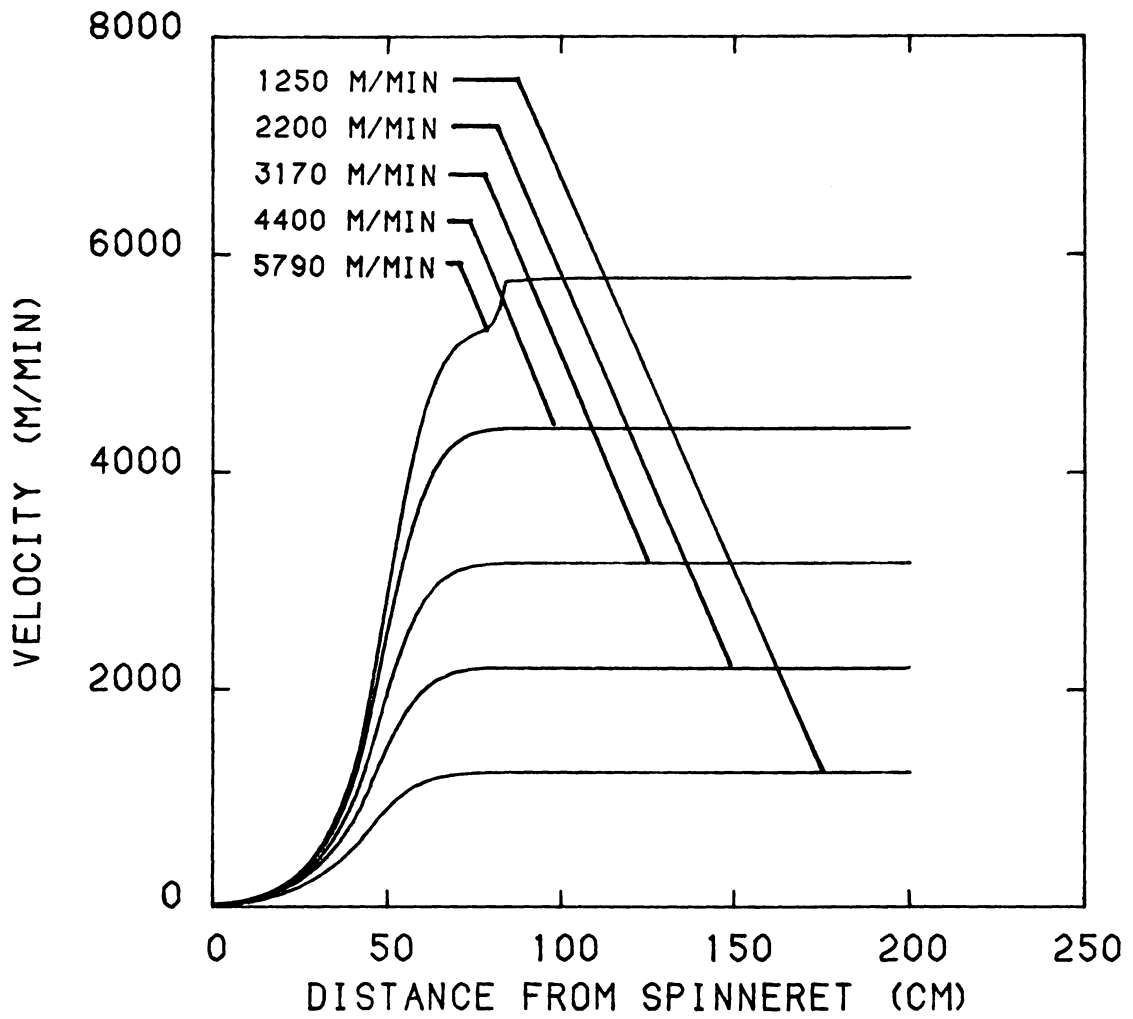


Figure 5.4 Predicted velocity profiles for BHS with a mass throughput of 5.069 g/min.

critical speed, for example, 4600 m/min in the case of CN9984 at 3.073 g/min throughput (Figure 5.1), a region of rapid localized increase in velocity occurs, following the initial deformation region and just prior to leveling out at the final velocity. This localized deformation zone is coincident with the appearance of online crystallization confirmed by birefringence and crystalline index profiles which we shall discuss later. Note that the critical speed for BHS is lower than that for CN9984 for a particular throughput (compare Figure 5.1 to Figure 5.2 and Figure 5.3 to Figure 5.4). Also note that the critical speed is higher for either resin for 5 g/min throughput compared to a throughput of 3 g/min.

Figures 5.5 to 5.8 show the corresponding predicted temperature profiles. At take-up velocities lower than the critical values, the temperature profiles along the spinline are essentially independent of take-up velocity. As take-up velocity increases the cooling rate of a volume element in the filament increases due to the increased velocity of the element through the cooling medium. However, the element also traverses the distance from the spinneret to take-up device in a shorter time period. The decreased cooling time is almost balanced by the increased cooling rate and the net effect is that the change of temperature with distance along the spinline is almost independent of take-up speed, provided no other factors are involved.

At take-up speeds higher than the critical speed an increase in temperature within a very small distance on the spinline followed by a gradual decrease in temperature is observed. This increase in temperature is due to release of crystallization heat and is associated

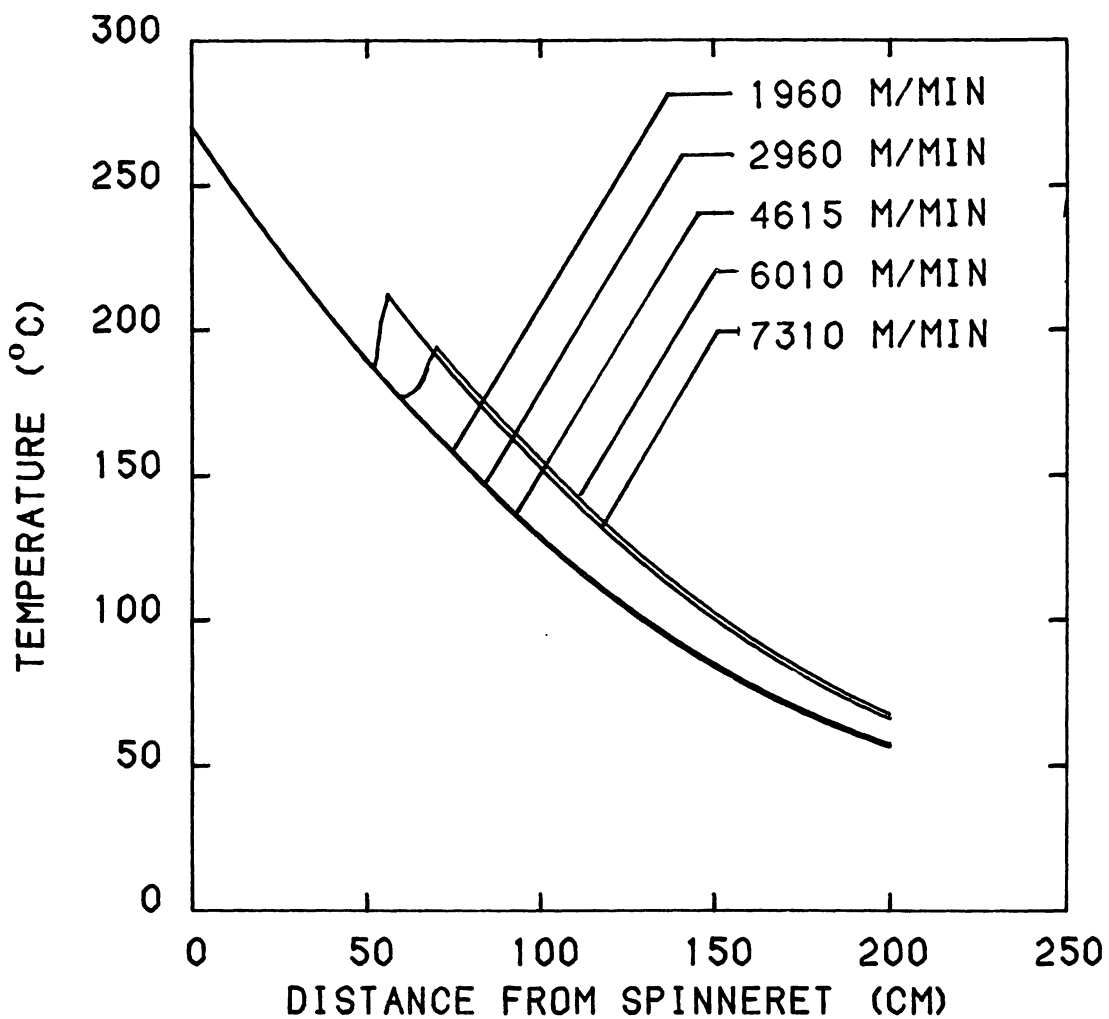


Figure 5.5 Predicted temperature profiles for CN9984 with a mass throughput of 3.073 g/min.

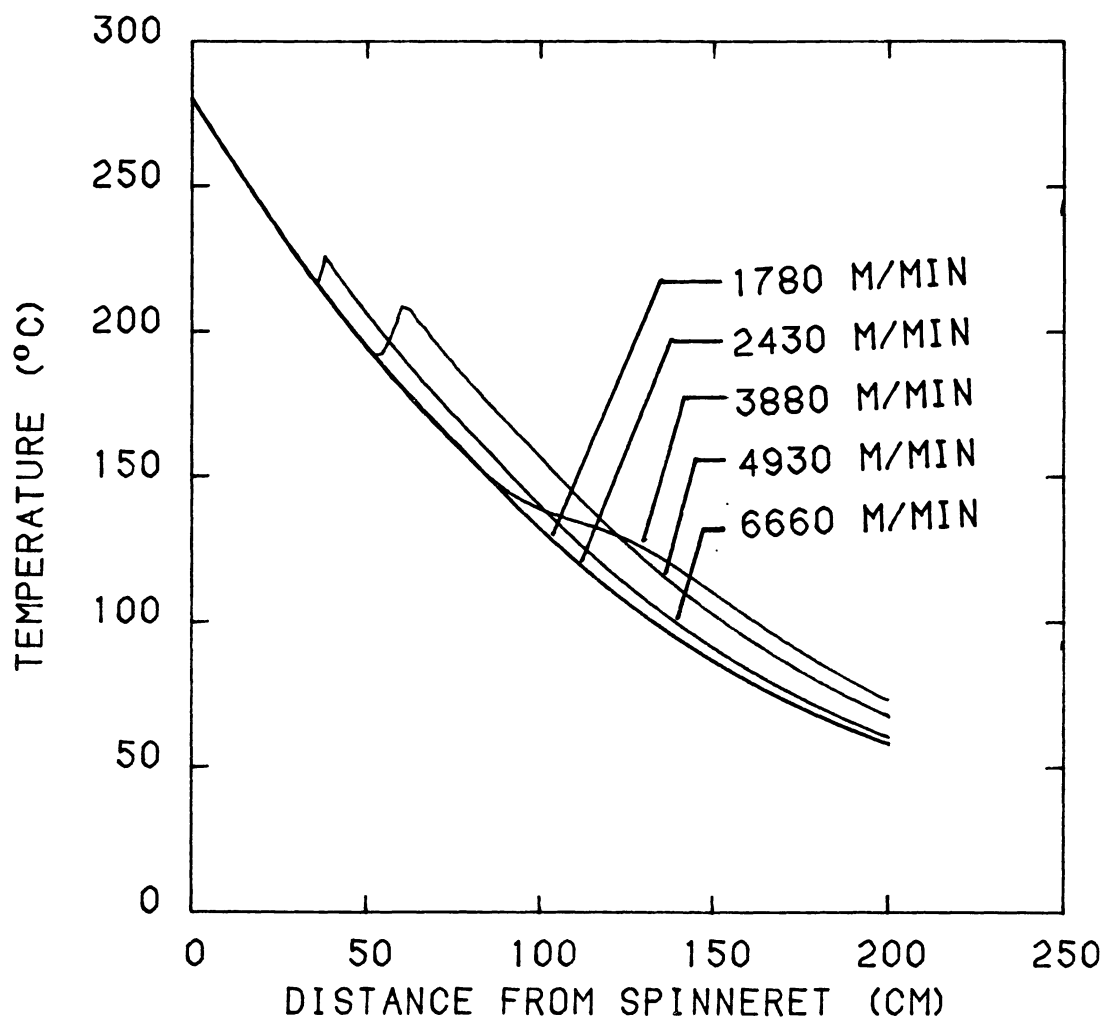


Figure 5.6 Predicted temperature profiles for BHS with a mass throughput of 2.993 g/min.

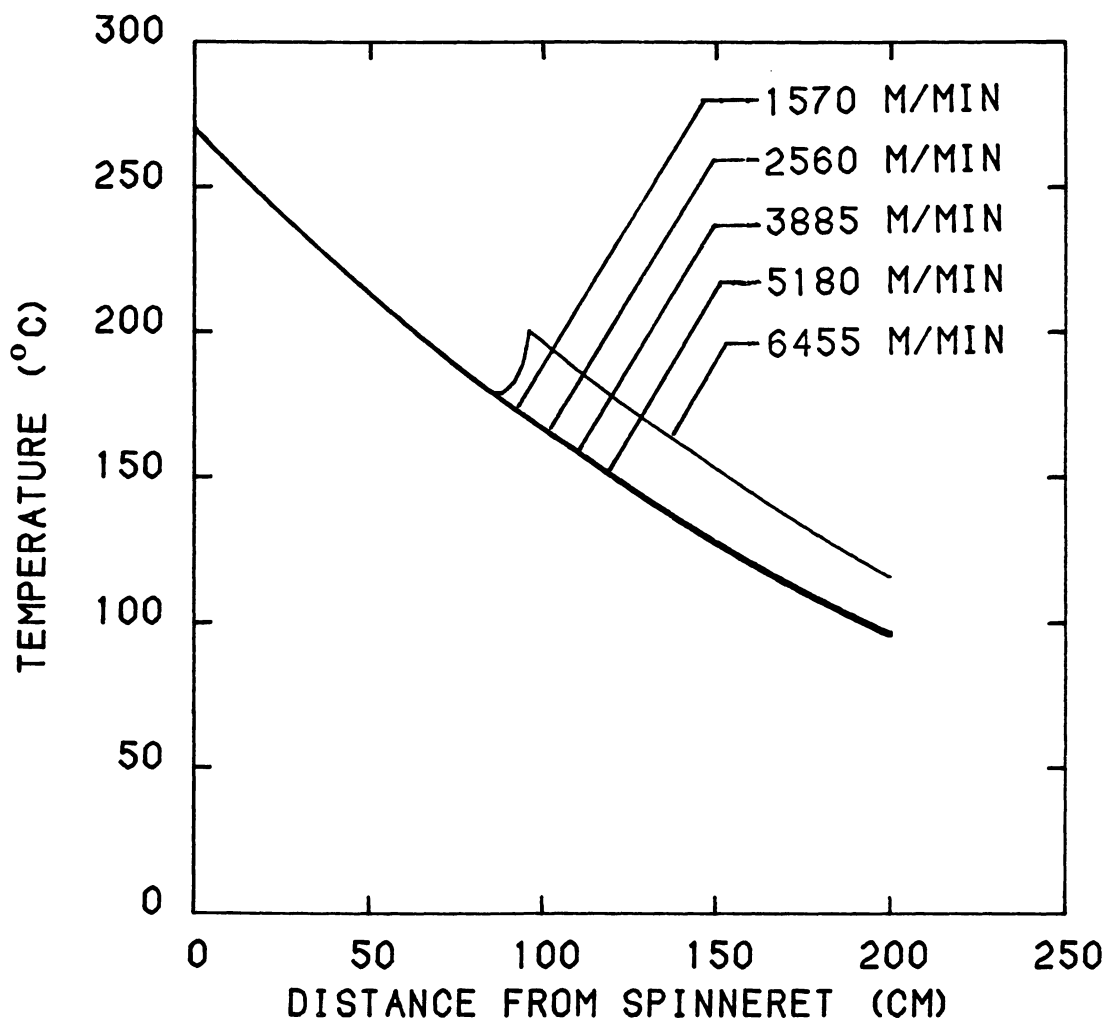


Figure 5.7 Predicted temperature profiles for CN9984 with a mass throughput of 5.154 g/min.

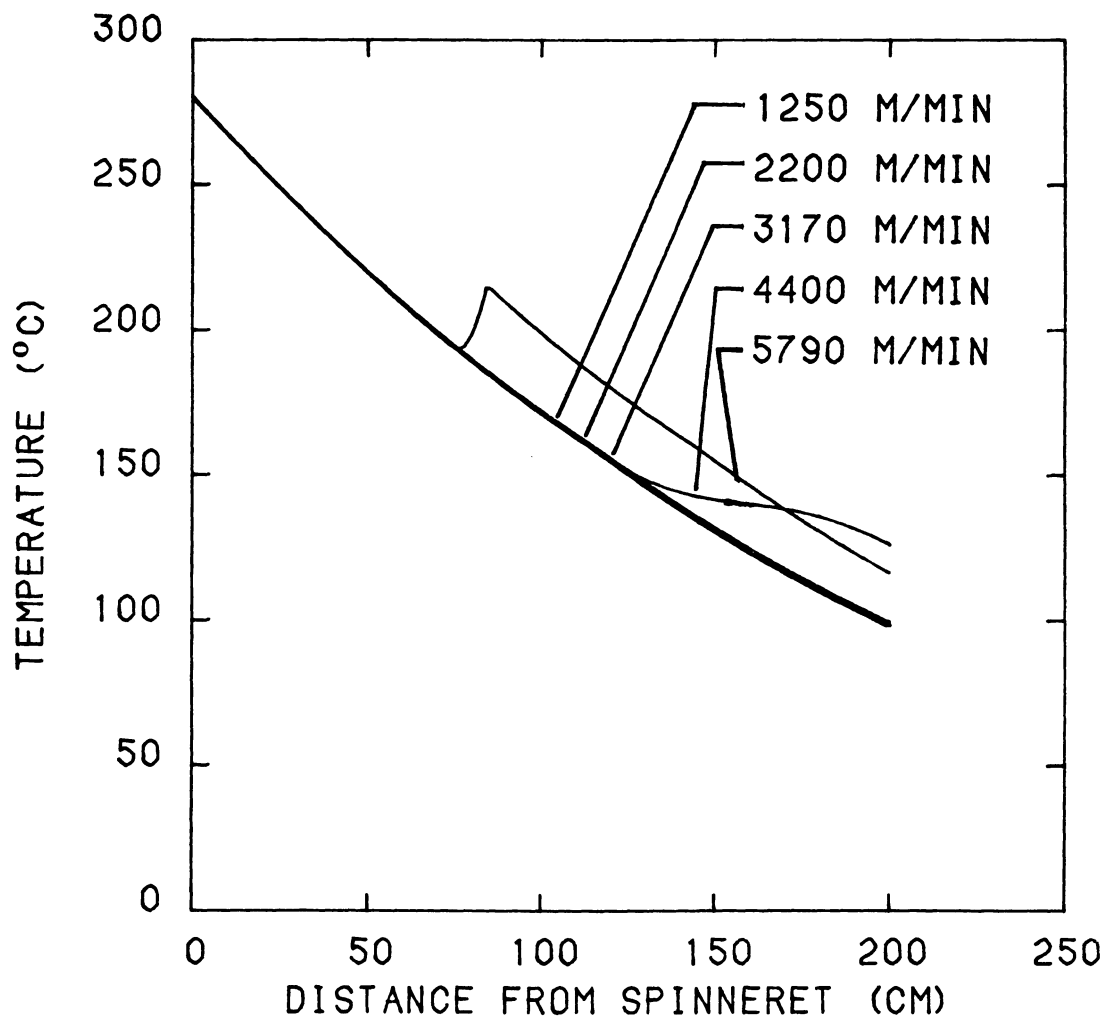


Figure 5.8 Predicted temperature profiles for BHS with a mass throughput of 5.069 g/min.

with crystallization at high degrees of supercooling. Once crystallization begins, heat is being released more rapidly than it can be transferred to the surroundings. The accumulation of heat in the localized region where crystallization is occurring results in a local increase in temperature until a new heat balance is achieved. This phenomenon, known as recalescence, is well known in the literature on phase transformations in metallic alloys. As take-up velocity is increased beyond the critical speed, the recalescence occurs closer to the spinneret, indicating that the onset of crystallization is occurring at higher temperature. These effects cause the temperature profiles to be strongly dependent on the take-up velocity in the take-up velocity regime above the critical take-up speed required to cause crystallization on the spinline.

Comparison of temperature profiles for CN9984 and BHS resins indicate that, in the absence of the effect of crystallization, decrease of filament temperature with distance from the spinneret is almost independent of molecular weight of the resin, but it is strongly dependent on mass throughput. The latter effect is understandable on the basis that, at a given take-up velocity, cooling rates are much higher for a throughput of 3 g/min compared to that for 5 g/min because of higher surface to volume ratio in the former case. Once the critical take-up velocity for crystallization on the threadline is exceeded, the temperature profiles become functions of resin molecular weight because of the strong dependence of crystallization behavior on resin molecular weight. This effect is discussed in more detail later.

Figures 5.9 to 5.12 show the corresponding predicted diameter profiles. These profiles show initially a drawdown region followed by a leveling out at the final diameter. The diameter drawdown is faster for BHS and 3 g/min throughput conditions compared to that for CN9984 and 5 g/min conditions. At take-up speeds greater than the critical speed, a sudden diameter drawdown occurs within a small distance on the spinline. This sudden drawdown has been called "necking" because its shape is analogous to that of necks and shoulders that occur in the drawing process. The neck corresponds to the localized deformation region of the velocity profile and the rise in temperature observed in the temperature profile due to online crystallization. Note that at much higher take-up speeds than critical speed the neck moves closer to the spinneret and also that it moves closer to spinneret or appears at lower take-up speed in case of the higher molecular weight BHS resin or the lower mass throughput of 3 g/min compared to that for the CN9984 resin and 5 g/min throughput, respectively.

Figures 5.13 to 5.16 show corresponding velocity gradient profiles. These profiles basically indicate the change of deformation with distance as a function of spinline distance. The peak in the velocity gradient profile corresponds to the position at which the rate of deformation is a maximum. The value of the maximum in the velocity gradient increases with increasing take-up speeds; it shifts closer to the spinneret for BHS and 3 g/min conditions compared to that for CN9984 and 5 g/min conditions. At speeds higher than the critical speed a second peak appears in the velocity gradient profiles which corresponds

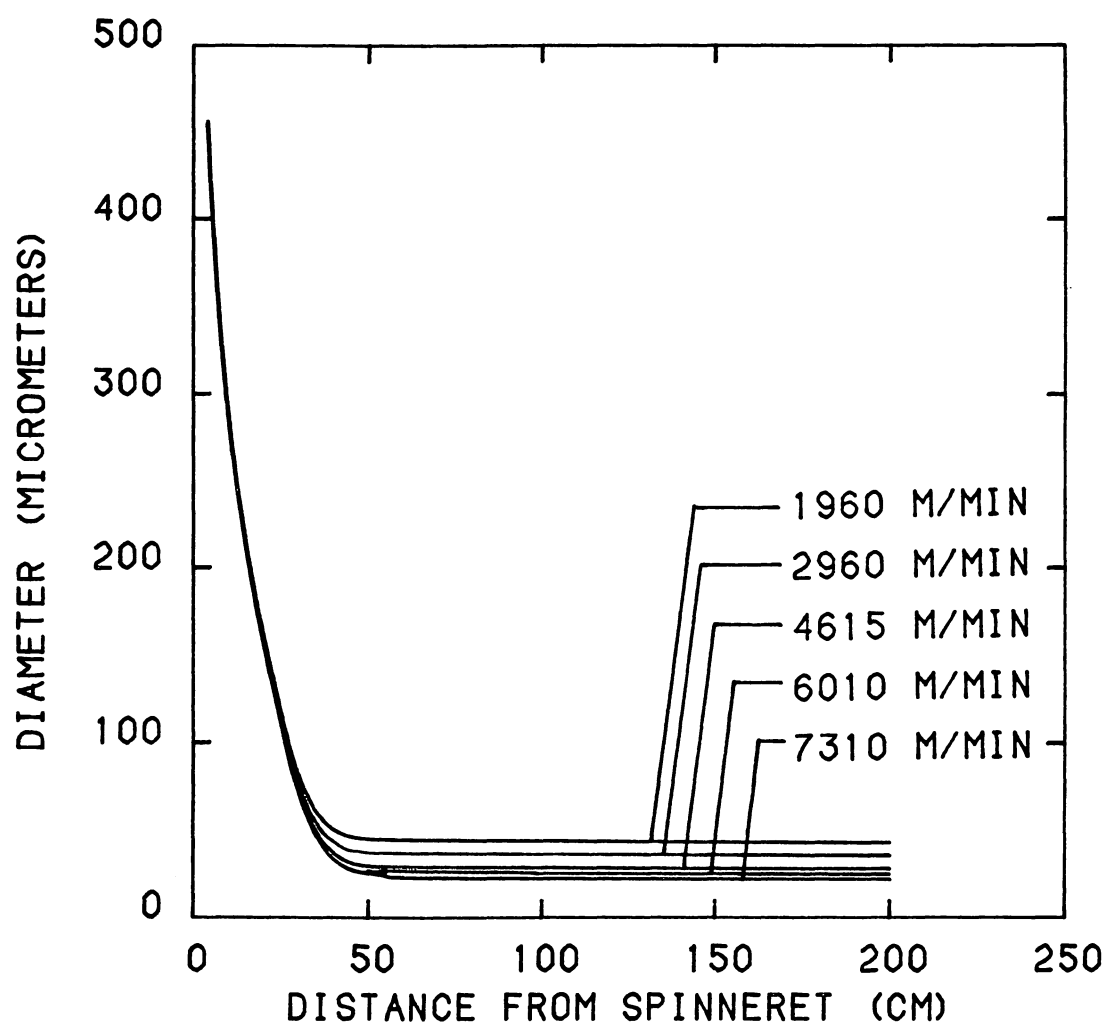


Figure 5.9 Predicted diameter profiles for CN9984 with a mass throughput of 3.073 g/min.

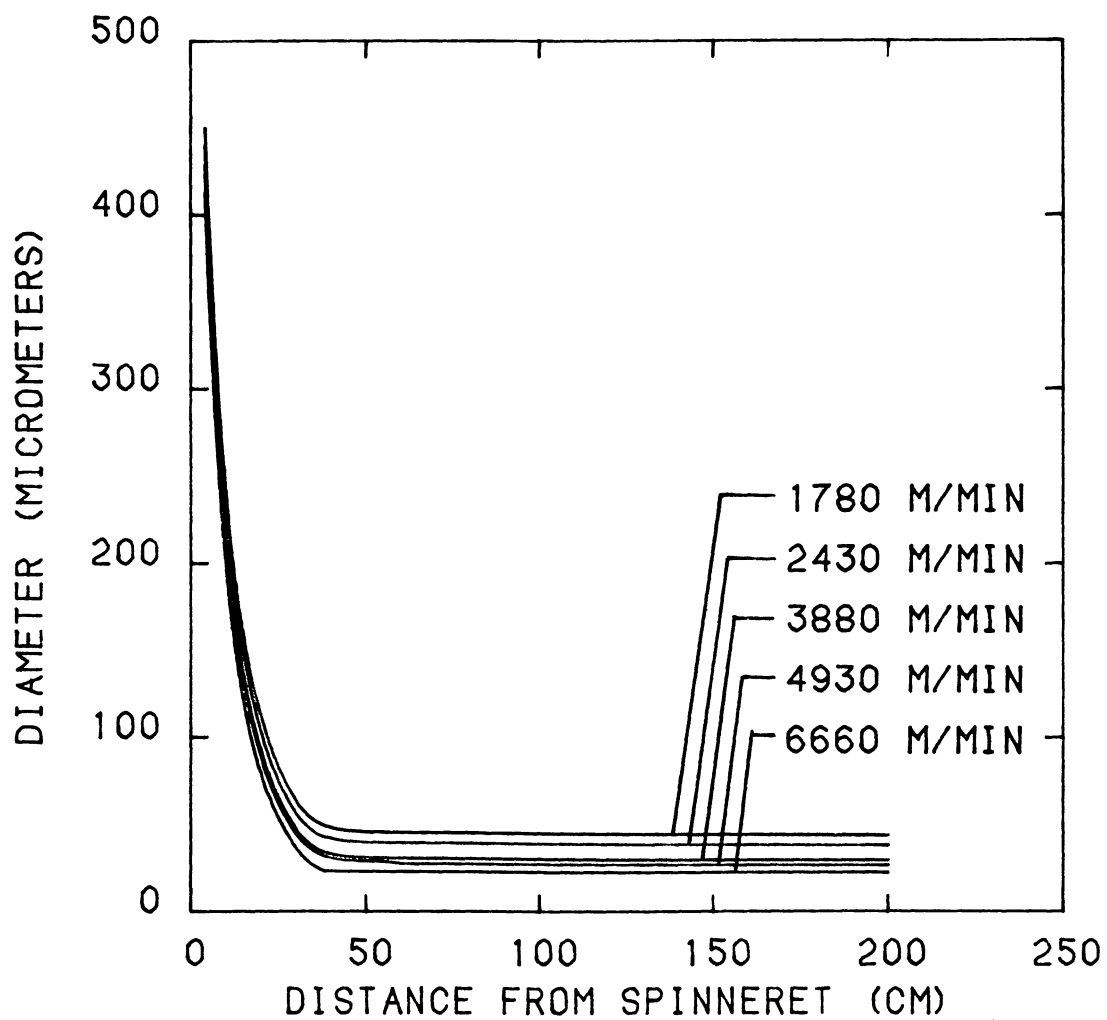


Figure 5.10 Predicted diameter profiles for BHS with a mass throughput of 2.993 g/min.

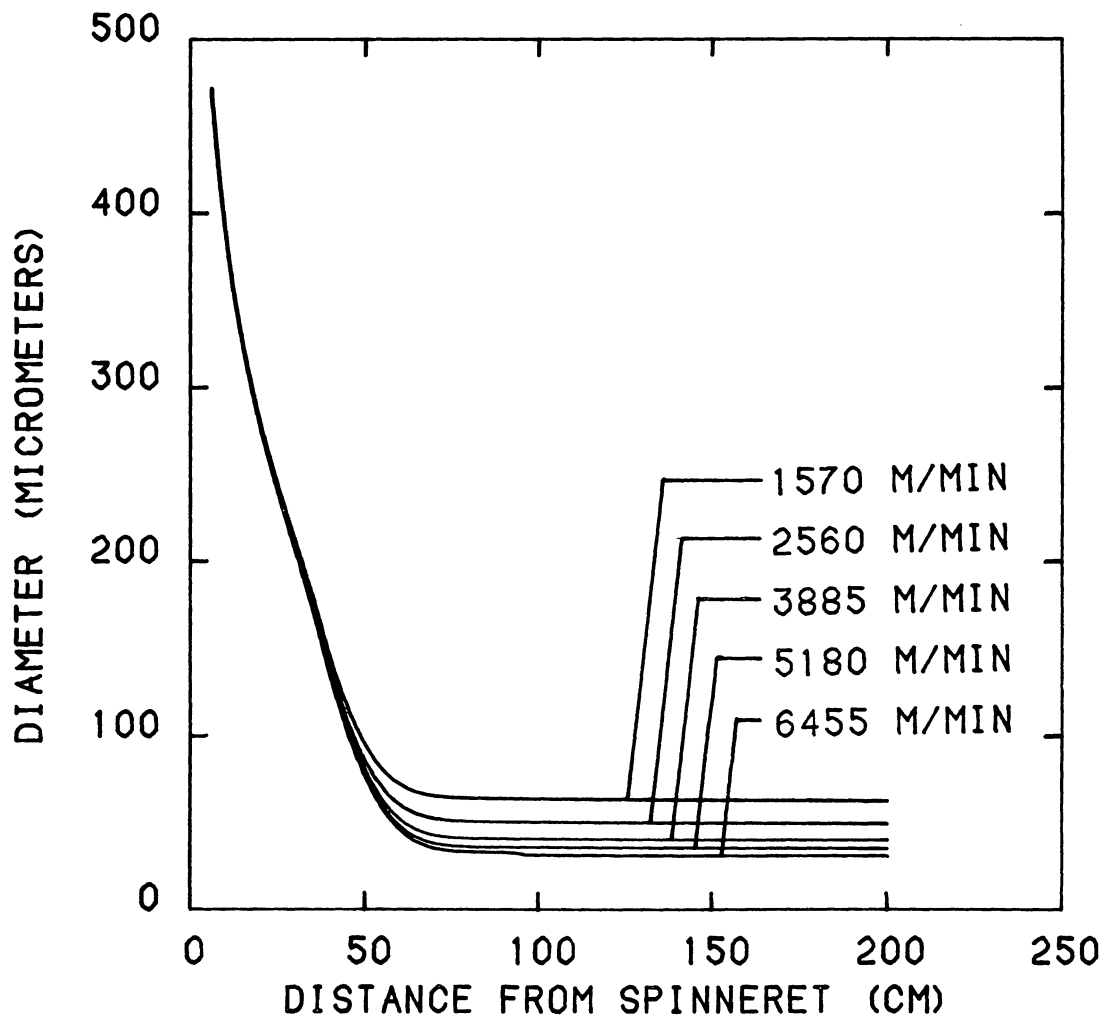


Figure 5.11 Predicted diameter profiles for CN9984 with a mass throughput of 5.154 g/min.

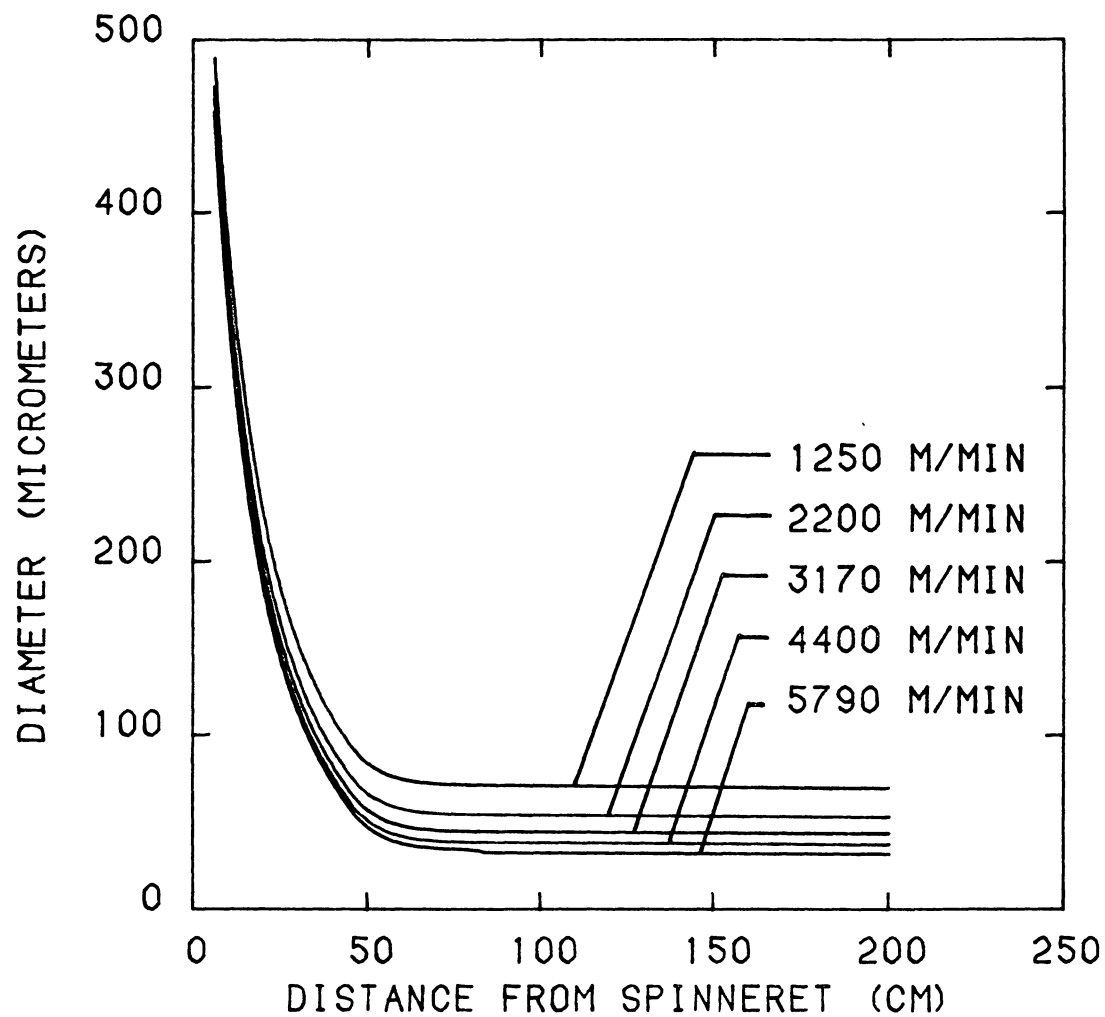


Figure 5.12 Predicted diameter profiles for BHS with a mass throughput of 5.069 g/min.

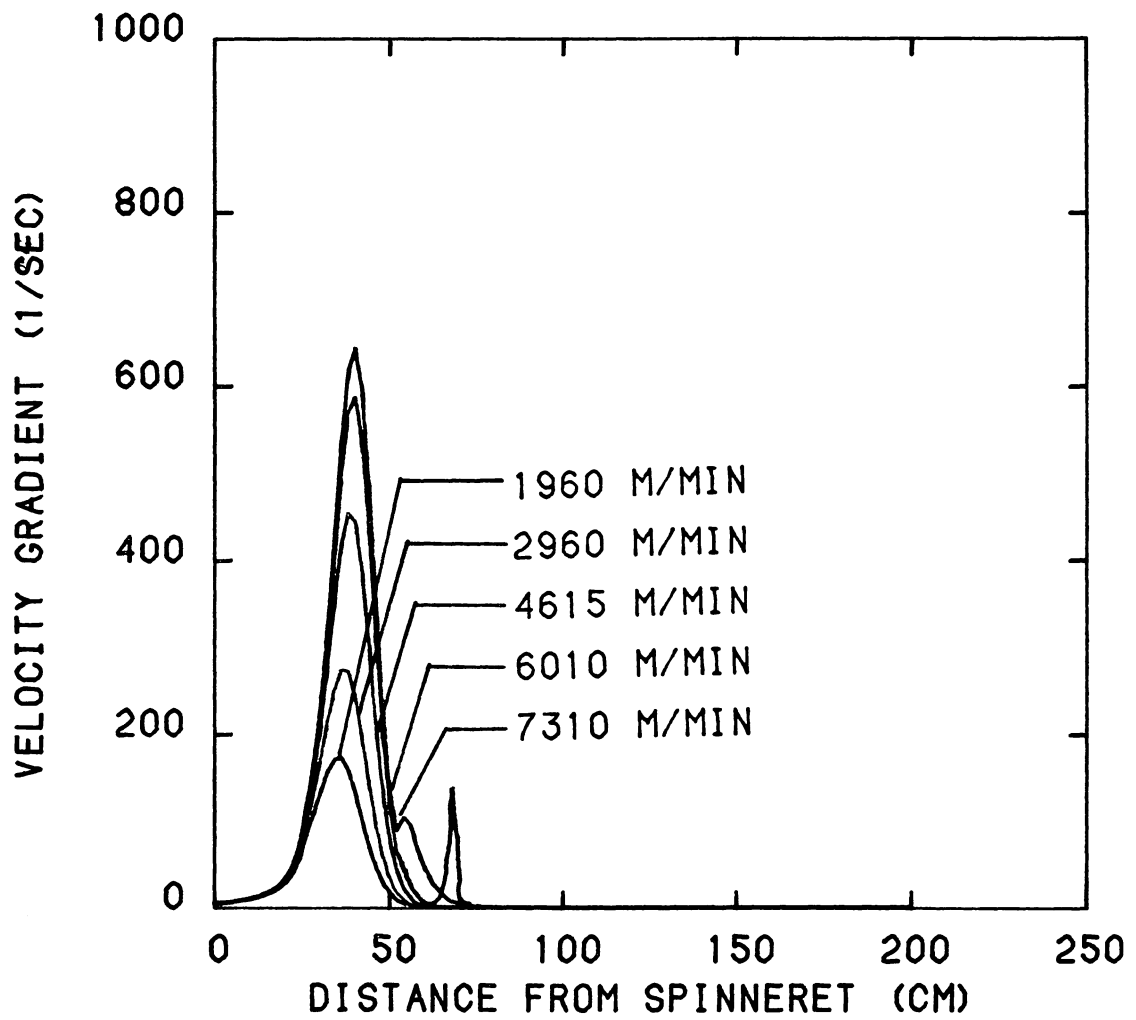


Figure 5.13 Predicted velocity gradient profiles for CN9984 with a mass throughput of 3.073 g/min.

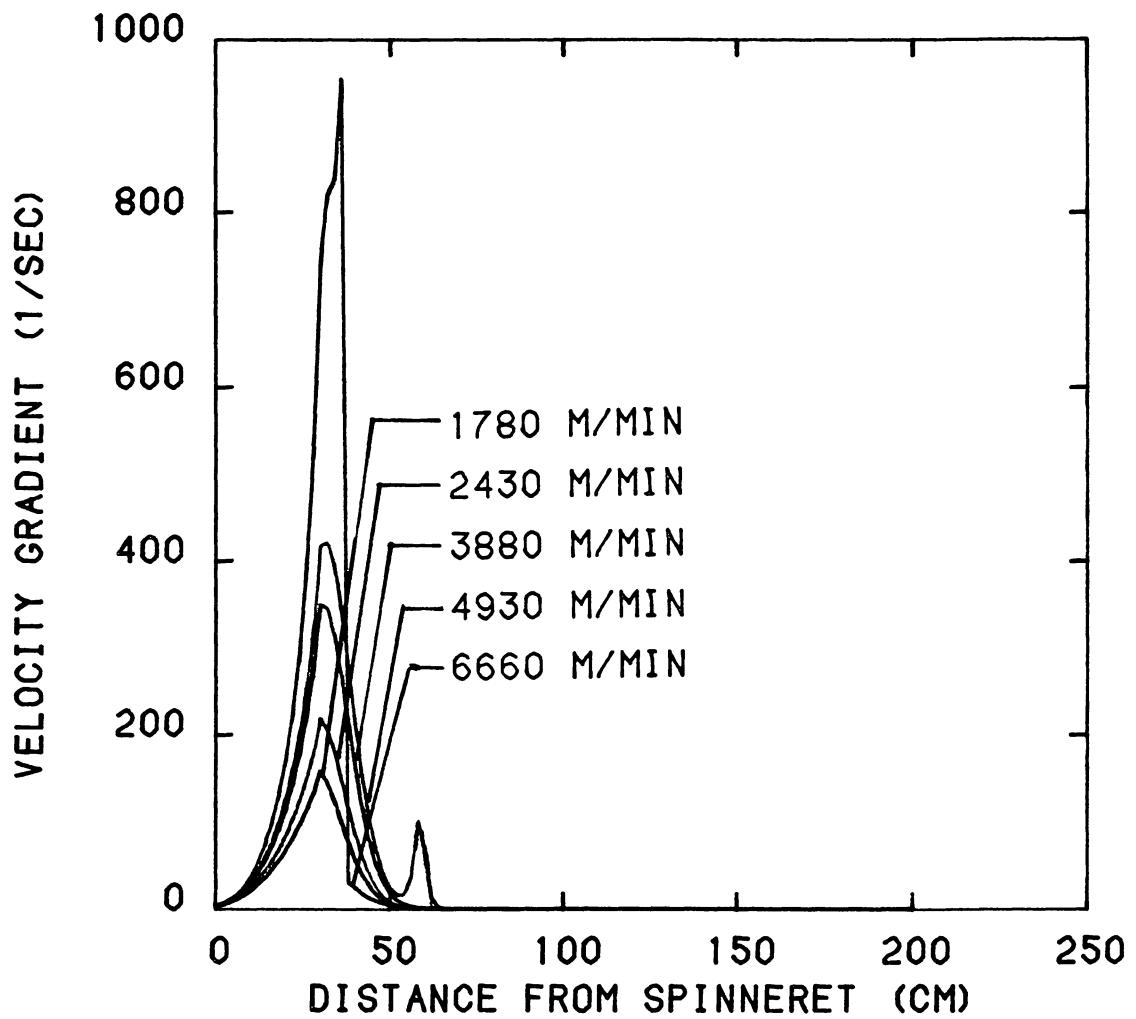


Figure 5.14 Predicted velocity gradient profiles for BHS with a mass throughput of 2.993 g/min.

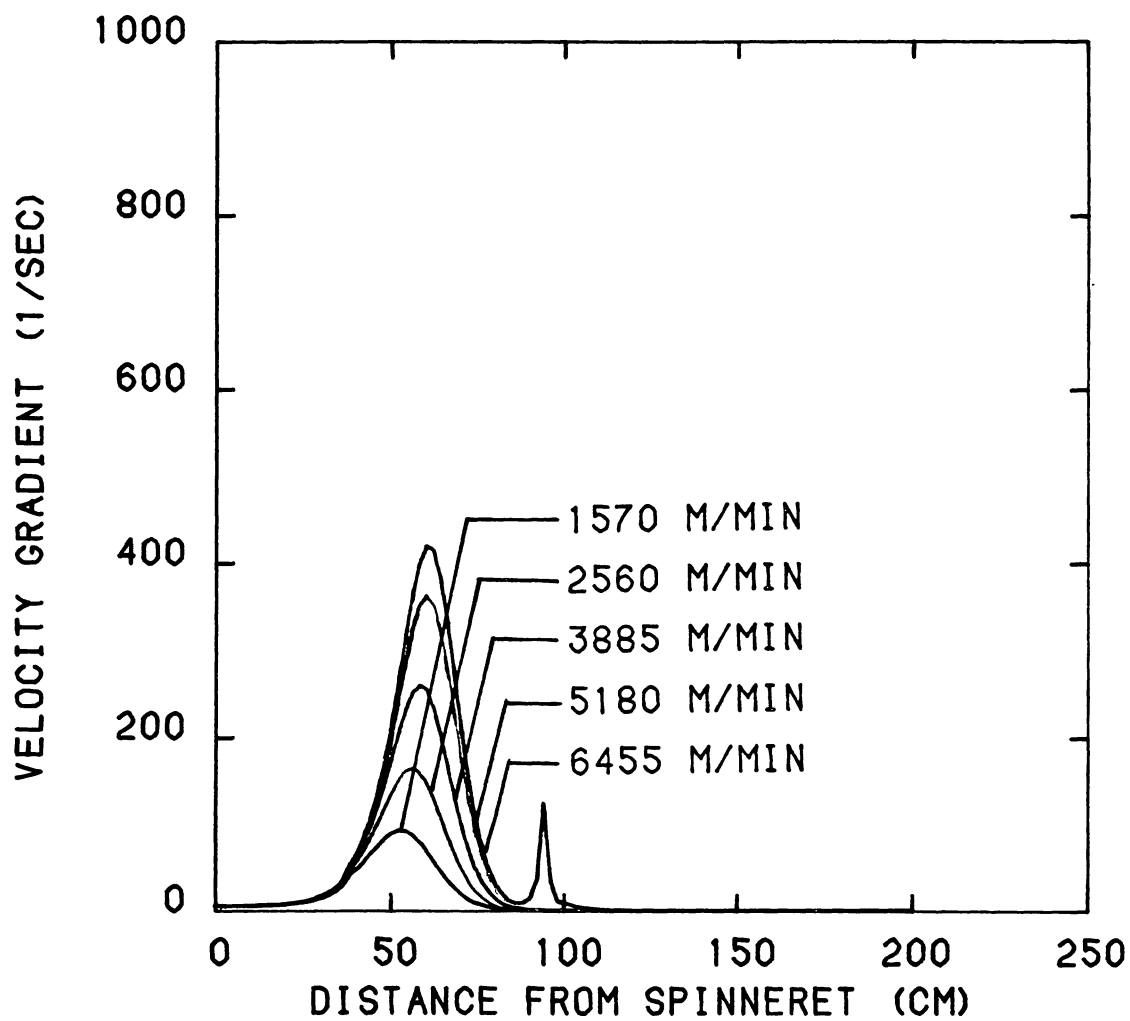


Figure 5.15 Predicted velocity gradient profiles for CN9984 with a mass throughput of 5.154 g/min.

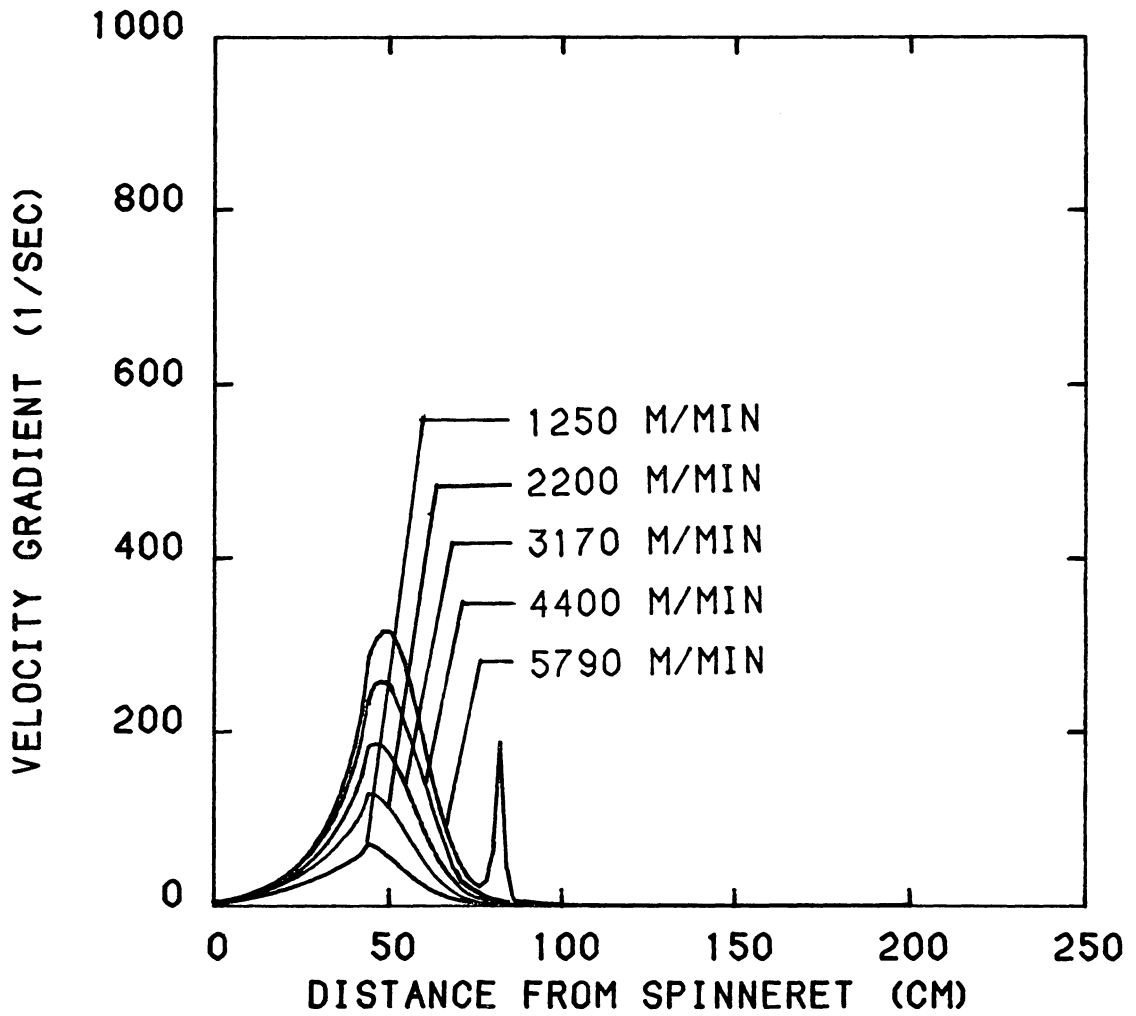


Figure 5.16 Predicted velocity gradient profiles for BHS with a mass throughput of 5.069 g/min.

to the localized jump in velocity profile or neck in the diameter profile.

Figures 5.17 to 5.20 show the predicted rheological force profiles and Figures 5.21 to 5.24 show the corresponding predicted spinline stress profiles. At higher speeds the increase in rheological force with distance from the spinneret is much greater than that at the lower speeds. This results from the large contributions to the total force of the air drag and inertial force contributions at high speeds. The values of rheological force associated with BHS and 3 g/min conditions are much higher than those for CN9984 and 5 g/min conditions. This suggests that the higher melt viscosity of high molecular weight resin (BHS) develops higher tension compared to that developed by the lower molecular weight resin (CN9984). The spinline stress is the tension developed within the filament divided by the cross sectional area. The spinline stress rises substantially in the initial deformation region because of substantial rise in melt viscosity due to cooling of filament and because the cross sectional area is decreasing. Higher spinline stresses are developed with increase in spinning speed and at speeds higher than the critical speed a slight jump in stress appears corresponding to the neck in the diameter profile. Comparison of spinline stress profiles for BHS and 3 g/min conditions with those for CN9984 and 5 g/min conditions indicate that the higher molecular weight resin and lower throughput supports a higher level of stresses.

So far we have essentially discussed the profiles describing dynamics of high speed melt spinning of nylon-6. We shall now proceed to profiles describing structure development.

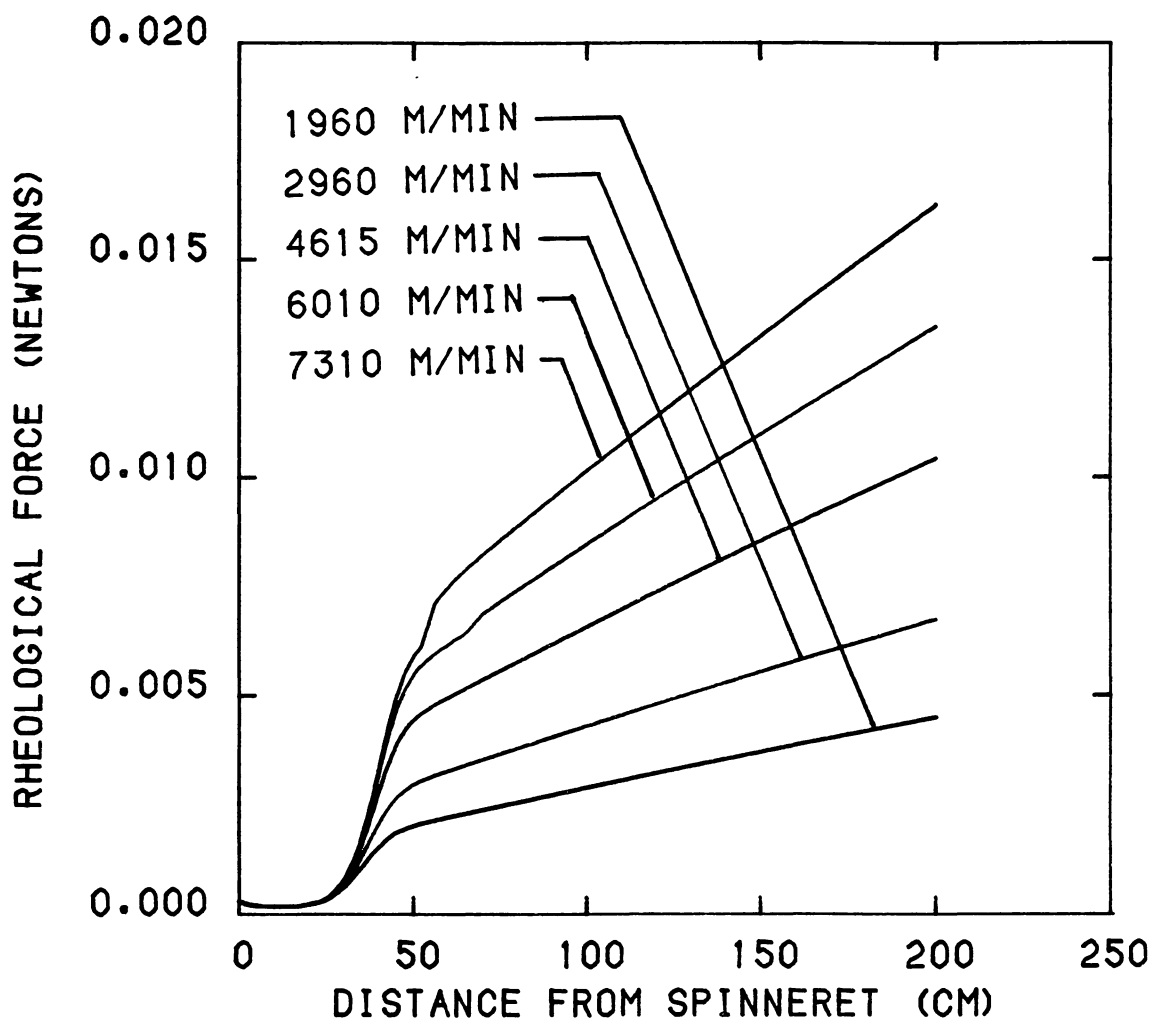


Figure 5.17 Predicted rheological force profiles for CN9984 with a mass throughput of 3.073 g/min.

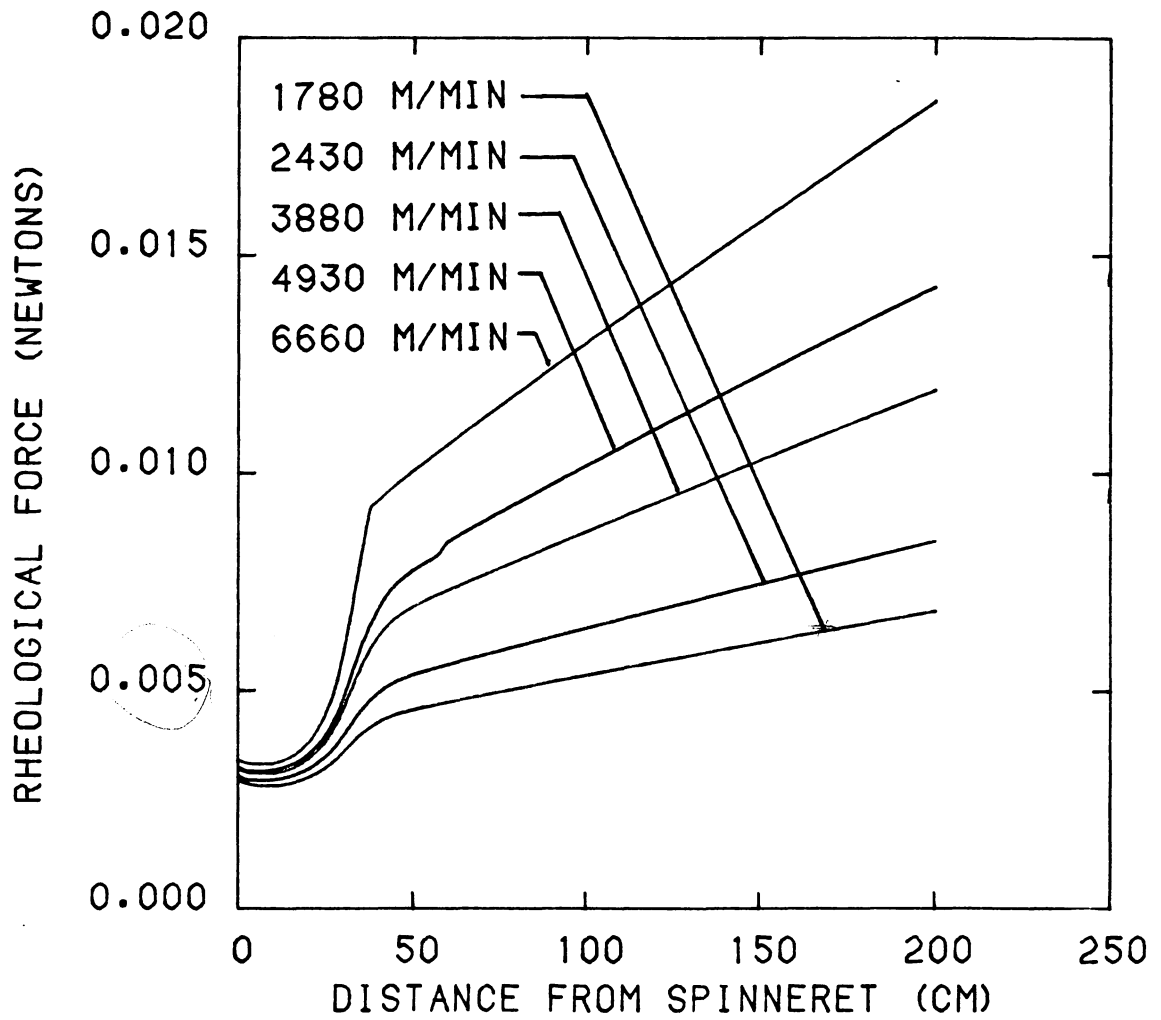


Figure 5.18 Predicted rheological force profiles for BHS with a mass throughput of 2.993 g/min.

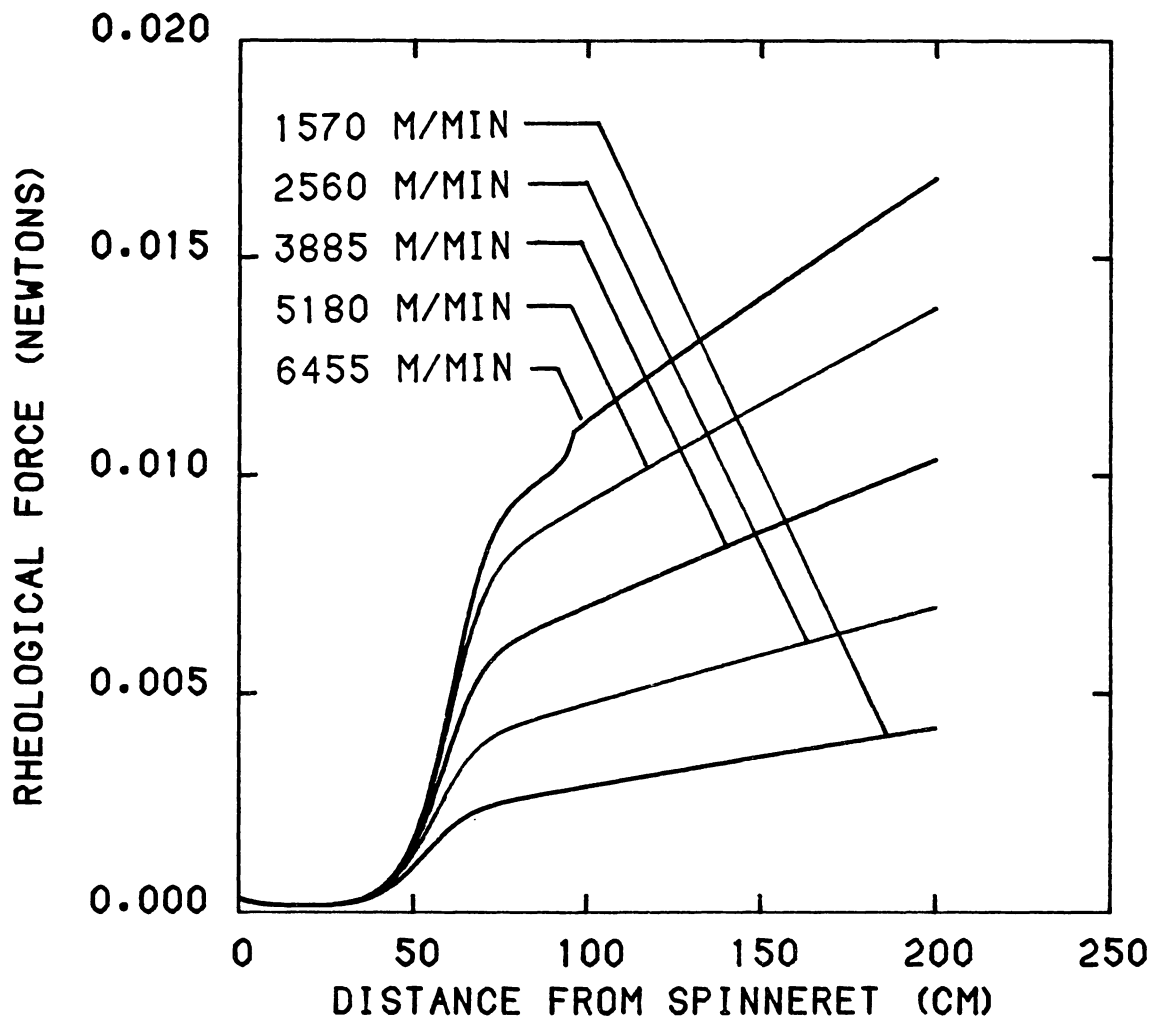


Figure 5.19 Predicted rheological force profiles for CN9984 with a mass throughput of 5.154 g/min.

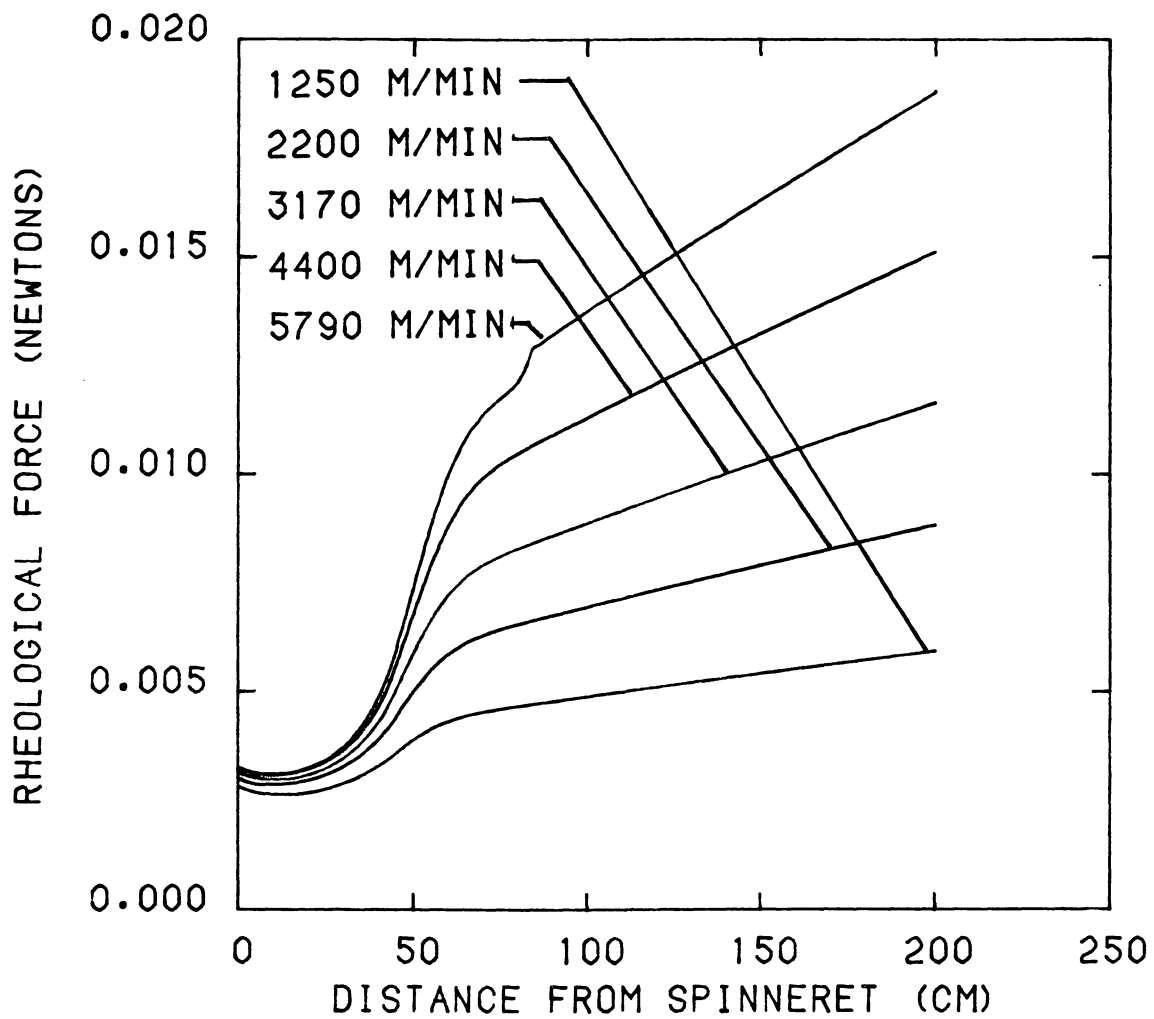


Figure 5.20 Predicted rheological force profiles for BHS with a mass throughput of 5.069 g/min.

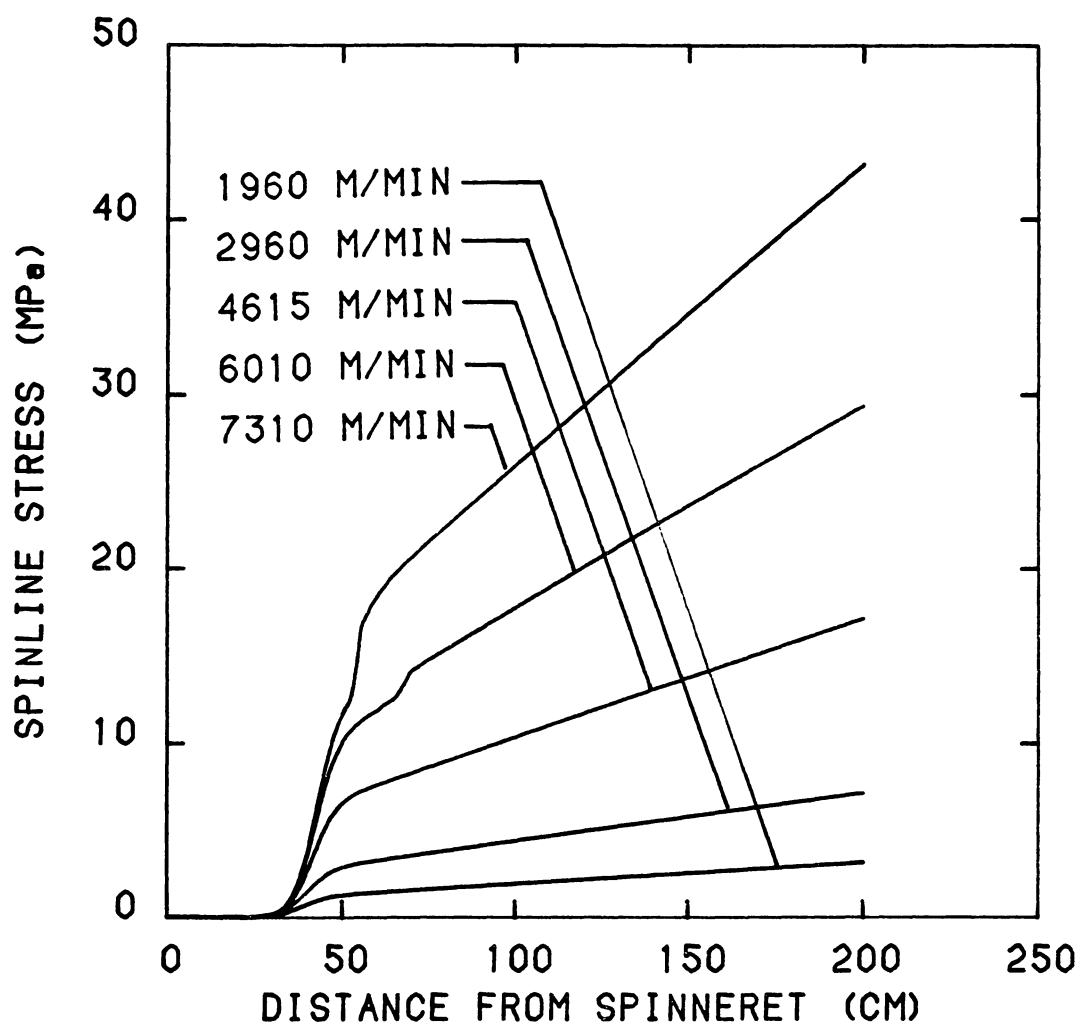


Figure 5.21 Predicted spinline stress profiles for CN9984 with a mass throughput of 3.073 g/min.

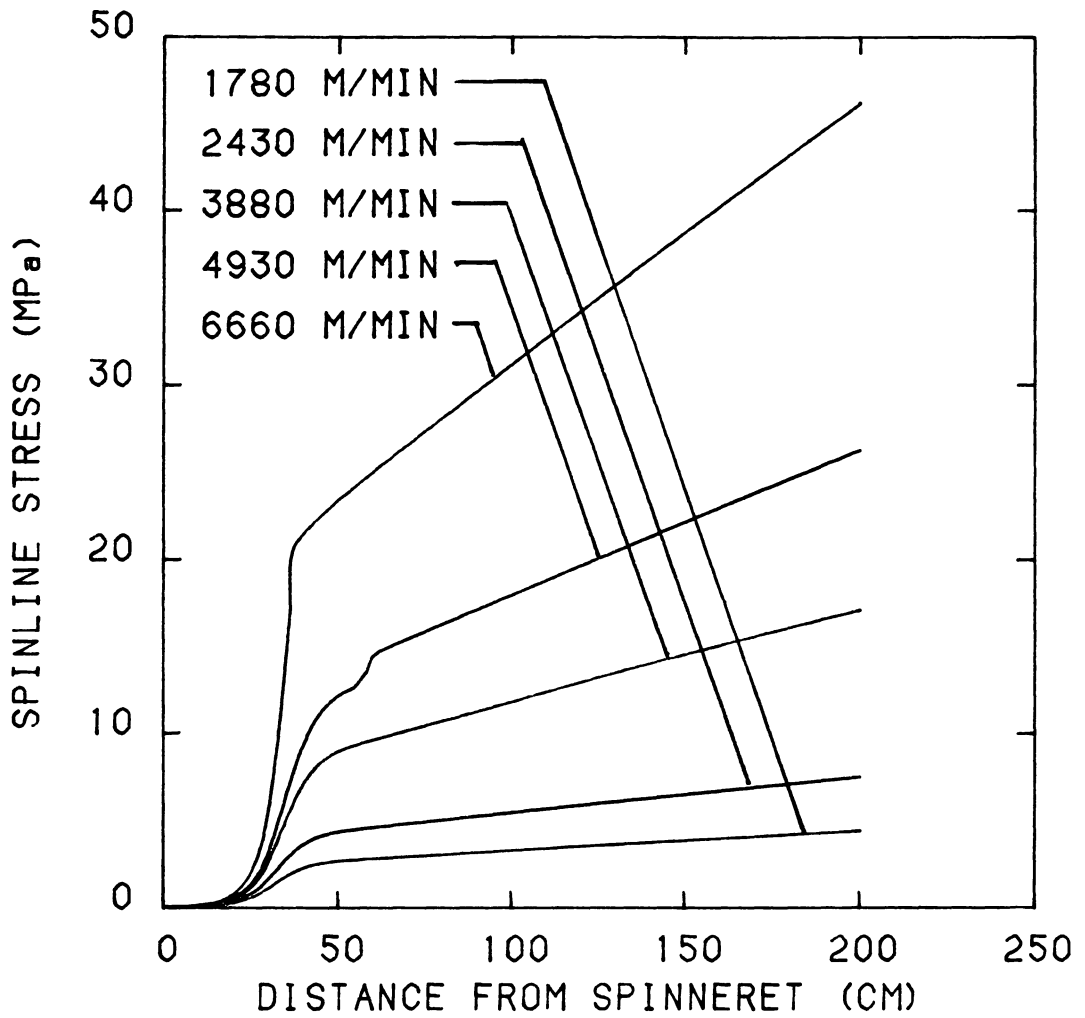


Figure 5.22 Predicted spinline stress profiles for BHS with a mass throughput of 2.993 g/min.

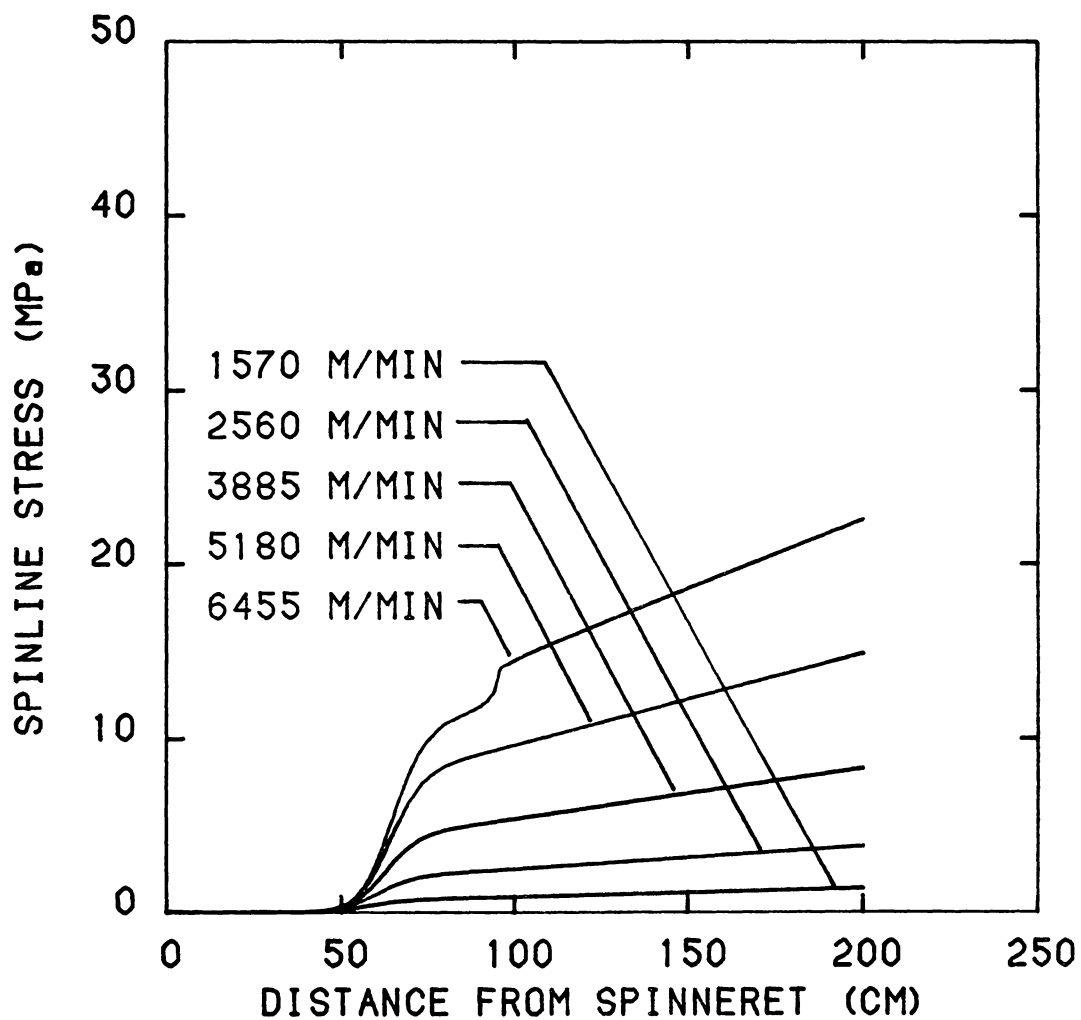


Figure 5.23 Predicted spinline stress profiles for CN9984 with a mass throughput of 5.154 g/min.

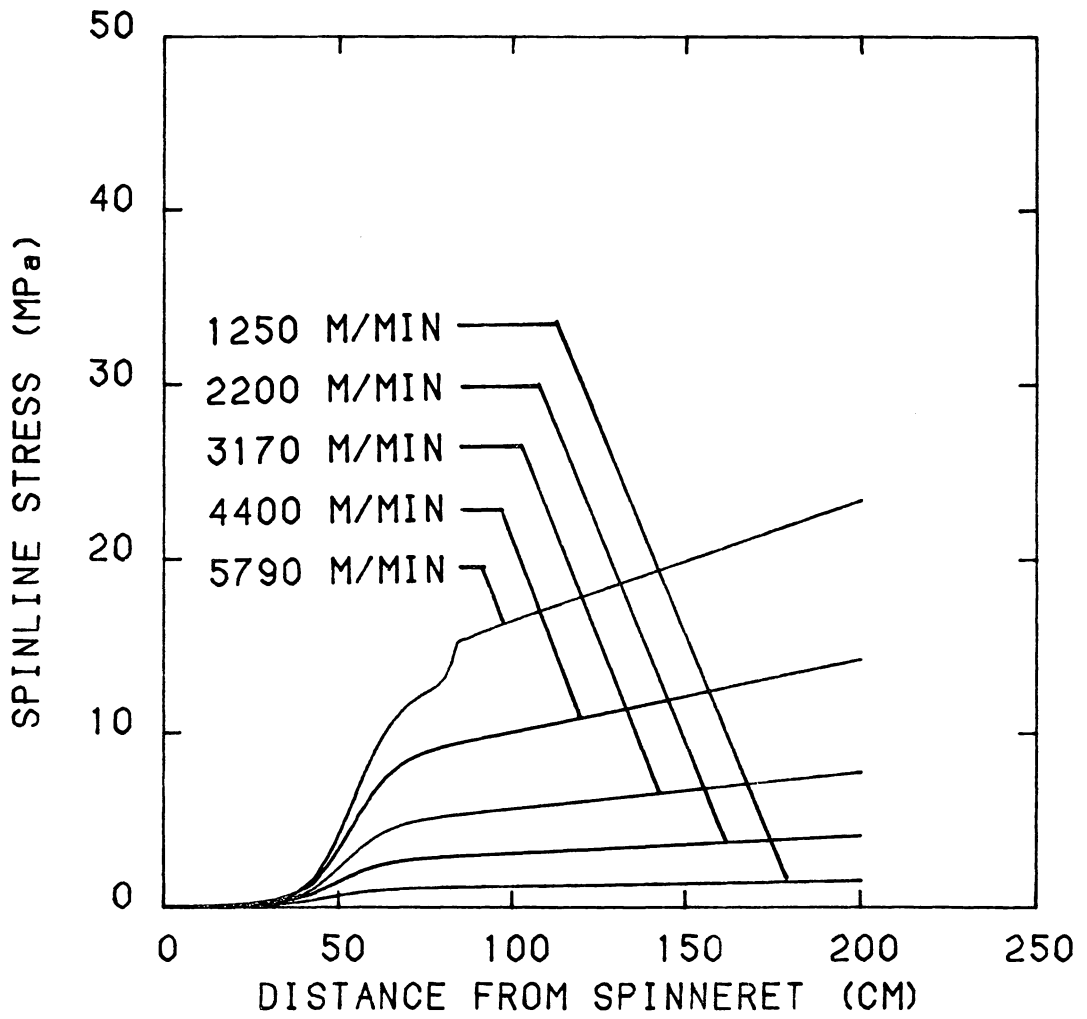


Figure 5.24 Predicted spinline stress profiles for BHS with a mass throughput of 5.069 g/min.

Figures 5.25 to 5.28 show the predicted amorphous orientation factor (f_a) profiles as a function of distance from the spinneret. These profiles indicate that f_a increases rapidly in the region of rapid filament drawdown and then levels out at a certain value. The values of f_a being higher for higher take-up speeds than for lower take-up speeds. The values of f_a are relatively higher for higher molecular weight resin, BHS, and a lower mass throughput of 3 g/min compared to those for the lower molecular weight resin, CN9984, and throughput of 5 g/min, respectively. The value of f_a corresponding to critical speed is about 0.25 indicating that even relatively small value of amorphous orientation factor is sufficient to cause stress induced crystallization to occur on the spinline. It is of interest to note that the model predicts a sudden increase in amorphous orientation factor when the critical velocity is exceeded. This seems to result from the rapid drawdown in the diameter profile and may not be realistic due to the fact that no account is taken in the calculations of the conversion of oriented chains to crystalline material. This effect should tend to deplete the amorphous regions of oriented molecules.

Figures 5.29 to 5.32 show corresponding crystalline index profiles. These profiles indicate that at lower take-up speeds no crystallization takes place on the spinline but at speeds higher than the critical speed online crystallization appears. With further increase in spinning speed beyond the critical speed the onset of crystallization occurs closer to the spinneret and at higher temperature. At the highest spinning speeds the development of the profile is nearly instantaneous. Crystallization

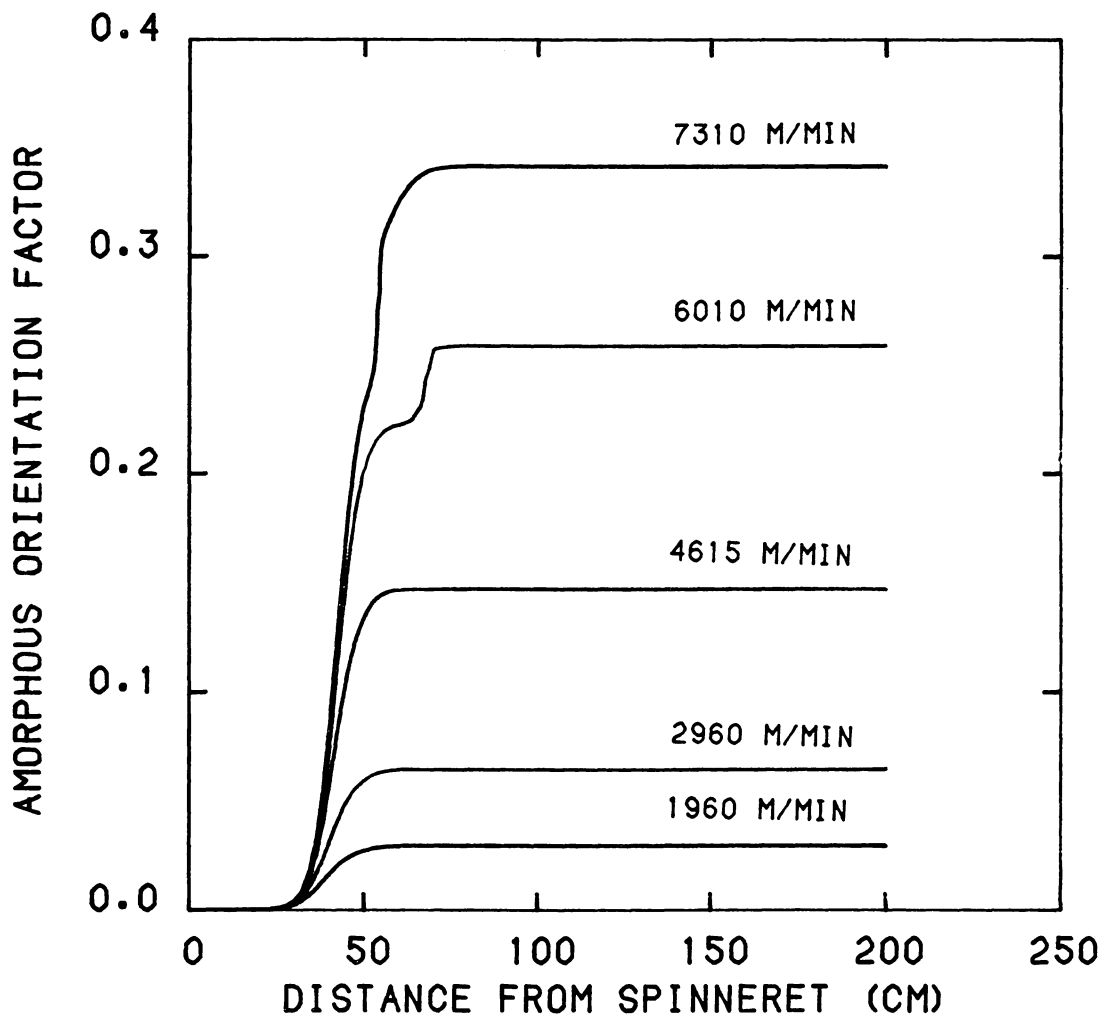


Figure 5.25 Predicted amorphous orientation factor profiles for CN9984 with a mass throughput of 3.073 g/min.

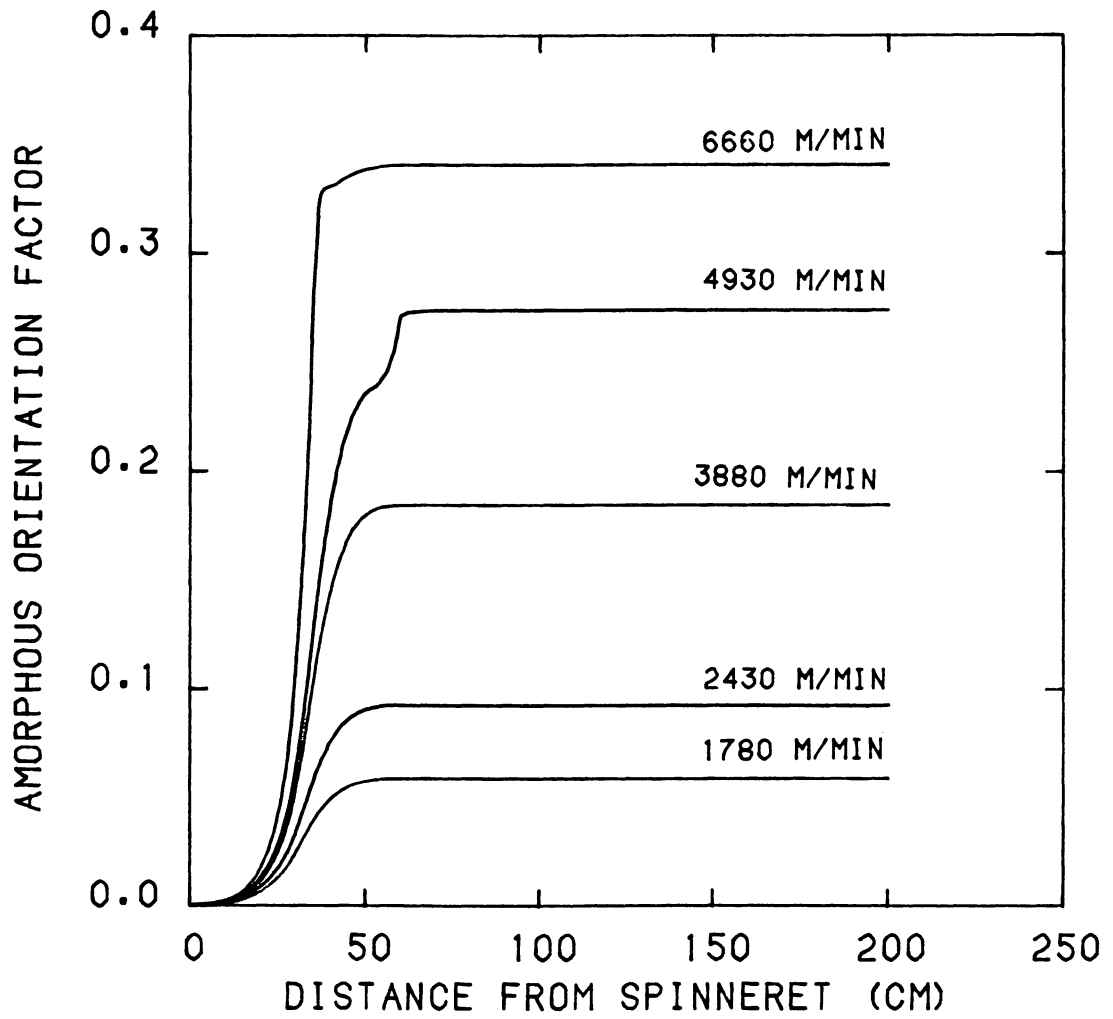


Figure 5.26 Predicted amorphous orientation factor profiles for BHS with a mass throughput of 2.993 g/min.

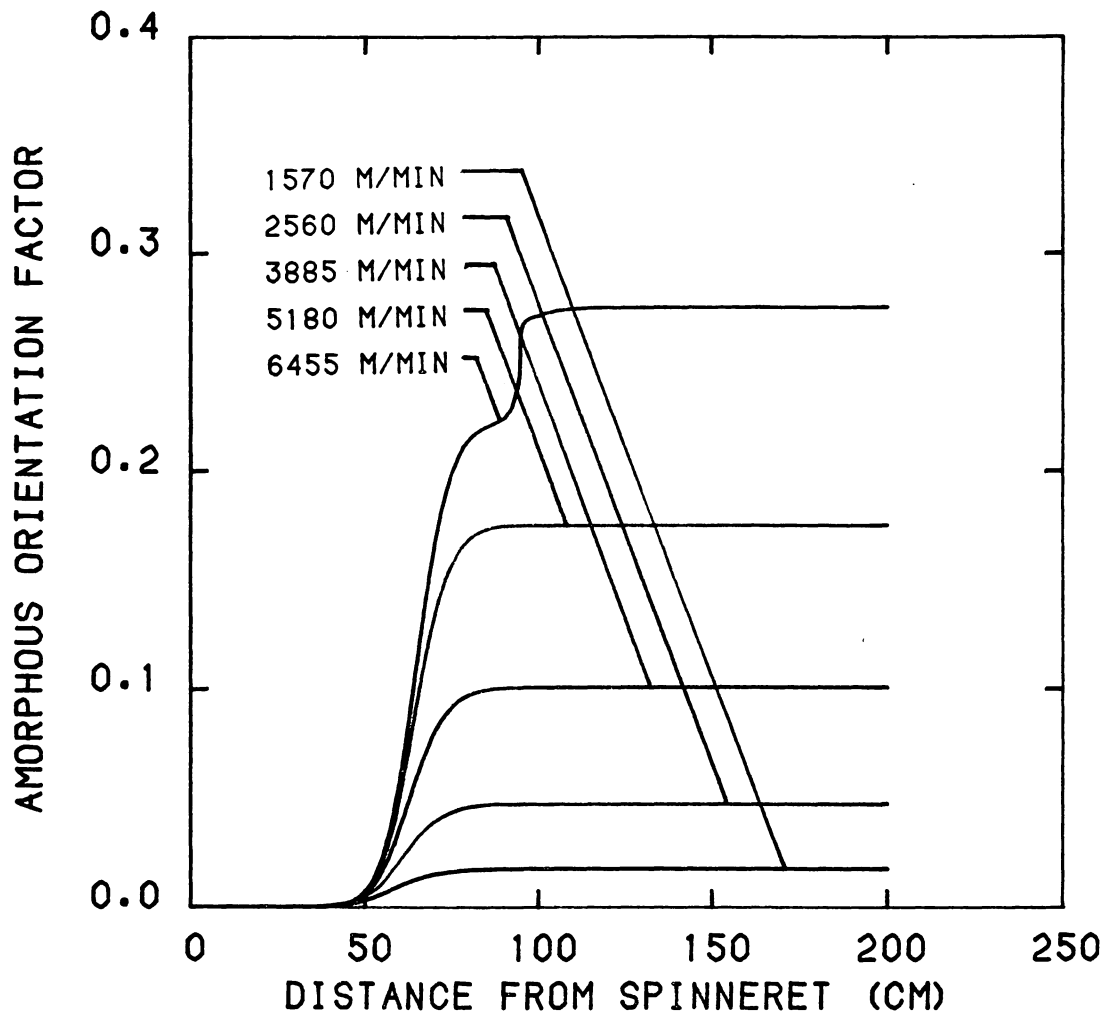


Figure 5.27 Predicted amorphous orientation factor profiles for CN9984 with a mass throughput of 5.154 g/min.

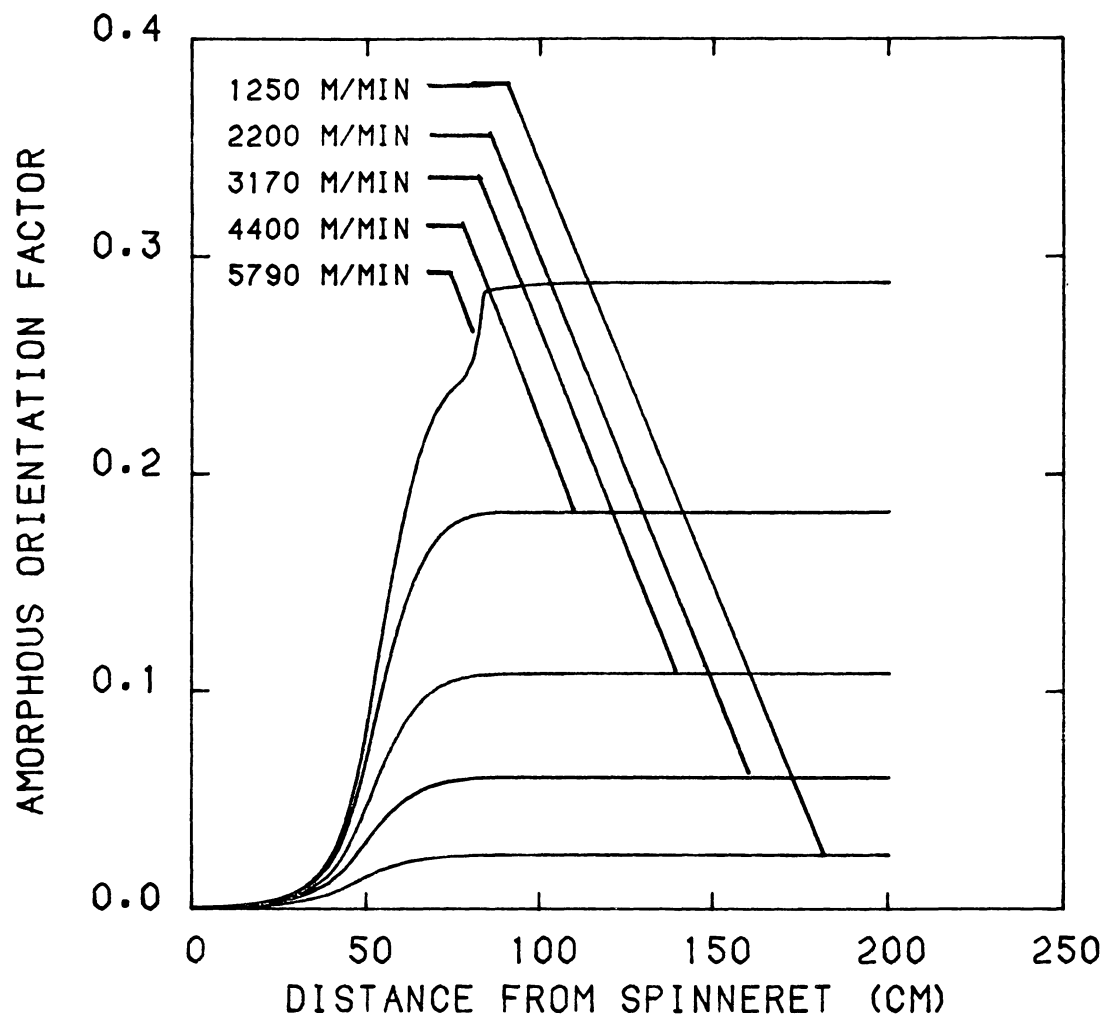


Figure 5.28 Predicted amorphous orientation factor profiles for BHS with a mass throughput of 5.069 g/min.

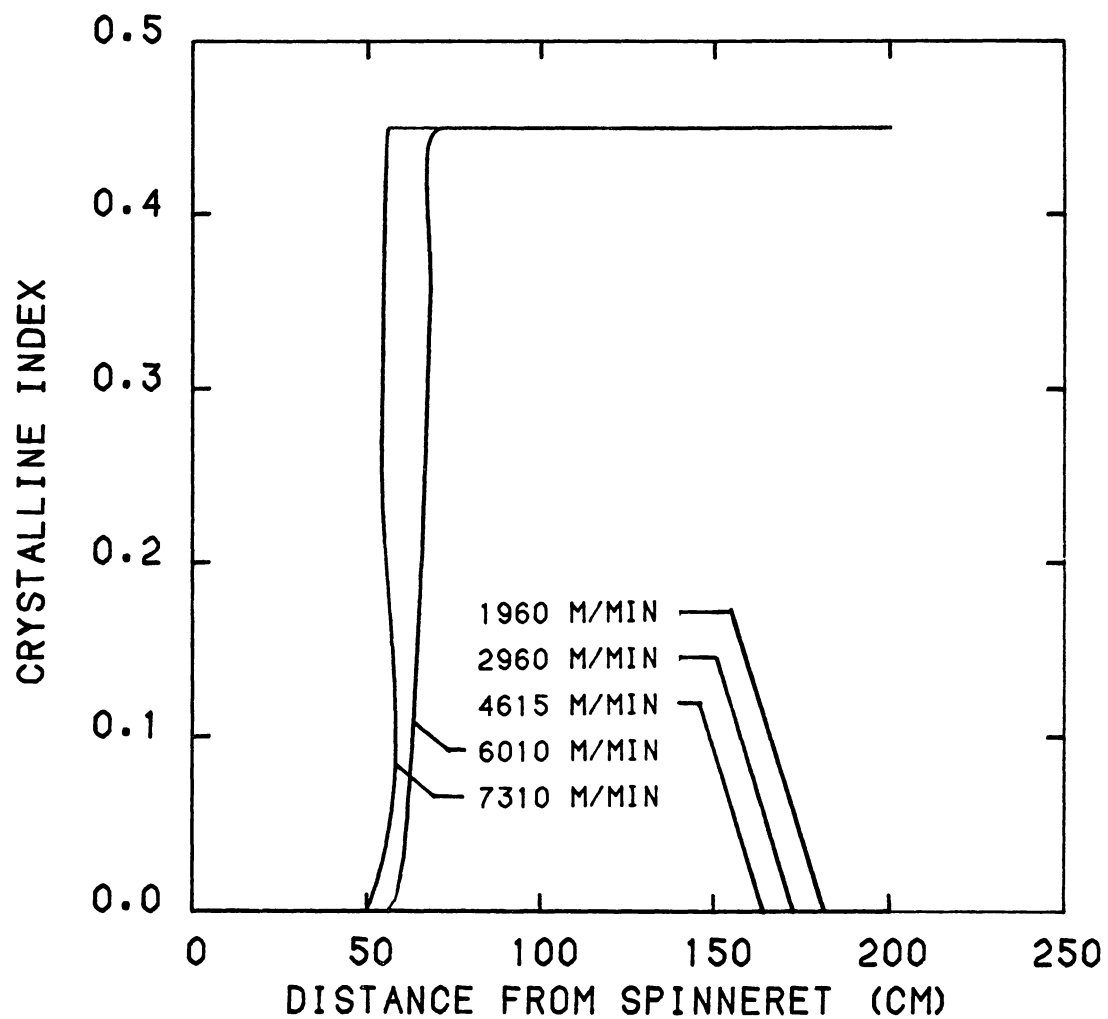


Figure 5.29 Predicted crystalline index profiles for CN9984 with a mass throughput of 3.073 g/min.

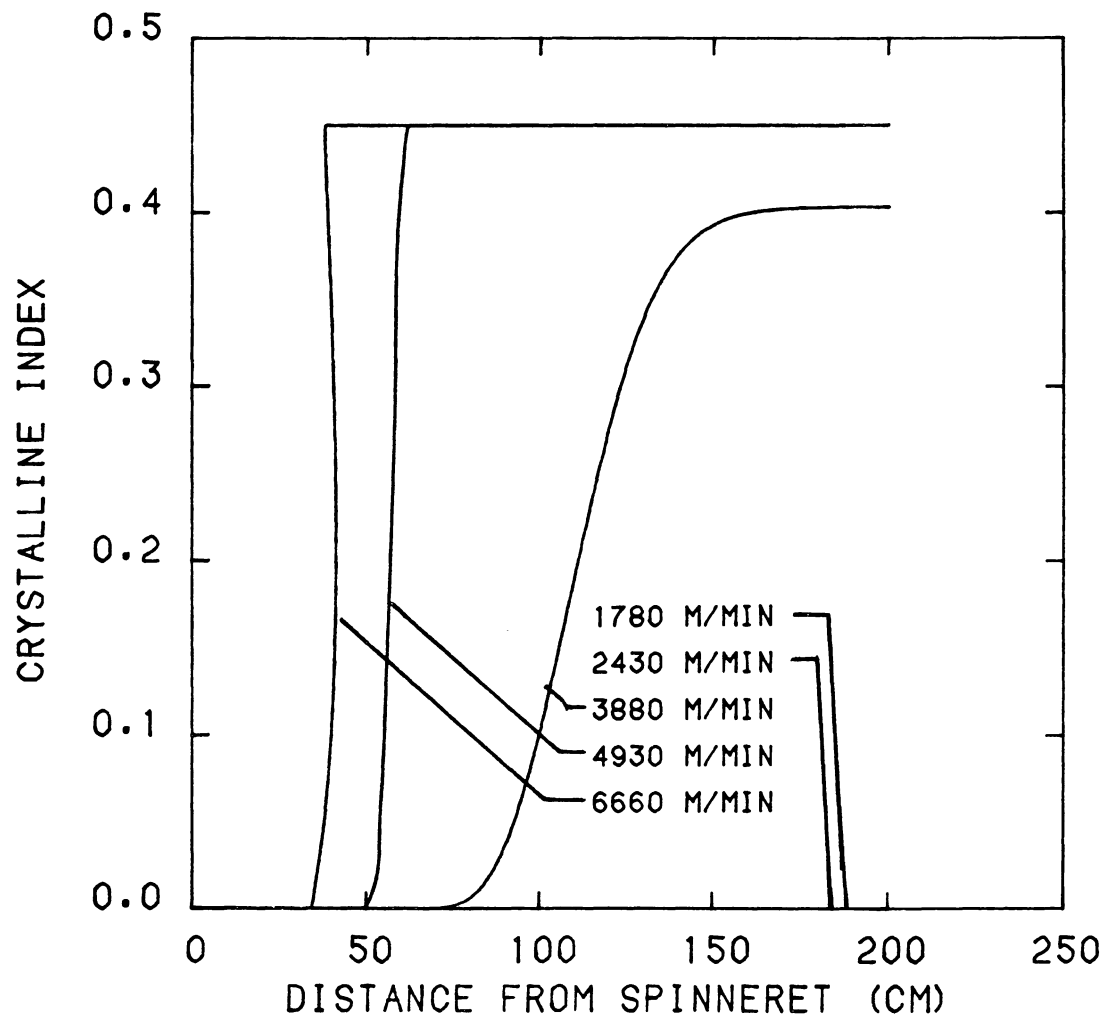


Figure 5.30 Predicted crystalline index profiles for BHS with a mass throughput of 2.993 g/min.

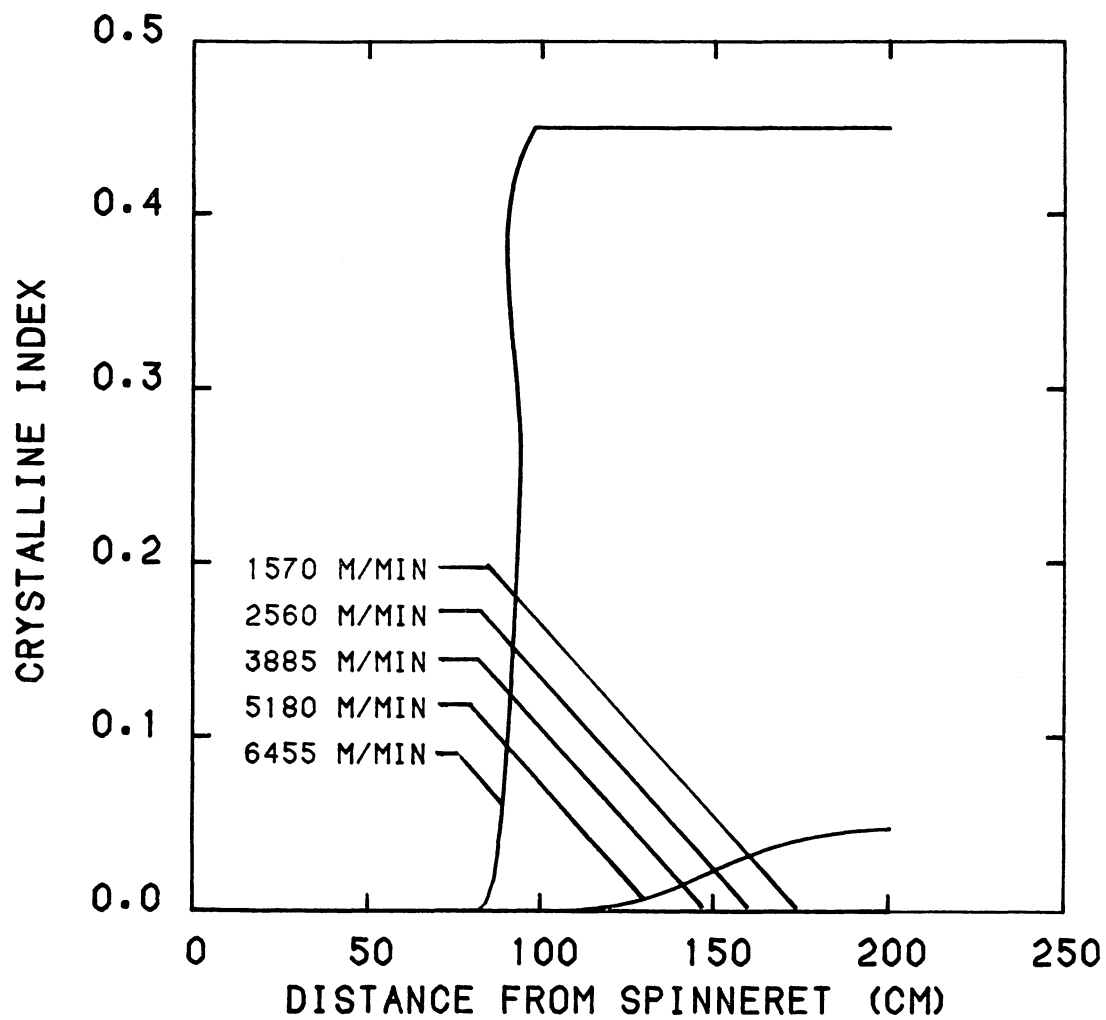


Figure 5.31 Predicted crystalline index profiles for CN9984 with a mass throughput of 5.154 g/min.

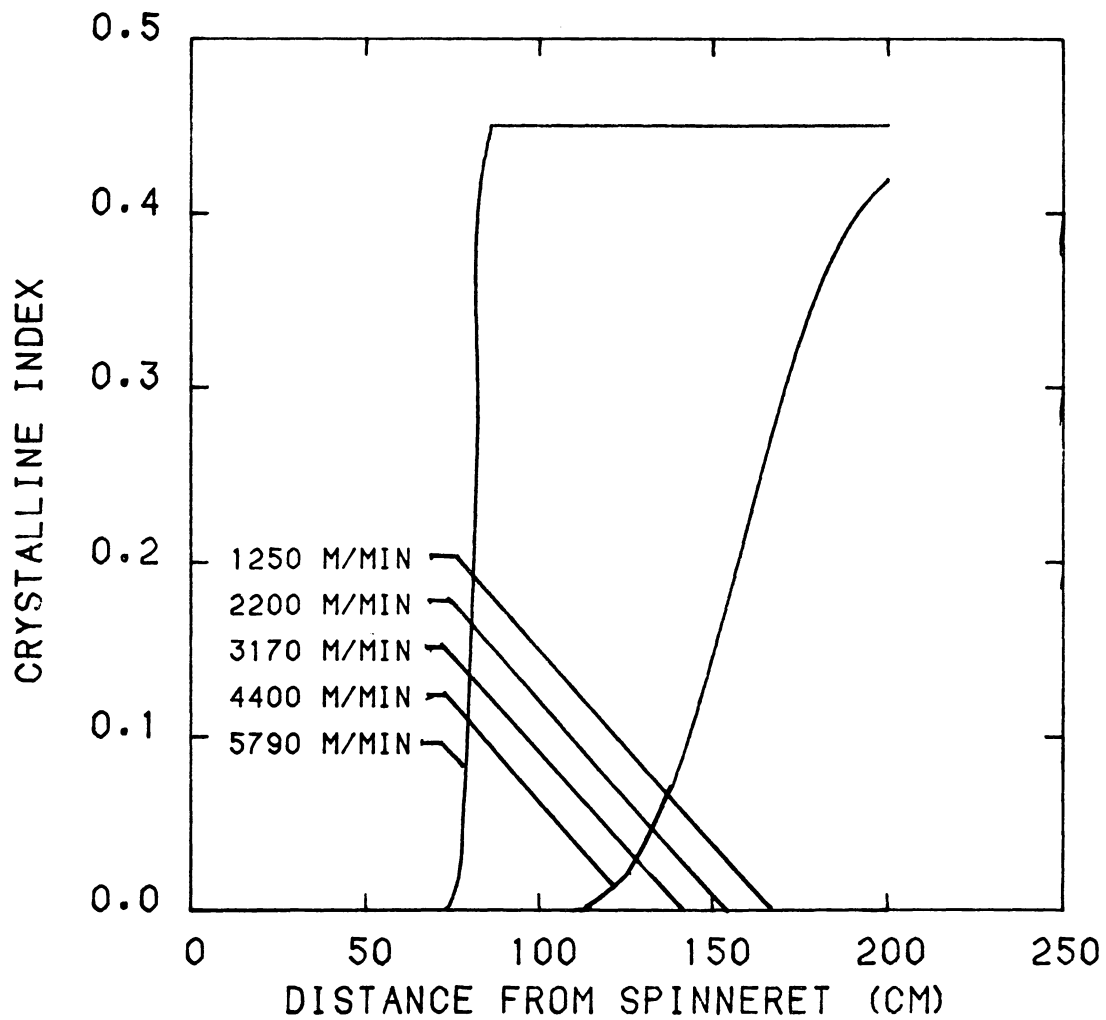


Figure 5.32 Predicted crystalline index profiles for BHS with a mass throughput of 5.069 g/min.

appears at lower speeds for the BHS resin and 3 g/min throughput conditions than that for the CN9984 resin and 5 g/min conditions.

Figures 5.33 to 5.36 show the predicted birefringence profiles as a function of the distance from the spinneret. At take-up speeds lower than critical speeds the birefringence gradually increases and levels out at a certain value. At higher speeds a substantial jump in birefringence occurs corresponding to the onset of crystallization on the spinline. The birefringence subsequently levels out at a much higher value than that for the lower take-up speeds. At still higher speeds the jump in birefringence occurs closer to the spinneret, indicating that crystallization is occurring closer to the spinneret and at higher temperature. The jump in birefringence occurs at relatively lower speeds for the BHS resin and 3 g/min throughput conditions than for the CN9984 resin and 5 g/min conditions.

Discussions

Initial attempts at mathematical modeling of the melt spinning process (78,79,81,83-86,274-278) were mostly for PET and involved low to intermediate spinning speeds. Considering the small element of spinline to be cylindrical the problem can be handled rigorously using the cylindrical co-ordinate (r, θ, z) system. However, in the above studies basic assumptions were made to make the problem mathematically tractable. The problem was reduced to solving ordinary differential equations rather than partial differential equations involved in rigorous analysis. Typically, the assumptions were that the process is at steady state, variations occur only in the z direction (or variation

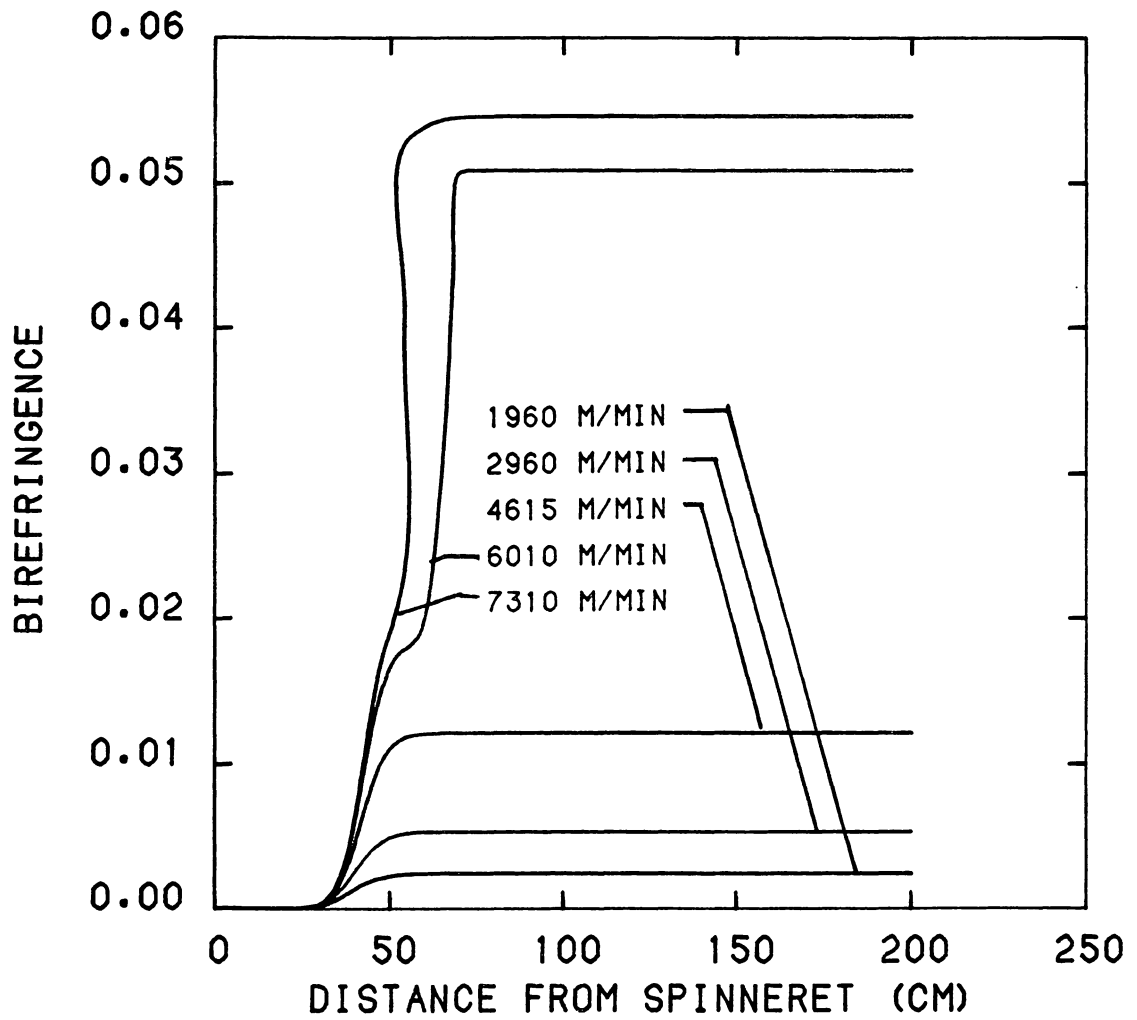


Figure 5.33 Predicted birefringence profiles for CN9984 with a mass throughput of 3.073 g/min.

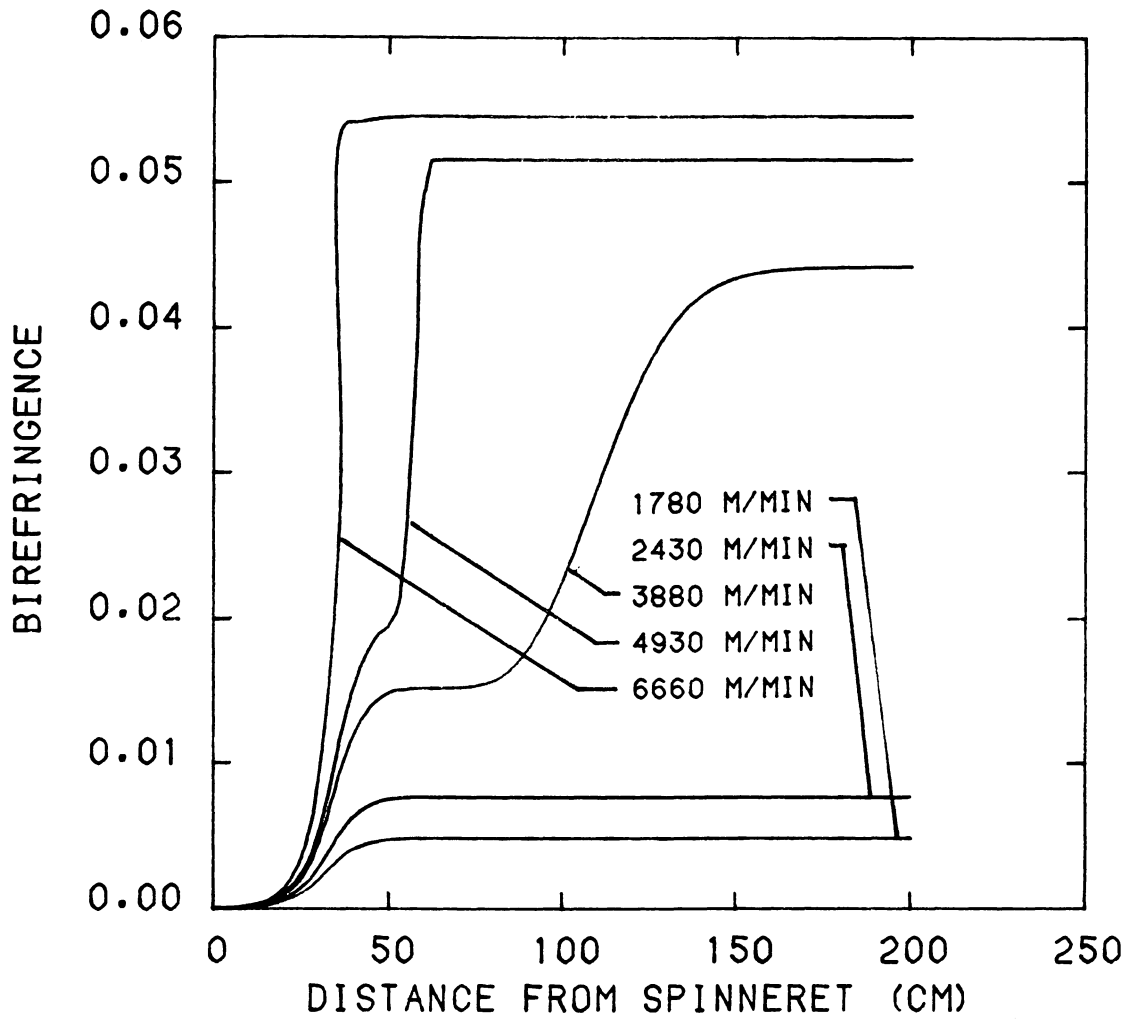


Figure 5.34 Predicted birefringence profiles for BHS with a mass throughput of 2.993 g/min.

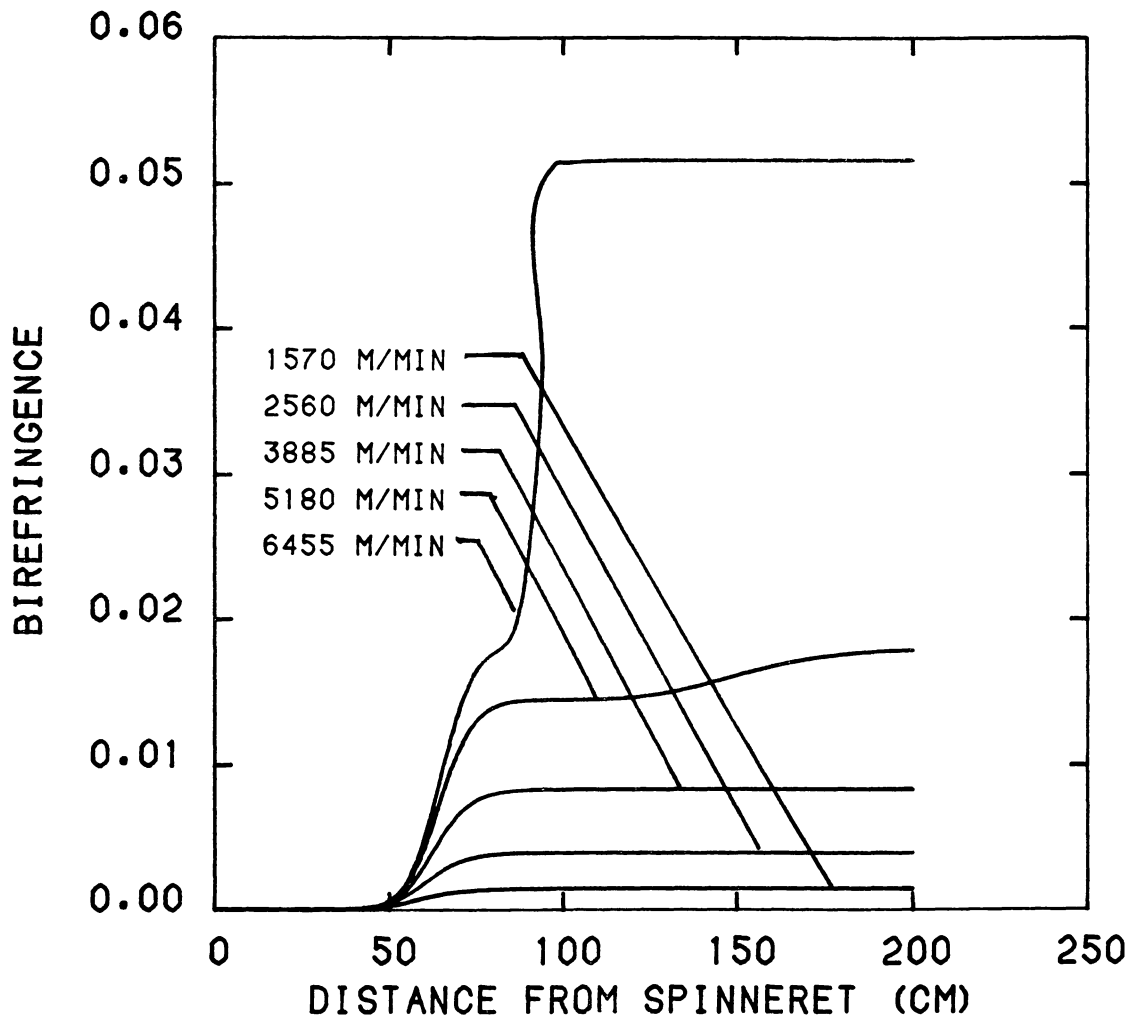


Figure 5.35 Predicted birefringence profiles for CN9984 with a mass throughput of 5.154 g/min.

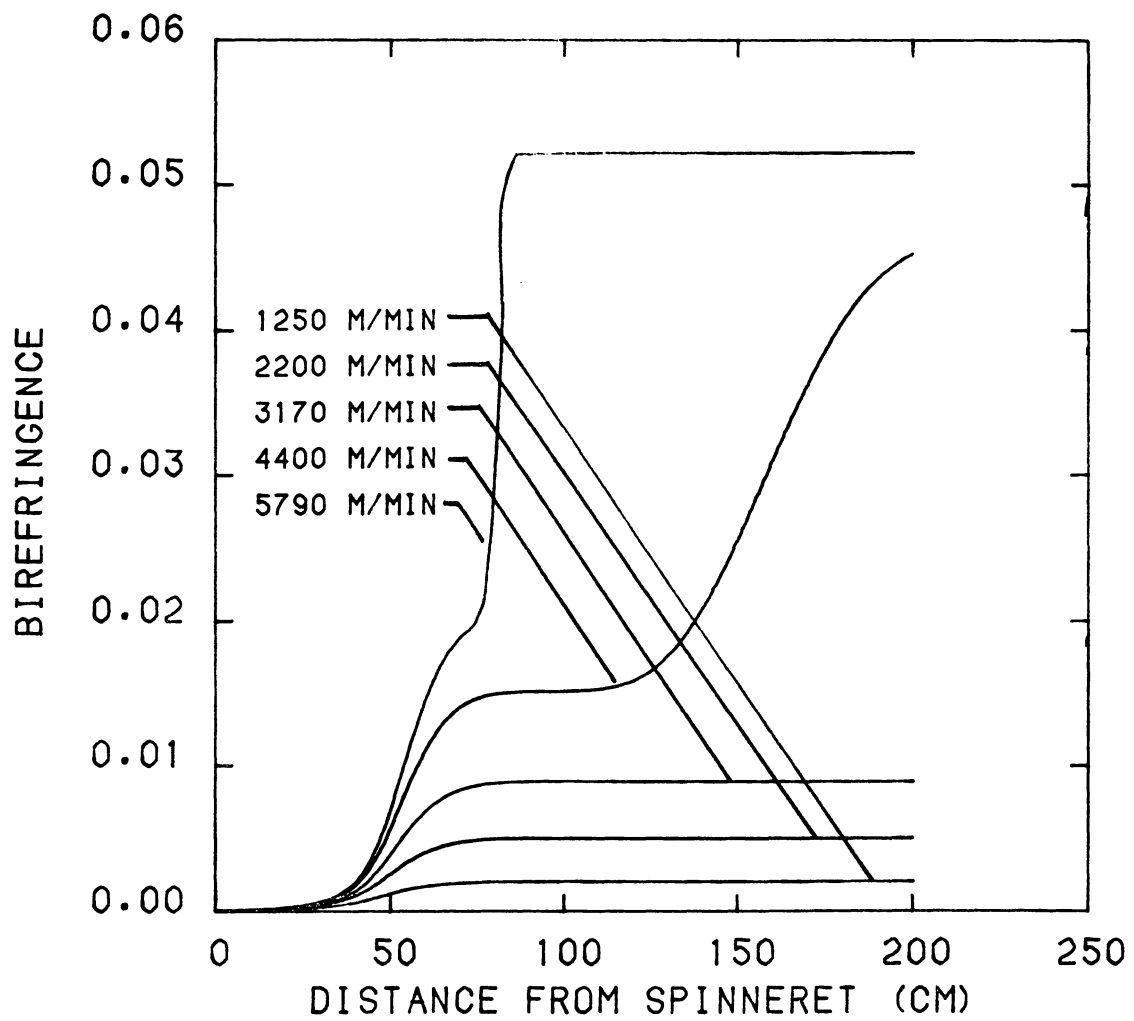


Figure 5.36 Predicted birefringence profiles for BHS with a mass throughput of 5.069 g/min.

in r and θ directions are negligible), only convective heat transfer is involved (conduction, radiation and heat generation due to crystallization are negligible), etc. Only Yasuda (275-277) attempted to consider radial variations along with variation in the z direction. The solutions of the model were presented in terms of velocity, diameter, temperature and stress profiles which mostly describe dynamics of the process. The mechanical properties of melt spun fibers largely depend on structure formation in the filaments. Predictions for structure development were not possible from the above studies because crystallization kinetics were not included in the model.

Kikutani (87) proposed a model based on the earlier model of George (85), but with a crystallization kinetics model including temperature and orientation effects for high speed spinning of PET. Katayama and Yoon (291) also have tried to introduce the polymer crystallization aspects in their simulation of high speed spinning of PET. Kase (292) has attempted to analyse the differences due to steady state condition and transient behavior of high speed spinning of PET through mathematical modeling. The effect of crystallization has also been considered by Koyama et al. (34). Bai (32) followed Kikutani's approach, and he predicted a "necking" region beyond about 4000 m/min which was coincident with experimental observations. Zieminski (33) attempted a generalized version of the model first proposed by Kikutani (87) for the high speed spinning behavior of crystallizable polymers. He applied the model to high speed melt spinning of nylon-66 and polypropylene. He concluded that orientation induced crystallization occurred in nylon-66 for spinning speeds greater than 4000 m/min. He showed that the effects

were relatively insensitive to variation in Avrami exponent in the range of 1 to 3 and to the variation of the exponent of crystallinity in elongational viscosity expression in the range from 2 to 12.

As described in detail in an earlier section, the model considered in this study is basically similar to that of Ziemiński (33). In addition to the basic equations of the model, the input physical properties, key parameters and relationships for nylon-6 from the literature are very important. Accuracy of these properties, parameters and relationships as a function of key variables is very critical in getting accurate predictions from the model. Therefore it is important to consider the accuracy of these data and the errors that may exist.

Various important properties and/or parameters involved in modeling of high speed melt spinning include density, specific heat, elongational viscosity, modulus, heat transfer coefficient, drag coefficient, crystallization rate constant, etc. Of these, the first four are material properties, and, in the literature they are described as a function of temperature and/or crystallinity and/or molecular weight of the polymer. Of the four material properties the density, specific heat and modulus have been recognized as strong functions of temperature and rather insignificant dependence on molecular weight. The strong temperature dependence of these properties have been studied experimentally over a broad range of temperature and have been reported independently by various researchers. The relations for density from the literature (133) are given in equations (5-4) and (5-5). From these relations the calculated density ranges from about 1.06 g/cm^3 (for nylon-6 melt at temperature of 280°C) to 1.17 g/cm^3 (for totally

crystalline nylon-6 at 25°C; theoretical densities for γ and α crystalline forms are 1.17 and 1.23 g/cm³, respectively). Thus, the maximum conceivable error band for density is about 0.09 g/cm³ in density values. The actual error band must be much smaller than this. In any case the error in density would seem to introduce errors in computations of only a few per cent at most. The relations for specific heat (282) likewise are given in equations (5-18) and (5-19). From these relations the specific heat ranges from about 0.40 (for solid nylon-6 at 25°C) to about 0.65 (for nylon-6 melt at 280°C). Thus, again the maximum error band in specific heat may not be greater than about ± 0.13 from the arithmetic average of the range, and it is likely to be much smaller. Consequently, the error bands in density and specific heat are unlikely to cause a major difference in the model predictions. The discrete data for Young's modulus versus temperature (285) were interpolated since there is no mathematical relationship reported in the literature. The temperature range of measurement was from 25 to 240°C and several nylon-6 resins with different molecular weights were studied. It was reported that modulus is strongly affected by temperature and relatively less dependent on molecular weight of resin. The data appear to be reliable to about two significant figures. In any case, the modulus enters the calculation only in formulating the stress level developed along the spinline and resulting birefringence. Thus, again the errors involved in the use of these data are unlikely to cause major differences in the model predictions.

There are no reported direct experimental measurements of elongational viscosity of condensation polymers including nylon-6,

nylon-66 and PET. For these fiber forming polymers it is assumed that elongational viscosity is independent of extension rate and is equal to the Trouton viscosity. Further, it is assumed that these polymer melts are Newtonian fluids and their Trouton viscosity is considered to be three times the shear viscosity. Experimental rheological measurements of the shear viscosity of nylon-6 have been reported in the literature and they indicate that it behaves like a Newtonian fluid i.e. shear viscosity is relatively independent of shear rate in the range of measurements. Also the shear viscosity is reported as a strong function of temperature and molecular weight. The relationships established for temperature dependence of shear viscosity involved measurements over a narrow range of temperature (generally above T_m). In melt spinning, however, polymer extensional flow occurs over a very wide range of temperature; therefore, an extrapolation of shear viscosity data to lower temperatures was made to arrive at the elongational viscosity at temperatures below the melting temperature. A change of Arrhenius form to WLF form for temperature dependence was also assumed. It is likely that this extrapolation may lead to far different calculated values of elongational viscosity compared to actual values and, consequently, may lead to major differences in the model predictions.

Heat transfer coefficient and drag coefficient involved in melt spinning have been studied extensively in the literature using both simplified and rigorous approaches. Heat transfer coefficient has significant indirect role in the melt spinning problem. It has a major effect on the temperature profile of the filament, and quite a few properties described above have strong temperature dependence. The heat

transfer coefficient (h) relation of Kase and Matsuo (78) used in the model is given in equation (5-16). It is in terms of spinning variables and consequently error associated with h will result both from errors associated with calculated spinning variables and from errors in the coefficients of equation (5-16). It is difficult to assess the potential errors that may therefore be introduced by the heat transfer relationship. However, it should be possible to estimate the relative error from a comparison of calculated and experimental temperature profiles. This will be considered in some detail in the next chapter.

Drag coefficient also has a significant role in that the rheological force prediction, particularly at high speeds, is strongly affected by air drag force contributions. The rheological force primarily determines spinline stresses which affect molecular orientation. The air drag coefficient of Sakiadis (46) given in equation (5-10) was used in the present calculations. It is possible that Sakiadis' formulation may not be accurate for present study but this will not be known until the comparison of predictions with some experimental data is made. If necessary, several other formulae for C_d are available from literature which could be tried.

There are no reported experimental evaluations of crystallization rate constant measured under conditions of molecular orientation involved in melt spinning. A major reason for unavailability of these data is that under molecular orientation the crystallization rate is so high that experimental measurements are quite difficult. Another reason is that it is difficult to devise experiments that will allow measurements of crystallization rate under a range of both orientation

and temperature. Ziabicki (12) has proposed a simple empirical relationship expressing crystallization rate constant as temperature and orientation dependent given in equation (5-31). In using this relationship all parameters involved have been reported experimentally except the weighting factor c for orientation dependence. It seems that the form and numerical values involved in this factor c are very critical in getting realistic crystalline index and total birefringence profiles, but this information is essentially unavailable in the literature. The values used in the present predictions were little more than guesses. Thus, this may represent a major source of differences between experimental results and predictions from the model.

In Chapter 3 the experimental diameter, temperature and birefringence profiles have already been shown. In this chapter the predicted profiles from the model with input properties for nylon-6 from literature have been reported. A discussion of which of the key properties are accurately known from the literature followed the model predictions. It is reasonable now that the predictions be compared with experimental results in order to check the validity and quantitative success of the model. It is also clear from the above discussion that there may be some opportunity to improve the model by using the experimental profiles in appropriate ways. These aspects are developed in detail in the next chapter.

CHAPTER 6

IMPROVEMENT OF MODEL THROUGH EXPERIMENTAL RESULTS

Comparison of Model Predictions Based on Literature Parameters to Online Experimental Profiles

In order to check the validity and quantitative success of the model, a comparison of model predictions and online experimental profiles was made in terms of diameter profiles (shown in Figures 6.1 to 6.4), temperature profiles (shown in Figures 6.5 to 6.8) and birefringence profiles (shown in Figures 6.9 to 6.12). In all the figures points are experimental results and solid lines give the corresponding model predictions.

From these comparisons it is clear that the trends predicted by the model are qualitatively consistent with experimental results as far as the effects of take-up speeds, mass throughput and molecular weight of resin are concerned. At high take-up speeds necking in the diameter profile, rise in temperature of the filament and a jump in the birefringence of the filament was both predicted and observed. Increase of mass throughput from 3 g/min to 5 g/min causes a reduction in the rate of drawdown in diameter with distance, a reduction of the rate of temperature decrease with distance and lower birefringence values. Increasing the molecular weight of the resin causes faster drawdown in the diameter profile, higher birefringence values but temperature profiles are relatively independent of molecular weight. Each of these features was qualitatively predicted by the model and also observed experimentally. However, as far as quantitative comparison is concerned,

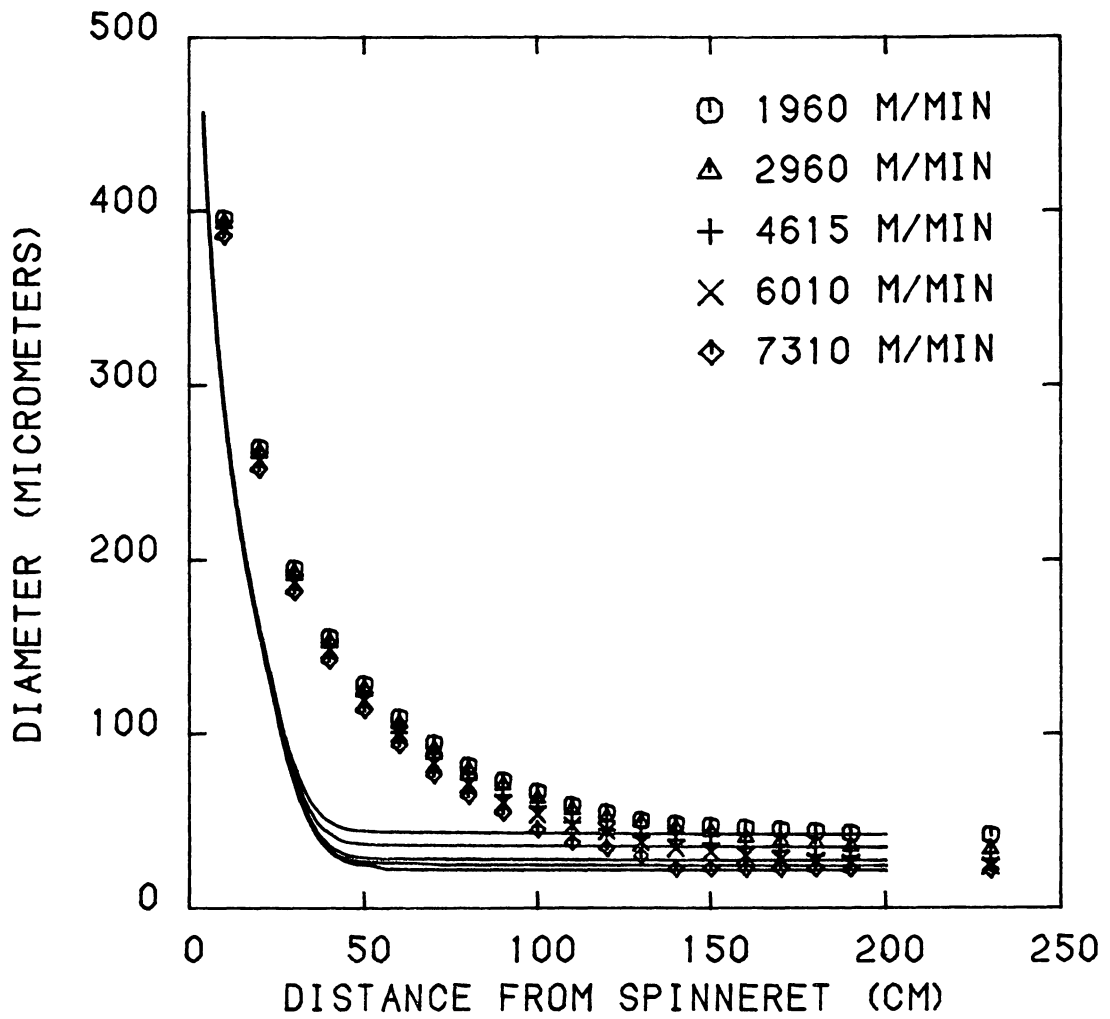


Figure 6.1 Comparison of predicted and experimental diameter profiles for CN9984 with a mass throughput of 3.073 g/min.

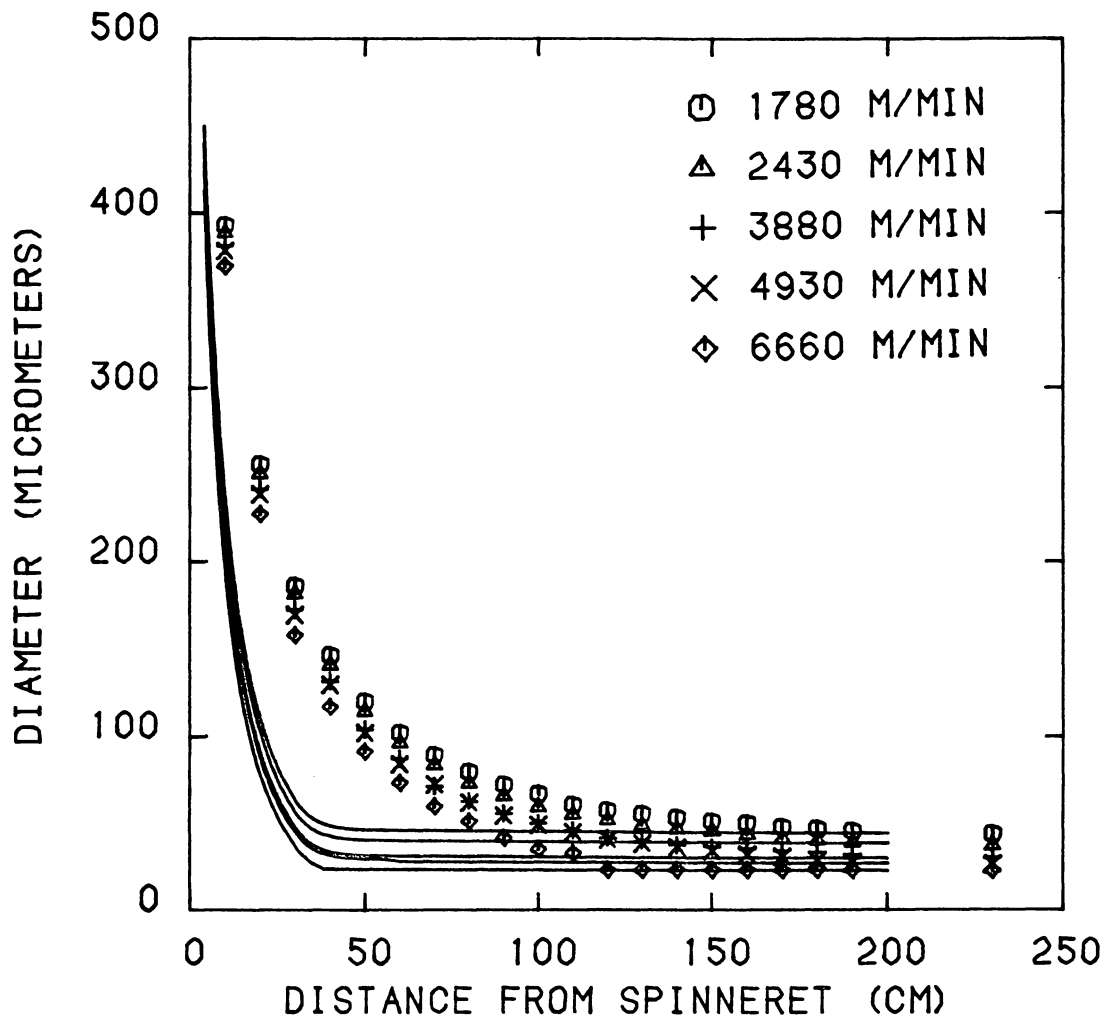


Figure 6.2 Comparison of predicted and experimental diameter profiles for BHS with a mass throughput of 2.993 g/min.

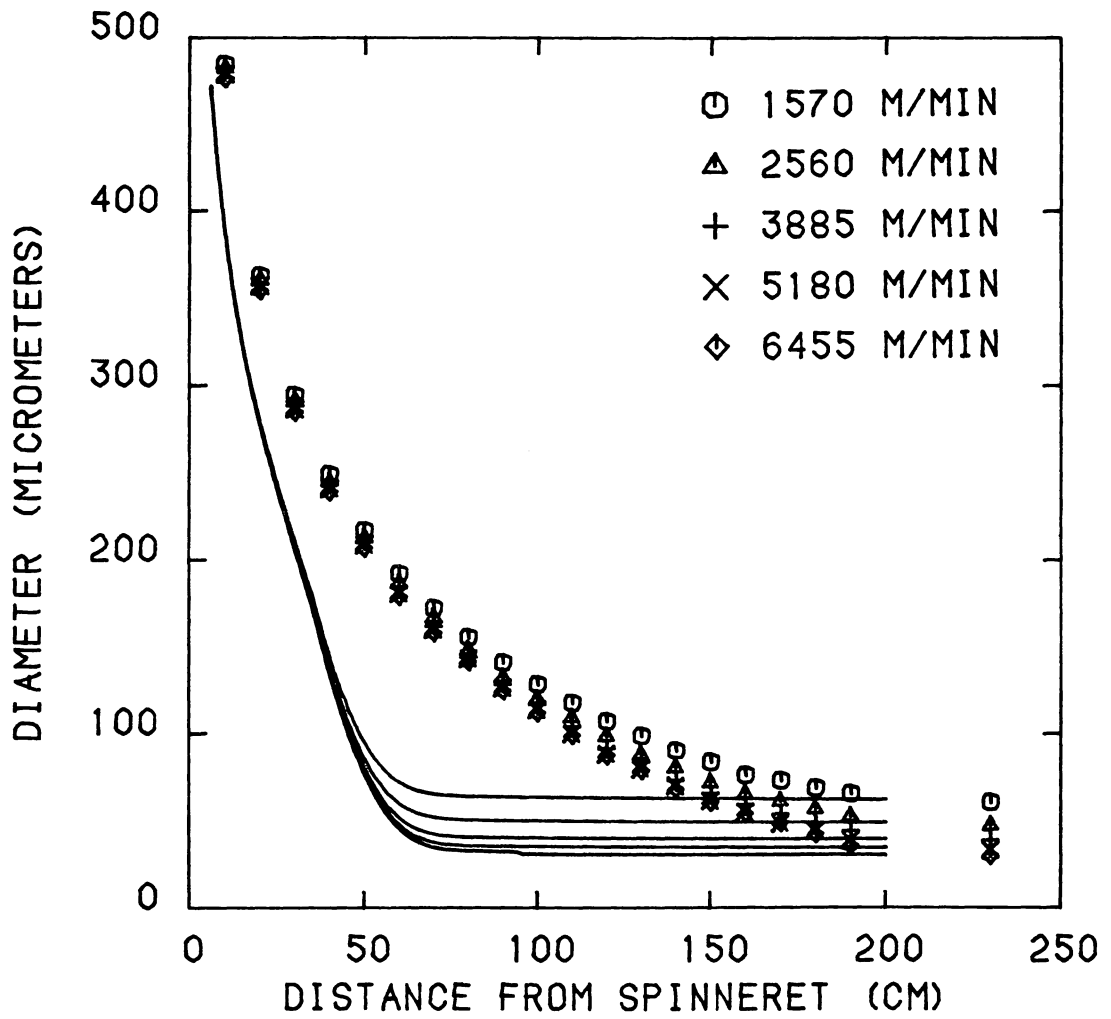


Figure 6.3 Comparison of predicted and experimental diameter profiles for CN9984 with a mass throughput of 5.154 g/min.

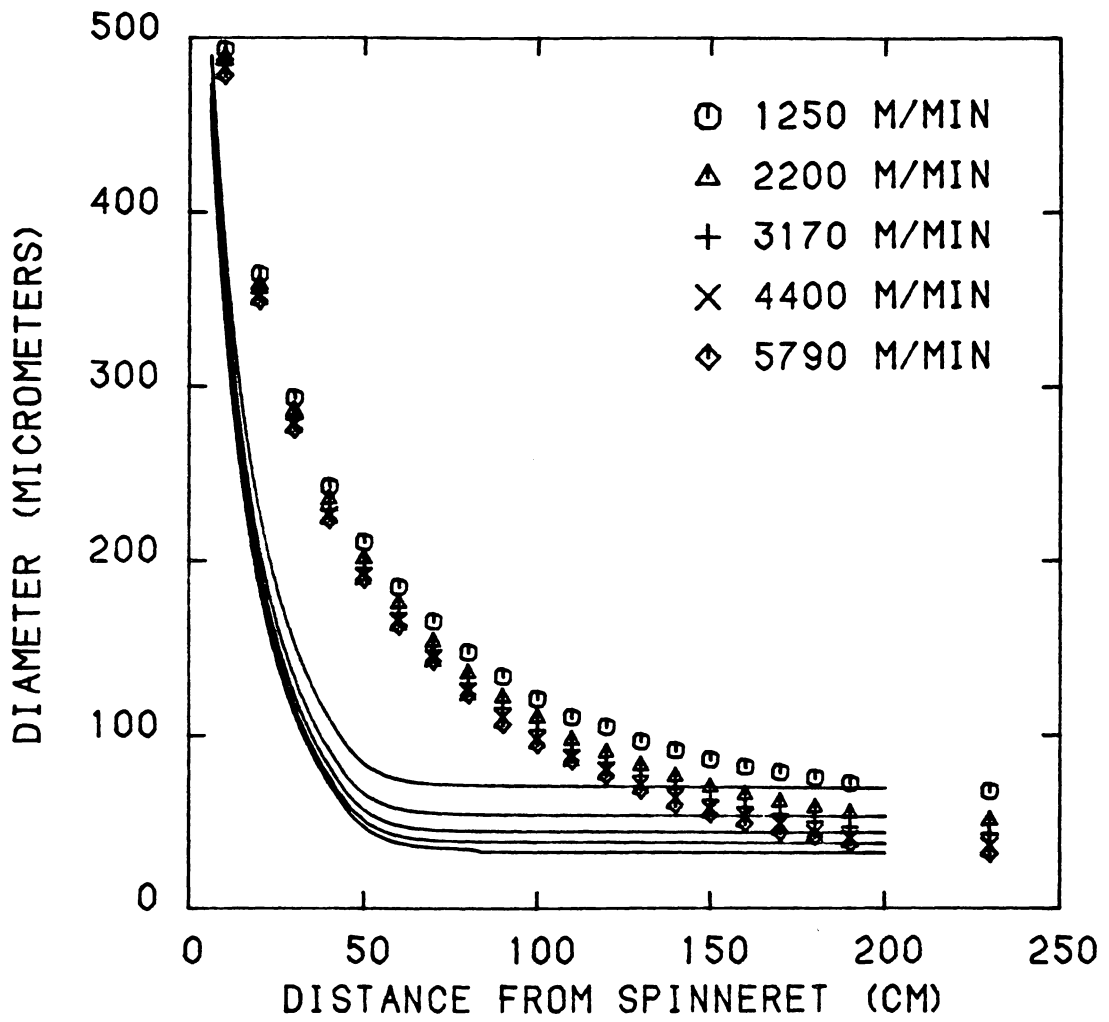


Figure 6.4 Comparison of predicted and experimental diameter profiles for BHS with a mass throughput of 5.069 g/min.

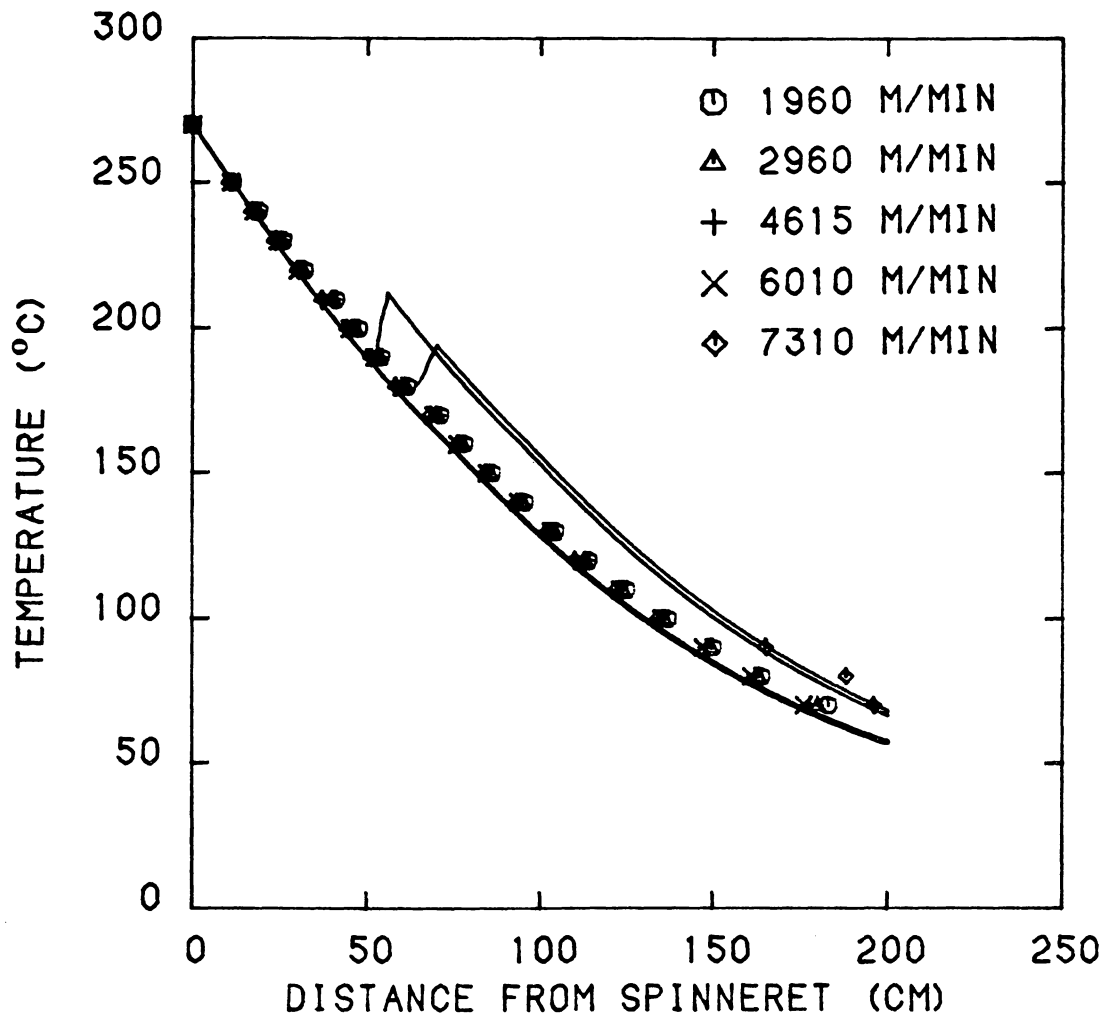


Figure 6.5 Comparison of predicted and experimental temperature profiles for CN9984 with a mass throughput of 3.073 g/min.

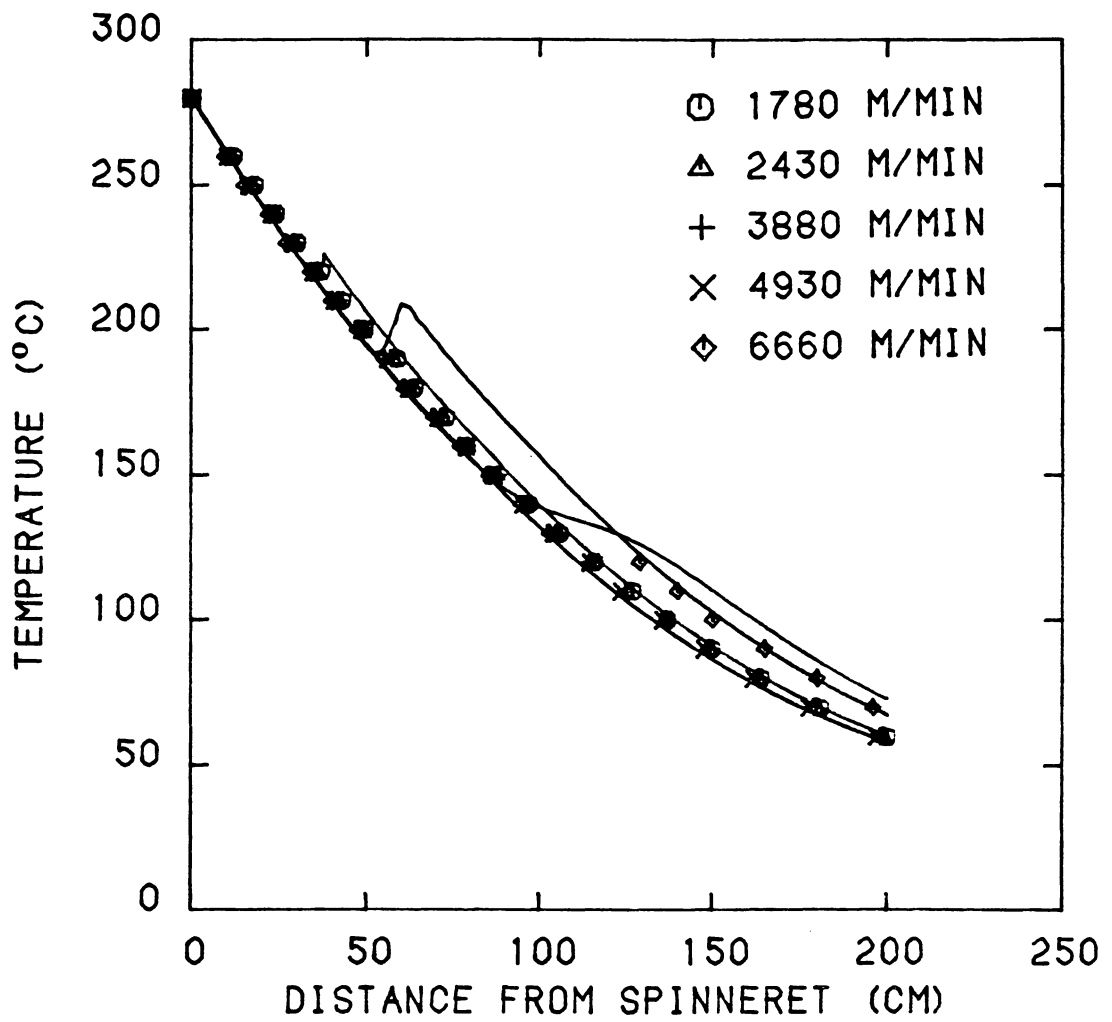


Figure 6.6 Comparison of predicted and experimental temperature profiles for BHS with a mass throughput of 2.993 g/min.

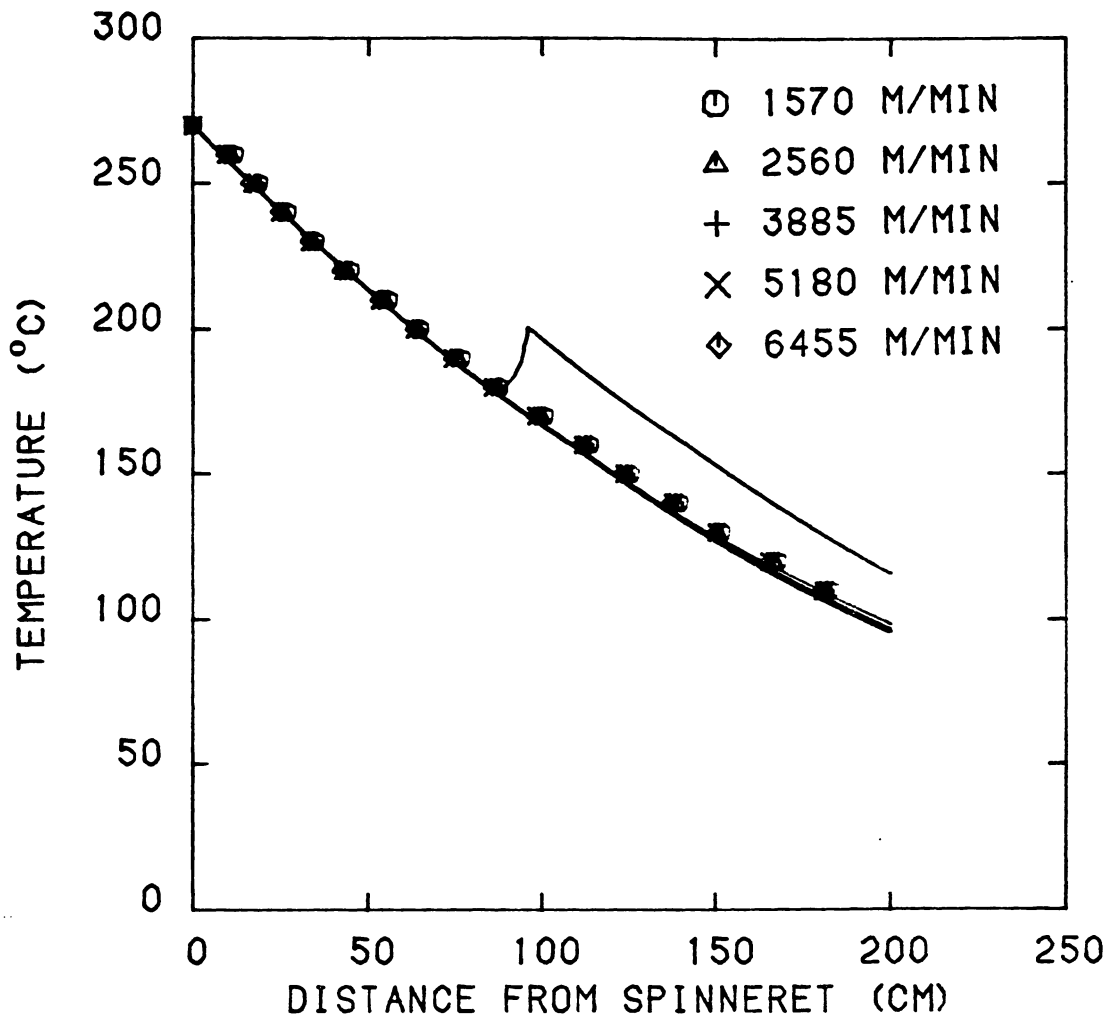


Figure 6.7 Comparison of predicted and experimental temperature profiles for CN9984 with a mass throughput of 5.154 g/min.

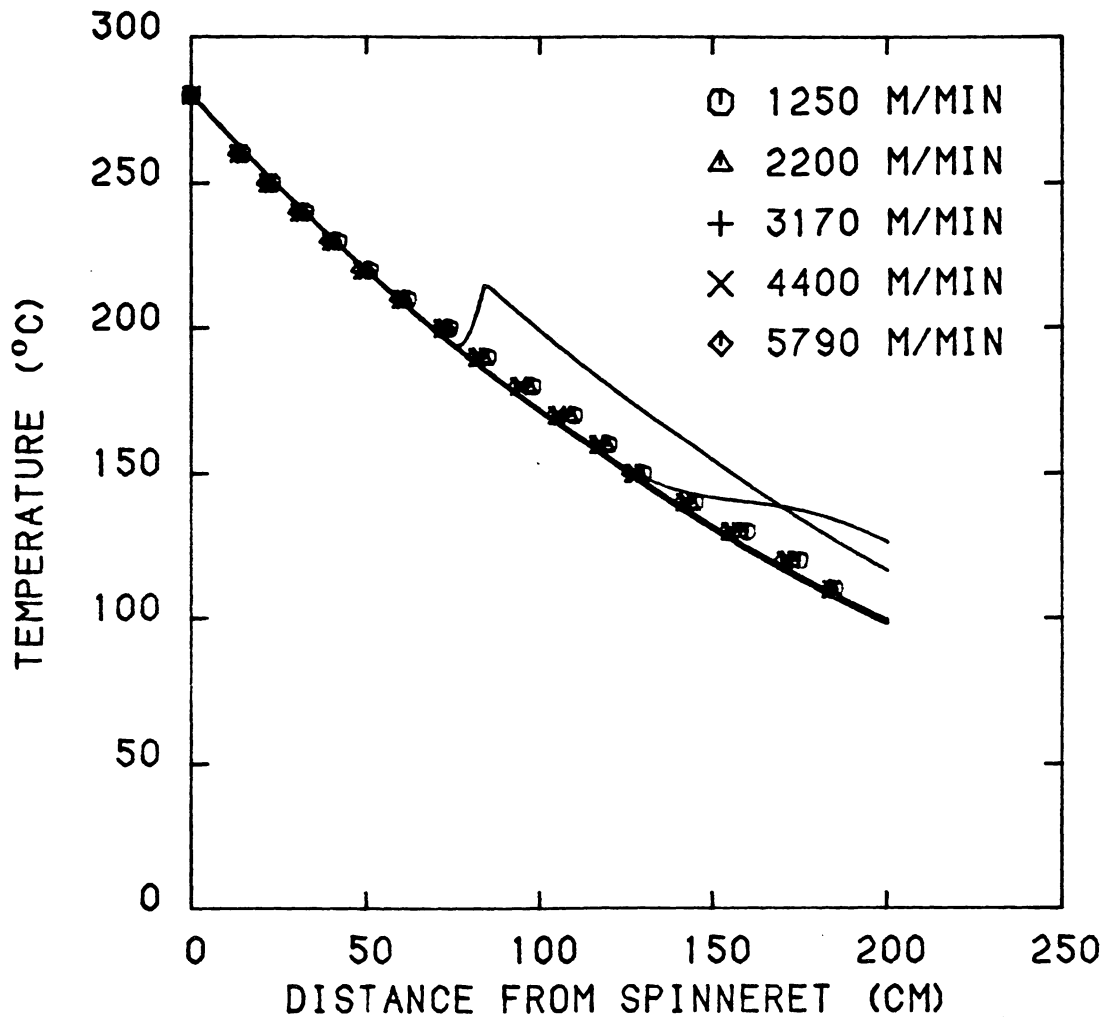


Figure 6.8 Comparison of predicted and experimental temperature profiles for BHS with a mass throughput of 5.069 g/min.

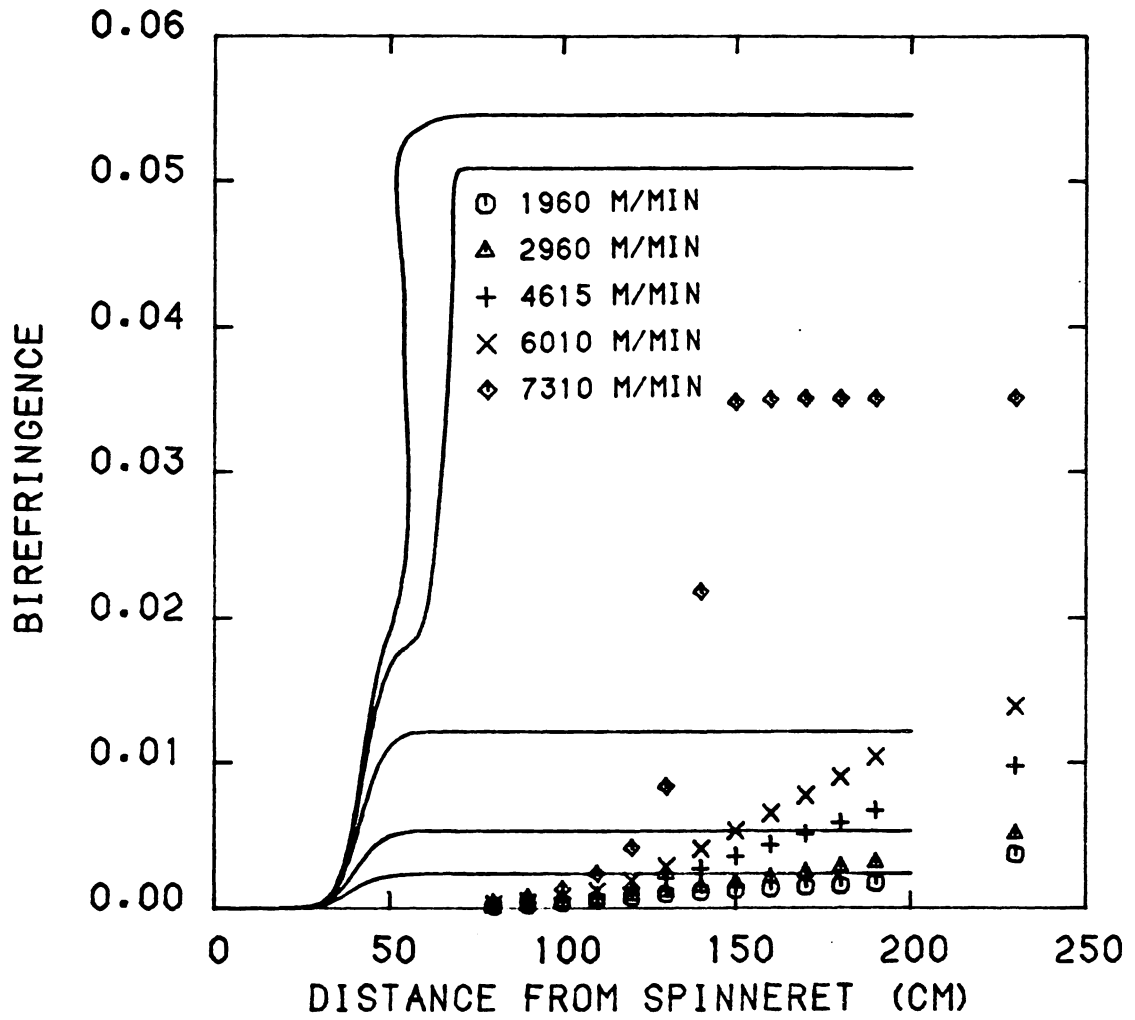


Figure 6.9 Comparison of predicted and experimental birefringence profiles for CN9984 with a mass throughput of 3.073 g/min.

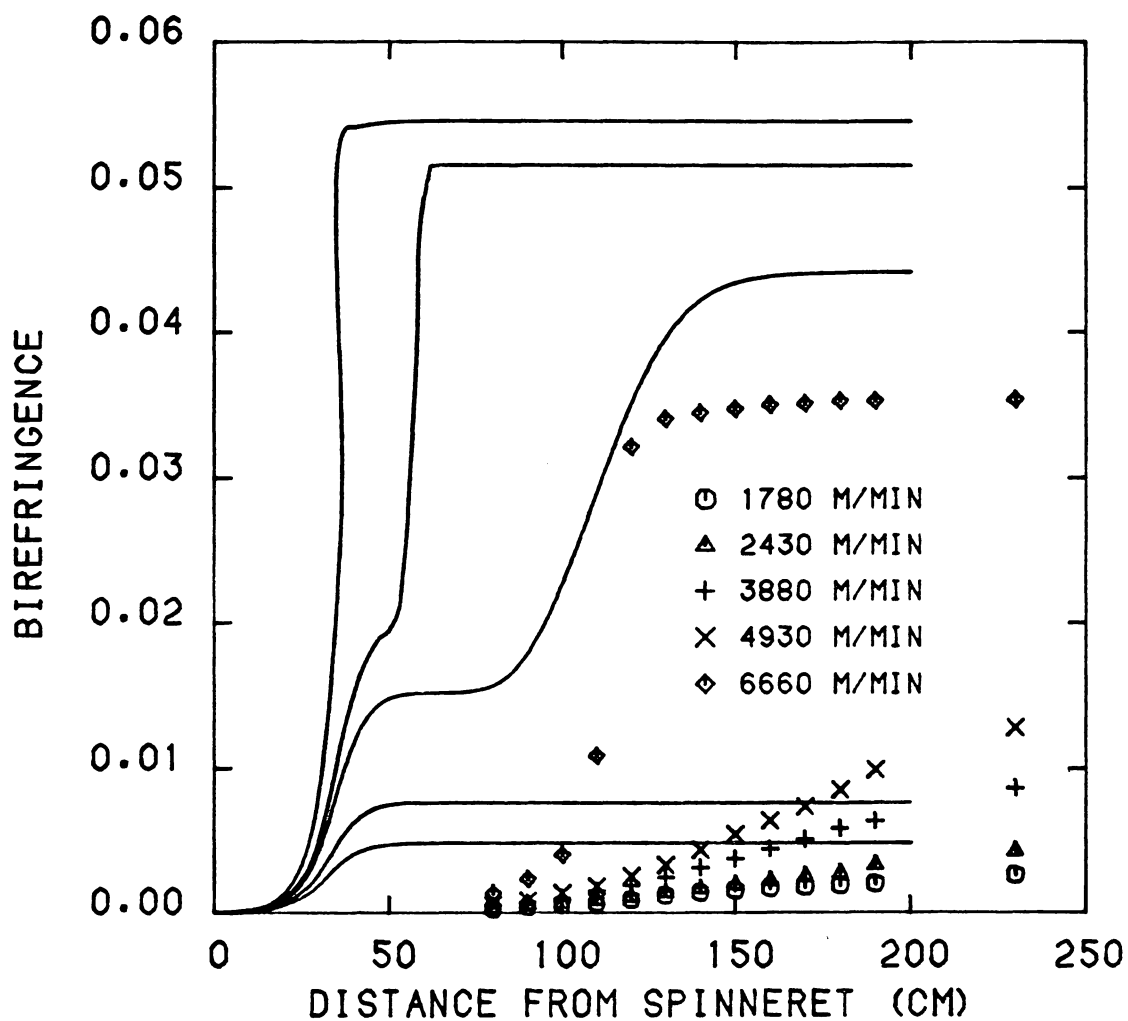


Figure 6.10 Comparison of predicted and experimental birefringence profiles for BHS with a mass throughput of 2.993 g/min.

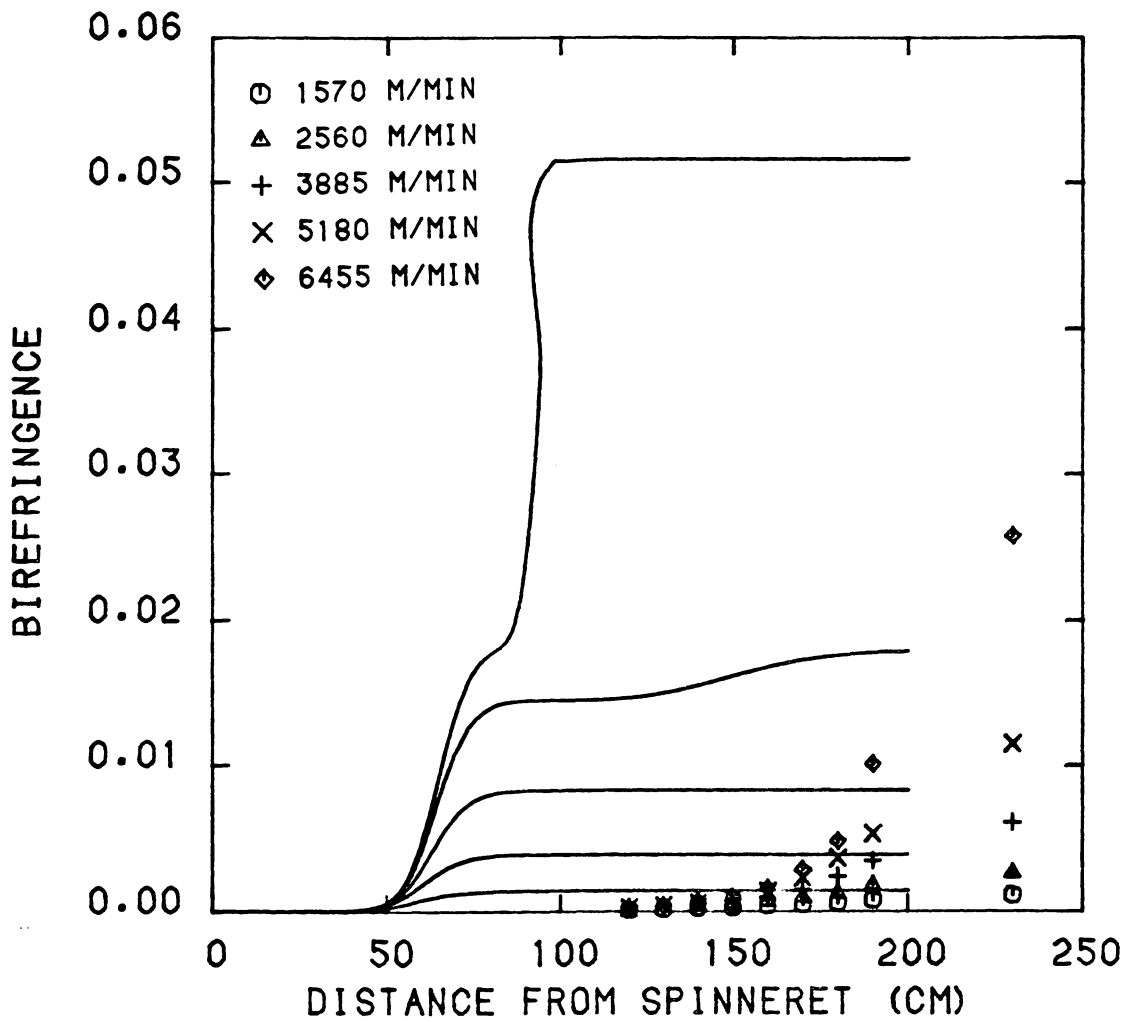


Figure 6.11 Comparison of predicted and experimental birefringence profiles for CN9984 with a mass throughput of 5.154 g/min.

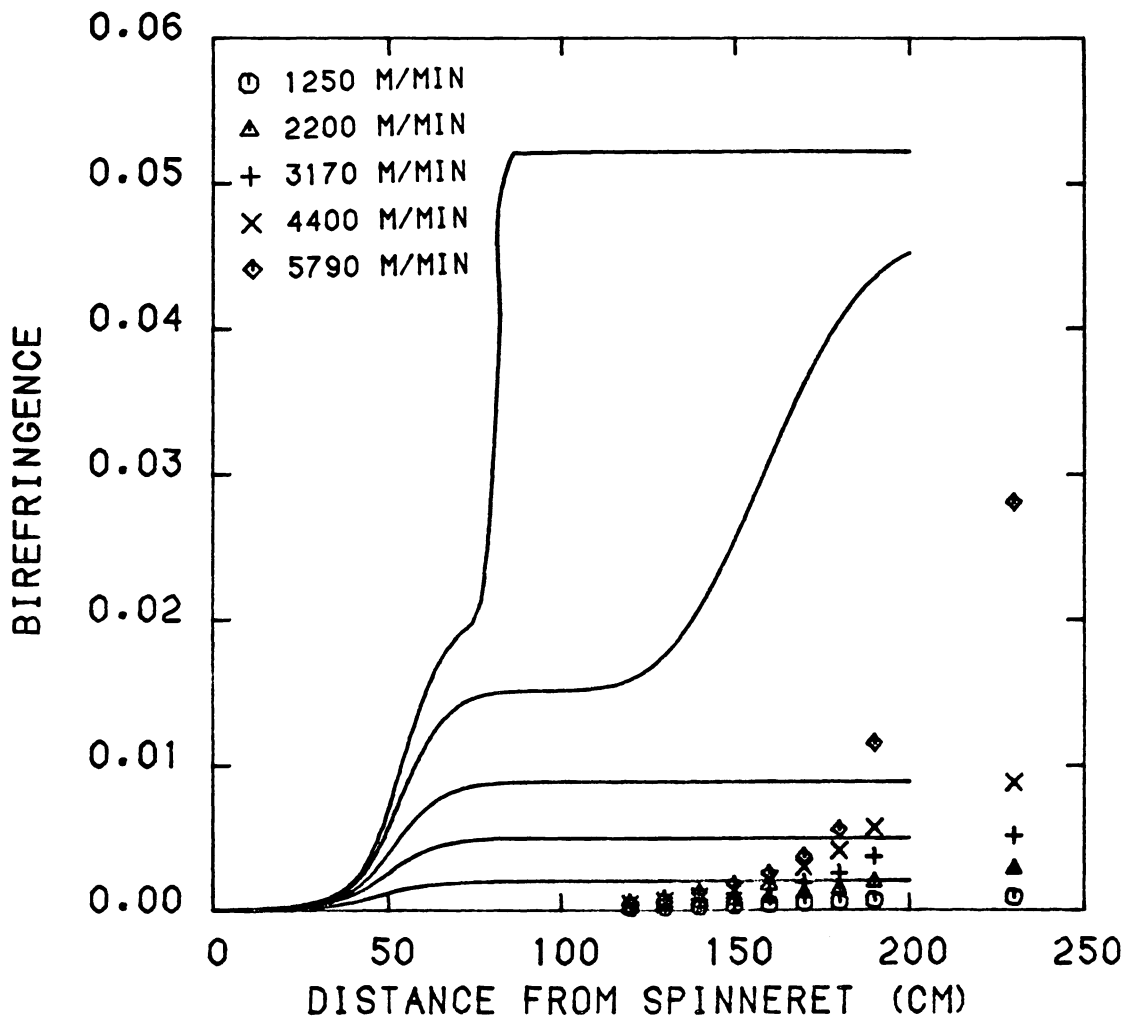


Figure 6.12 Comparison of predicted and experimental birefringence profiles for BHS with a mass throughput of 5.069 g/min.

in all cases the model predicts relatively faster drawdown and jump in birefringence closer to the spinneret indicating earlier onset of crystallization than is observed experimentally. Temperature profiles at lower speeds are in good agreement with model predictions and birefringence is overpredicted by the model at high speeds. These differences are due to inaccuracies in the physical properties input from the literature and perhaps to inadequacies in the model. The former seems more likely since the qualitative features of the experimental results are all reproduced by the model. The input physical properties and relations are not precise for the nylon-6's studied here, but were estimated by combining various results in the literature, as discussed in the preceding chapter. Further, even small errors in input properties can lead to substantial effects on the profiles predicted by the model. It is possible to bring the model predictions into better agreement with the experimental results by finding appropriate functions for critical properties such as elongational viscosity, heat transfer coefficient, crystallization rate constant, etc. This was attempted through an inversion procedure which is described in the following sections.

Analytical Inversion Procedure

As pointed out in previous sections, the mathematical model is used to calculate temperature, velocity and stress profiles from the process conditions and literature relations for key parameters and properties. The most important inputs in relation to the diameter and temperature profiles are extensional viscosity and heat transfer coefficient, which are key relations for dynamics of the process. These literature

relations are generally developed over restricted ranges of variables because of experimental design and limitations. In the so-called "inversion procedure" the procedure of the mathematical model is reversed in that the experimentally measured diameter (or velocity) and temperature profiles and a single tension measurement in the bottom region of the spinline are used to calculate the extensional viscosity and heat transfer coefficient relations over the region of measured temperature-deformation rate plane. The scope of this procedure is both broad and limited. It is broad in the sense that there are no restrictions on the process conditions (especially on spinning speeds) for the experimental profiles. However, the procedure is limited to smooth regions of measured profiles because the key step in the inversion procedure is to calculate velocity and temperature gradients through derivatives of the velocity and temperature profiles, respectively. Thus, process conditions involving online crystallization leading to a plateau in the temperature profile or necking in the diameter profile will lead to errors (or singularities) in calculating the gradients. These conditions or regions must be avoided. Having discussed the scope of the inversion procedure, we now shall describe the step-by-step development of the procedure, which can be numerically solved by CSMP available on UTCC's IBM 370 computer system.

First the discrete experimental diameter and temperature data are fitted to smooth functions through regression models. George and Deeg (280) suggested the following form of regression models

$$\log(V - V_0) = \sum_{i=1}^N A_i (\log z)^i + A_{N+1} \quad (6-1)$$

$$T = \sum_{i=1}^N B_i (\log z)^i + B_{N+1} \quad (6-2)$$

where N is order of fitting and A_i and B_i are regression coefficients.

In our case the CSMP function generator statements fit the data with the available regression models in its library and specifically we did not have to provide any restriction on the form of the regression models.

The diameter function was converted to velocity function simply through continuity. Then these fitted functions were differentiated to calculate the velocity gradient, dV/dz , and temperature gradient, dT/dz .

Secondly, the heat balance equation (5-15) and constitutive equation (5-20) were rearranged as follows

$$h = -\frac{W C_p}{\pi D (T - T_a)} \left(\frac{dT}{dz} \right) \quad (6-3)$$

$$\eta = \sigma \left(\frac{dV}{dz} \right)^{-1} \quad (6-4)$$

Note that the second term in equation (5-15), which is for heat of crystallization, was disregarded assuming that the measured temperature profile did not have a crystallization plateau or that the plateau region was disregarded before generating the fitting function. The spinline stress, σ , is given by

$$\sigma = \frac{F_{rheo}}{(\pi D^2/4)} \quad (6-5)$$

Calculation of F_{rheo} involves integration of the differential force balance, equation (5-6), namely

$$dF_{rheo} = dF_{iner} + dF_{drag} - dF_{grav} \quad (6-6)$$

where inertia, drag and gravity force components were calculated from experimental profiles through integration of equations (5-7) to (5-9), respectively. Since the single tension data measured at the bottom of the spinline is used, the integration of equation (6-6) was done from the bottom upward to the spinneret, and this did not involve a guess of initial rheological force at the spinneret. These results, together with the values of dT/dz and dV/dz are then introduced into equations (6-3) and (6-4) to provide calculation of heat transfer coefficient and extensional viscosity, respectively.

The numerically calculated values of extensional viscosity and heat transfer coefficient were then fitted, through regression analysis, to suitable equations. For example, for the extensional viscosity an Arrhenius form was assumed according to

$$\eta = \text{const} \exp\left(\frac{E_{\eta}}{T + 273}\right) \quad (6-7)$$

where E_{η} is the activation energy for flow and the preexponential constant has molecular weight dependence. These parameters were obtained as coefficients of the regression analysis. For heat transfer coefficient a relation was used of the form

$$h = \text{const} \left(\frac{V}{A}\right)^p \quad (6-8)$$

where again constant and exponent p were obtained as the coefficients of regression analysis.

The program developed was tested with error free calculated diameter and temperature data from the mathematical model. After successful testing the experimental diameter and temperature data were

used. George and Deeg (280) have extended the testing approach in that first the test was performed with error free calculated data and then they determined the method's sensitivity to error by inducing normal random errors in the calculated data.

CSMP was used in the inversion procedure for performing derivatives of the velocity and temperature fitting functions of the form of equations (6-1) and (6-2) and also for integration of equation (6-6).

Inversion Procedure Results

Before the inversion procedure was applied to actual experimental data it was critical to test both the mathematical development and the developed computer code. The test results of the inversion procedure using error free test function solutions, generated by using the mathematical model, are shown in Figures 6.13 to 6.20. Input to the computer program for the inversion procedure was discrete diameter and temperature data at 10 cm intervals on the spinline (to imitate experimental data input) and one tension data at the bottom of the spinline. The function generator statements of CSMP fit these data to generate fitting functions. In all these figures the solid lines indicate original data (solutions) from the mathematical model and the points result from either the fitting functions or the calculations of the inversion procedure.

Velocity, diameter and temperature profiles (Figures 6.13, 6.14 and 6.15 respectively) show a very good fit assuring that correct fitting functions are generated. Differentiation of velocity and temperature functions lead to velocity gradient (dV/dz) and temperature gradient

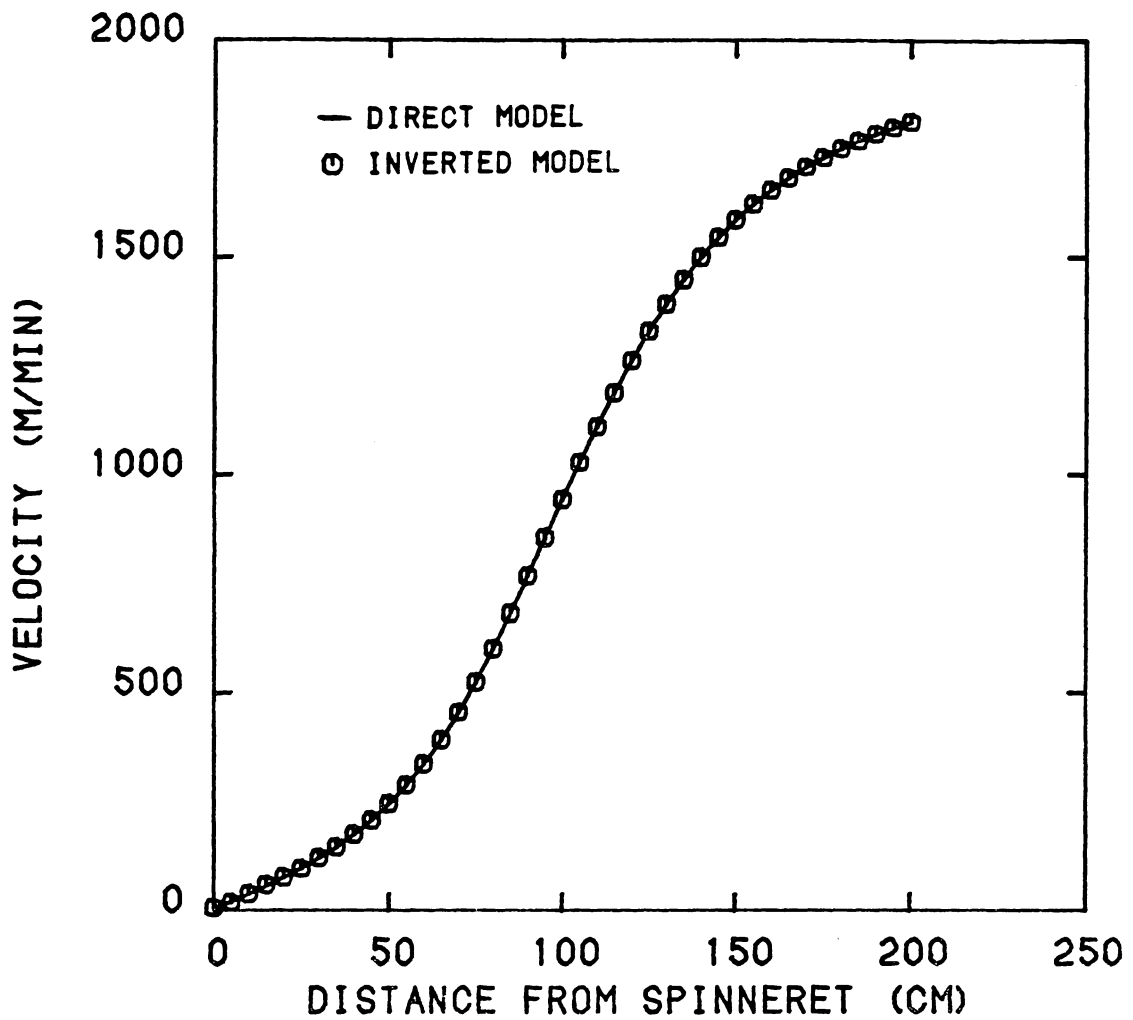


Figure 6.13 Test comparison of inversion procedure for velocity profiles for CN9984 with a mass throughput of 3.073 g/min and take-up speed of 1960 m/min.

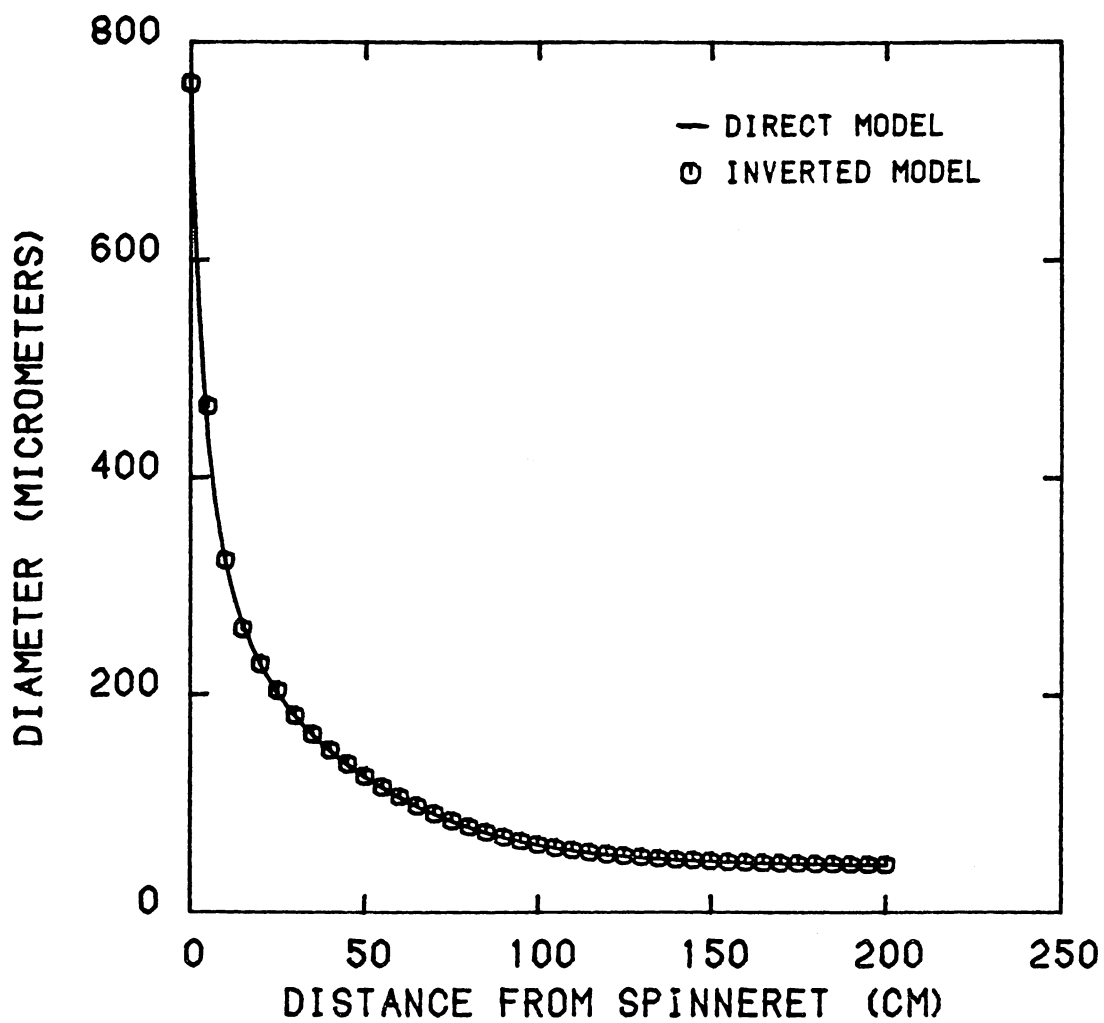


Figure 6.14 Test comparison of inversion procedure for diameter profiles for CN9984 with a mass throughput of 3.073 g/min and take-up speed of 1960 m/min.

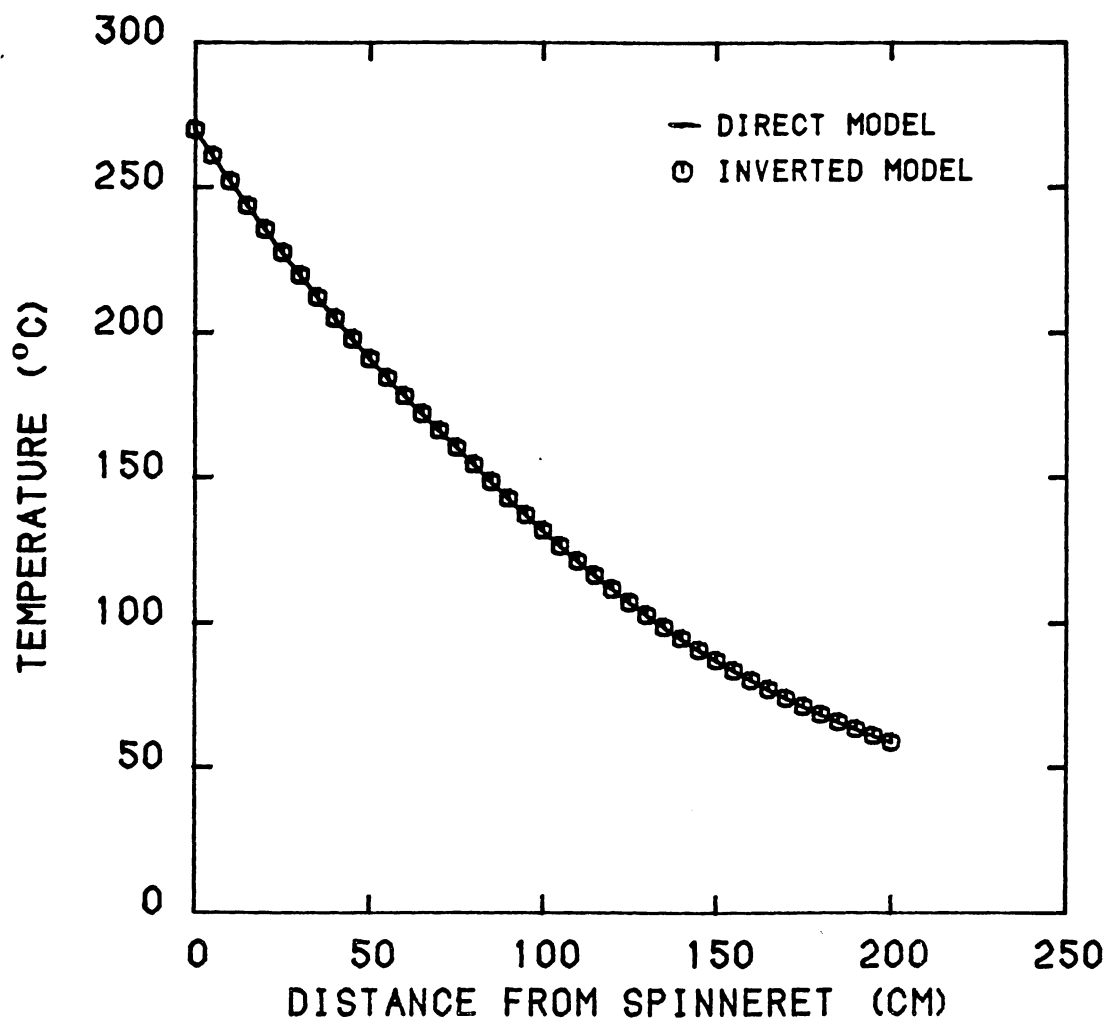


Figure 6.15 Test comparison of inversion procedure for temperature profiles for CN9984 with a mass throughput of 3.073 g/min and take-up speed of 1960 m/min.

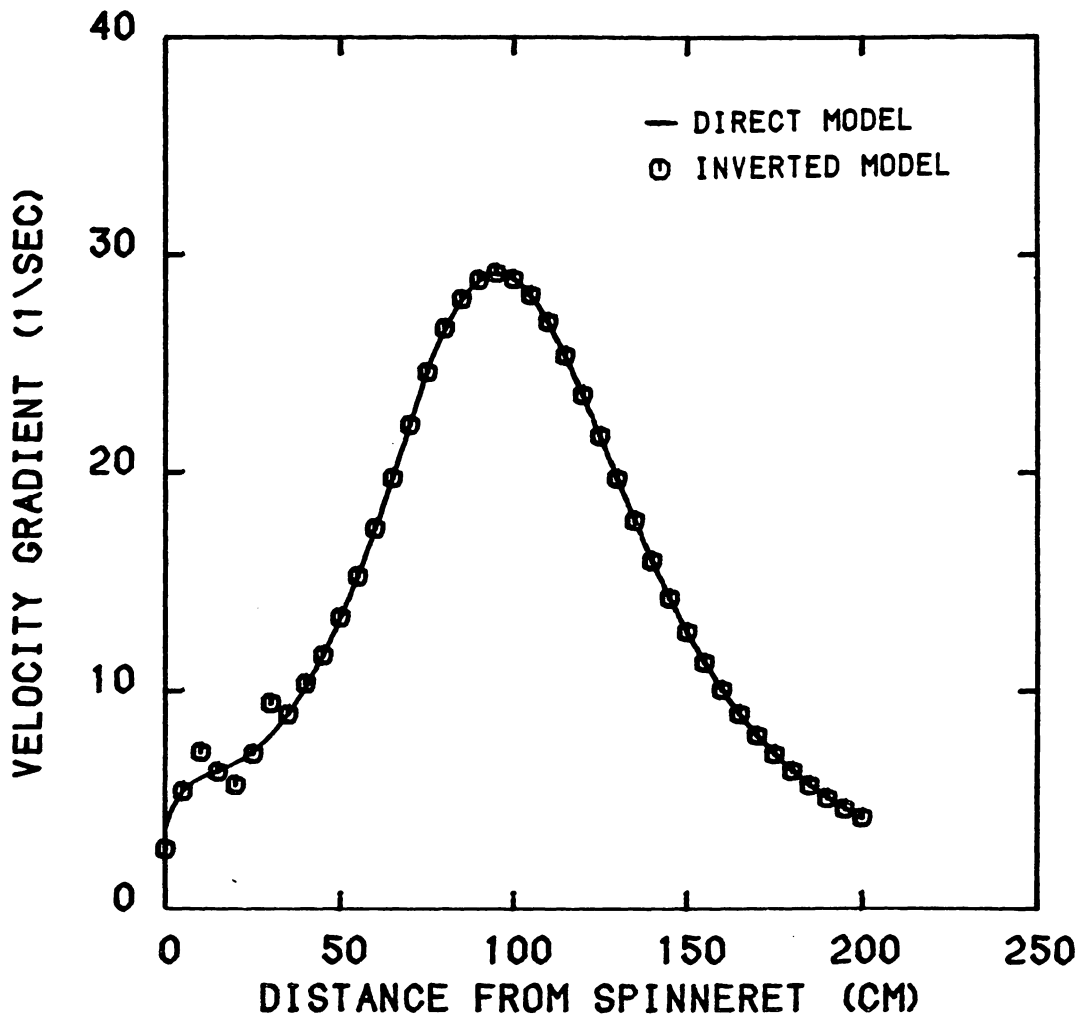


Figure 6.16 Test comparison of inversion procedure for velocity gradient profiles for CN9984 with a mass throughput of 3.073 g/min and take-up speed of 1960 m/min.

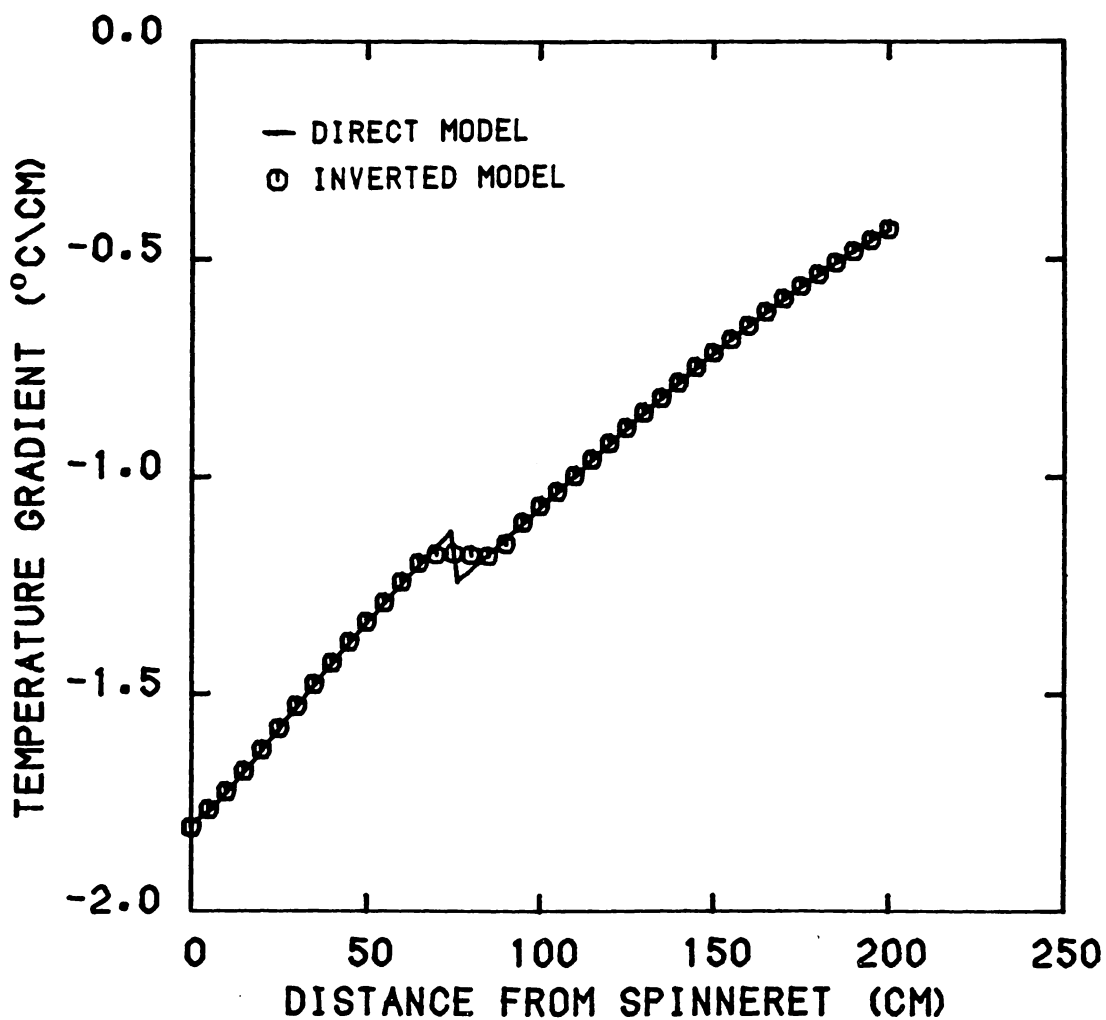


Figure 6.17 Test comparison of inversion procedure for temperature gradient profiles for CN9984 with a mass throughput of 3.073 g/min and take-up speed of 1960 m/min.

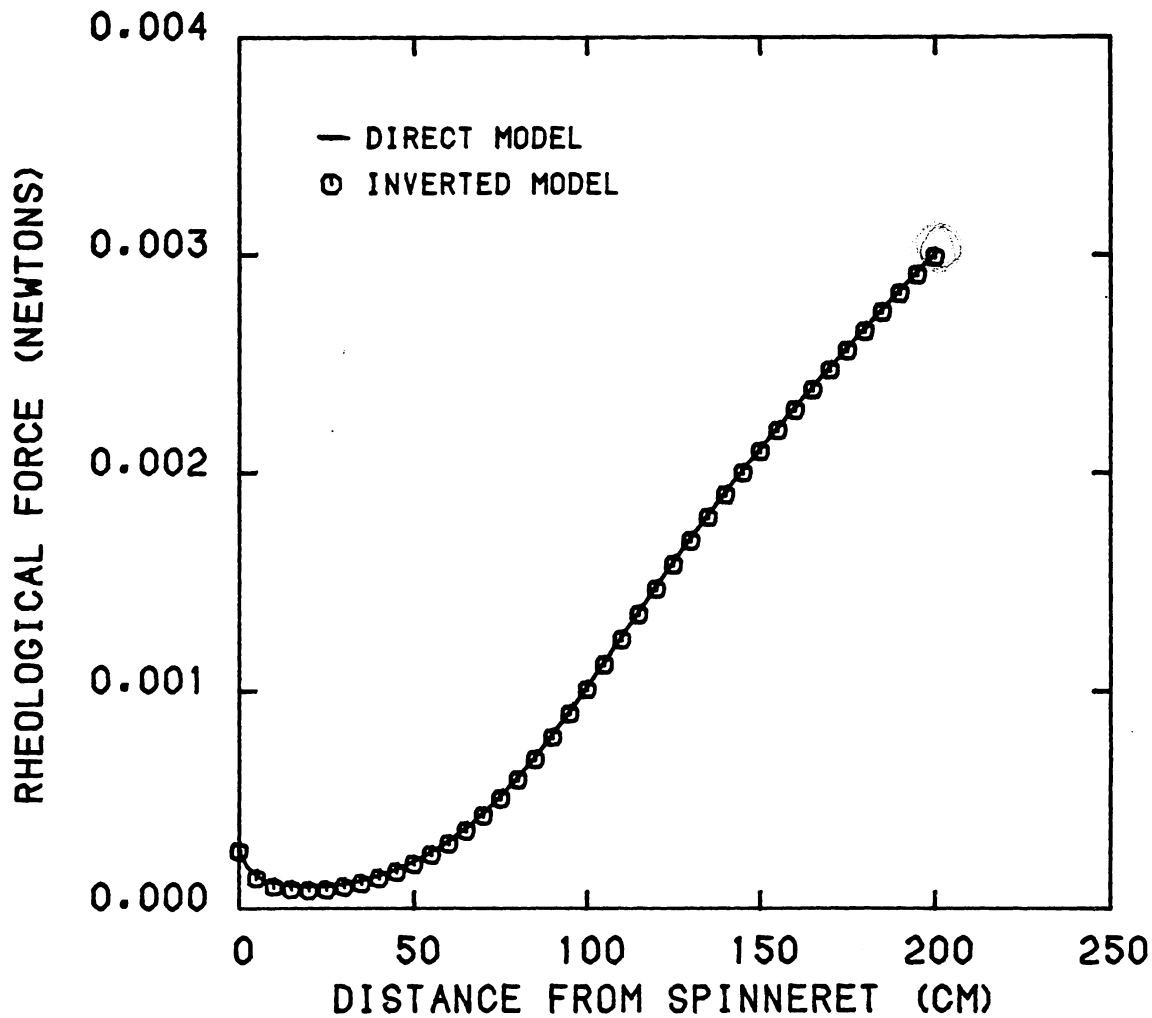


Figure 6.18 Test comparison of inversion procedure for rheological force profiles for CN9984 with a mass throughput of 3.073 g/min and take-up speed of 1960 m/min.

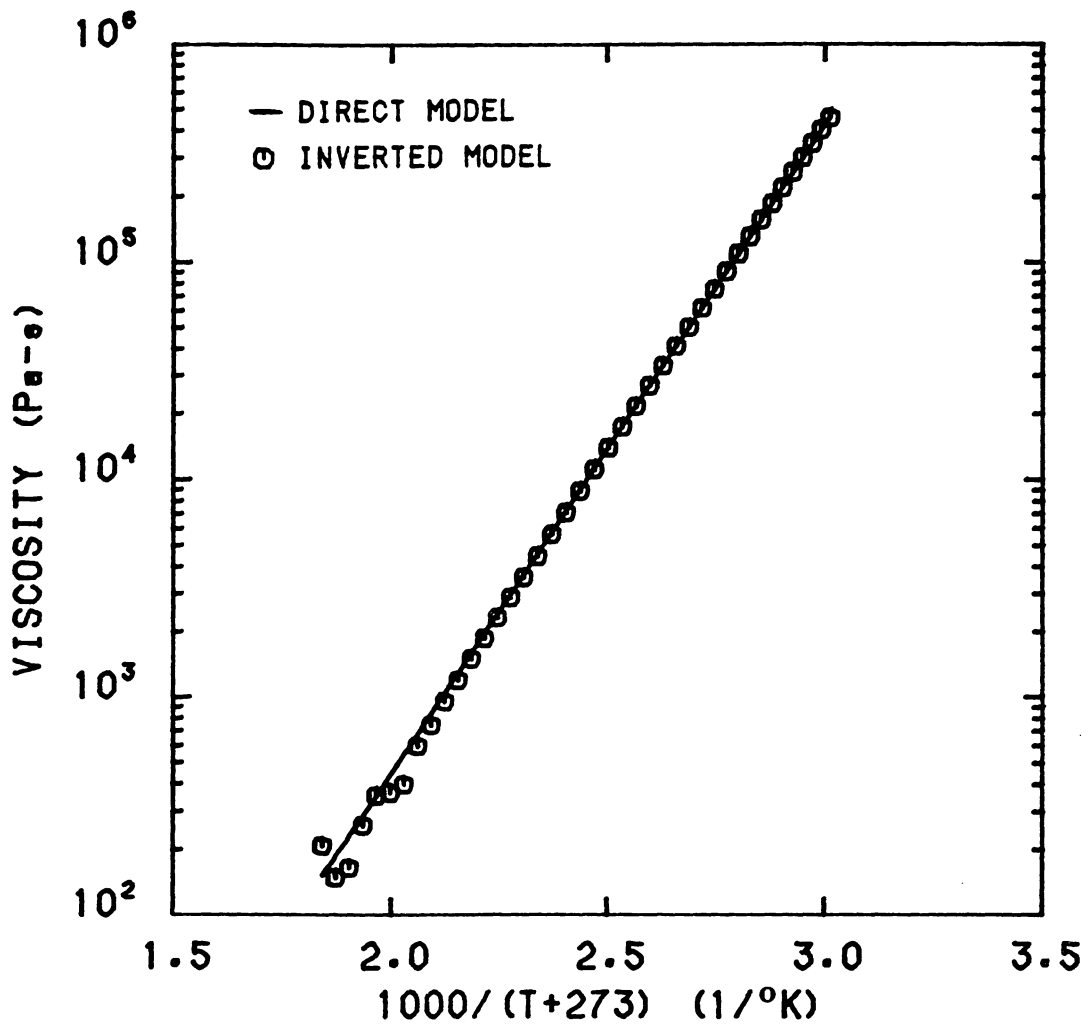


Figure 6.19 Test comparison of inversion procedure for viscosity profiles for CN9984 with a mass throughput of 3.073 g/min and take-up speed of 1960 m/min.

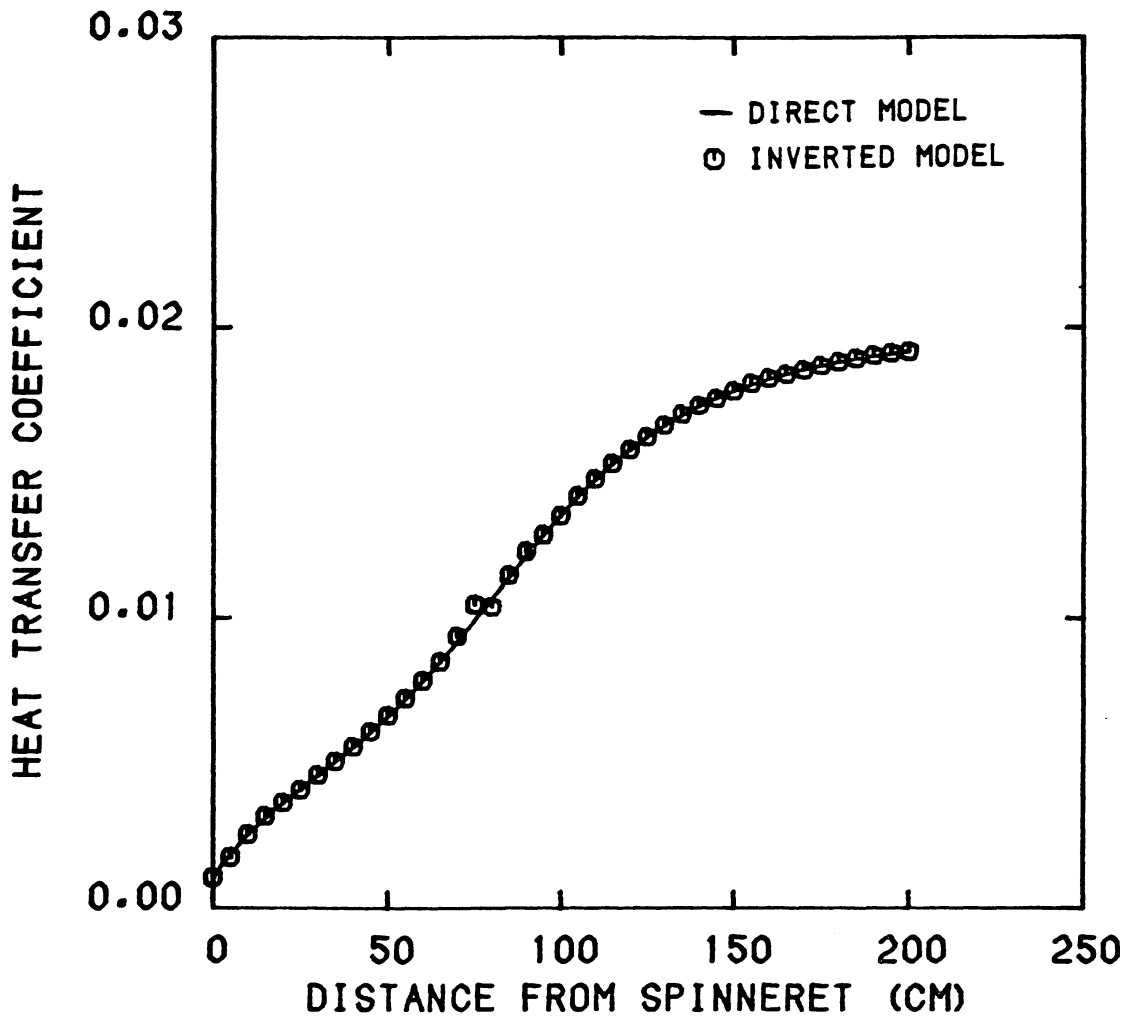


Figure 6.20 Test comparison of inversion procedure for heat transfer coefficient profiles for CN9984 with a mass throughput of 3.073 g/min and take-up speed of 1960 m/min.

(dT/dz). The resulting values computed from the fitting functions are in good agreement with the actual values (see Figures 6.16 and 6.17) except in the initial portion of the spinline for dV/dz. Good agreement for rheological force (see Figure 6.18) indicates that the mathematics in the program are correctly set up to integrate the differential equation for rheological force from the bottom of the spinline where a single tension input was given. Figures 6.19 and 6.20 for viscosity and heat transfer coefficient, respectively, show that the input relations in the mathematical model are reproduced by the inversion procedure with very good agreement.

After successful testing of the inversion procedure, the experimental data for the lower take-up speeds (where no online crystallization occurred) for both resins and two different mass throughputs were used in the inversion procedure and discrete values for elongational viscosity and heat transfer coefficient were obtained. These discrete calculated values were then regressed to obtain a suitable form of mathematical relation for elongational viscosity and heat transfer coefficient. The results are shown in Figures 6.21 to 6.28. In these figures the solid lines show the regressed relations and points give the discrete calculated values from the inversion procedure. The regressed relations for elongational viscosity and heat transfer coefficient for various sets of experimental data are as shown below.

For CN9984

for 3 g/min throughput

$$\eta = 0.054 \exp\left(\frac{5149}{T + 273}\right) \quad (6-9)$$

$$h = 1.32 \times 10^{-4} \left(\frac{V}{A}\right)^{0.261} \quad (6-10)$$

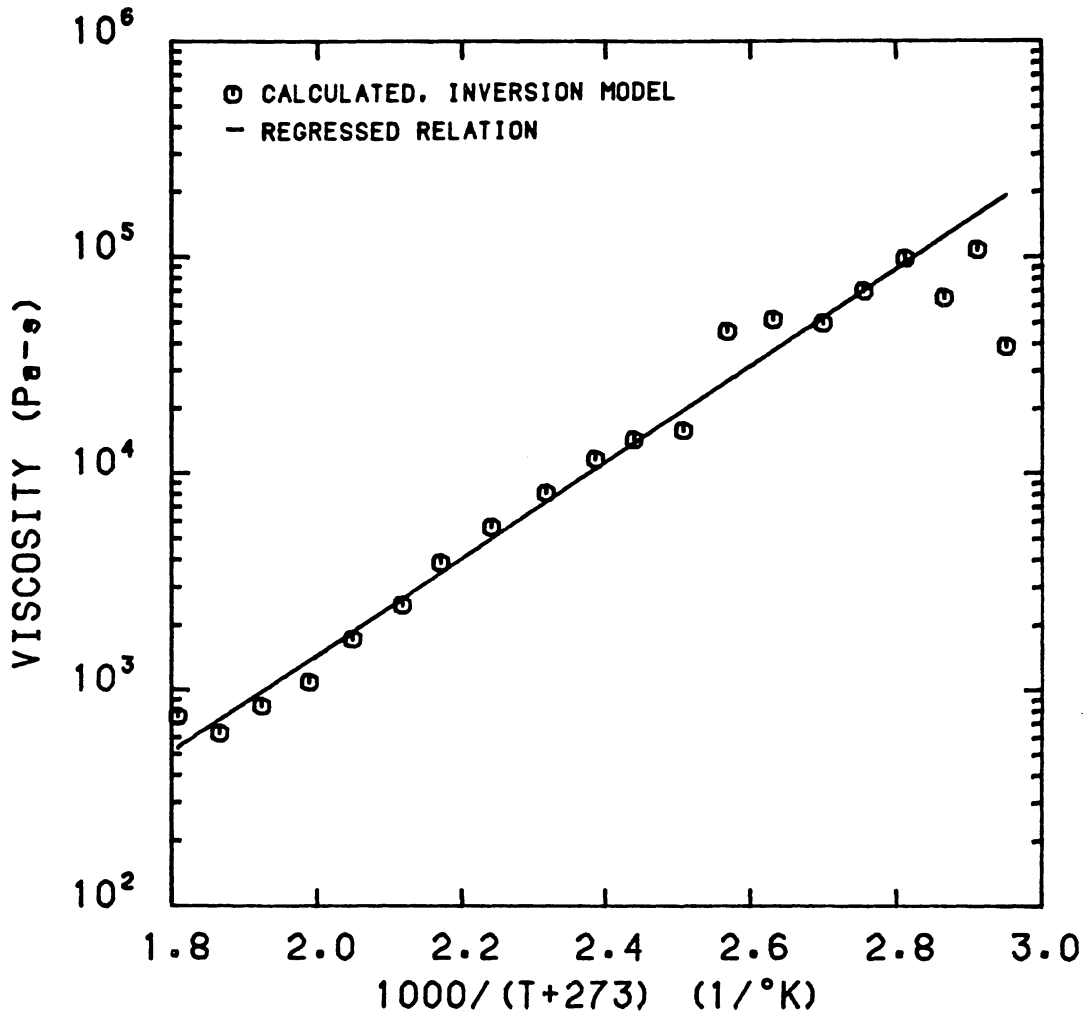


Figure 6.21 Calculated and regressed viscosity relation from inversion procedure for CN9984 with a mass throughput of 3.073 g/min and take-up speed of 1960 m/min.

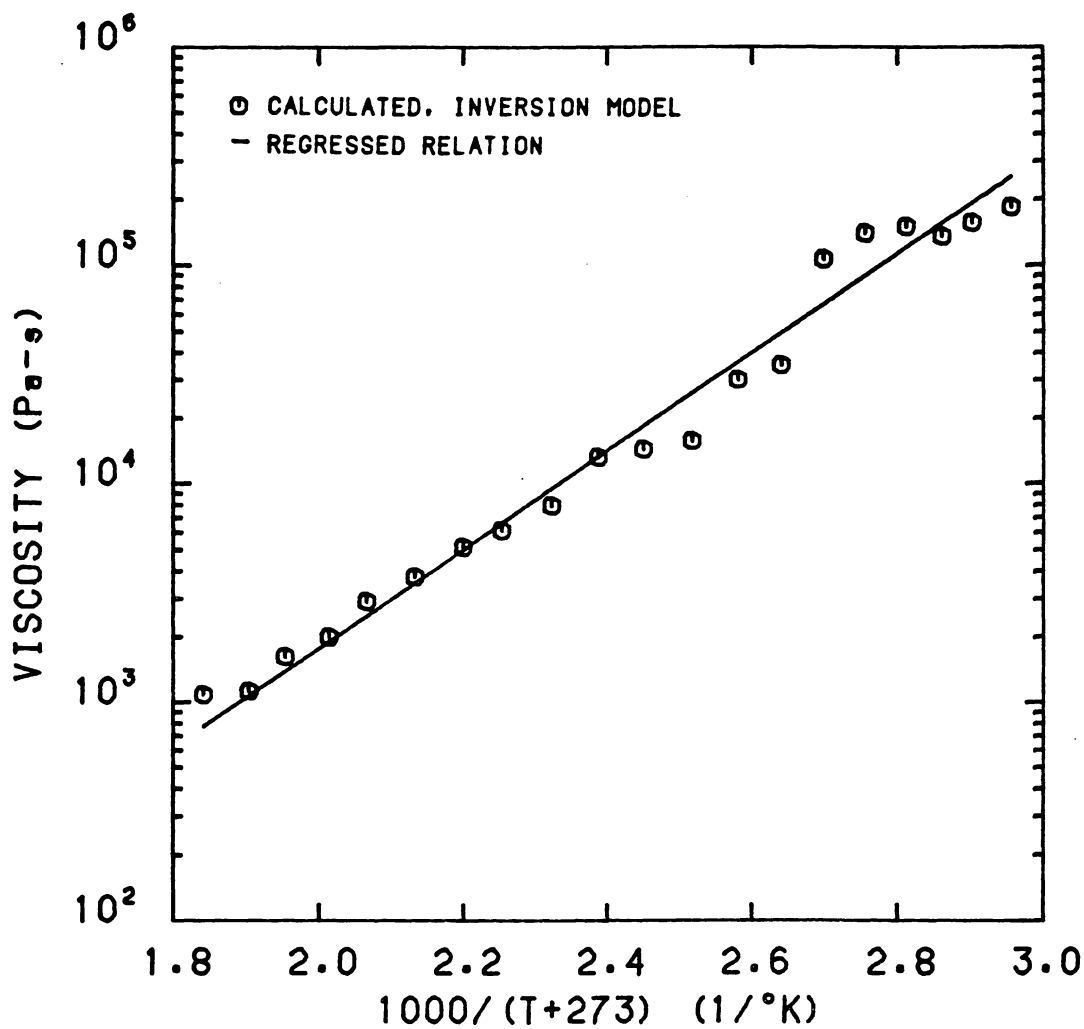


Figure 6.22 Calculated and regressed viscosity relation from inversion procedure for BHS with a mass throughput of 2.993 g/min and take-up speed of 1780 m/min.

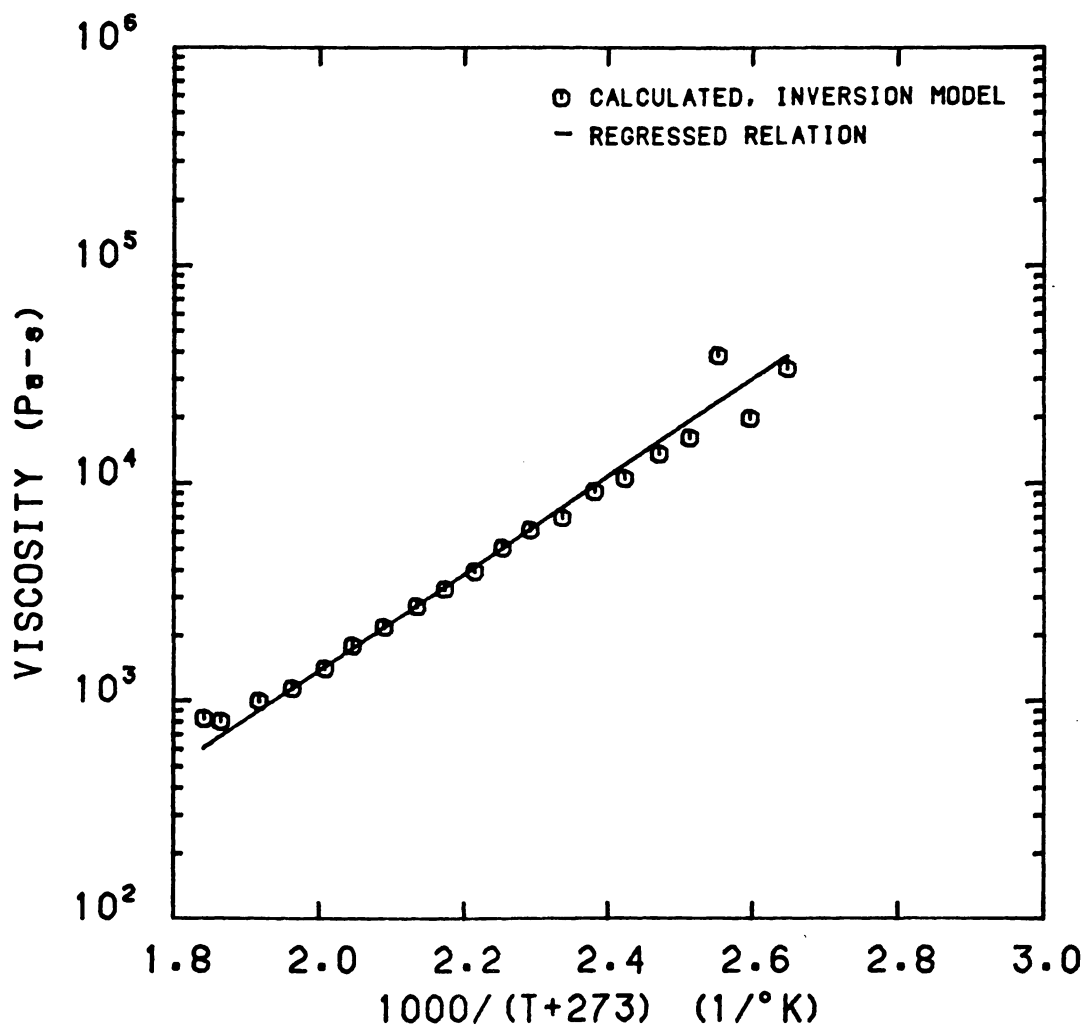


Figure 6.23 Calculated and regressed viscosity relation from inversion procedure for CN9984 with a mass throughput of 5.154 g/min and take-up speed of 1570 m/min.

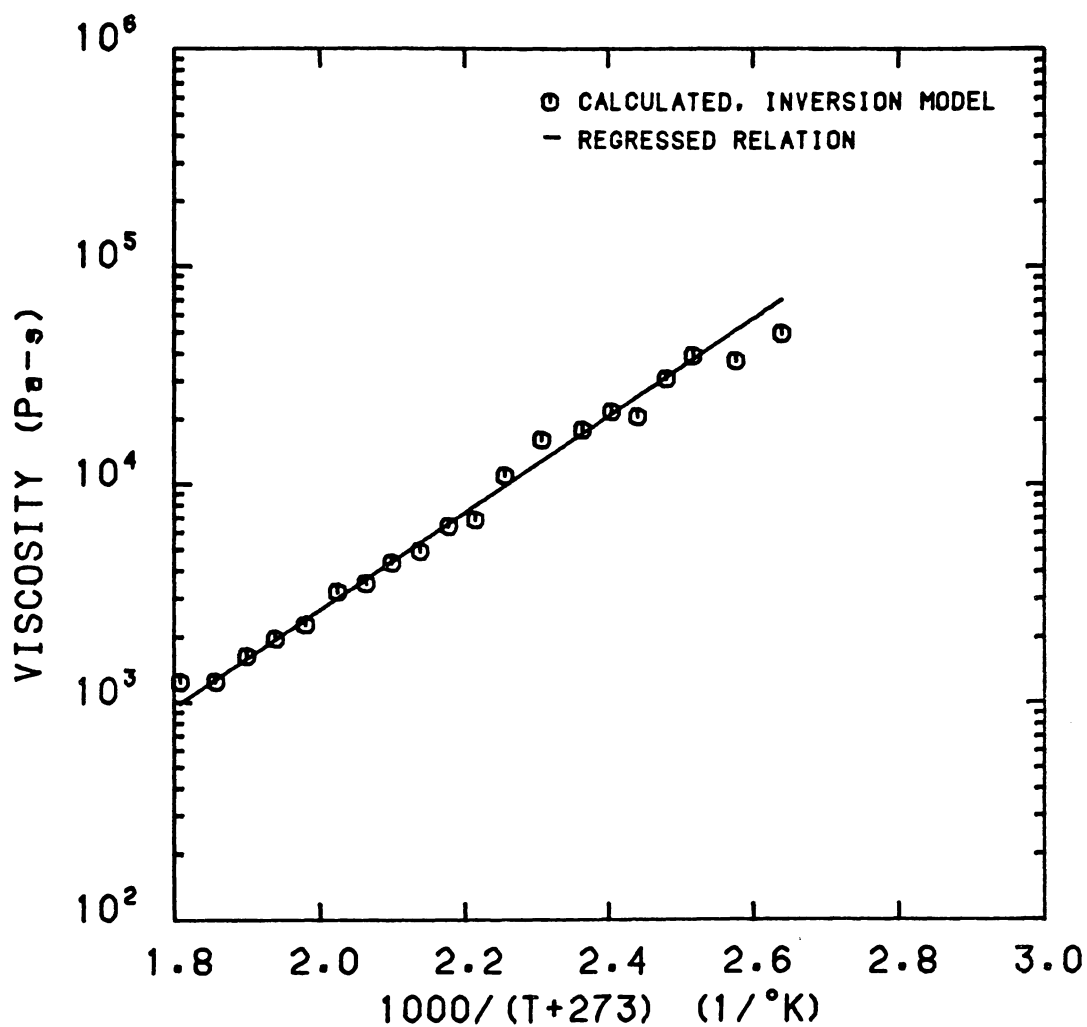


Figure 6.24 Calculated and regressed viscosity relation from inversion procedure for BHS with a mass throughput of 5.069 g/min and take-up speed of 1250 m/min.

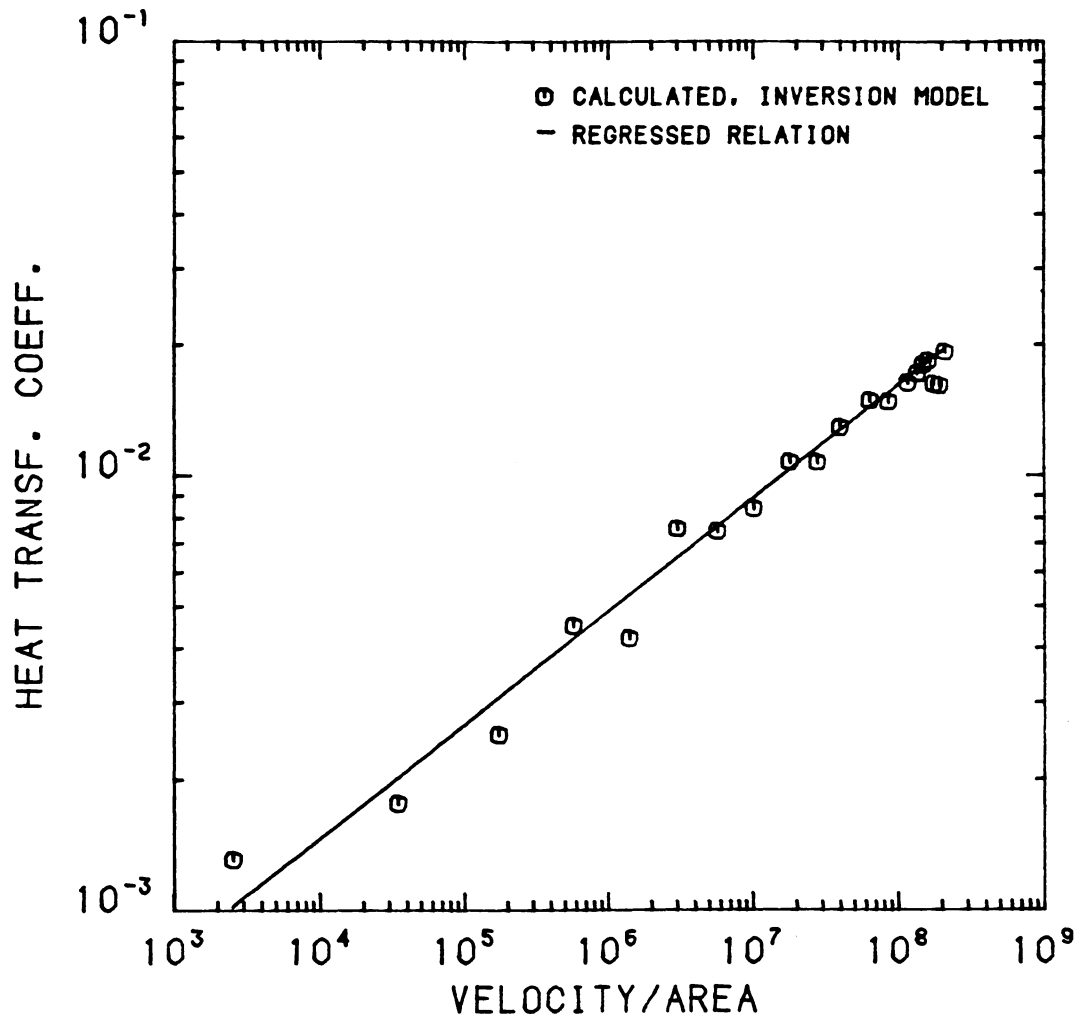


Figure 6.25 Calculated and regressed heat transfer coefficient relation from inversion procedure for CN9984 with a mass throughput of 3.073 g/min and take-up speed of 1960 m/min.

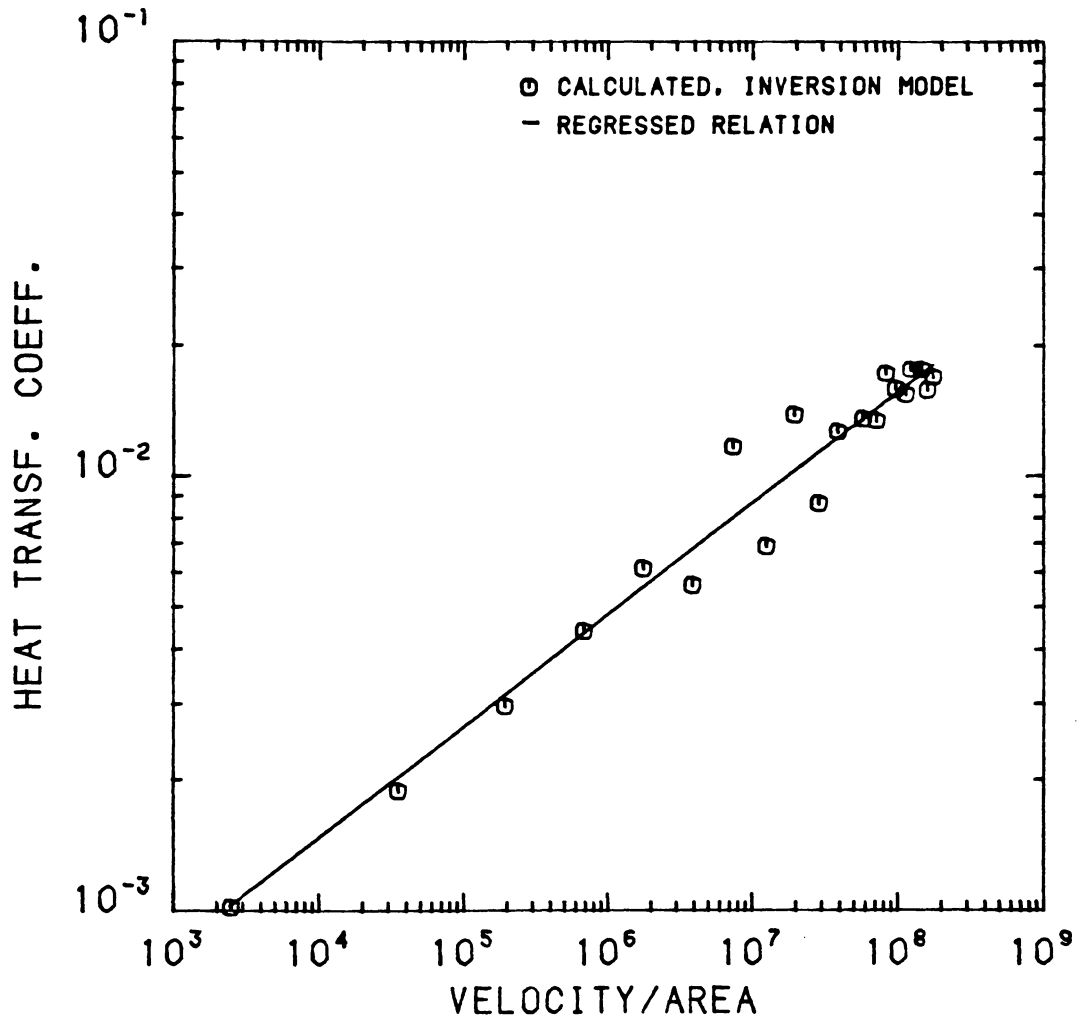


Figure 6.26 Calculated and regressed heat transfer coefficient relation from inversion procedure for BHS with a mass throughput of 2.993 g/min and take-up speed of 1780 m/min.

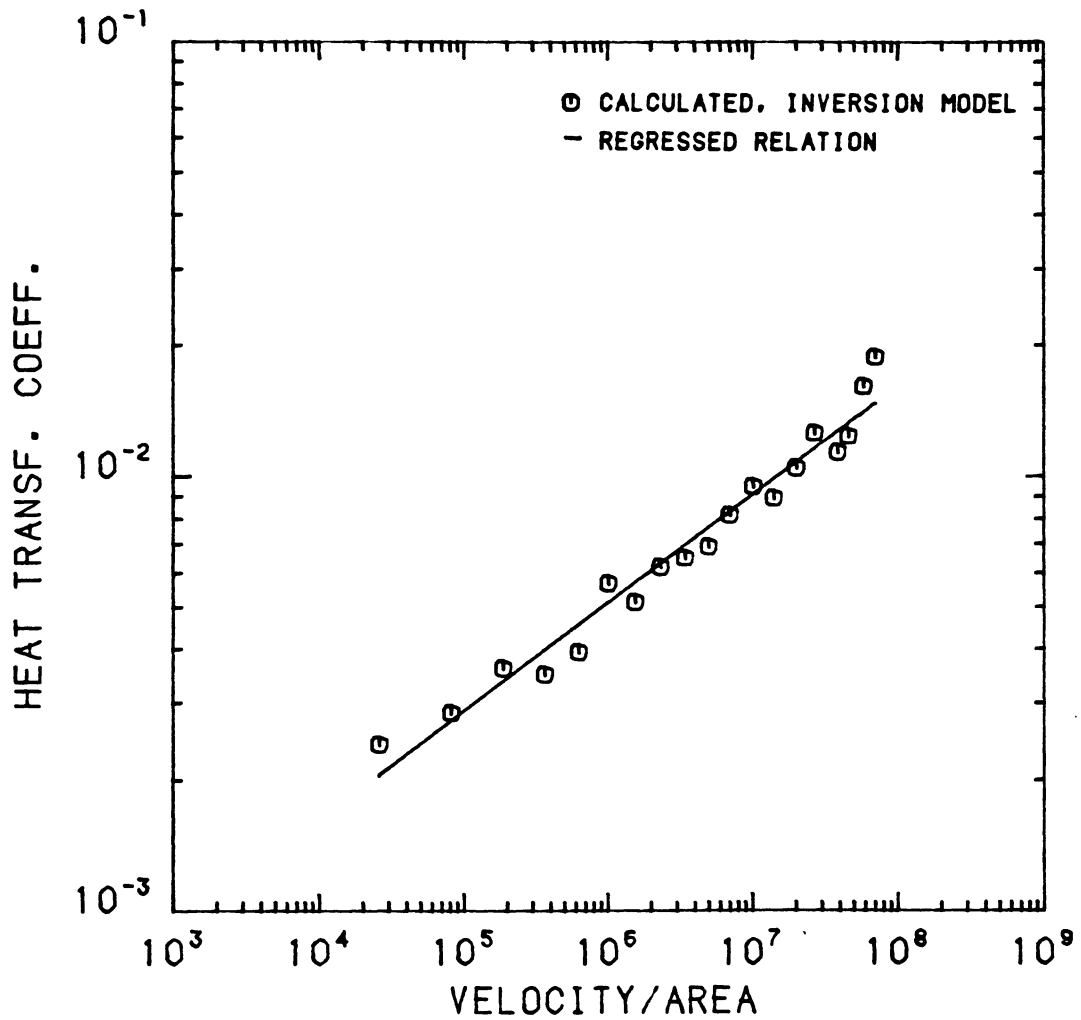


Figure 6.27 Calculated and regressed heat transfer coefficient relation from inversion procedure for CN9984 with a mass throughput of 5.154 g/min and take-up speed of 1570 m/min.

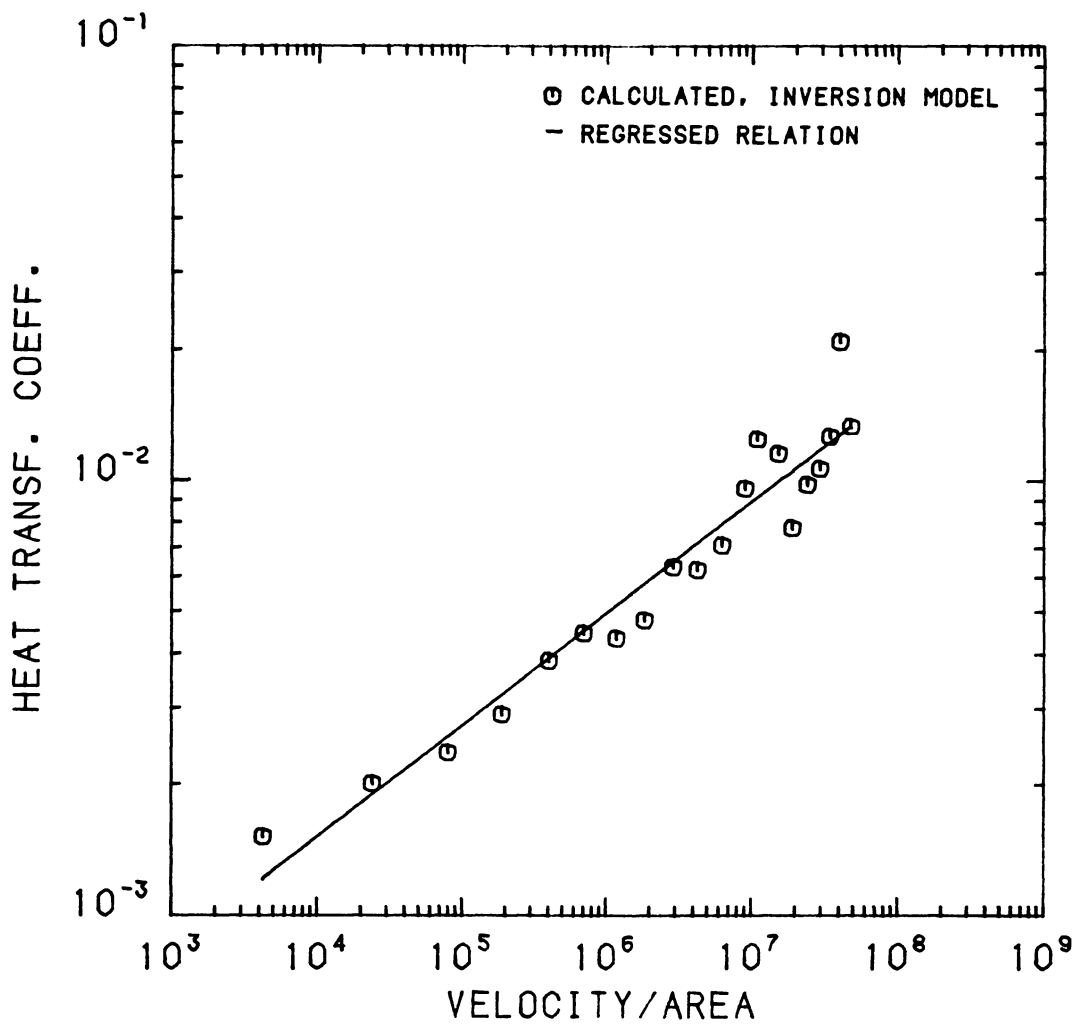


Figure 6.28 Calculated and regressed heat transfer coefficient relation from inversion procedure for BHS with a mass throughput of 5.069 g/min and take-up speed of 1250 m/min.

for 5 g/min throughput

$$\eta = 0.047 \exp\left(\frac{5138}{T + 273}\right) \quad (6-11)$$

$$h = 1.64 \times 10^{-4} \left(\frac{V}{A}\right)^{0.249} \quad (6-12)$$

and for BHS

for 3 g/min throughput

$$\eta = 0.089 \exp\left(\frac{5140}{T + 273}\right) \quad (6-13)$$

$$h = 1.38 \times 10^{-4} \left(\frac{V}{A}\right)^{0.257} \quad (6-14)$$

for 5 g/min throughput

$$\eta = 0.093 \exp\left(\frac{5168}{T + 273}\right) \quad (6-15)$$

$$h = 1.41 \times 10^{-4} \left(\frac{V}{A}\right)^{0.258} \quad (6-16)$$

Note that regressed equations for elongational viscosity of each resin for two different mass throughputs have similar values of both the preexponential factor and the activation energy for flow (compare equation (6-9) to equation (6-11) and equation (6-13) to equation (6-15)). Therefore, the data for both mass throughputs were combined and further regressed to a common equation for each resin.

For CN9984

$$\eta = 0.054 \exp\left(\frac{5140}{T + 273}\right) \quad (6-17)$$

and for BHS

$$\eta = 0.092 \exp\left(\frac{5150}{T + 273}\right) \quad (6-18)$$

The temperature dependence of elongational viscosity is of the Arrhenius type and the activation energy is almost independent of the molecular weight of the resin. The preexponential constants have molecular weight dependence and equations (6-17) and (6-18) can be rearranged to reflect this dependence. Considering the viscosity average molecular weight (M_v)

and intrinsic viscosity (IV) for CN9984 to be 23,500 and 0.862, and the corresponding values for BHS to be 53,200 and 1.525, respectively gives

$$\eta = 7.80 \times 10^{-5} (M_v)^{0.65} \exp\left(\frac{5140}{T + 273}\right) \quad (6-19)$$

$$\eta = 0.062 (IV)^{0.93} \exp\left(\frac{5140}{T + 273}\right) \quad (6-20)$$

The regressed equations for heat transfer coefficient (equations (6-10), (6-12), (6-14) and (6-16)) indicate that the value of regressed coefficients is quite similar for each resin and for the two different mass throughputs. This also confirms the fact that heat transfer coefficient involved in melt spinning is not a material property. The heat transfer coefficient data for both mass throughputs and both resins were combined and then regressed to obtain a common equation:

$$h = 1.43 \times 10^{-4} \left(\frac{V}{A}\right)^{0.256} \quad (6-21)$$

Discussion of Inversion Procedure Results

There have been several studies in which independent measurements of elongational flows of various polymer melts were carried out. White (287) has reviewed measurements of elongational viscosity of PS, LDPE, HDPE, and PP melts. The various studies reviewed concluded that linear polyolefins such as HDPE and PP exhibit an elongational viscosity which decreases with elongation rate. Cogswell (288) also found similar results for linear isotactic poly(4-methyl pentene-1). White further pointed out that introduction of long chain branching as in LDPE changes the behavior observed for HDPE and makes the melt deformation hardening

and consequently elongational viscosity becomes an increasing function of elongation rate. Cogswell (200,288,289) also noted similar behavior in other polymers, generally atactic, amorphous and with small degrees of branching, including PS, PMMA and polyisobutylene. Elongational viscosities for these cases were found to be generally increasing function of elongation rate or were constant. This varying behavior of elongational viscosity with polymer type was attributed to differences in molecular weight distribution (MWD) and glass transition temperature (T_g). This suggestion was based on a study (287) of PP which revealed that narrowing the MWD of PP led to elongational viscosity changing from a decreasing to an increasing function of elongation rate and comparison of behavior of PS with HDPE or PP which have very dissimilar T_g . Han and his coworkers (56,80,203) developed a semi-empirical generalized equation for elongational viscosity as a function of the elongation rate and temperature. Kase and Matsuo (79) also developed a similar relation and applied it to PP melt spinning data. They reported that calculated elongational viscosity was a strong function of temperature and relatively independent of elongation rate for the range of elongation rate studied. From these studies, however, there is no direct indication of dependence of elongational viscosity on molecular weight. In some cases the Trouton law has been confirmed to be true. In this case the elongational viscosity is three times the shear viscosity in the limit of zero elongation rate. Rheological measurements of shear flow indicate that melt shear viscosity has a power law form for molecular weight dependence with exponent ranging from 3 to 3.5.

For polymers like nylons and polyesters the established elongational viscosity measurement technique for polyolefins could not be applied directly because the melts of these polymers have too low a viscosity to measure tensile force at constant elongation rate particularly under isothermal conditions at temperatures above the melting point. There have been attempts to use the melt spinline as an elongational rheometer to arrive at elongational viscosity.

Hill and Cuculo (205) experimentally investigated isothermal elongational flow behavior of PET monofilaments by using an isothermal chamber immediately below the spinneret. Take-up speeds studied were in the range of 400 to 1600 m/min. They also tried to characterize the non-isothermal region of the spinline which involves higher elongation rates compared to that within the isothermal chamber. Elongational viscosity was found to be slightly dilatant over the elongation rate range investigated, but it was highly dependent on temperature.

Lin and Hauenstein (290) studied molecular weight dependence of PET elongational viscosity using the melt spinline. The values of elongational viscosity for his experiments were expressed mathematically as follows.

For 0.56 IV PET

$$\log \eta = \frac{1900}{T} - 1.77 \quad (6-22)$$

and for 0.84 IV PET

$$\log \eta = \frac{1900}{T} - 1.50 \quad (6-23)$$

Note that the temperature dependence was of Arrhenius type and the coefficient 1900 is independent of molecular weight. The equations (6-22) and (6-23) can be rearranged in exponential form and the

preexponent can be expressed in terms of IV dependence to obtain a common equation:

$$\eta = 0.0041(IV)^{1.53} \exp\left(\frac{4375}{T + 273}\right) \quad (6-24)$$

Note that the earlier reported equation (6-20) for elongational viscosity from our experimental data for nylon-6 had similar form and IV dependence as in equation (6-24).

A study of nylon-6 using the melt spinline was carried out by Ishibashi et al. (43). They studied four different nylon-6 resins with different number average molecular weight in the range of 18,500 to 24,100 and take-up speeds in the range of 500 to 1500 m/min. They report that elongational viscosity was relatively independent of both molecular weight and take-up speed but was a strong function of temperature. The elongational viscosity values were consistently expressed by the equation

$$\eta = 33.32 \exp\left(\frac{3250}{T + 273}\right) \quad (6-25)$$

Note again that the temperature dependence was of Arrhenius type. Hamana et al. (41) also reported the elongational viscosity of nylon-6 as a function of temperature using the melt spinline. The viscosity average molecular weight of their polymer was 16,000. We regressed their data assuming the Arrhenius exponential temperature dependence. The regression analysis gave a correlation coefficient of 0.97 indicating the chosen form for temperature dependence was correct. This equation is

$$\eta = 0.128 \exp\left(\frac{4702}{T + 273}\right) \quad (6-26)$$

Bankar et al. (25) calculated the elongational viscosity for nylon-6 with number average molecular weight of 23000 using diameter and temperature measurements on spinline. Their data were regressed considering the Arrhenius temperature dependence and we found a coefficient of correlation of 0.98 again indicating that the chosen form of regressed equation was correct. This equation is

$$\eta = 17.17 \exp\left(\frac{3230}{T + 273}\right) \quad (6-27)$$

Bankar et al. also compared their results with results of Ishibashi et al. (43) and that of Hammana et al. (41) for nylon-6 and concluded that their results were intermediate to those reported by the other two studies.

The numerical values of coefficients in equations (6-25), (6-26) and (6-27) differ from our findings; this may be due to the fact that the molecular weight of resin, take-up speed and mass flow rate studied were different from our study. It may also be due to differences between the experimental procedures and corrections applied for air drag to take-up tension to obtain rheological force. Ishibashi et al., Bankar et al. and in present study Sakiadis (46) formulation for air drag was used while Hamana et al. used their own equation for air drag.

In the mathematical model of the present study the elongational viscosity equation was arrived at using the Trouton law and the zero shear melt viscosity relation (283). This gave

$$\eta = 3 * 2.2956X10^{-19}(M_w)^{3.4} \exp\left(\frac{6855}{T + 273}\right) \quad (6-28)$$

The equation (6-28) was useful to incorporate molecular weight effect as the earlier reported studies for nylon-6 did not clearly illuminate the molecular weight effect.

The elongational viscosity results for both CN9984 and BHS resins from experimental data and that used in the mathematical model given by equations (6-19) and (6-28), respectively and that reported by Ishibashi et al., Hamana et al. and Bankar et al. given by equations (6-25), (6-26) and (6-27), respectively are compared in Figure 6.29. We have also included three times the experimental zero shear viscosity reported by Koyama et al. (34) for CN9984 and BHS resins given by points in Figure 6.29. The experimental elongational viscosities of the present study are intermediate to those from equation (6-28). The results from Koyama et al.'s experimental shear viscosity are relatively in good agreement, particularly for CN9984, with the results of present study. Both Bankar et al. and Ishibashi et al.'s results are relatively larger at higher temperature (lower reciprocal temperature), but they are in fair agreement at lower temperature as compared to the results from the present study. Hamana et al.'s results are closest to the results of present study as compared to all other results in spite of use of different air drag formulation.

As discussed above the present elongational viscosity calculations were made using Sakiadis air drag coefficient. To further understand the effect of air drag correction the calculations were also made using Hamana et al.'s equation for air drag. This equation is quite similar to other reported equations both in form and numerical values of coefficients. The results for CN9984 with mass throughput of 3.073 g/min

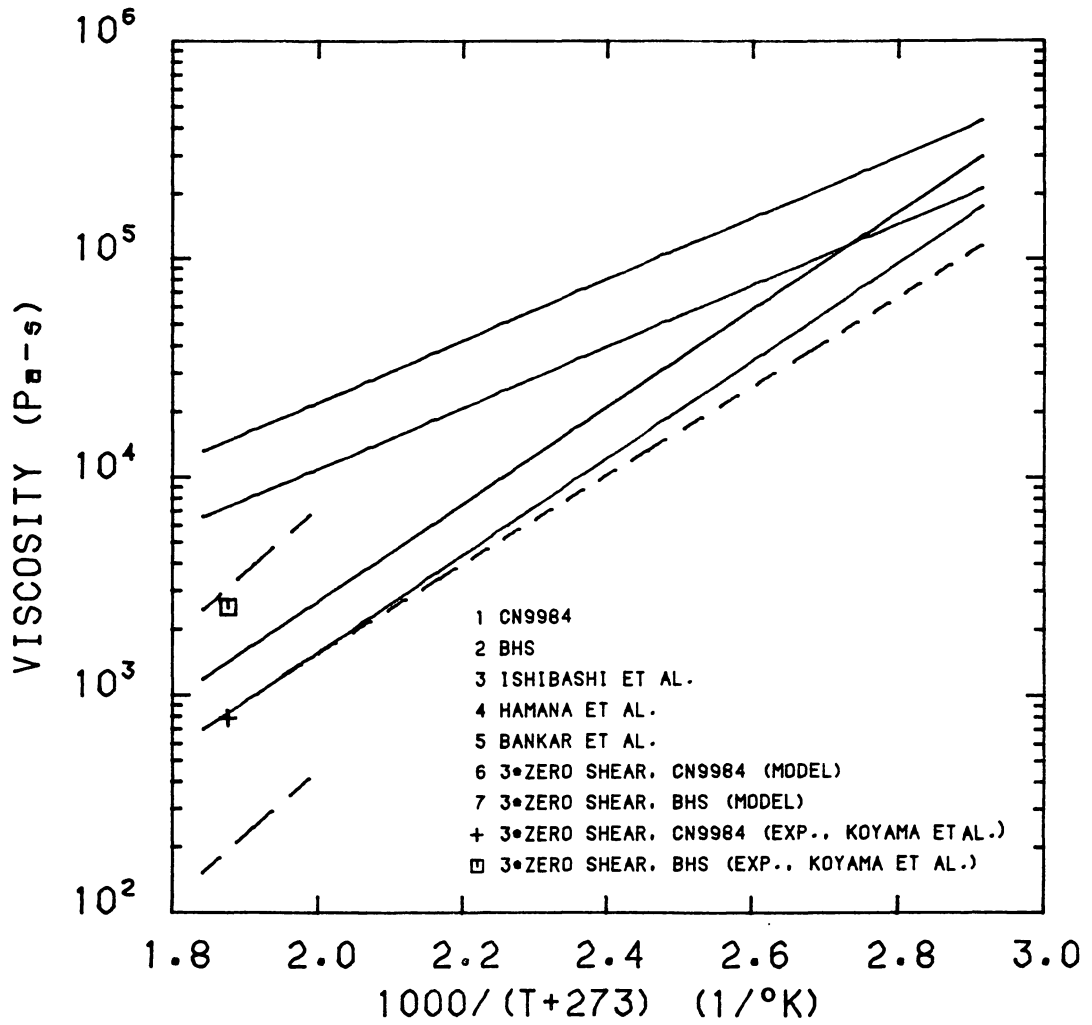


Figure 6.29 Comparison of elongational viscosities from inversion procedure of present experimental data, those from model and those from the literature.

and take-up speed of 1960 m/min are given in Figure 6.30. The points indicate the calculated data and the solid and dashed lines indicate the regressed equations from the calculated data. It seems that there is not much effect due to air drag correction for the above mentioned conditions. The differences in the experimental elongational viscosities from various studies, including the present study, thus seem to depend very much on techniques used for the online measurements of diameter, temperature and tension.

Investigations reported for heat transfer coefficient involved in melt spinning unfortunately are not as detailed in terms of spinning variables as for elongational viscosity. This may be due, in part, to the fact that in most of the initial investigations attempts were made to understand melt spinning behavior under isothermal conditions. Under the non-isothermal conditions knowledge of temperature variation of the spinline became necessary and then estimation of the heat transfer coefficient from basic chemical engineering principles was considered. Ziabicki and Kedzierska (214), Barnett (215), Copley et al. (216), Morrison (217), and others asserted that heat transfer mechanisms involved in melt spinning are radiation, free convection and forced convection; of these radiative heat loss has been considered to be negligible.

Theoretical and experimental conditions to obtain the heat transfer coefficient were varied in several studies (218-223). In theoretical studies laminar and turbulent boundary layer theories for a continuous cylinder moving axially in an air stream has been considered. In experimental studies, free and forced convection of an axial air stream

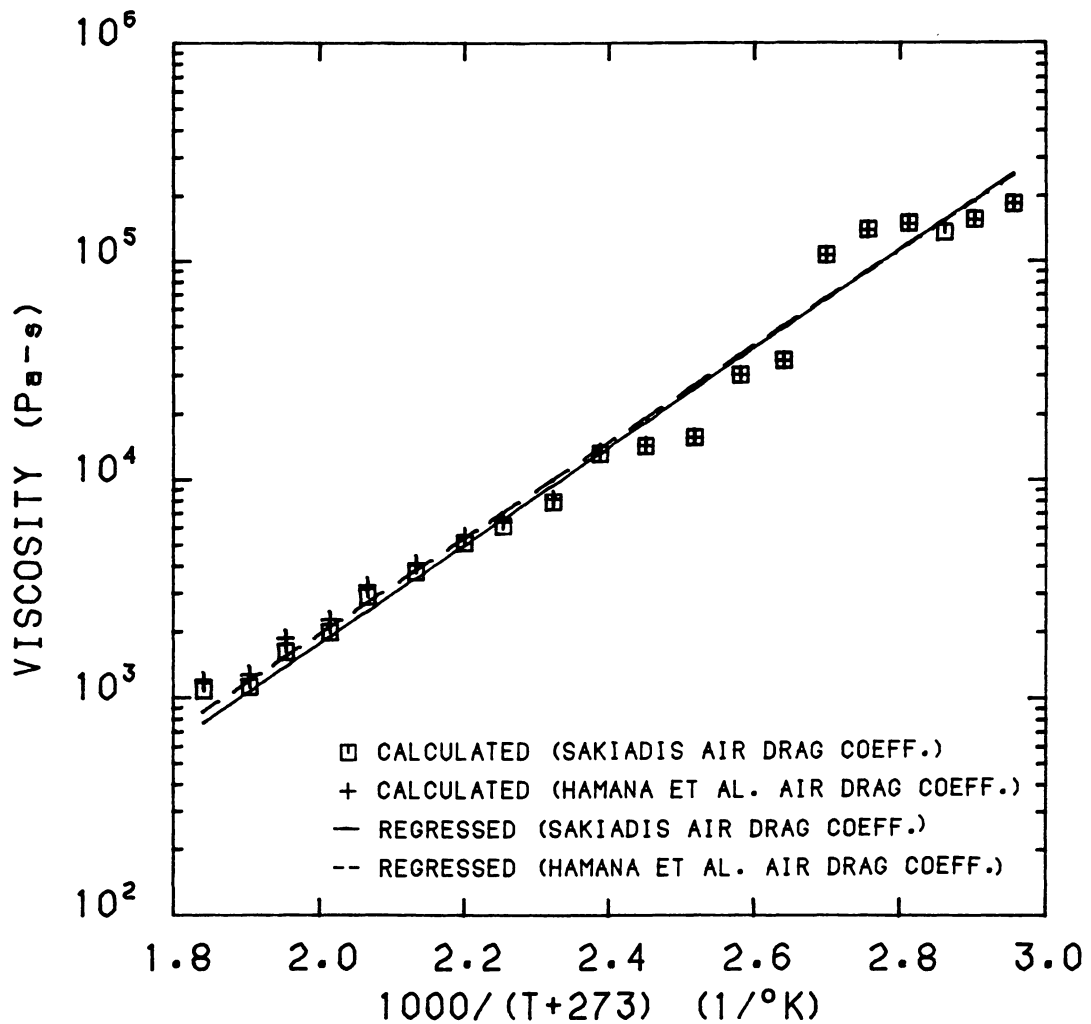


Figure 6.30 Comparison of elongational viscosities from inversion procedure for CN9984 with a mass throughput of 3.073 g/min and take-up speed of 1960 m/min using Sakiadis's and Hamana et al.'s air drag coefficients.

over thin wires, axial motion of filament in stationary air, cross air stream and axial motion of the filament, etc. have been considered. The heat transfer coefficient in melt spinning has been expressed in terms of various dimensionless groups rather than in terms of spinning variables.

Kase and Matsuo (78) arrived at an empirical relationship for heat transfer coefficient using a stationary hot wire in an axial air stream. This relation is

$$Nu = 0.42 Re^{0.334} \quad (6-29)$$

where $Nu = (hD/k_a)$ and $Re = (VD/\nu_a)$; k_a and ν_a are thermal conductivity and kinematic viscosity of air, respectively. Equation (6-29) can be expressed in terms of the spinning velocity (V) and filament cross sectional area (A) using $k_a \nu_a^{-0.334} = 1.22 \times 10^{-4}$ (274) and $D = (4A/\pi)^{\frac{1}{2}}$.

The resulting equation is

$$h = 4.73 \times 10^{-5} \left(\frac{V}{A} \right)^{0.334} \quad (6-30)$$

Sano (293) found for axial motion of a filament in stationary air

$$Nu = 0.25 + 0.15 Re^{0.36} \quad (6-31)$$

which also can be expressed as

$$h \simeq 1.56 \times 10^{-5} + 1.45 \times 10^{-5} \left(\frac{V}{A} \right)^{0.36} \quad (6-32)$$

George (274) presented Broyer's (294) relation for melt spinning data as

$$h = 1.37 \times 10^{-4} \left(\frac{V}{A} \right)^{0.259} \quad (6-33)$$

The equation (6-33) was used in the mathematical model of this study.

Note that the earlier reported regressed equation (6-21) for heat transfer coefficient from the present experimental data is similar in

form to that given by equations (6-30), (6-31), (6-32) and (6-33), but the numerical values of the coefficients differ slightly.

In Figure 6.31 heat transfer coefficient results of the present study are compared with those of Kase and Matsuo, Sano and Broyer. Sano's results are relatively lower but there is good agreement in the results of Kase and Matsuo, Broyer and the present study. There is exceptionally good, perhaps fortuitously good, agreement with Broyer's results. Broyer's equation (6-33) was used in the mathematical model and that is why we already had a good agreement between experimental and predicted temperature profiles at lower spinning speeds before crystallization occurs in the spinline.

Studies reporting measurements of temperature profile (215-217) mostly have found that the profiles are relatively independent of material parameters such as molecular weight. There are no reported studies indicating dependence of heat transfer coefficient on variables such as elongation rate except through the change in velocity or cross sectional area that might result as an incidental part of the experiment. Our findings for nylon-6 melt spinning are in good accord with these earlier generalizations.

Comparison of Experimental Online Profiles and Predictions of Improved Model

The inversion procedure and its results described above provided an opportunity to improve the model by using the regressed relations for elongational viscosity and heat transfer coefficient. These are key relations because overall deformation or diameter drawdown trends are

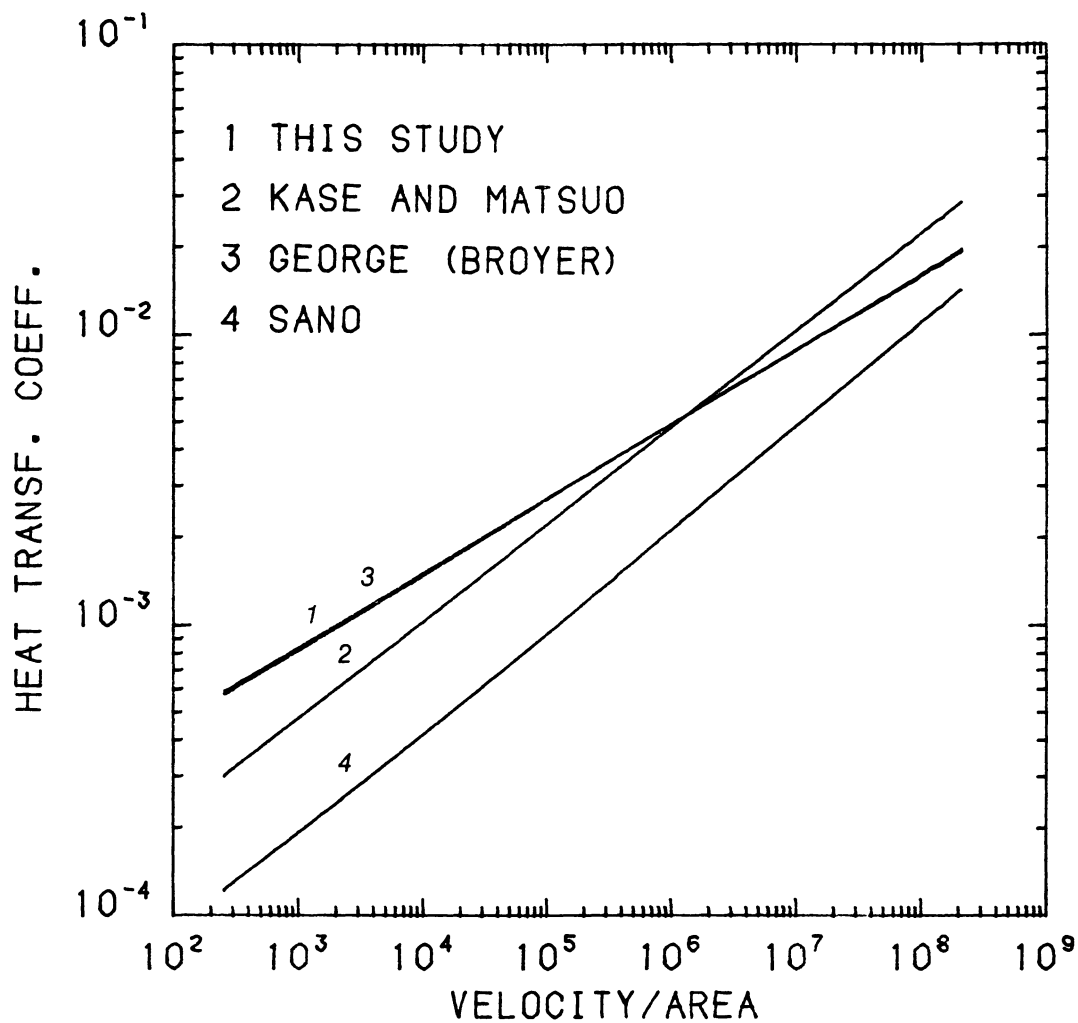


Figure 6.31 Comparison of heat transfer coefficients from inversion procedure of present experimental data and those from the literature.

controlled essentially by elongational viscosity, and the temperature of the spinline is controlled by the heat transfer coefficient. The latter effect is quite important because the key parameters used in the model are temperature dependent.

The most important parameters remaining to be described adequately are the crystallization kinetics parameters. These are key to predict the onset of online crystallization and to accurately predict the trends in birefringence jump due to crystallization at high speeds. The crystallization rate constant was assumed to involve both temperature and orientation dependent terms, and it was assumed that it is of the form suggested by Ziabicki (12):

$$K = K_{max} \exp \left[-4 \ln 2 \left(\frac{T - T_{max}^0}{D^0} \right)^2 + c f_a^2 \right] \quad (6-34)$$

The critical needs in the application of above equation (6-34) are to have reliable data for isothermal crystallization rates at different temperatures, and information on the parameter c which describes the effect of molecular orientation. While some information is available for the effect of temperature on the quiescent isothermal kinetics, there is no reliable reported information on crystallization in oriented systems and consequently the form and value of the parameter c is not known. Initially a constant value of 200 for c computed from Bragato and Gianotti's (76) data for PET was tried but it did not result in good agreement for birefringence predictions with experimental results as shown in Figures 6.9 to 6.12. A possibility of simple change for the parameter c from a constant value of 200 to 100 was explored to obtain a better agreement for birefringence results. In Figure 6.32 the

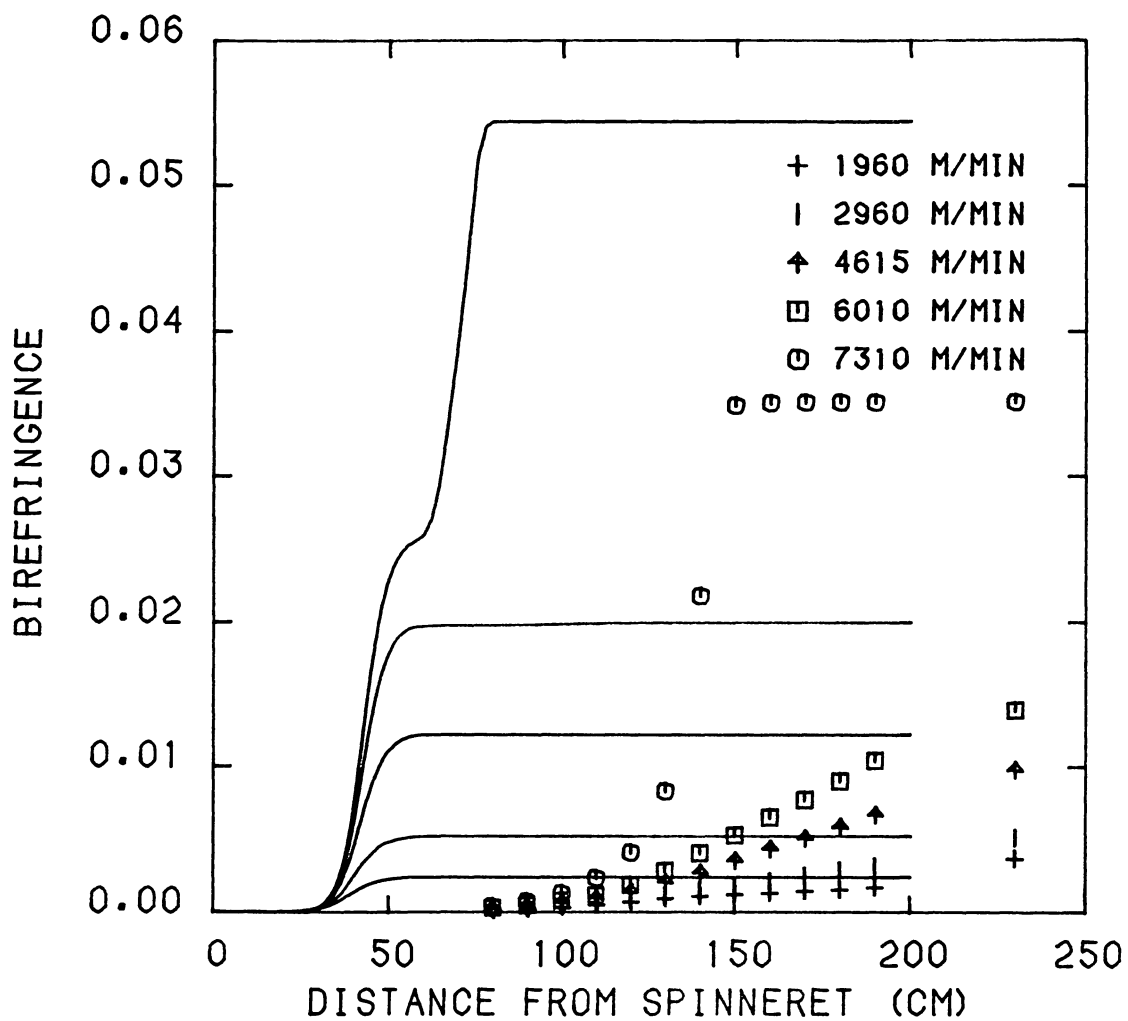


Figure 6.32 Comparison of predicted and experimental birefringence profiles for CN9984 with a mass throughput of 3.073 g/min and $c = 100$.

comparison of experimental birefringence data for CN9984 with mass throughput of 3.073 g/min and model predictions with $c = 100$ is shown. Comparison of Figure 6.9 and Figure 6.32 indicates that the critical take-up speed beyond which the crystallization occurs in the spinline has increased to about 6000 m/min for $c = 100$ from about 4600 m/min for $c = 200$. However, the onset of jump in birefringence still occurs much earlier in the spinline than observed experimentally. Also, the value of birefringence after crystallization is overpredicted. The reason for these differences seems to be that the value of c does not entirely determine the birefringence after crystallization, but stress level developed and consequently the value of amorphous orientation factor plays an important role.

Before trying further changes in the value of c the regressed relations for elongational viscosity and heat transfer coefficient from the inversion procedure were incorporated into the mathematical model and then the predictions were made. This resulted in good agreement of predicted and experimental diameter, temperature and birefringence profiles at lower spinning speeds before crystallization occurs in the spinline. The value of c was then found to be critical to get good agreement at higher speeds. A constant value of $c = 800$ provided a good agreement in birefringence profiles for CN9984 with mass throughput of 3.073 g/min at all the spinning speeds as shown in Figure 6.33. The same value of c for same resin with mass throughput of 5.154 g/min predicted jump in birefringence profiles (due to crystallization) whereas experimentally no jump in birefringence was seen in the range of take-up

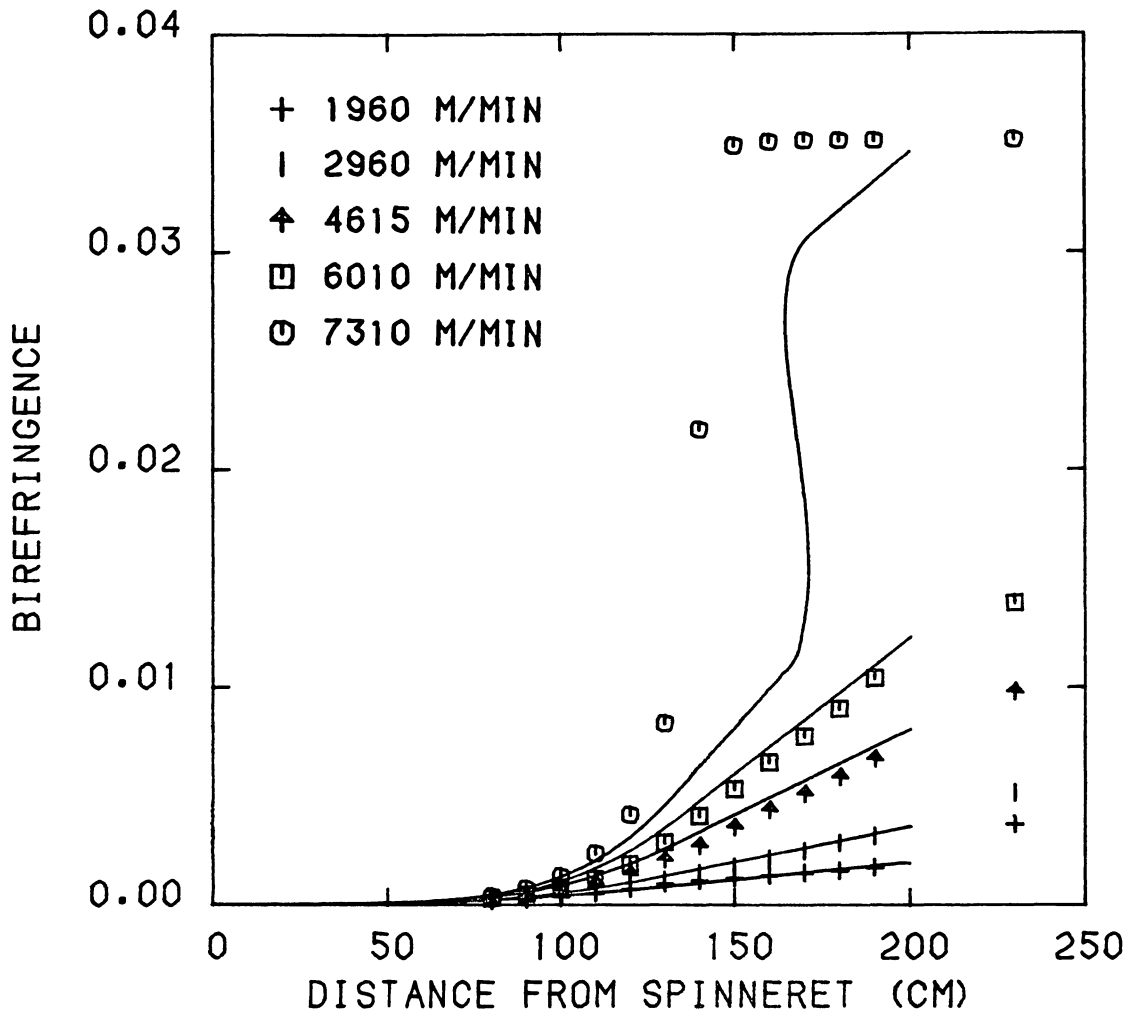


Figure 6.33 Comparison of predicted (from improved model) and experimental birefringence profiles for CN9984 with a mass throughput of 3.073 g/min and $c = 800$.

speeds studied as shown in Figure 6.34. Thus, the constant value of c does not seem to be appropriate.

Zieminski (33) found that temperature dependent form of c was most suitable in getting good agreement for his birefringence data for high speed melt spun nylon-66. We followed a similar approach and found that the needed form of parameter c was $1.25 \times 10^5 / (T_m - T)$. This form of c was considered to incorporate the effect of different supercoolings involved with the variation of mass throughput. This simply means that the effect of orientation on crystallization rate is itself dependent on the temperature at which that orientation exists. Before using such a form for c the possibility of blowing rate constant was investigated when $T \approx T_m$. the rate constant for CN9984 with mass throughput of 3.073 g/min with $c = 1.25 \times 10^5 / (T_m - T)$ versus temperature are shown in Figure 6.35. At lower speeds the rate constant versus temperature curves exhibit a symmetrical distribution with maximum in rate constant, K_{max} , of about 0.14 at corresponding temperature, T_{max} , of about 145°C. With the increasing speeds, but before the crystallization occurs in the spinline, the value of K_{max} increased slightly, presumably because of increase in f_a . This type of behavior in the rate constant has been reviewed by Ziabicki (12) for some experimental studies of elastomers. At higher speeds, where the crystallization occurs in the spinline, initially the rate constant has the above discussed behavior, but a jump in rate constant takes place as some critical value of f_a is attained. Note that for temperature dependent form of c in the temperature range of $T \approx T_m$ the rate constant turned out to be essentially zero because of the fact that c is multiple of f_a^2 in equation (6-34) and value of f_a in

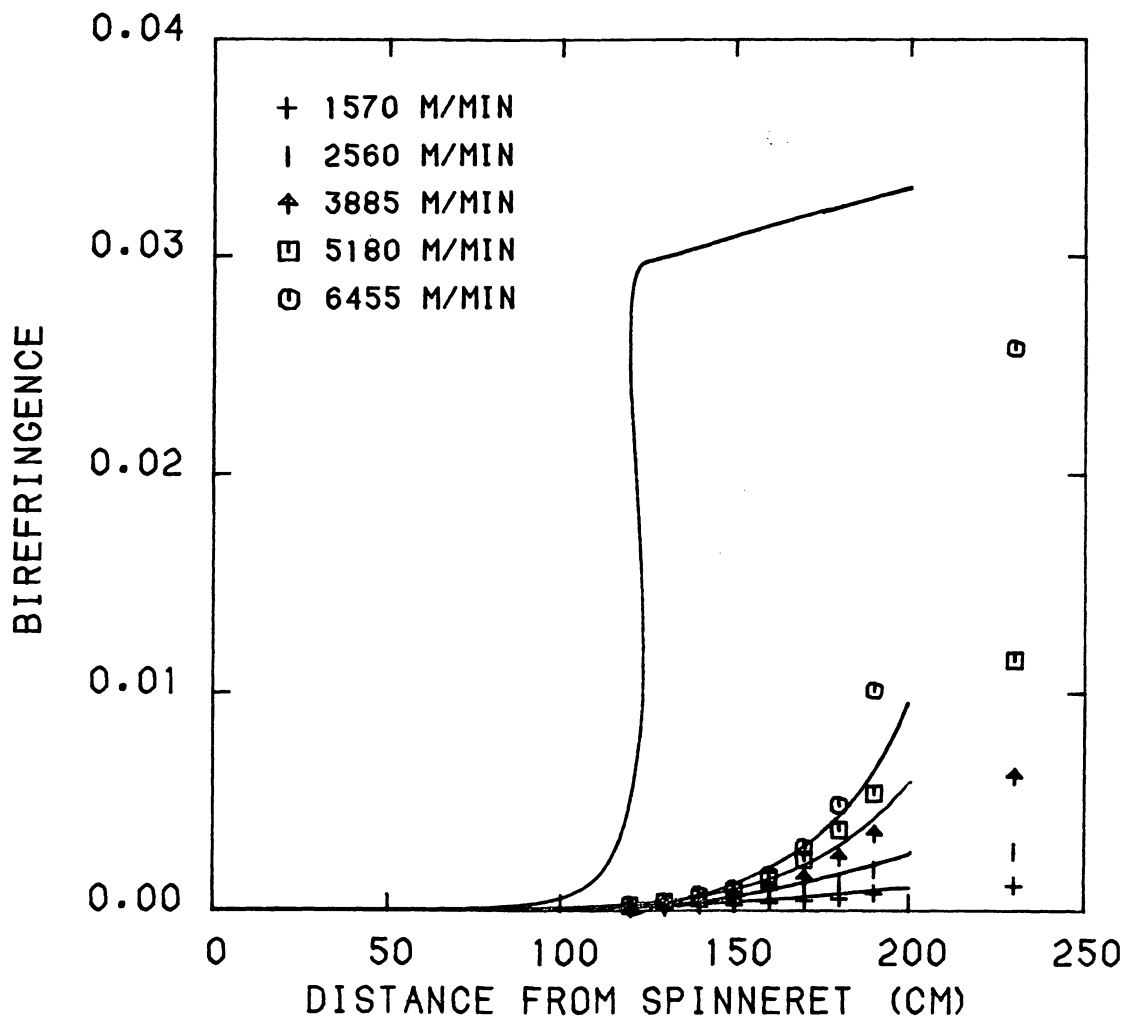


Figure 6.34 Comparison of predicted (from improved model) and experimental birefringence profiles for CN9984 with a mass throughput of 5.154 g/min and $c = 800$.

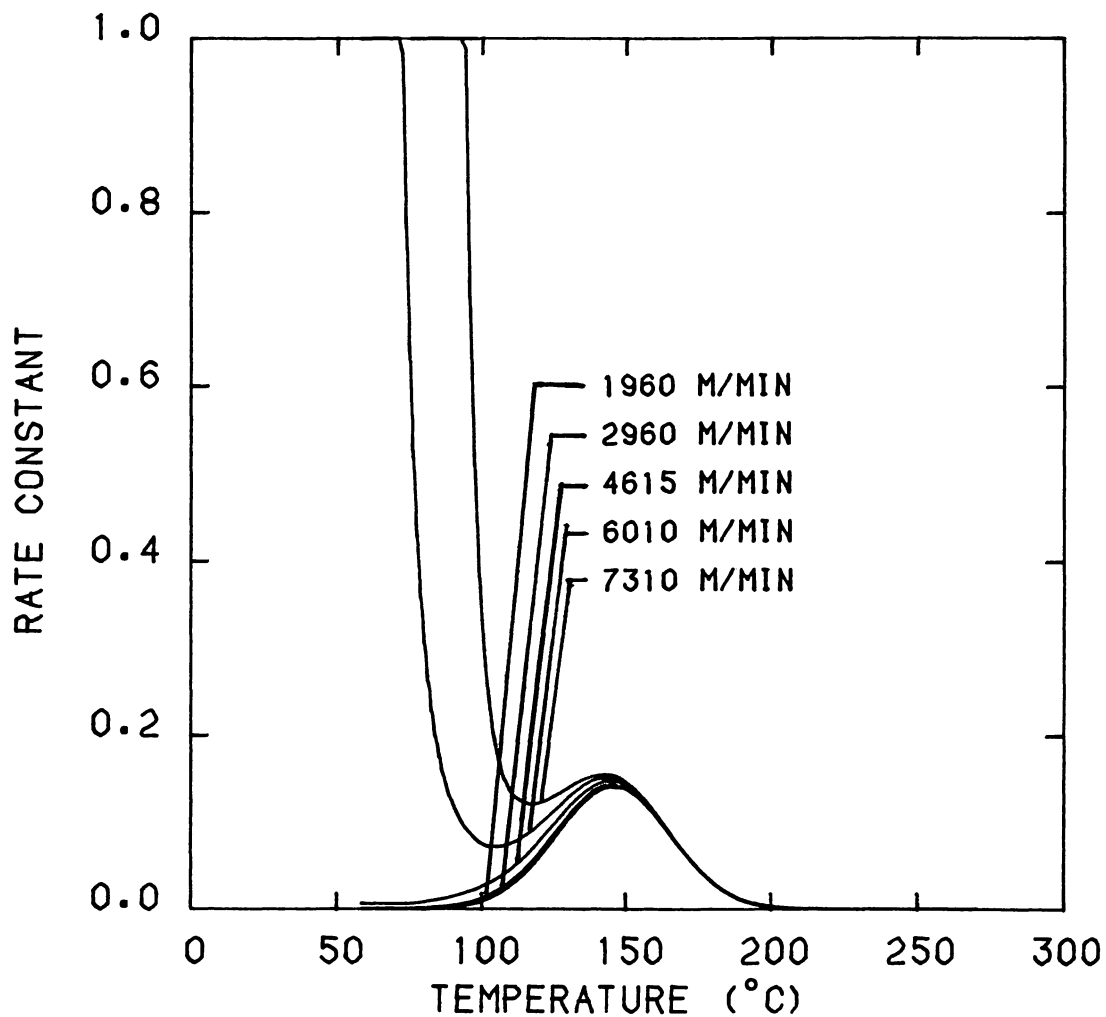


Figure 6.35 Rate constant versus temperature for CN9984 with a mass throughput of 3.073 g/min and $c = 1.25 \times 10^5 / (T_m - T)$.

the above temperature range is of the order of 10^{-5} to 10^{-4} . The singularity at $T = T_m$ was further avoided by incorporating a condition in the computer program.

The regressed relations for elongational viscosity and heat transfer coefficient and the above discussed parameter c were incorporated into the mathematical model (given in Appendix F) and the new calculations were made. Comparison of the improved model predictions and the experimental online profiles is shown in Figures 6.36 to 6.39 for diameter, in Figures 6.40 to 6.43 for temperature and in Figures 6.44 to 6.47 for birefringence profiles. It is important to note that the temperature dependent form of c has provided good agreement in birefringence profiles for two different mass throughputs (compare Figure 6.44 and Figure 6.46 for CN9984 resin) unlike the preliminary result obtained using a constant value of c as discussed earlier in comparison of Figure 6.33 and 6.34. The temperature dependent form of c , with same numerical value, also provided good agreement for both molecular weights of nylon-6 except for some minor differences at high speeds. Although the necking is predicted by the model, the positions on the spinline does not match exactly; temperature profile shows an increase in temperature rather than a plateau observed experimentally and there is a difference in position where the birefringence jump takes place. Thus, it seems that the value of c is independent of molecular weight, presumably because c is a coefficient of amorphous orientation factor (f_a) in the rate constant equation and the value of f_a is determined by the stress level developed. The take-up speeds at which the same stress level develops is different for different molecular

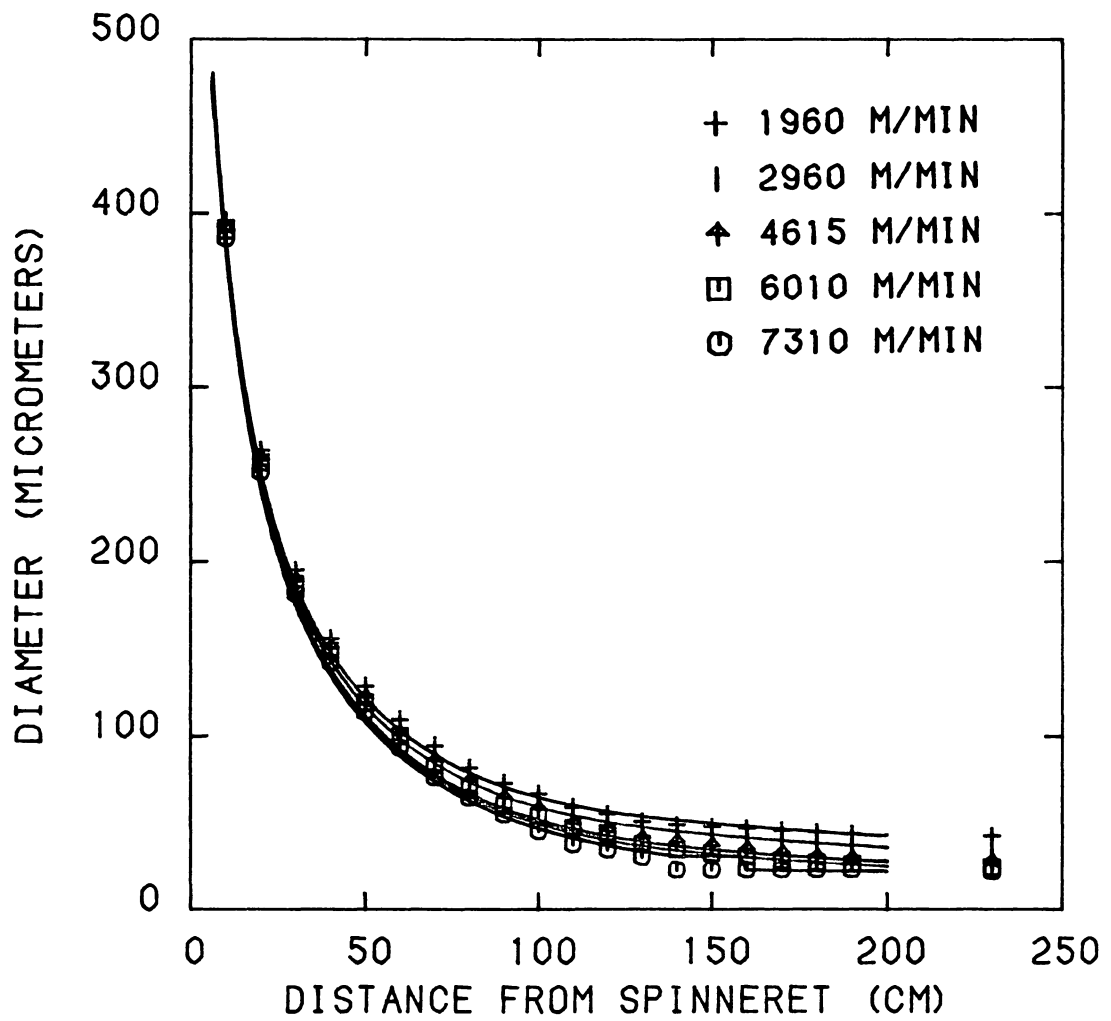


Figure 6.36 Comparison of predicted (from improved model) and experimental diameter profiles for CN9984 with a mass throughput of 3.073 g/min.

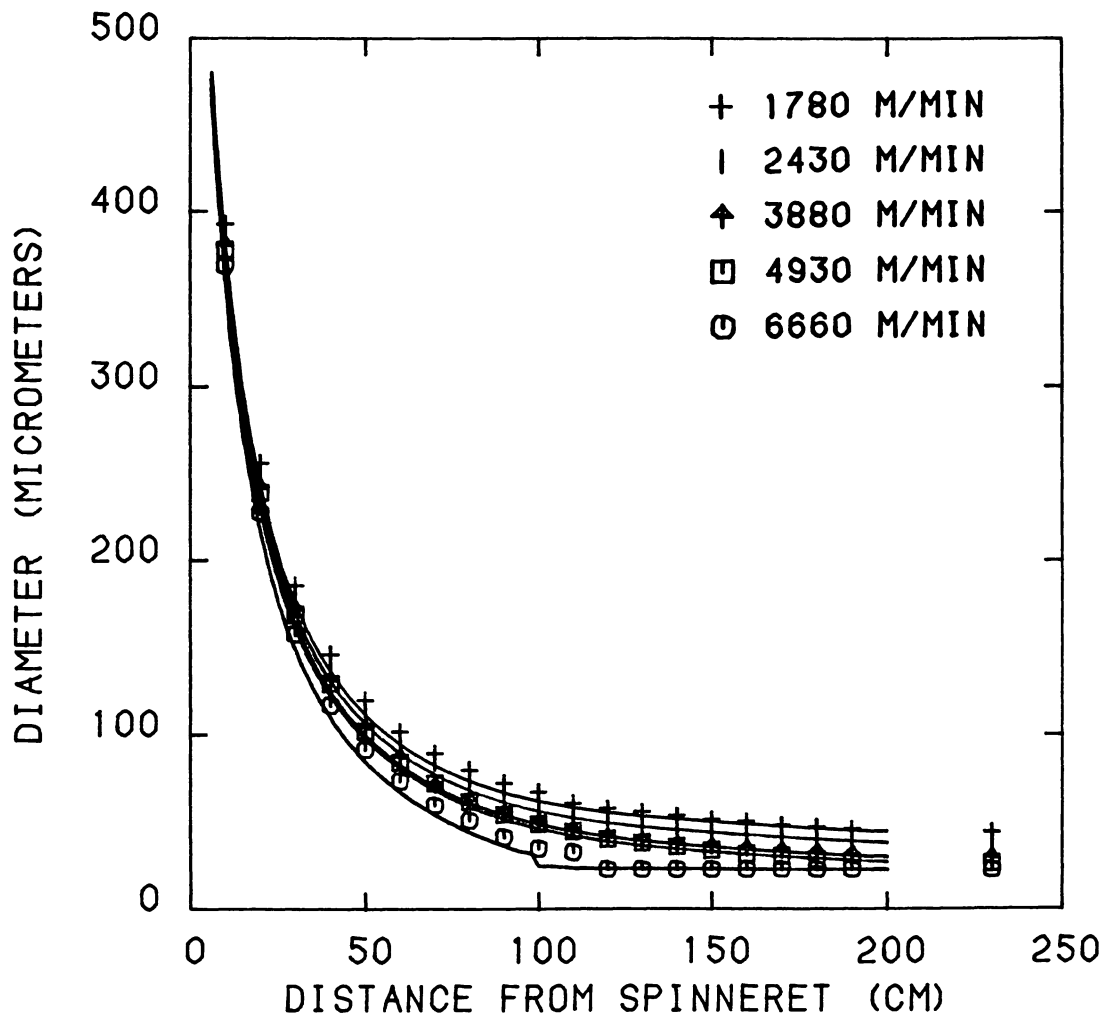


Figure 6.37 Comparison of predicted (from improved model) and experimental diameter profiles for BHS with a mass throughput of 2.993 g/min.

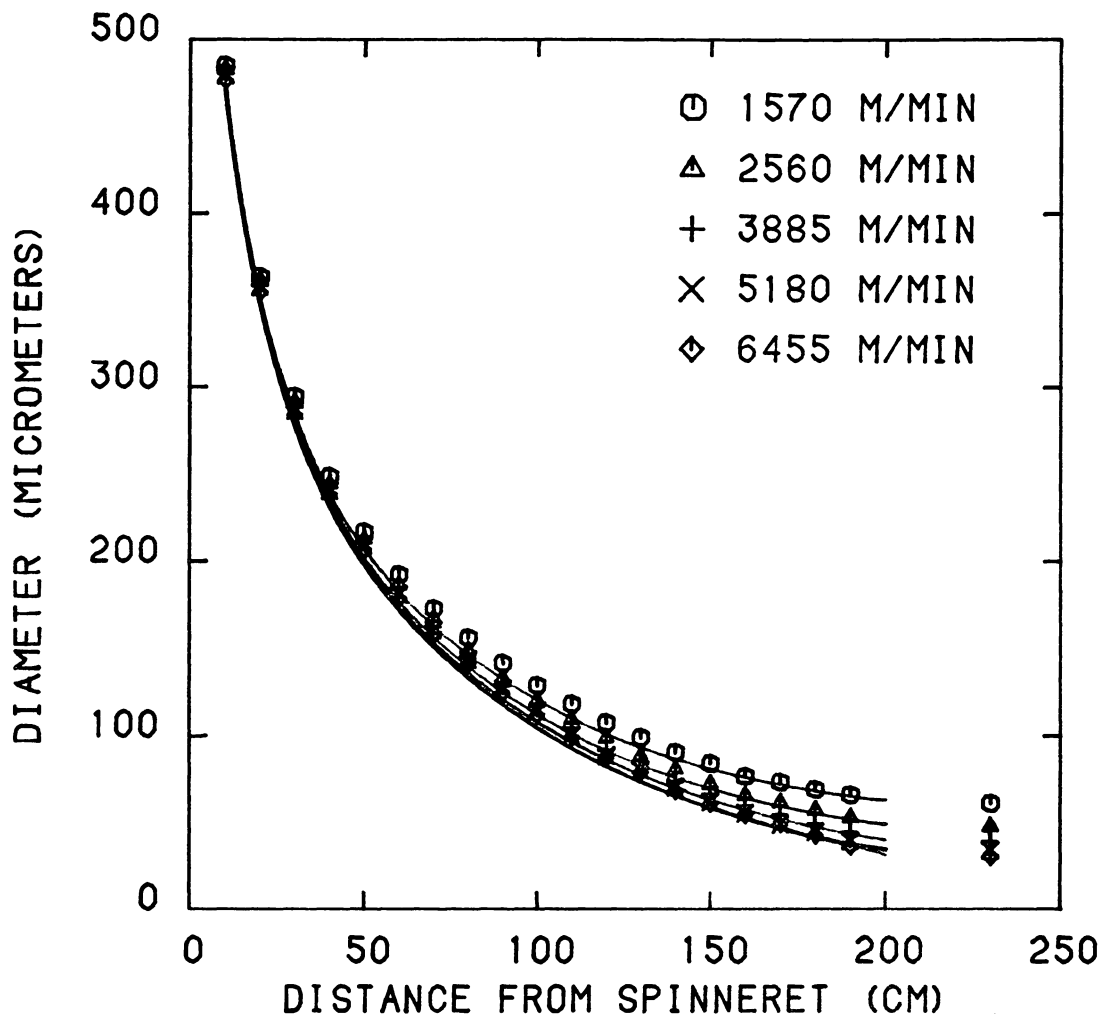


Figure 6.38 Comparison of predicted (from improved model) and experimental diameter profiles for CN9984 with a mass throughput of 5.154 g/min.

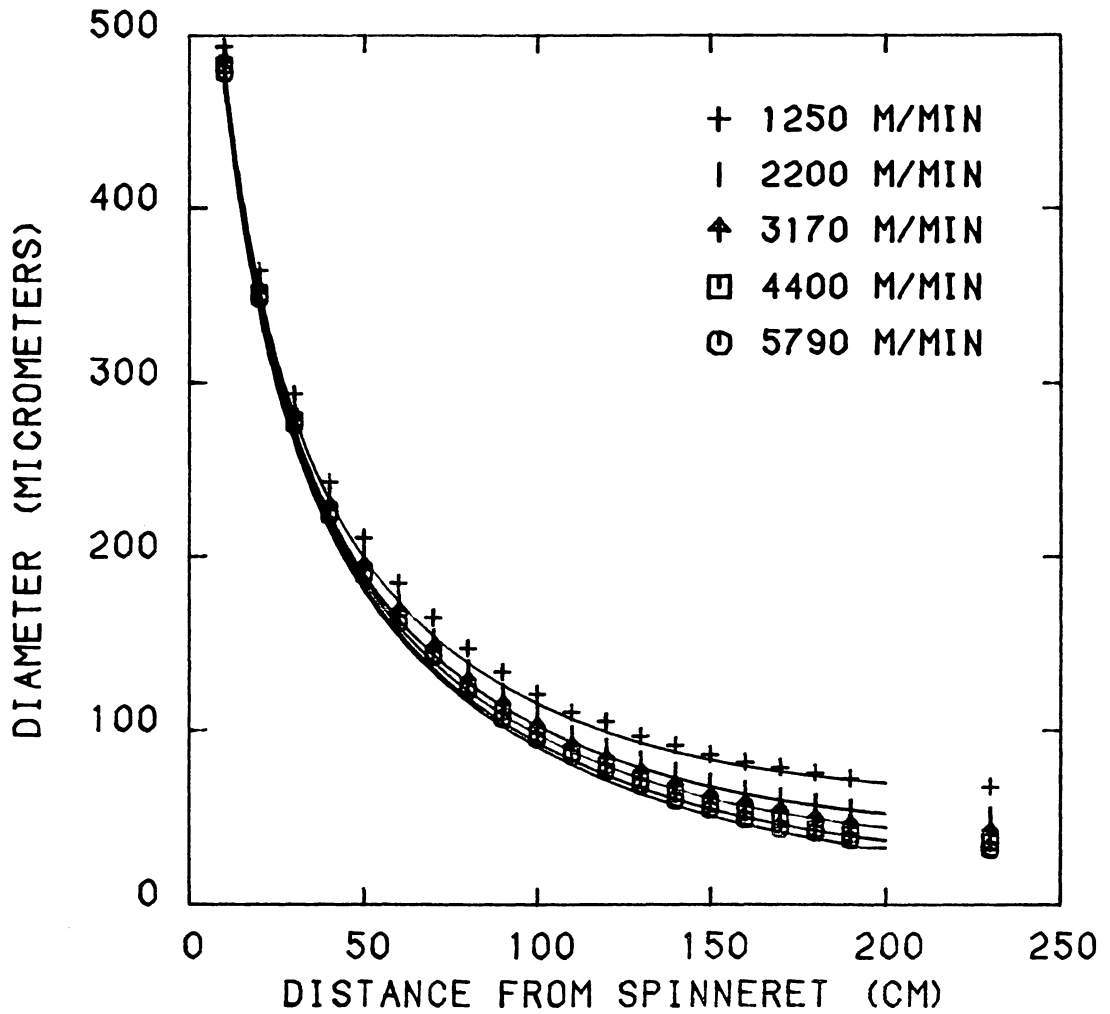


Figure 6.39 Comparison of predicted (from improved model) and experimental diameter profiles for BHS with a mass throughput of 5.069 g/min.

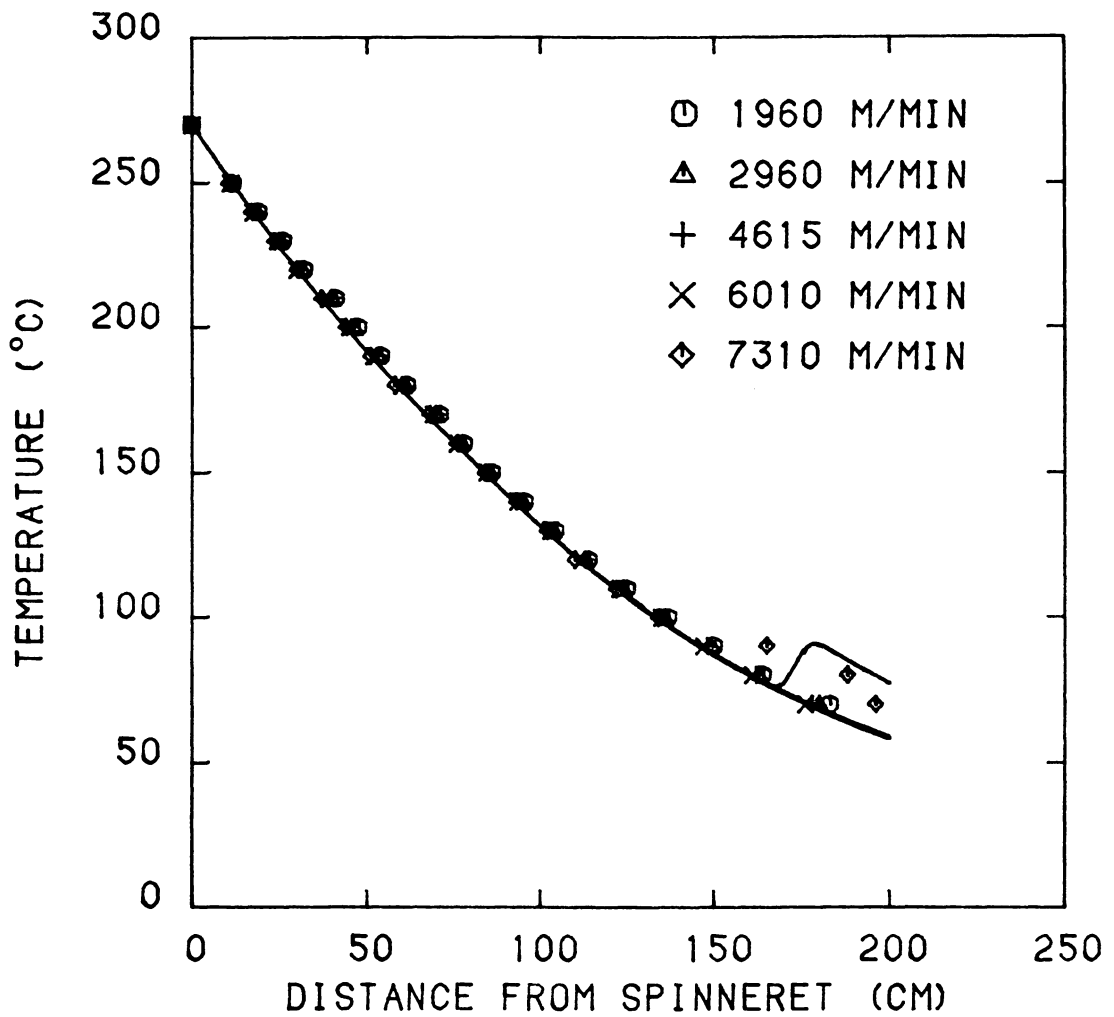


Figure 6.40 Comparison of predicted (from improved model) and experimental temperature profiles for CN9984 with a mass throughput of 3.073 g/min.

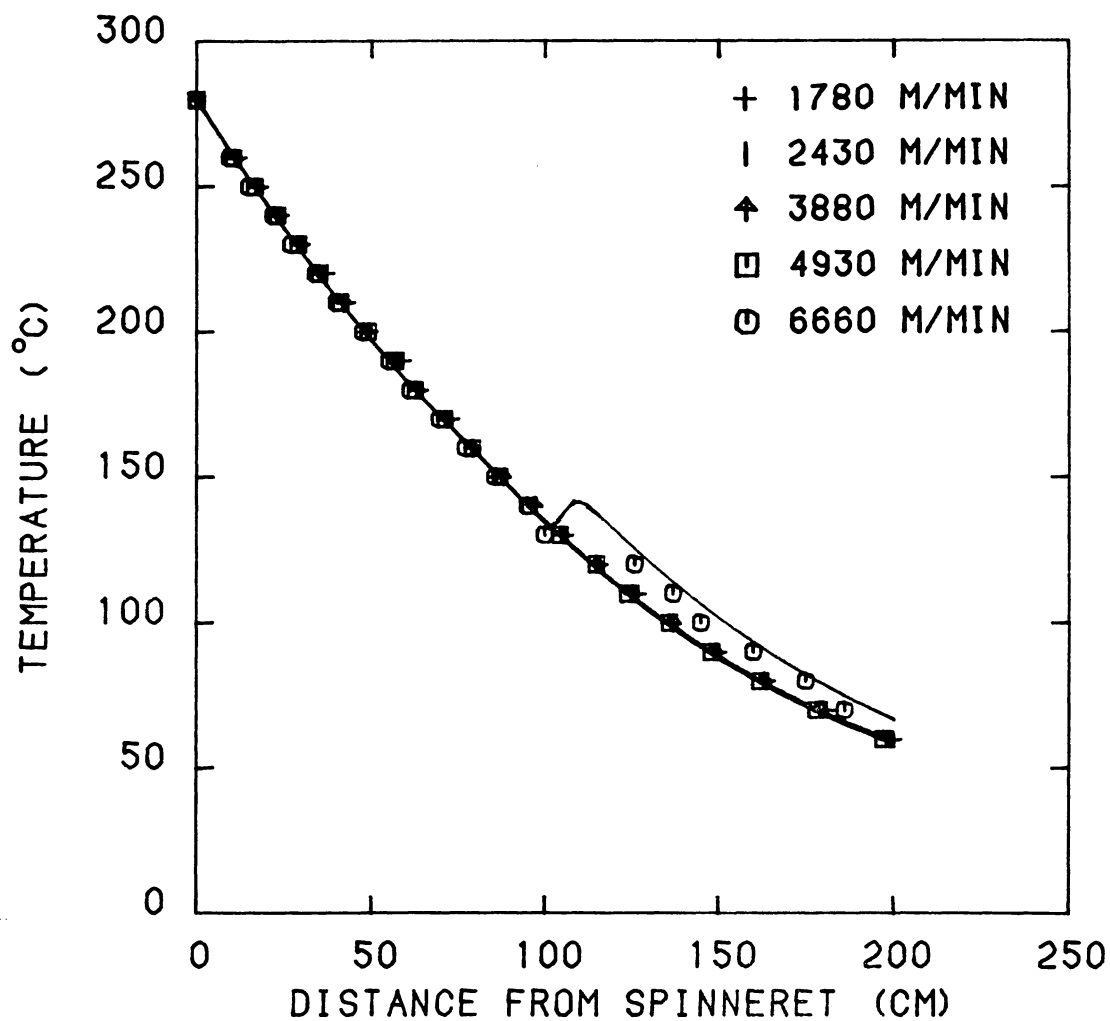


Figure 6.41 Comparison of predicted (from improved model) and experimental temperature profiles for BHS with a mass throughput of 2.993 g/min.

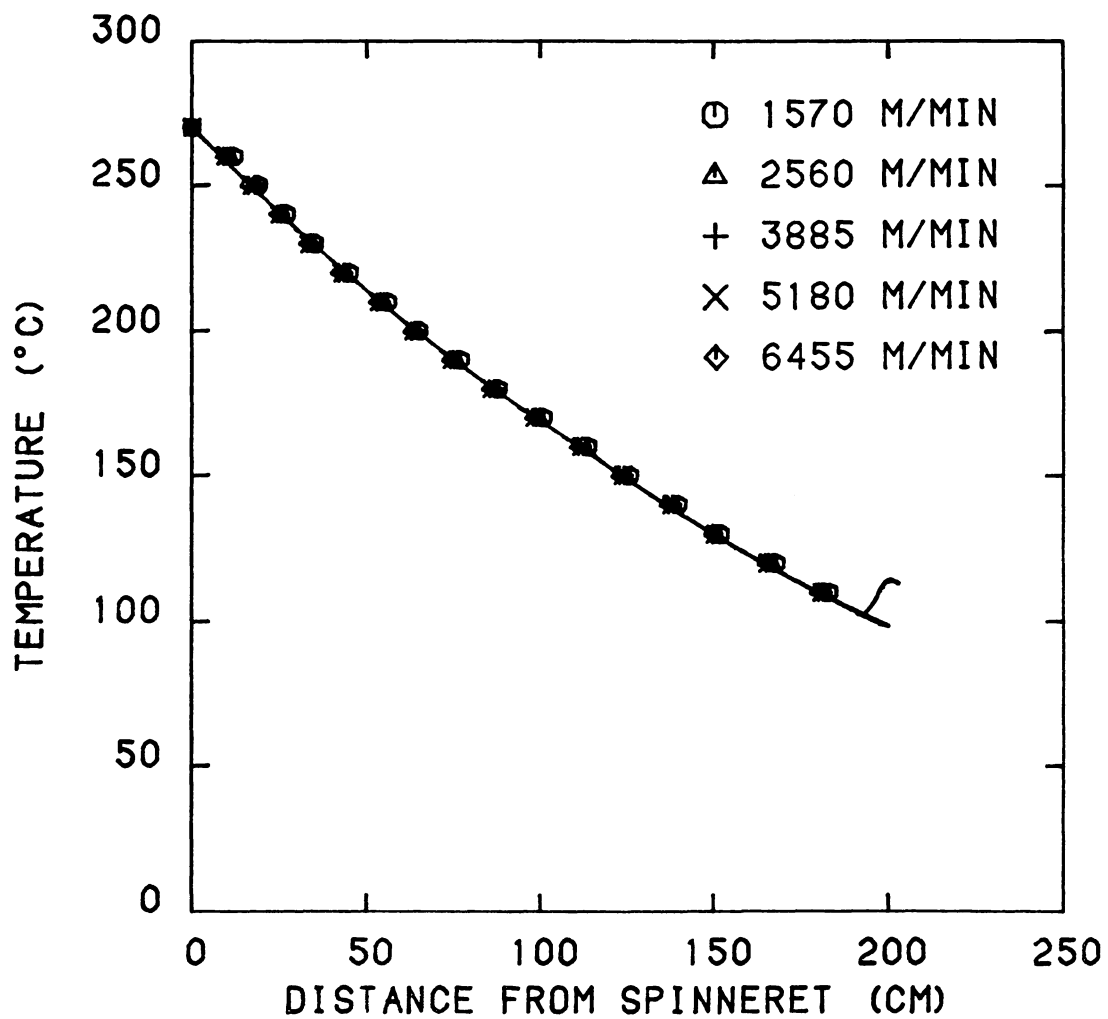


Figure 6.42 Comparison of predicted (from improved model) and experimental temperature profiles for CN9984 with a mass throughput of 5.154 g/min.

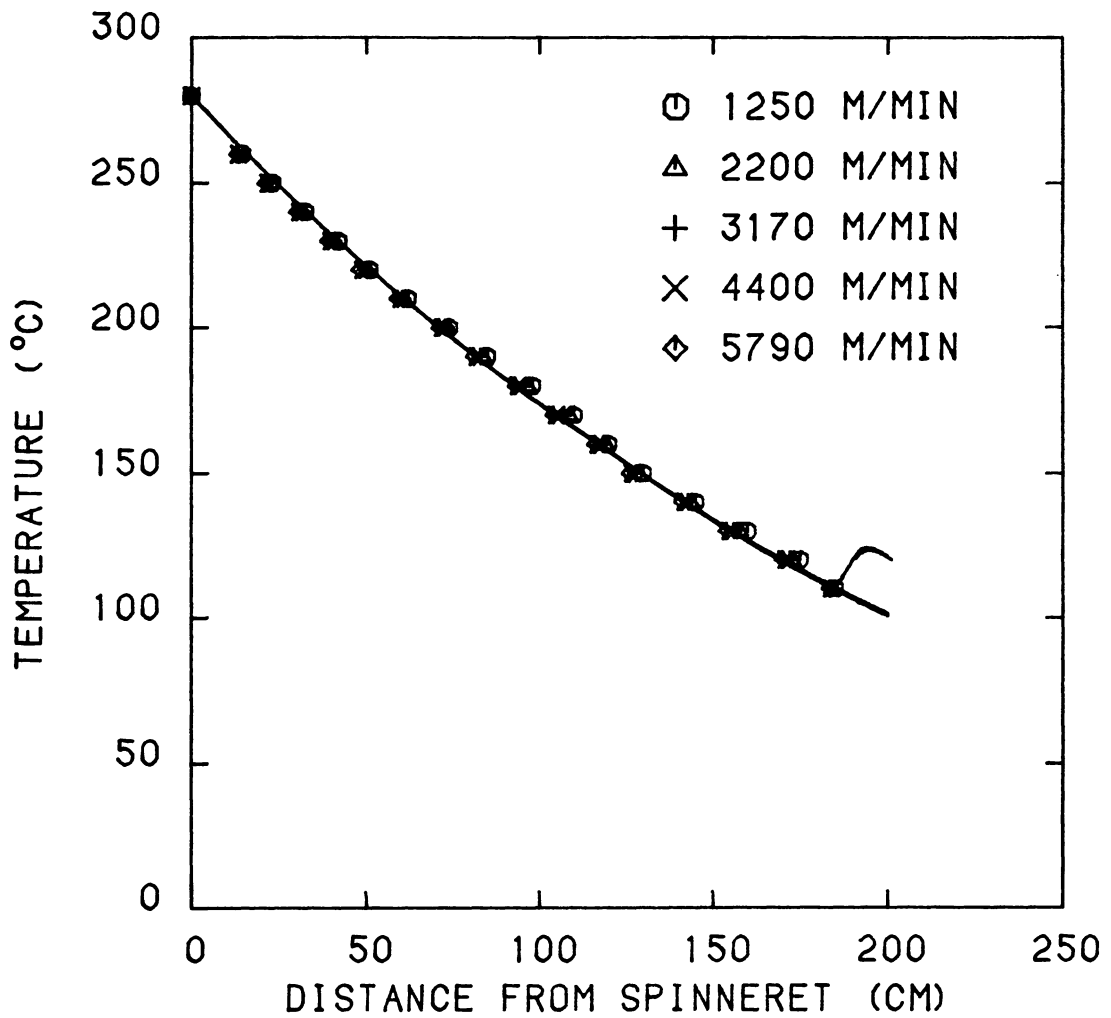


Figure 6.43 Comparison of predicted (from improved model) and experimental temperature profiles for BHS with a mass throughput of 5.069 g/min.

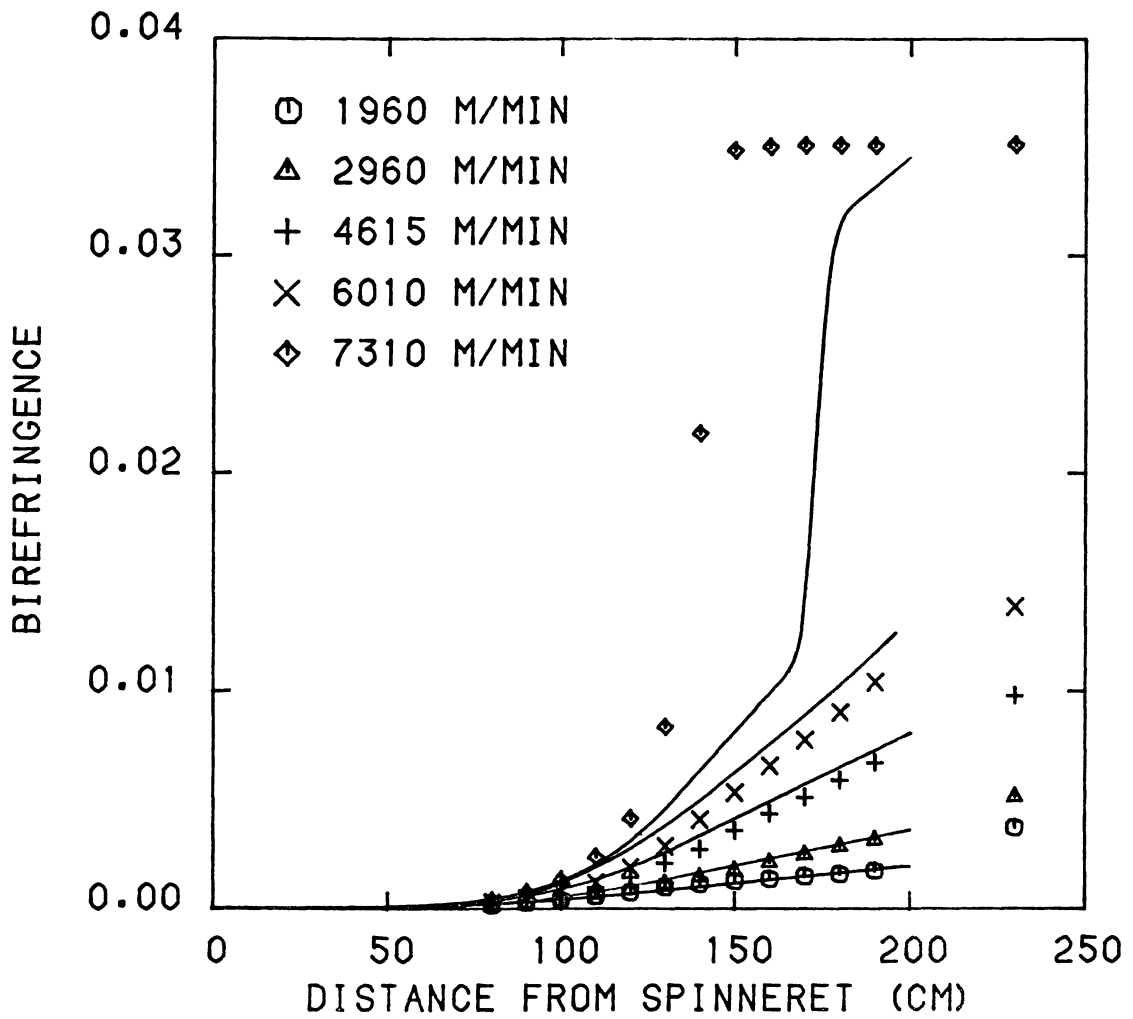


Figure 6.44 Comparison of predicted (from improved model) and experimental birefringence profiles for CN9984 with a mass throughput of 3.073 g/min.

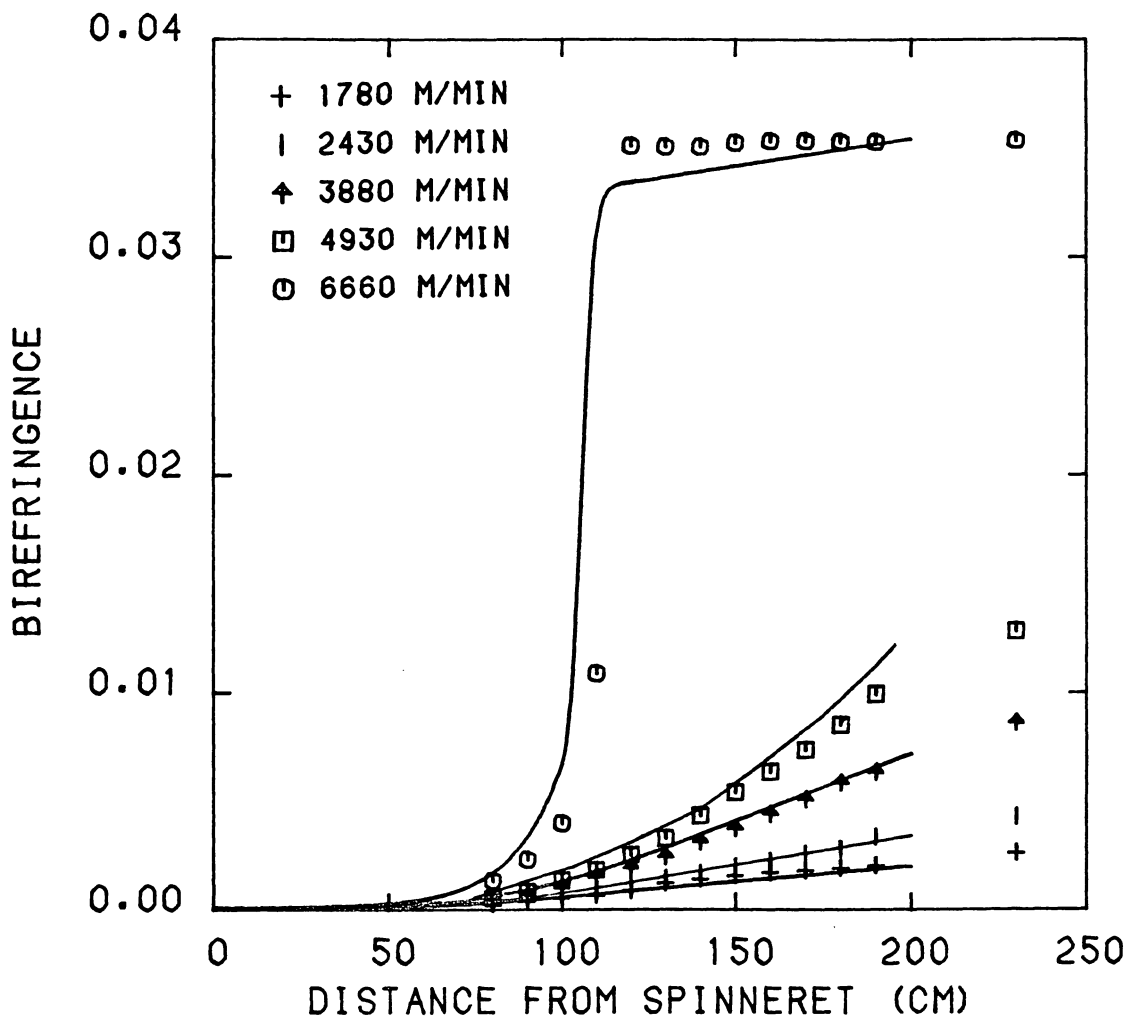


Figure 6.45 Comparison of predicted (from improved model) and experimental birefringence profiles for BHS with a mass throughput of 2.993 g/min.

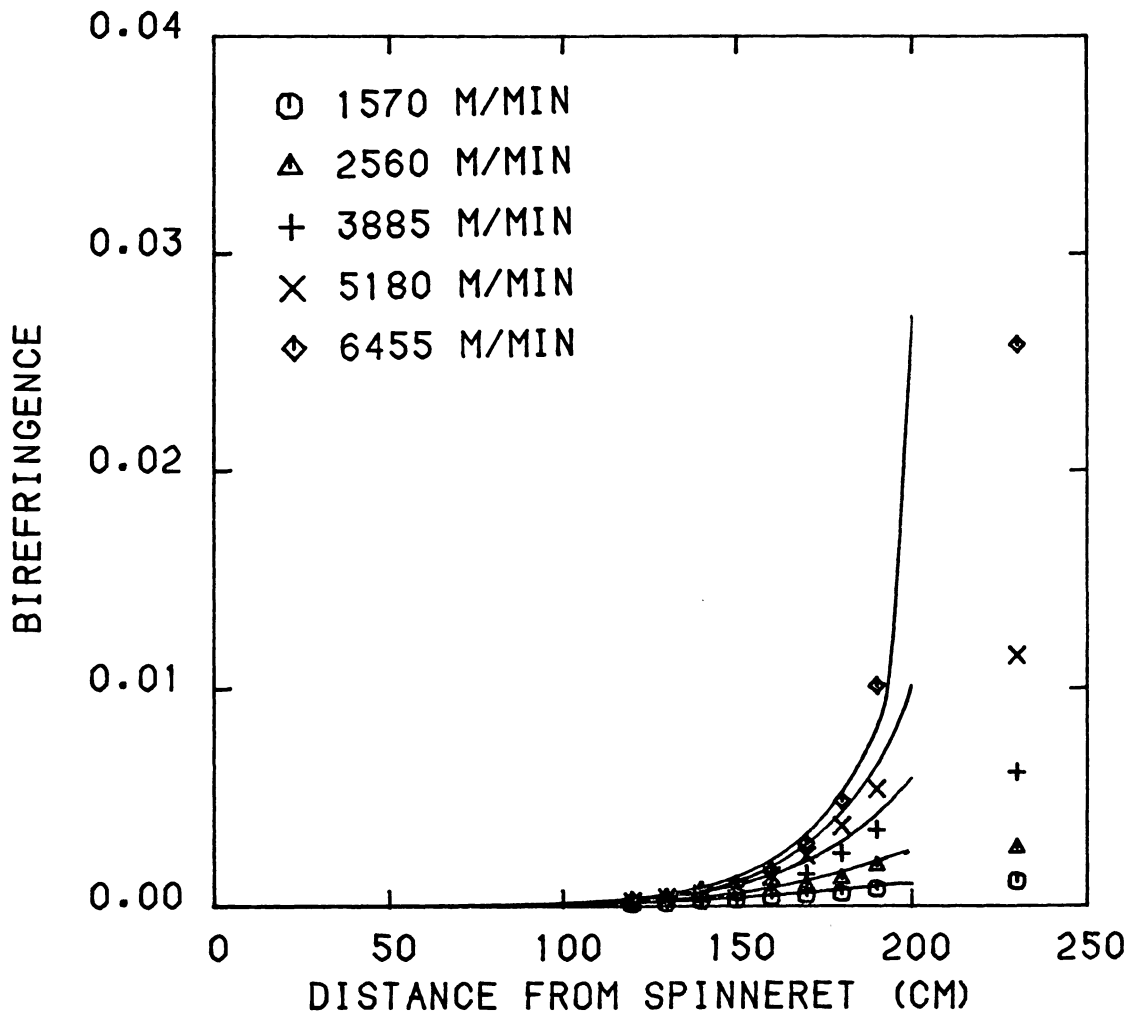


Figure 6.46 Comparison of predicted (from improved model) and experimental birefringence profiles for CN9984 with a mass throughput of 5.154 g/min.

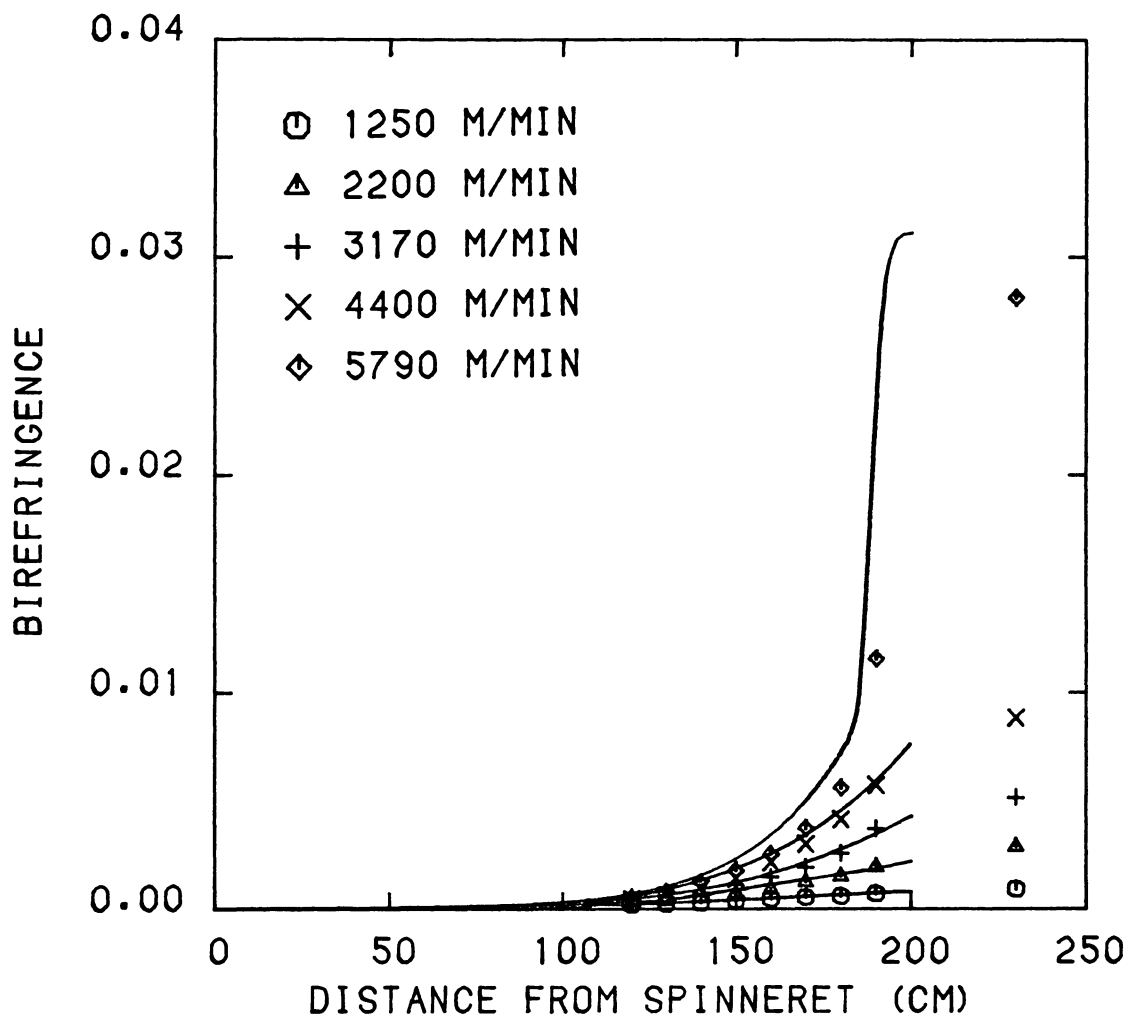


Figure 6.47 Comparison of predicted (from improved model) and experimental birefringence profiles for BHS with a mass throughput of 5.069 g/min.

weights and that is why the crystallization occurs at different take-up speeds for the two resins. BHS, the higher molecular weight resin, develops higher stress level than CN9984, the lower molecular weight resin, at the same take-up speed because of higher viscosity of BHS.

CHAPTER 7

CONCLUSIONS AND RECOMMENDATIONS

The major objective of this research was to understand the physics of fiber formation during high speed melt spinning of nylon-6. This objective has been achieved by developing a mathematical model and by checking its validity and quantitative success through experimentation.

The mathematical model developed is capable of predicting variations in dynamics and structure development with resin and process variables. The development of the model included deriving working relationships based on fundamental equations of continuity, momentum and energy and the models for rheological behavior of nylon-6, birefringence and molecular orientation and crystallization kinetics. These working relationships were reduced to ordinary differential equations using physically reasonable assumptions. The model was applied to two different molecular weight nylon-6 polymers melt spun at two different mass throughputs. This involved numerical integration of the working relationships, use of the physical properties of nylon-6 from the literature and the specification of processing parameters. The dynamic predictions were in terms of velocity, diameter, temperature, velocity gradient, rheological force and stress profiles and the structure formation predictions were in terms of amorphous orientation factor, birefringence and crystalline index profiles.

The online experimental measurements of diameter, temperature and birefringence profiles for both resins and two different mass throughputs were key to check and verify the quantitative success of

model predictions. Essentially non-contact measurement techniques were employed to ensure data with the least error possible. A non-contact diameter measurement technique was developed to collect numerous data and then a statistical method was employed to obtain the most probable diameter. The statistical method also provided the accurate estimate of errors involved in measurement. The model predictions with literature physical property inputs were then compared with the experimental results. The model predictions were qualitatively consistent with the trends observed in experimental results. These trends are summarized below:

1. At low spinning speeds, nylon-6 crystallizes on the bobbin rather than in the spinline.
2. High spinning speeds produce high spinline stresses and increased molecular orientation which induces crystallization in the spinline.
3. Further increase of spinning speeds after onset of crystallization causes crystallization to initiate closer to the spinneret and at higher temperature.
4. Increasing the molecular weight of the resin produces higher spinline stresses (due to higher melt viscosity) and induces online crystallization at a lower critical take-up velocity or at a higher temperature and smaller distance from the spinneret at chosen high take-up velocities.
5. Lowering the mass throughput has similar effects as for increasing the molecular weight.
6. Under some spinning conditions (generally lower mass

throughput and high speeds) the energy released by crystallization increases the local filament temperature which decreases the melt viscosity, allowing rapid local deformation or neck formation in the spinline.

The model predictions based on literature input physical properties were not quantitatively satisfactory. In particular the predictions showed faster drawdown and earlier onset of crystallization than observed experimentally.

An analytical inversion procedure was developed to extract critical input properties of elongational viscosity and heat transfer coefficient for the nylon-6's studied from online experimental diameter and temperature profiles. Incorporation of these properties into the model gave good quantitative agreement between model predictions and experimental profiles.

The continuation of this work is recommended in at least three possible areas. These areas are model applications, model improvements and refinement in experimental measurements.

In this work the analysis for the melt spinning process with a constant mass throughput and for a single filament has been successfully developed. Multifilament yarn spinning producing constant denier yarns is of importance in commercial operations. Further, these conditions demand effective quench stacks around the spinline, the simplest of such systems is transverse cross air flow. In addition to nylon-6, a great interest lies in melt spinning of nylon-66, PET and polyolefins. These different polymers may need the application of different constitutive

equation to account for their rheological behavior, molecular weight distribution effects, different crystallization behavior, etc.

The above discussed model applications provide an opportunity to incorporate further possible improvements in the model. The radial variations in this study were neglected in order to reduce the mathematical complexity of the problem. However, the multifilament yarn spinning with quench system may incorporate radial variations that affect properties of the individual filaments significantly. With the availability of improved numerical computer softwares the effect of radial variations can be handled. Also the multifilament yarn spinning with quench system lead to the variation in quench medium velocity and medium temperature within the filament bundle and consequently the variability in yarn properties. Utilization of finite element analysis for air drag and heat transfer effects can be of importance in understanding these effects quantitatively.

The experimental measurements really provide opportunity to verify the predictability of the model and consequently refinement in these measurements seems to be most important aspect of successful modeling. In this study computer controlled measurement of diameter provided statistically calculated diameter and, more importantly, the estimate of error associated with such measurement. A similar approach can be adopted in other measurements; particularly in online temperature measurements because of significant temperature dependence of physical properties. The simultaneous measurements of diameter, temperature, birefringence and tension profile at a particular position in the spinline and at a particular set of process conditions is critical to

reduce the effect due to day to day differences in process conditions
and environment.

REFERENCES

LIST OF REFERENCES

1. Haynes, W., in "Cellulose, The Chemical That Grows", Doubleday, Garden City, 1953.
2. Swan, J. W., English Pat., 5978 (1883).
3. de Chardonnet, H., U.S. Pat., 394,559 (1888); French Pat., 165,349 (1884); French Pat., 172,207 (1885).
4. de Chardonnet, U.S. Pat., 531,158 (1894).
5. Stearn, C. H., English Pat., 1020 (1898).
6. Kaufman, M., in "The First Century of Plastics", Plastics Institute, London, 1963.
7. Carothers, W. H. and G. J. Berchet, J. Am. Chem. Soc., 52, 5289 (1930).
8. Carothers, W. H. and J. W. Hill, J. Am. Chem. Soc., 54, 1566 (1932).
9. Carothers, W. H. and J. W. Hill, J. Am. Chem. Soc., 54, 1579 (1932).
10. Carothers, W. H. and F. J. van Natta, J. Am. Chem. Soc., 55, 4714 (1932).
11. Ziabicki, A., in "Man-Made Fibers", H. F. Mark, S. M. Atlas and E. Cernia, Eds., Interscience, New York, 1967.
12. Ziabicki, A., "Fundamentals of Fiber Formation", Interscience, New York, 1976.
13. Acierno, D., J. N. Dalton, J. M. Rodriguez and J. L. White, J. Appl. Polym. Sci., 15, 2395 (1971).
14. Chen, I. J., G. E. Hagler, L. E. Abbott, D. C. Bogue, and J. L. White, Trans. Soc. Rheol., 16, 473 (1972).
15. Abbott, L. E. and J. L. White, Appl. Polym. Symp., 20, 247 (1973).
16. Dees, J. R. and J. E. Spruiell, J. Appl. Polym. Sci., 18, 1053 (1974).
17. White, J. L., K. C. Dharod and E. S. Clark, J. Appl. Polym. Sci., 18, 2539 (1974).
18. White, J. L. and Y. Ide, in "Fiber and Yarn Processing", J. L. White, Ed., Appl. Polym. Symp., 27, 61 (1975).

19. Spruiell, J. E. and J. L. White, *Polym. Eng. Sci.*, 15, 660 (1975).
20. Spruiell, J. E. and J. L. White, in "Fiber and Yarn Processing", J. L. White, Ed., *Appl. Polym. Symp.*, 27, 121 (1975).
21. White, J. L. and J. F. Roman, *J. Appl. Polym. Sci.*, 20, 1005 (1976).
22. Ide, Y. and J. L. White, *J. Appl. Polym. Sci.*, 20, 2511 (1976).
23. Bankar, V. G., Ph.D. Dissertation, University of Tennessee-Knoxville, 1976.
24. Nadella, H., H. Henson, J. E. Spruiell and J. L. White, *J. Appl. Polym. Sci.*, 21, 3003 (1977).
25. Bankar, V., J. E. Spruiell and J. L. White, *J. Appl. Polym. Sci.*, 21, 2135 (1977).
26. Bankar, V., J. E. Spruiell and J. L. White, *J. Appl. Polym. Sci.*, 21, 2341 (1977).
27. Danford, M. D., J. E. Spruiell and J. L. White, *J. Appl. Polym. Sci.*, 22, 3351 (1978).
28. Nadella, H., J. E. Spruiell and J. L. White, *J. Appl. Polym. Sci.*, 22, 3121 (1978).
29. Gianchandani, J., M.S. Thesis, University of Tennessee-Knoxville, 1980.
30. Gianchandani, J., J. E. Spruiell and E. S. Clark, *J. Appl. Polym. Sci.*, 27, 3527 (1982).
31. Suryadevara, J., M. S. Thesis, University of Tennessee-Knoxville, 1983.
32. Bai, C. C., Ph.D. dissertation, University of Tennessee-Knoxville, 1984.
33. Zieminski, K. F., Ph.D. dissertation, University of Tennessee-Knoxville, 1986.
34. Koyama, K., J. Suryadevara and J. E. Spruiell, *J. Appl. Polym. Sci.*, 31, 2203 (1986).
35. Keller, A. and M. J. Machin, *J. Macromol. Sci. - Phys.*, B1, 41 (1967).
36. Fung, P. Y. F. and S. H. Carr, *J. Macromol. Sci.*, B6, 621 (1972).

37. Samuels, R. J., "Structured Polymer Properties", John Wiley, New York, 1974.
38. Simpson, P. G., J. H. Southern and R. C. Ballman, Text. Res. Inst., 51, 97 (1981).
39. Chappel, F. P., M. F. Culpin, R. G. Godsen and T. C. Tanter, J. Appl. Chem., 14, 12 (1964).
40. Ziabicki, A. and K. Kedzierska, J. Appl. Polym. Sci., 6, 111 (1962).
41. Hamana, I., M. Matsui and S. Kato, Milliand Textilberichte, 50, 382 (1969).
42. Hamana, I., M. Matsui and S. Kato, Milliand Textilberichte, 50, 499 (1969).
43. Ishibashi, T., K. Aoki and T. Ishii, J. Appl. Polym. Sci., 14, 1597 (1970).
44. Matowich, M. A. and J. R. A. Pearson, IEC Fund., 8, 512, (1969).
45. Sano, Y. and K. Orii, Sen-I Gakkaishi, 24, 212 (1968).
46. Sakiadis, B. C., A.I.Ch.E. J., 7, 467 (1961).
47. Cogswell, F. N., Appl. Polym. Symp., 27, 3 (1975).
48. Ishizuka, O. and K. Koyama, Polymer, 21, 164 (1980).
49. Koyama, K. and O. Ishizuka, Sen-I Gakkaishi, 36, 472 (1980).
50. Ide, Y. and J. L. White, J. Appl. Polym. Sci., 22, 1061 (1978).
51. Minoshima, W., J. L. White and J. E. Spruiell, Polym. Eng. Sci., 20, 1166 (1980).
52. Tanaka, H. and J. L. White, Polym. Eng. Rev., 1, 89 (1981).
53. Chan, Y., J. L. White and Y. Oyanagi, J. Rheol., 22, 507 (1978).
54. Lobe, V. M. and J. L. White, Polym. Eng. Sci., 19, 617 (1979).
55. Tanaka, H. and J. L. White, Polym. Eng. Sci., 20, 949 (1980).
56. Han, C. D. and R. R. Lamonte, Trans. Soc. Rheo., 16, 447 (1972).
57. Hill, J. W. and J. A. Cuculo, J. Appl. Polym. Symp., 33, 3 (1976).
58. Denn, M. M., Ann. Rev. Fluid Mech., 12, 365 (1980).

59. White, J. L., *Polym. Eng. Rev.*, 1, 299 (1981).
60. Shimizu, J., K. Toriumi and Y. Imai, *Sen-I Gakkaishi*, 33, 255 (1977).
61. Shimizu, J., N. Okui and Y. Imai, *Sen-I Gakkaishi*, 35, 405 (1979).
62. Shimizu, J., N. Okui and Y. Imai, *Sen-I Gakkaishi*, 36, 166 (1980).
63. Shimizu, J., N. Okui, A. Kaneko and K. Toriumi, *Sen-I Gakkaishi*, 34, 65 (1978).
64. Shimizu, J., N. Okui, T. Kikutani and K. Toriumi, *Sen-I Gakkaishi*, 34, 93 (1978).
65. Shimizu, J., N. Okui and T. Kikutani, *Sen-I Gakkaishi*, 37, 135 (1981).
66. Shimizu, J., N. Okui, T. Kikutani, A. Ono and A. Takaku, *Sen-I Gakkaishi*, 37, 143 (1981).
67. Shimizu, J., *Sen-I Gakkaishi*, 38, 499 (1982).
68. Shimizu, J., N. Okui, Y. Imai, S. Nishide and A. Takaku, *J. Polym. Sci., Polym. Phys. Ed.*, 21, 275 (1983).
69. Shimizu, J., and N. Okui, *Sen-I Gakkaishi*, 39, 445 (1983).
70. Shimizu, J., T. Kikutani, A. Takaku and N. Okui, *Sen-I Gakkaishi*, 40, 63 (1984).
71. Shimizu, J., T. Kikutani, A. Takaku and N. Okui, *Sen-I Gakkaishi*, 40, 177 (1984).
72. Heuvel, H. M. and R. Huisman, *J. Appl. Polym. Sci.*, 22, 2229 (1978).
73. Heuvel, H. M. and R. Huisman, *J. Polym. Sci., Polym. Phys. Ed.*, 19, 121 (1981).
74. Hamidi, A., A. S. Abhiraman and P. Asher, *J. Appl. Polym. Sci.*, 28, 567 (1983).
75. Yasuda, H., *Sen-I Gakkaishi*, 38, 514 (1982).
76. Bragato, G. and G. Gianotti, *Eur. Polym. J.*, 19, 795 (1983).
77. Bragato, G. and G. Gianotti, *Eur. Polym. J.*, 19, 803 (1983).
78. Kase, S. and T. Matsuo, *J. Polym. Sci.*, 3, 2541 (1965).
79. Kase, S. and T. Matsuo, *J. Appl. Polym. Sci.*, 11, 251 (1967).

80. Lamonte, R. R. and C. D. Han, *J. Appl. Polym. Sci.*, 16, 3285 (1972).
81. Fisher, R. J. and M. M. Denn, *AICHE J.*, 23, 23 (1977).
82. Matsui, M. and D. C. Bogue, *Polym. Eng. Sci.*, 16, 735 (1976).
83. Prastaro, A. and P. Parrini, *Textile Res. J.*, 45, 118 (1975).
84. Gagon, D. K. and M. M. Denn, *Polym. Eng. Sci.*, 21, 844 (1981).
85. George, H. H., Paper presented at second joint meeting of U. S. and Japanese Rheological Societies, Kona, Hawaii, April 1979.
86. Dutta, A. and V. M. Nadkarni, *Textile Res. J.*, 54, 35 (1984).
87. Kikutani, T., Ph.D. Thesis, Tokyo Institute of Technology, 1982.
88. Schlack, P., German Pat., 748,253 (1938); U.S. Pat., 2,241,321 (1941).
89. Sbroli, W., in "Man-Made Fibers" vol. 2, H. Mark, S. Atlas and E. Cernia, Eds., Wiley, New York, 1967.
90. Bradley, T., (American Cynamid), U.S. Pat., 2,379,413.
91. Joyce, R. M., (E.I. DuPont de Nemours), U.S. Pat., 2,251,519.
92. Schrenk, H. A., (American Enka), U.S. Pat., 2,735,839.
93. Coffman, D. D., N. L. Cox and E. L. Martin, *J. Polym. Sci.*, 3, 85 (1948).
94. Miyake, A., *J. Polym. Sci.*, 44, 223 (1960).
95. Sweeney, W. and J. Zimmerman, *Ency. Polym. Sci. Tech.*, 10, 467 (1969).
96. *Ency. Polym. Sci. Tech.*, 10, 399 (1969).
97. Schule, E. C., *Ency. Chem. Tech.*, 16, 97 (1968).
98. Brill, R., *Z. Physik. Chem.*, B53, 61 (1943).
99. Wallner, L. G., *Monatsh. Chem.*, 79, 279 (1948).
100. Holmes, D. R., C. W. Bunn and D. J. Smith, *J. Polym. Sci.*, 17, 159 (1955).
101. Kinoshita, Y., *Makromol. Chem.*, 33, 1 (1959).
102. Trifan, D. S. and J. F. Terenzi, *J. Polym. Sci.*, 28, 443 (1958).

103. Slichter, W. P., *J. Polym. Sci.*, 36, 259 (1959).
104. Ziabicki, A. and K. Kedzierska, *J. Appl. Polym. Sci.*, 2, 14 (1959).
105. Ziabicki, A., *Kolloid Z.*, 167, 132 (1959).
106. Tsuruta, M., H. Arimoto and M. Ishibashi, *Kobunshi Kagaku*, 15, 619 (1958).
107. Arimoto, H., *Chemistry of High Polymers*, Tokyo, 19,204 (1962).
108. Kawayguchi, Y., O. Yoshizaki and E. Nagai, *Chemistry of High Polymers*, Tokyo, 20, 337 (1963).
109. Ota, T., O. Oshizaki and E. Nagai, *J. Polym. Sci.*, A-2, 4865 (1964).
110. Ueda, S. and T. Kimura, *Chemistry of High Polymers*, Tokyo, 15, (1958).
111. Vogelsong, D. C., *J. Polym. Sci.*, A-1, 1055 (1963).
112. Arimoto, H., *J. Polym. Sci.*, A-2, 2283 (1964).
113. Bradbury, E. M., L. Brown, A. Elliot and D. A. D. Perry, *Polymer*, 6, 465 (1965).
114. Miyasaka, K. and K. Ishikawa, *J. Polym. Sci.*, A-2, 1317 (1968).
115. Roldan, L. G. and H. S. Kaufman, *J. Polym. Sci.*, B-1, 603 (1963).
116. Arimoto, H., M. Ishibashi, M. Hirai and V. Chatani, *J. Polym. Sci.*, A-3, 317 (1965).
117. Bradbury, E. M. and A. Elliot, *Polymer*, 4, 47 (1963).
118. Illers, H. K., H. Haberkon and P. Simak, *Makromol. Chem.*, 158, 285 (1972).
119. Parker, J. P. and P. H. Lindenmeyer, *J. Appl. Polym. Sci.*, 21, 821 (1977).
120. Murthy, N. S., S. M. Aharoni and A. B. Szollosi, *J. Polym. Sci.*, Polym. Phys. Ed., 23, 2549 (1985).
121. Stepniak, R. F., A. Garton, D. J. Carlsson and D. M. Wiles, *J. Polym. Sci.*, 23, 1747 (1979).
122. Stepniak, R. F., A. Garton, D. J. Carlsson and D. M. Wiles, *J. Polym. Sci.*, Polym. Phys. Ed., 17, 987 (1979).

123. Roldan, L. G., R. Rahl and A. R. Peterson, J. Polym. Sci., C-8, 145 (1965).
124. Dismore, P. F. and W. O. Statton, J. Polym. Sci., C-13, 133 (1966).
125. Kyotani, M. and S. Mitsuhashi, J. Polym. Sci., A-2, 1497 (1972).
126. Heuvel, H. M., R. Huisman and K. C. J. B. Lind, J. Polym. Sci., Polym. Phys. Ed., 14, 921 (1976).
127. Heuvel, H. M. and R. Huisman, J. Appl. Polym. Sci., 26, 713 (1981).
128. Salem, D. R., R. A. F. Moore and H. D. Weigmann, Private communic.
129. Allen, P. W., Trans. Faraday Soc., 48, 1178 (1952).
130. Burnett, B. B. and W. F. McDevit, J. Appl. Phys., 28, 1101 (1957).
131. Cefelin, P., M. Chmelir and O. Wienterte, Czechoslov Chem. Commun., 25, 1267 (1960).
132. Inoue, M., J. Polym. Sci., 55, 753 (1961).
133. Inoue, M., J. Polym. Sci., A-1, 2013 (1963).
134. Magill, J. H., Polymer, 3, 43 (1962).
135. Magill, J. H., Polymer, 3, 665 (1962).
136. Geil, P. H., in "Polymer Single Crystals", Interscience, New York, 1963.
137. Geil, P. H., J. Polym. Sci., 44, 449 (1960).
138. Nagai, E. and M. Ogawa, J. Polym. Sci., B-3, 295 (1965).
139. Ogawa, M., T. Ota, D. Yoshizaki and E. Nagai, J. Polym. Sci., B-1, 57 (1963).
140. Holland, V. F., Paper presented at Elec. Micro. Soc. Am. Meeting, Milwauki, August 1960.
141. Clark, E. S. and C. A. Garber, Intern. J. Polymeric Mat., 1, 31 (1971).
142. Hermans, P. H., "Contribution to the Physics of Cellulose Fibers", Elsevier, New York, 1946.
143. Ziabicki, A., J. Appl. Polym. Sci., 2, 24 (1959).
144. Stein, R. S., in "Rheology" vol. 15, F. R. Eirich, Ed., Academic Press, New York, 1969.

145. Stein, R. S. and F. H. Norris, *J. Polym. Sci.*, 21, 381 (1956).
146. Wilchinsky, Z. W., *J. Appl. Phys.*, 30, 792 (1959).
147. Wilchinsky, Z. W., *J. Appl. Phys.*, 31, 1969 (1960).
148. Hoshino, S., J. Powers, D. G. Legrand, H. Kawai and R. S. Stein, *J. Polym. Sci.*, 58, 185 (1962).
149. Samuels, R. J., *J. Polym. Sci.*, A-3, 1741 (1965).
150. Sakoaku, K., N. Morosoff and A. Peterlin, *J. Polym. Sci., Polym. Phys. Ed.*, 11, 31 (1973).
151. Dumbleton, J. H., D. R. Buchanan and B. B. Bowles, *J. Appl. Polym. Sci.*, 12, 2067 (1968).
152. Prevorsek, D. C., P. J. Hargeet, R. K. Sharma and A. Reimschuessel, *J. Macromol. sci.*, B-8, 127 (1973).
153. Starkweather, H., J. F. Whitney and D. R. Johnson, *J. Polym. Sci.*, A-1, 715 (1963).
154. Hearle, J. W. S., *J. Text. Inst.*, 53, 449 (1962).
155. Keller, A., *J. Polym. Sci.*, 15, 13 (1955).
156. Ziabicki, A. and K. Kedzierska, *J. Appl. Polym. Sci.*, 6, 361 (1962).
157. Furukawa, J., T. Kitao, S. Yamashita and S. Ohaya, *J. Polym. Sci.*, 9, 299 (1971).
158. Kitao, T., S. Ohaya, J. Furukawa and S. Yamashita, *J. Polym. Sci., Polym. Phys. Ed.*, 11, 1091 (1973).
159. Katayama, K., T. Amano and K. Nakamura, *Kolloid Z.-Z. Polym.*, 226, 125 (1967).
160. Aggarwal, S. L., G. P. Tilley and O. J. Sweeting, *J. Polym. Sci.*, 51, 551 (1961).
161. Ishikawa, K., *J. Polym. Sci.*, 7, 1259 (1969).
162. Southern, J. H., N. Weeks, R. S. Porter and R. G. Crystal, *Die Molekularie Chemie*, 162, 19 (1972).
163. Henson, H. M. and J. E. Spruiell, Paper presented at the Div. of Cellulose, Paper and Text. Chem., Philadelphia, 1955.
164. Clark, E. S. and J. E. Spruiell, *Polym. Eng. Sci.*, 16, 176 (1976).

165. Nylon Tech. Serv. Man., E.I. DuPont de Nemours and Co., Wilmington, Delaware, 1952.
166. Binsbergen, F. L., *nature*, 211, 516 (1966).
167. Garber, C. and E. S. Clark, *J. Macromol. Sci. - Phys.*, B6, 499 (1970).
168. Slichter, W. P., *J. Appl. Phys.*, 26, 1099 (1955).
169. Slichter, W. P., *J. Appl. Phys.*, 35, 77 (1958).
170. Starkweather, H., "Nylon Plastics", M. Kohan, Ed., Wiley, New York, 1973.
171. Nakamura, K., T. Watanabe, K. Katayama and T. Amano, *J. Appl. Polym. Sci.*, 16, 1077 (1972).
172. Dumbleton, J. H., *Text. Res. J.*, 40, 1035 (1970).
173. Benaim, E., M.S. Thesis, University of Tennessee-Knoxville, 1978.
174. Ishibashi, T. and T. Ishii, *J. Appl. Polym. Sci.*, 20, 335 (1976).
175. Ishibashi, T. and J. Furukawa, *J. Appl. Polym. Sci.*, 20, 1421 (1976).
176. Pasika, W. M., A. C. West III and E. L. Thurston, *J. Polym. Sci., Polym. Phys. Ed.*, 10, 2313 (1972).
177. Wasiak, A. and A. Ziabicki, in "Fiber and Yarn Processing", J. L. White, Ed., *Appl. Polym. Symp.*, 27, 111 (1975).
178. Ruland, N., *Polymer*, 5, 89 (1964).
179. Hiram, M. and A. Tanimura, *J. Macromol. Sci.*, B-19, 205 (1981).
180. Kiyotosukuri, T., H. Hagesaw and R. Imamura, *Sen-I Gakkaishi*, 26, 399 (1970).
181. Hancock, T., J. E. Spruiell and J. L. White, "Wet Spinning of Aliphatic and Aromatic Polyamides", *Polym. Sci. Eng. Rep. No. 54*, January, 1976.
182. Shimizu, J., A. watanabe and K. Toriumi *Sen-I Gakkaishi*, 30, 35 (1974).
183. Hasegawa, K., *Sen-I Gakkaishi*, 38, 521 (1982).
184. George, H. H., A. Holt and A. Buckley, *Polym. Eng. Sci.*, 23, 95 (1983).

185. Lecluse, C., "High Speed Spinning of Polyamide 66", Rhone-Poulenc Fibers Company Report, 1984.
186. Colclough, M. L. and R. Baker, J. Mater. Sci., 13, 2531 (1978).
187. Heuvel, H. M. and R. Huisman, J. Appl. Polym. Sci., 26, 713 (1981).
188. Ziabicki, A., Kolloid Z., 175, 14 (1961).
189. Ziabicki, A. and K. Kedzierska, Kolloid Z., 171, 51 (1960).
190. Trouton, F. T., Proc. Royal Soc., A77, 426 (1906).
191. Andrews, E. H., in "Fiber Structure", J. W. S. Hearle and R. H. Peters, Eds., Butterworth and Text. Inst., Manchester, London, 1962.
192. Aoki, H., Y. Suzuki and A. Ishimoto, unpublished work.
193. Kwon, Y. D. and P. C. Prevorsek, J. Appl. Polym. Sci., 23, 3105 (1979).
194. Gould, J. and F. S. Smith, J. Text. Inst., 1, 38 (1980).
195. Kubo, S., in "High Speed Fiber Spinning", A. Ziabicki and H. Kawai, Eds., John Wiley and Sons, New York, 1985.
196. Matsui, M., Trans. Soc. Rheol., 20, 465 (1976).
197. Shimizu, J., N. Okui and K. Tamai, Sen-I Gakkaishi, 39, 398 (1983).
198. William, M. L., R. F. Landel and J. D. Ferry, J. Am. Chem. Soc., 77, 3701 (1955).
199. Ballman, R. L., Rheol. Acta, 4, 137 (1965).
200. Cogswell, F. N., Rheol. Acta, 8, 187 (1969).
201. Meissner, J., Rheol. Acta, 8, 78 (1969).
202. Meissner, J., Rheol. Acta, 10, 230 (1971).
203. Han, C. D., R. R. Lamonte and T. Shah, J. Appl. Polym. Sci., 16, 3307 (1972).
204. Kase, S. and T. Matsuo, J. Text. Mach. Soc. Japan, 18, 188 (1965).
205. Hill, J. W. and J. A. Cuculo, J. Appl. Polym. Sci., 18, 2569 (1974).

206. Spearot, J. A. and A. B. Metzner, *Trans. Soc. Rheol.*, 16, 495 (1972).
207. Matovich, M. A. and J. R. A. Pearson, *Ind. Eng. Chem. Fund.*, 8, 512 (1969).
208. White, J. L., *J. Appl. Polym. Sci.*, 8, 2339 (1964).
209. Larson, R. G., *J. Rheol.*, 27, 475 (1983).
210. Ziabicki, A., in "High Speed Fiber Spinning", A. Ziabicki and H. Kawai, Eds., John Wiley, New York, 1985.
211. Nakamura, K., T. Watanabe, K. Katayama and T. Amano, *J. Appl. Polym. Sci.*, 18, 615 (1974).
212. Andrews, E. H., *Brit. J. Appl. Phys.*, 10, 39 (1959).
213. Wilhelm, V. G., *Kolloid Z.*, 208, 97 (1966).
214. Ziabicki, A. and K. Kedzierska, *Chemie Stosowana*, 4, 151 (1960).
215. Barnett, T. R., *J. Am. Chem. Soc., Div. Polym. Chem. Prepr.*, 7, 691 (1966).
216. Copley, M., N. H. Chamberlain and K. W. Hiller, *J. Am. Chem. Soc., Div. Polym. Chem. Prepr.*, 7, 679 (1966).
217. Morrison, M. E., *A.I.Ch.E. J.*, 16, 57 (1970).
218. Vasudevan, G. and S. Middleman, *AICHE J.*, 16, 614 (1970).
219. Glicksman, L. R., *Glass Technology*, 9, 131 (1968).
220. Sano, Y. and S. Nishikawa, *Kagaku Kogaku*, 28, 275 (1964).
221. Sano, Y. and N. Yamada, *Kagaku Kogaku*, 30, 997 (1966).
222. Mueller, A. C., *Trans. Am. Inst. Chem. Eng.*, 38, 613 (1942).
223. Roberts, J. K., "Heat and Thermodynamics", Blackie and Sons, London, 1940.
224. Fisher, J. C., J. H. Hollomon and D. J. Turnbull, *J. Appl. Phys.*, 19, 775 (1948).
225. Becker, R. and W. Doring, *Ann. D. Physik.*, 24, 719 (1935).
226. Devoy, C. and L. Mandelkern, *J. Chem. Phys.*, 52, 3827 (1970).
227. Turnbull, D. J., *J. Chem. Phys.*, 18, 198 (1950).

228. Cormia, R. L., F. P. Price and D. J. Turnbull, *J. Chem. Phys.*, 37, 1333 (1962).
229. Avrami, M., *J. Chem. Phys.*, 7, 1103 (1939).
230. Avrami, M., *J. Chem. Phys.*, 8, 212 (1940).
231. Avrami, M., *J. Chem. Phys.*, 9, 177 (1941).
232. Johnson, W. A. and R. F. Mehl, *Trans. Am. Inst. Min. Met. Eng.*, 135, 416 (1939).
233. Evans, R. U., *Trans. Faraday Soc.*, 41, 365 (1945).
234. Kolmogoroff, A. N., *Izvestiya Akad. Nauk. SSSR, Ser. Math.*, 1, 355 (1937).
235. Mandelkern, L., "Crystallization of Polymers", McGraw-Hill, New York, 1964.
236. Turnbull, D. and J. C. Fisher, *J. Chem. Phys.*, 17, 71 (1949).
237. Gornick, F. and L. Mandelkern, *J. Appl. Phys.*, 33, 907 (1962).
238. Burns, J. R. and D. J. Turnbull, *J. Appl. Phys.*, 37, 4021 (1966).
239. Hoffman, J. D., J. J. Weeks and W. M. Murphy, *J. Res. NBS*, 63A, 67 (1959).
240. Hoffman, J. D. and J. I. Lauritzen, *J. Res. NBS*, 79A, 613 (1975).
241. Ziabicki, A., *Appl. Polym. Symp.*, 6, 1 (1967).
242. Wood, L. A. and K. Bekkedahl, *J. Appl. Phys.*, 17, 362 (1946).
243. Takayanagi, M. and T. Kusumoto, *Kogyo Kagaku Zasshi*, 62, 587 (1959).
244. Inoue, M., *J. Polym. Sci.*, 55, 753 (1961).
245. Schultz, J. M., *J. Polym. Sci.*, 7, 821 (1969).
246. Boon, J., *J. Polym. Sci.*, 16, 1739 (1967).
247. Ozawa, T., *Polymer*, 12, 150 (1971).
248. Nakamura, K., K. Katayama and T. Amano, *J. Appl. Polym. Sci.*, 17, 1031 (1973).
249. Katz, J. R., *Kolloid Z.*, 36, 300 (1925).
250. Treloar, L. R. G., *Trans. Faraday Soc.*, 37, 84 (1941).

251. Gent, A. N., *Trans. Faraday Soc.*, 8, 369 (1954).
252. Kim, H. G. and L. Mandelkern, *J. Polym. Sci.*, 6, 181 (1968).
253. Kobayashi, K. and T. Nagasawa, "Formation of Fibers and Development of Their Structure", edited by Soc. Fiber Sci. and Tech., Japan, Kagaku Dojin, Kyoto, 1969.
254. Kobayashi, K. and T. Nagasawa, *J. Macromol. Sci. - Phys.*, B4, 331 (1970).
255. Kawai, T., T. Matsumoto, M. kato and H. Maeda, *Kolloid Z.*, 222, 1 (1968).
256. Pennings, A. J. and M. F. J. Pijpers, *Macromolecules*, 3, 261 (1970).
257. Pennings, A. J., J. M. A. A. van der Mark and H. C. Booji, *Kolloid Z.*, 236, 99 (1970).
258. Kamato, R., K. Ehara, T. Matsumoto, T. kawai and H. Maeda, *Sen-I Gakkaishi*, 26, 80 (1970).
259. Wasiak, A., Ph.D. thesis, *Inst. Fund. Tech. Res. Report*, 29, 1974.
260. Smith, F. S. and R. D. Steward, *Polymer*, 15, 283 (1974).
261. Ziabicki, A., *Polimery*, 17, 301 (1972).
262. Ziabicki, A., *Colloid and Polym. Sci.*, 252, 207 (1974).
263. Ishizuka, O. and K. Koyama, *Sen-I Gakkaishi*, 32, 43 (1976).
264. Ishizuka, O. and K. Koyama, *Sen-I Gakkaishi*, 32, 49 (1976).
265. Ishizuka, O. and K. Koyama, *Polymer*, 18, 913 (1977).
266. Ishizuka, O. and K. Koyama, *Polymer J.*, 12, 735 (1980).
267. Abhiraman, A. S., *J. Polym. Sci., Polym. Phys. Ed.*, 21, 583 (1983).
268. Krigbaum, W. R. and R. J. Roe, *J. Polym. Sci.*, 2, 4391 (1964).
269. Smith, K. J., A. Greene and A. Cifferi, *Kolloid Z.*, 194, 9 (1964).
270. Yamamoto, M. and J. L. White, *J. Polym. Sci.*, 9, 1399 (1971).
271. Jarecki, L., Ph.D. dissertation, *Inst. Fund. Tech. Res. Report* 29, 1974.

272. Ziabicki, A., *Polimery*, 18, 615 (1973).
273. Marrucci, G., *Trans. Soc. Rheology*, 16, 321 (1972).
274. George, H. H., *Polym. Eng. Sci.*, 22, 292 (1982).
275. Yasuda, H., H. Sugiyama and H. Yanagawa, *Sen-I Gakkaishi*, 35, 370 (1979).
276. Yasuda, H., H. Sugiyama and S. Hayashi, *Sen-I gakkaishi*, 40, 227 (1984).
277. Yasuda, H., H. Sugiyama and S. Hayashi, *Sen-I gakkaishi*, 40, 488 (1984).
278. Shenoy, A. V. and V. M. Nadkarni, *Textile Res. J.*, 54, 778 (1984).
279. Lu, F. and J. E. Spruiell, *J. Appl. Polym. Sci.*, in press.
280. George, H. H. and M. H. G. Deeg, paper presented at second annual meeting of Polymer Processing Society, Montreal, Canada, 1986.
281. Welty, J. R., C. E. Wicks and R. E. Wilson, "Fundamentals of Momentum, Heat and Mass Transfer", John Wiley, New York, 1969.
282. Marx, P., C. W. Smith, A. E. Worthington and M. Dole, *J. Chem. Phys.*, 59, 1015 (1955).
283. Pezzin, G. and G. B. Gechele, *J. Appl. Polym. Sci.*, 8, 2195 (1964).
284. Matsumoto, K. and M. Kiyodu, *Sen-I Gakkaishi*, 32, 365 (1976).
285. Greco, R., L. Nicodemo and L. Nicolais, *Macromolecules*, 9, 686 (1976).
286. Speckhart, F. H. and W. L. Green, "A Guide to using CSMP- The Continuous System Modelling Program", Prentice Hall, Englewood Cliffs, New Jersey, 1967.
287. White, J. L., *Appl. Polym. Symp.*, 33, 31 (1978).
288. Cogswell, F. N., *Appl. Polym. Symp.*, 27, 1 (1975).
289. Cogswell, F. N., *Trans. Soc. Rheol.*, 16, 383 (1972).
290. Lin, L. C. T. and J. Hauenstein, *J. Appl. Polym. Sci.*, 18, 3509, (1974).
291. Katayama, K. and M. G. Yoon, in "High Speed Fiber Spinning", A. Ziabicki and H. Kawai, Eds., John Wiley and Sons, New York, 1985.

292. Kase, S., in "High Speed Fiber Spinning", A. Ziabicki and H. Kawai, Eds., John Wiley and Sons, New York, 1985.
293. Sano, Y., in "Formation of Fibers and Development of Their Structure", edited by The Society of Fiber Science and Technology, Japan, Kagaku Dojin, Kyoto, 1969.
294. Broyer, E., Celanese Research Co., unpublished data, cited by ref. (274).

APPENDIXES

APPENDIX A

Program for data acquisition from the Zimmer diameter monitor.

```

1:      PROGRAM ZIMMER.FOR
2:  C
3:  C      THIS PROGRAM IS FOR DIAMETER DATA ACQUISITION FROM THE
4:  C      ZIMMER DIAMETER MEASURING MONITOR MODEL 460 A/2
5:  C
6:      DIMENSION IDATA(10,400)
7:      CALL FAINIT
8:      WRITE(1,80)
9:  80   FORMAT(1X, 'DATE:', 1X)
10:     READ(1,90)IDATE
11:  90   FORMAT(I10)
12:     WRITE(1,81)
13:  81   FORMAT(1X, 'MOLE. WT. OF RESIN:', 1X)
14:     READ(1,90)IRESIN
15:     WRITE(1,82)
16:  82   FORMAT(1X, 'MASS FLOW RATE (G/MIN):', 1X)
17:     READ(1,90)IMFR
18:     WRITE(1,83)
19:  83   FORMAT(1X, 'AIR PRESSURE (PSI):', 1X)
20:     READ(1,90)IPRESS
21:     WRITE(1,84)
22:  84   FORMAT(1X, 'POSITION FROM DIE (CMS):', 1X)
23:     READ(1,90)IPOSI
24:     WRITE(1,85)
25:  85   FORMAT(1X, 'ENTER VALUE OF M:', 1X)
26:     READ(1,40)M
27:     WRITE(1,86)
28:  86   FORMAT(1X, 'ENTER GAIN FACTOR:', 1X)
29:     READ(1,40)IGAIN
30:     WRITE(1,30)
31:  30   FORMAT(1X, 'ENTER CHANNEL NUMBER:', 1X)
32:     READ(1,40)ICHAN
33:  40   FORMAT(I6)
34:     WRITE(1,31)
35:  31   FORMAT(1X, 'ENTER UPPER LIMIT:', 1X)
36:     READ(1,40)LIMHI
37:     WRITE(1,32)
38:  32   FORMAT(1X, 'ENTER LOWER LIMIT:', 1X)
39:     READ(1,40)LIMLO
40:     WRITE(1,33)
41:  33   FORMAT(1X, 'ENTER SAMPLE TIME INTERVAL:', 1X)
42:     READ(1,40)IDLY
43:     DO 46 J=1,M
44:     DO 47 I=1,10
45:     CALL MSDLY(IDLY)
46:     CALL FADC(ICHAN, IDATA(I,J))

```

```

47:      IF(IDATA(I,J).GT.LIMHI) IDATA(I,J)=0
48:      IF(IDATA(I,J).LT.LIMLO) IDATA(I,J)=0
49:      ICONCK=INP(1)
50:      ICONK=ICONK.AND.127
51:      IF(ICONK.EQ.83) GO TO 60
52:      CALL SYNC
53: 47    CONTINUE
54: 46    CONTINUE
55:      CALL OPEN(7,'DATAFILEDAT',2)
56:      DO 21 J=1,M
57:      WRITE(1,50) IDATA(1,J), IDATA(2,J), IDATA(3,J), IDATA(4,J),
58: 1     IDATA(5,J), IDATA(6,J), IDATA(7,J), IDATA(8,J), IDATA(9,J),
59: 2     IDATA(10,J)
60:      WRITE(7,50) IDATA(1,J), IDATA(2,J), IDATA(3,J), IDATA(4,J),
61: 3     IDATA(5,J), IDATA(6,J), IDATA(7,J), IDATA(8,J), IDATA(9,J),
62: 4     IDATA(10,J)
63: 50    FORMAT(1X,10I6)
64: 21    CONTINUE
65:      ENDFILE 7
66: 60    STOP EXIT
67:      END
68: C
69:      SUBROUTINE FAINIT
70:      CALL OUT(130,15)
71:      CALL OUT(130,7)
72:      CALL OUT(131,207)
73:      CALL OUT(131,255)
74:      CALL OUT(131,7)
75:      RETURN
76:      END
77: C
78:      SUBROUTINE FADC(ICHAN, IDATA)
79:      CALL OUT(128, ICHAN)
80: 10    ISTAT=INP(129)
81:      ISTAT=ISTAT.AND.128
82:      IF(ISTAT.EQ.0) GO TO 10
83:      ILO=INP(133)
84:      IHI=INP(132)
85:      ILO=ILO.AND.255
86:      IHI=IHI.AND.15
87:      IF(IHI.LE.7) GO TO 20
88:      IHI=IHI.OR.240
89: 20    IDATA=IHI*256
90:      IDATA=IDATA.OR.ILO
91:      RETURN
92:      END
93: C
94:      SUBROUTINE MSDLY(IDLY)
95:      CALL STCTC(125,20, IDLY,5)
96:      RETURN
97:      END
98: C

```

```

99:      SUBROUTINE SECDLY(IDLY)
100:     CALL STCTC(125,40,IDLY,250)
101:     RETURN
102:     END
103: C
104:     SUBROUTINE MSDLY(IDLY)
105:     K2=5*IDLY
106:     CALL STCTC(125,240,K2,250)
107:     RETURN
108:     END
109: C
110:     SUBROUTINE STCTC(K0,K1,K2,K3)
111:     CALL OUT(195,87)
112:     CALL OUT(194,87)
113:     CALL OUT(193,87)
114:     CALL OUT(192,87)
115:     CALL OUT(195,K3)
116:     CALL OUT(194,K2)
117:     CALL OUT(193,K1)
118:     CALL OUT(192,K0)
119:     RETURN
120:     END
121: C
122:     SUBROUTINE SYNC
123: 10     ISYNC=INP(195)
124:     IF(ISYNC.NE.1) GO TO 10
125: 20     ISYNC=INP(195)
126:     IF(ISYNC.EQ.1) GO TO 20
127:     RETURN
128:     END

```

APPENDIX B

Program for statistical analysis of diameter data.

```

C THIS PROGRAM PROCESSES DATA COLLECTED FROM ZIMMER
C ONLINE DIAMETER MEASUREMENTS TO GET THE DISTRIBUTION
C OF DIAMETER VALUES. A COUNTER VARIABLE (IVAL) KEEPS
C TRACK OF NUMBER OF TIMES A PARTICULAR DIAMETER VALUE
C OCCURS. IT REJECTS THE DIAMETER VALUE LESS THAN ZERO
C AND KEEPS TRACK OF NUMBER OF REJECTED VALUES (TO GET
C PERCENT OF REJECTION FOR A MEASUREMENT).
C
C
C           DIMENSION IVAL(700),IV(10),XV(10),IDATA(10),YV(10)
C           DOUBLE PRECISION LUN1,LUN2
C
C INITIALIZE THE COUNTER FOR DIAMETER VALUES
C
C           DATA IVAL(700)/0/
C
C INITIALIZE COUNTER FOR REJECTED VALUES
C
C           IZ=0
C           WRITE(5,10010)
C           READ(5,10020) LUN1
C           OPEN(UNIT=32,FILE=LUN1)
C           DO 40 J=1,200
C             READ(32,*)IV(1),IV(2),IV(3),IV(4),IV(5),
1          IV(6),IV(7),IV(8),IV(9),IV(10)
C             DO 10 I=1,10
C
C DIVIDE THE DIAMETER VALUE BY A FACTOR FOR GAIN SETTING
C
C           XV(I)=IV(I)/10.
C
C CONVERT THE REAL VALUE TO INTEGER VALUE
C
C CORRECT DIAMETER VALUE FOR TRANSPARENCY OF FIBER
C
C           YV(I)=-0.014021164*(XV(I)-42.)+8.15
C           XV(I)=XV(I)*(1.0+YV(I)/100.)
C
C           IDATA(I)=XV(I)
C
C REJECT DAIMETER VALUES OF LESS THAN ZERO
C
C           IF(IDATA(I).LE.0) GO TO 20
C
C           IVAL(IDATA(I))=IVAL(IDATA(I))+1

```



```

                GO TO 10
20             IZ=IZ+1
10             CONTINUE
40             CONTINUE
                CLOSE (UNIT=32 ,FILE=LUN1)
                WRITE (5 ,10030)
                READ (5 ,10020) LUN2
                OPEN (UNIT=33 ,FILE=LUN2)
                WRITE (33 ,100) IZ
100            FORMAT (//5X , 'NO. OF REJECTED VALUES' , 5X , I6)
                WRITE (33 ,10040) LUN1
                WRITE (33 ,10050)
                DO 90 J=1 , 700
                IF (IVAL (J) .EQ. 0) GO TO 90
                WRITE (33 ,101) J , IVAL (J)
                WRITE (5 ,101) J , IVAL (J)
101            FORMAT (5X , I6 , 8X , I6)
90             CONTINUE
                CLOSE (UNIT=33 ,FILE=LUN2)
                STOP
10010          FORMAT (5X , 'ENTER THE NAME OF INPUT DATA FILE:' , $)
10020          FORMAT (A10)
10030          FORMAT (5X , 'ENTER THE NAME OF OUTPUT DATA FILE:' , $)
10040          FORMAT (//5X , 'THE RESULTING DISTRIBUTION FOR DATA SET:' , A10)
10050          FORMAT (//5X , 'DIAMETER' , 5X , 'NO. OF COUNTS' , //)
                END

```

APPENDIX C

Program for tensiometer data acquisition and statistical
calculation of average tension.

```

1:      PROGRAM TENSION.FOR
2:      EXTERNAL ADC,ADINIT
3:      DIMENSION GRAMS(10)
4:      CALL ADINIT
5:      CALL OPEN(7,'DATA1FILDAT',2)
6:      ICHAN2=2
7: 5    SUM1=0.0
8:      SUM2=0.0
9:      DO 10 I=1,50
10:     DO 15 J=1,6
11:     CALL ADC(ICHAN2,IRDG)
12:     GRAMS(J)=(FLOAT(IRDG)/2047.)*10.
13:     SUM1=SUM1+GRAMS(J)
14:     SUM2=SUM2+GRAMS(J)*GRAMS(J)
15: 15   CONTINUE
16:     WRITE(1,20)(GRAMS(J),J=1,6)
17:     WRITE(7,20)(GRAMS(J),J=1,6)
18: 20   FORMAT(1X,6F11.3)
19: 10   CONTINUE
20:     ENDFILE 7
21:     AVG=SUM1/300.
22:     SD=SQRT(SUM2-(SUM1*SUM1/300.))/(300.-1.)
23:     WRITE(1,30)
24: 30   FORMAT(1X,' ')
25:     WRITE(1,35)AVG,SD
26: 35   FORMAT(1X,'THE AVERAGE VALUE OF 300 DATA IS ',F11.3,
27: 1 +/- ',F11.3)
28:     WRITE(1,40)
29: 40   FORMAT(1X,'DO YOU WANT TO RUN AGAIN (1=YES,2=NO)?')
30:     READ(1,50)IANS
31: 50   FORMAT(I6)
32:     IF(IANS.EQ.2.0) GO TO 60
33:     GO TO 5
34: 60   END

```

APPENDIX D

CSMP Program for model of nylon-6 melt spinning

with literature property input.

```
//SIMHMW JOB ,BHEDA,GROUP=J41241,USER=P91688,
// PASSWORD=? ,TIME=5,REGION=256K
/*ROUTE PRINT UTKVX3.BHEDA
/*NOTIFY UTKVX3.BHEDA
//STEP1 EXEC CSMP3
//SYSIN DD *
TITLE NYLON-6 MELT SPINNING SIMULATION
INITIAL
*****
*
*       THE FOLLOWING SECTION CONTAINS THE PHYSICAL CONSTANTS
*
*
*****
CONSTANT PI=3.1415926,G=980.,DNA0=0.0825,C1=1.37E-4,C2=0.259,C13=0.167
CONSTANT C3=0.25,C4=0.15,C5=0.36,C6=2.2956E-18,VY=0.0
CONSTANT C8=-2.7725887,C9=0.087,C10=-8.86,C11=128.4,C12=200.
CONSTANT K=0.0003056,DELH=45.0,COP=1.8E-10,TS=140.
CONSTANT TMAX=146.,DO=46.,TM=228.,RMAX=0.14,TG=45.,N=3.,THI=0.45
CONSTANT D0=0.0762,T0=270.,TA=25.,AMN=23500.,W0=3.073
CONSTANT RHOA=6.62E-5,MU=2.8E-4
PARAMETER FRHE0=27.8982
LABEL MN=53200,W=2.9925 G/MIN,TS=140,FRHE0=94.0
FUNCTION AMOD=(15.,358.),(23.,338.),(31.,308.),(34.,288.),(38.,235.),...
              (44.,175.),(50.,138.),(56.,97.),(61.,85.),(66.,67.),...
              (74.,60.),(79.,56.),(83.,51.),(90.,48.5),(99.,44.8),...
              (108.,40.),(115.,38.),(123.,36.),(132.,34.5),...
              (139.,33.),(146.,32.),(155.,31.),(167.,30.),...
              (176.,29.),(186.,27.5),(195.,24.),(202.,20.7),...
              (206.,17.8),(210.,15.5),(215.,13.25),(219.,10.7),...
              (221.,5.95),(228.,4.6),(300.,1.0E-5)
FUNCTION ABETA=(-3.088,0.0005),(-2.7869,0.001),(-2.0873,0.005),...
              (-1.7856,0.01),(-1.0807,0.05),(-0.7724,0.1),...
              (-0.0113,0.5),(0.3757,1.0),(0.8781,2.0),...
              (1.2945,3.0),(1.6939,4.0),(2.0926,5.0),(2.4941,6.0),...
              (2.8993,7.0),(3.3076,8.0),(3.7184,9.0),(4.1325,10.0),...
              (4.5464,11.0),(4.9628,12.0),(5.3806,13.0),...
              (5.7995,14.0),(6.2195,15.0),(6.6403,16.0),...
              (7.0619,17.0),(7.4842,18.0),(7.9071,19.0),...
              (8.3306,20.0),(8.7546,21.0)
RENAME TIME=DIST
W=W0/60.0
RHO0=1./(0.8816+0.000564*T)
V0=4.0*W/RHO0/PI/D0/D0
BIA0=COP*4.0*FRHE0/PI/D0/D0
```

```

ETA=C6*(AMN**3.4)
ETA1=3.*1.75E-12*(AMN**3.4)
THEMIN=0.01

```

```

*****
*
* INITIALIZE THE FOLLOWING VARIABLES:
* TE - A PARAMETER WHICH TELLS THE KINETICS SECTION THAT THE TEMP
* HAS DROPPED BELOW TM
* DTH - CRYSTALLIZATION RATE (1/SEC)
* THE - CRYSTALLINITY
* TO - TEMPORARY CRYSTALLINITY USED IN KINETICS SECTION
* ZO - DISTANCE FROM SPINNERET AT WHICH CRYSTALLIZATION BEGINS (CM)
* TC - TIME BEGINNING WITH CRYSTALLIZATION (SEC)
* DTC - TIME GRADIENT FOR CRYSTALLIZATION TIME (CM/SEC)
* T - TEMPERATURE OF FIBER (C)
* V - VELOCITY OF THE FIBER (CM/SEC)
* D - DIAMETER OF THE FIBER (CM)
* BIA - AMORPHOUS BIREFRINGENCE OF THE FIBER
*
*****

```

```

TE=-1.0
DTH=0.0
THE=0.0
TO=THE
ZO=0.0
TC=0.0
DTC=0.0
T=T0
V=V0
D=D0
BIA=BIA0
C7=PI/W
DYNAMIC

```

```

*****
*
* THIS SECTION EVALUATES THE PHYSICAL PROPERTIES OF THE POLYMER
*
*****

```

```

PROCEDURE RHO=FUN(T,THE)
  IF(T.GT.228.) RHO=1./(0.8816+0.000564*T)
  IF(T.LE.228.) RHO=1./((0.8816+0.000564*T)-(0.0292+0.000326*T)*THE)
ENDPROCEDURE
PROCEDURE CP=FUNC(T)
  IF(T.GT.160.) CP=0.577+0.000336*T
  IF(T.LE.160.) CP=0.325+0.0015*T
ENDPROCEDURE
PROCEDURE VIS=FUNCT(T,ETA,ETA1,C10,C11,TM,THE,THI,AMN,THEMIN,VS)
  IF(THE.LE.THEMIN) VS=1.0
  IF(THE.GT.THEMIN) VS=EXP(4.5*((THE/THI)**12.))
  IF(T.GT.TM) VIS=3.*ETA*EXP(6855./(T+273))*VS
  IF(T.LE.TM.AND.T.GT.TS) VIS=ETA1*EXP(C10*(T-TM)/(T+101.6-TM))*VS
  IF(T.GT.TS) KOUT=-1

```

```

      IF(KOUT.GT.0) GO TO 89
      IF(T.LE.TS) KOUT=1
89     CONTINUE
      IF(T.LE.TS) VIS=1.0E30
ENDPROCEDURE
MOD=(1.0E8)*AFGEN(AMOD,T)
*****
*
*           THIS BEGINS THE DYNAMIC SECTION OF THE SIMULATION
*
*****
REN=RHOA*V*D/MU
FINER=W*(V-V0)
DFGRA=W*G/V
FGRAV=INTGRL(0.0,DFGRA)
ZETA=8.0*SQRT(DIST/REN/D)
PROCEDURE CD,ZATA,BETA=TEST(ZETA,REN)
      IF(ZETA.LE.0.0) GO TO 29
      ZATA=ALOG10(ZETA)
      BETA=AFGEN(ABETA,ZATA)
      CD=4./BETA/REN
      GO TO 30
29     CD=0.0
30     CONTINUE
ENDPROCEDURE
DFDRA=PI*CD*RHOA*V*V*D
FDRAG=INTGRL(0.0,DFDRA)
DFRHE=(W*DV + DFDRA - DFGRA)
FRHEO=INTGRL(FRHEO,DFRHE)
FRHEON=1.E-5*FRHEO
STRES=4.0*FRHEO/PI/D/D
STRESP=1.0E-7*STRES
PROCED DV=OLIVE(STRES,VIS,T,TG)
      DV=STRES/VIS
      IF(T.LE.TG) DV=0.0
ENDPROCEDURE
V=INTGRL(V0,DV)
VM=V*0.6
DTIM=1.0/V
TIM=INTGRL(0.0,DTIM)
D=SQRT(4.0*W/RHO/PI/V)
DM=D*10000.0
AR=PI*D*D/4.
H=C1*((V/AR)**C2)*((1.+(8.*VY/VM)**2.))**C13)
DT=(C7*D*H*(TA-T)+DELH*DTH/V)/CP
T=INTGRL(T0,DT)
*****
*
*           THIS PROCEDURE CONTAINS THE CRYSTALLIZATION KINETICS
*
*****
PROCED DTHE,DTH,THE,RATE=G(TE,V,T,TM,TG,C8,C12,TMAX,RMAX,DO,FA,THI,TO)

```

```

IF(T.GE.TM.AND.TE.LE.0.0) GO TO 10
IF(T.LE.TG) GO TO 10
IF(TO.GE.THI) GO TO 10
IF(TE.LE.0.0) Z0=DIST
TE=1.0
DTC=1.0/V
TC=INTGRL(0,DTC)
IF(T.GE.TM) GO TO 10
B1=C8*(T-TMAX)*(T-TMAX)/DO/DO + C12*FA*FA
B2=B1
IF(B1.GT.174.) B2=174.
RATE=RMAX*EXP(B2)
DTHE=RATE/V
IF(DTHE.GT.2.0E23) DTHE=2.0E23
SUM=INTGRL(0,DTHE)
IF(SUM.GT.1.5E25) SUM=1.5E25
S1=SUM**N
S2=0.0
IF(S1.LT.174.) S2=EXP(-S1)
DTH=N*RATE*(SUM**(N-1.0))*S2*THI
THE=THI*(1.0-S2)
TO=THE
GO TO 20
10 DTH=0.0
THE=TO
20 JOB=1.0
ENDPROCEDURE
DBIA=COP*DV*MOD/V-BIA*MOD/VIS/V
BIA=INTGRL(BIA0,DBIA)
BIC=THE*C9
BIT=(1.0-THE)*BIA + BIC
FA=BIA/DNA0
SDR=V/V0
DENI=W*90000.0/V
*****
*
* THIS COMPLETES THE DYNAMIC SECTION *
*
* THE FOLLOWING SECTIONS PRINT THE RESULTS OF THE SIMULATION *
*
*****
PRINT T,RATE
*RANGE DM,VM,T,THE,BIA,FA,FRHEO,FGRAV,FINER,FDRAG,STRES,DTH,DV, ...
* VIS,MOD,CP,CD,REN,NUL,H,BIC,BIT,SDR,DTHE,RATE
*PRINT VM,DV,DM,T,DT,THE,DTH,BIA,DBIA,BIC,BIT,FA,VIS,MOD,REN,NUL,...
* CP,H,TIM,FRHEO,FINER,FDRAG,FGRAV,STRES,SDR,DTHE,RATE
*PRTPLT THE,FA,STRES
*PRTPLT VM,DM,T

```

```
*****  
*                                     *  
* THE STIFF OPTION WAS USED IN THE SOLUTION OF THESE O.D.E.S *  
*                                     *  
*****  
METHOD STIFF  
NOSORT  
TIMER FINTIM=200.0,DELMIN=1.0E-12  
END  
STOP
```

APPENDIX E

CSMP Program for inversion procedure.

```
//SIMHMW JOB ,BHEDA,GROUP=J41241,USER=P91688,
// PASSWORD=?,TIME=5,REGION=256K
/*ROUTE PRINT UTKVX3.BHEDA
/*NOTIFY UTKVX3.BHEDA
//STEP1 EXEC CSMP3
//SYSIN DD *
TITLE INVERSION, 53200, 2.9925 G/MIN, V=1780 M/MIN
INITIAL
CONSTANT PI=3.1415926,G=980.
CONSTANT D0=0.0762,T0=280.,TA=25.,MN=53200.,W0=2.9925
CONSTANT RHOA=6.62E-5,MU=2.8E-4
CONSTANT FL=320.,FGRAVL=42.735,FDRAGL=126.33,FINERL=140.48
FUNCTION ADIA=(0.0,0.0762),(10.,0.039296),(20.,0.025596), ...
              (30.,0.0186),(40.,0.014634),(50.,0.012003), ...
              (60.,0.010204),(70.,0.008929),(80.,0.00797), ...
              (90.,0.007223),(100.,0.006688),(110.,0.006045), ...
              (120.,0.005724),(130.,0.005509),(140.,0.005295), ...
              (150.,0.00508),(160.,0.004972),(170.,0.004757), ...
              (180.,0.00465),(190.,0.004542)
FUNCTION ATEMP=(0.0,280.),(11.8,260.),(18.1,250.), ...
               (24.2,240.),(29.9,230.),(37.,220.),(43.1,210.), ...
               (49.4,200.),(58.8,190.),(64.,180.),(73.,170.),...
               (79.1,160.),(86.2,150.),(97.2,140.),(106.,130.),...
               (116.,120.),(127.1,110.),(137.1,100.),(149.9,90.),...
               (163.8,80.),(181.,70.),(200.,60.)
FUNCTION ABETA=(-3.088,0.0005),(-2.7869,0.001),(-2.0873,0.005), ...
              (-1.7856,0.01),(-1.0807,0.05),(-0.7724,0.1), ...
              (-0.0113,0.5),(0.3757,1.0),(0.8781,2.0), ...
              (1.2945,3.0),(1.6939,4.0),(2.0926,5.0),(2.4941,6.0), ...
              (2.8993,7.0),(3.3076,8.0),(3.7184,9.0),(4.1325,10.0),...
              (4.5464,11.0),(4.9628,12.0),(5.3806,13.0), ...
              (5.7995,14.0),(6.2195,15.0),(6.6403,16.0), ...
              (7.0619,17.0),(7.4842,18.0),(7.9071,19.0), ...
              (8.3306,20.0),(8.7546,21.0)
RENAME TIME=DIST
W=W0/60.0
RHO0=1./(0.8816+0.000564*T)
V0=4.0*W/RHO0/PI/D0/D0
DIST=0.0
T=T0
V=V0
D=D0
DD0=SLOPE(ADIA,3,0.0)
DT0=SLOPE(ATEMP,3,0.0)
DV0=-DD0*(V0**1.5)/SQRT(W/PI/RHO0)
DV=DV0
```



```

C7=PI/W
DYNAMIC
D=FUNGEN(ADIA,5,DIST)
AR=PI*D*D/4.
T=FUNGEN(ATEMP,5,DIST)
TK=1000./(T+273.)
RHO=1./(0.8816+0.000564*T)
PROCEDURE CP=FUNC(T)
    IF(T.GT.160.) CP=0.577+0.000336*T
    IF(T.LE.160.) CP=0.325+0.0015*T
ENDPROCEDURE
REN=RHO*V*D/MU
FINER=W*(V-V0)
DFGRA=W*G/V
FGRAV=INTGRL(0.0,DFGRA)
ZETA=8.0*SQRT(DIST/REN/D)
PROCEDURE CD,ZATA,BETA=TEST(ZETA,REN)
    IF(ZETA.LE.0.0) GO TO 29
    ZATA=ALOG10(ZETA)
    BETA=AFGEN(ABETA,ZATA)
    CD=4./BETA/REN
    GO TO 30
29    CD=0.0
30    CONTINUE
ENDPROCEDURE
DFDRA=PI*CD*RHO*V*V*D
FDRAG=INTGRL(0.0,DFDRA)
FRHEO=FL*(FGRAVL-FGRAV)-(FDRAGL-FDRAG)-(FINERL-FINER)
FRHEON=1.0E-5*FRHEO
DTIM=1.0/V
TIM=INTGRL(0.0,DTIM)
V=4.*W/PI/D/D/RHO
DV=DERIV(DV0,V)
DT=DERIV(DT0,T)
VIS=FRHEO*V*RHO/W/DV
VISP=1.0E-1*VIS
H=DT*CP*SQRT(W*RHO*V/PI)/2./(TA-T)
HX=V/AR
DM=D*10000.0
VM=V*0.6
PRINT HX,H
*PRINT TK,VIS
*PRINT FGRAV,FDRAG,FINER
*PRINT VM,DM,T,DV,DT,FRHEO,VIS,H
METHOD STIFF
NOSORT
TIMER FINTIM=190.0,DELMIN=1.0E-12
END
STOP

```

APPENDIX F

CSMP Program for improved model of nylon-6 melt spinning.

```
//SIMHMW JOB ,BHEDA,GROUP=J41241,USER=P91688,
// PASSWORD=?,TIME=5,REGION=256K
/*ROUTE PRINT UTKVX1.BHEDA
/*NOTIFY UTKVX1.BHEDA
//STEP1 EXEC CSMP3
//SYSIN DD *
TITLE MN=53,200, W=2.9953 G/MIN
INITIAL
CONSTANT PI=3.1415926,G=980.,DNA0=0.0825,C1=1.37E-4,C2=0.259,C3=0.167
CONSTANT C4=5.E-17,C5=-2.7725887,C6=0.087,C7=5140.
CONSTANT DELH=45.0,COP=1.0E-10,C12=4.5,TS=100.
CONSTANT TMAX=146.,DO=46.,TM=228.,RMAX=0.14,TG=45.,N=3.,THI=0.25
CONSTANT DO=0.0762,T0=280.,TA=25.,AMV=53200.,W0=2.9925
CONSTANT RHOA=6.62E-5,MU=2.8E-4,VY=0.0,C8=1.25E5
PARAMETER FRHE0=97.3
FUNCTION AMOD=(15.,358.),(23.,338.),(31.,308.),(34.,288.),(38.,235.),...
(44.,175.),(50.,138.),(56.,97.),(61.,85.),(66.,67.), ...
(74.,60.),(79.,56.),(83.,51.),(90.,48.5),(99.,44.8), ...
(108.,40.),(115.,38.),(123.,36.),(132.,34.5), ...
(139.,33.),(146.,32.),(155.,31.),(167.,30.), ...
(176.,29.),(186.,27.5),(195.,24.),(202.,20.7), ...
(206.,17.8),(210.,15.5),(215.,13.25),(219.,10.7), ...
(221.,5.95),(228.,4.6),(300.,1.0E-5)
FUNCTION ABETA=(-3.088,0.0005),(-2.7869,0.001),(-2.0873,0.005), ...
(-1.7856,0.01),(-1.0807,0.05),(-0.7724,0.1), ...
(-0.0113,0.5),(0.3757,1.0),(0.8781,2.0), ...
(1.2945,3.0),(1.6939,4.0),(2.0926,5.0),(2.4941,6.0), ...
(2.8993,7.0),(3.3076,8.0),(3.7184,9.0),(4.1325,10.0),...
(4.5464,11.0),(4.9628,12.0),(5.3806,13.0), ...
(5.7995,14.0),(6.2195,15.0),(6.6403,16.0), ...
(7.0619,17.0),(7.4842,18.0),(7.9071,19.0), ...
(8.3306,20.0),(8.7546,21.0)
RENAME TIME=DIST
W=W0/60.0
RHO0=1./(0.8816+0.000564*T)
ETA=7.8E-4*(AMV)**0.65
V0=4.0*W/RHO0/PI/DO/DO
BIA0=COP*4.0*FRHE0/PI/DO/DO
THEMIN=0.01
TE=-1.0
DTH=0.0
THE=0.0
TO=THE
Z0=0.0
TC=0.0
DTC=0.0
```

```

T=T0
V=V0
D=D0
BIA=BIA0
C9=PI/W
DYNAMIC
PROCEDURE RHO=FUN(T,THE)
  IF(T.GT.228.) RHO=1./(0.8816+0.000564*T)
  IF(T.LE.228.) RHO=1./((0.8816+0.000564*T)-(0.0292+0.000326*T)*THE)
ENDPROCEDURE
PROCEDURE CP=FUNC(T)
  IF(T.GT.160.) CP=0.577+0.000336*T
  IF(T.LE.160.) CP=0.325+0.0015*T
ENDPROCEDURE
PROCEDURE VIS=FUNCT(T,ETA,TM,C7,THE,THI,C12,AMN,TP,C4,THEMIN)
  IF(THE.LE.THEMIN) FAC=1.0
  IF(THE.GT.THEMIN) FAC=EXP(C12*((THE/THI)**12.))
  IF(T.GE.TS) VIS=ETA*EXP(C7/(T+273.))*FAC
  IF(T.GT.TS) KOUT=-1
  IF(KOUT.GT.0) GO TO 89
  IF(T.LE.TS) KOUT=1
89  CONTINUE
  IF(T.LT.TS) VIS=1.0E30
ENDPROCEDURE
MOD=(1.0E8)*AFGEN(AMOD,T)
REN=RHOA*V*D/MU
FINER=W*(V-V0)
DFGRA=W*G/V
FGRAV=INTGRL(0.0,DFGRA)
ZETA=8.0*SQRT(DIST/REN/D)
PROCEDURE CD,ZATA,BETA=TEST(ZETA,REN)
  IF(ZETA.LE.0.0) GO TO 29
  ZATA=ALOG10(ZETA)
  BETA=AFGEN(ABETA,ZATA)
  CD=4./BETA/REN
  GO TO 30
29  CD=0.0
30  CONTINUE
ENDPROCEDURE
DFDRA=PI*CD*RHOA*V*V*D
FDRAG=INTGRL(0.0,DFDRA)
DFRHE=(W*D*V + DFDRA -DFGRA)
FRHEO=INTGRL(FRHEO,DFRHE)
STRES=FRHEO*RHO*V/W
PROCED DV=OLIVE(STRES,VIS,T,TG)
  DV=STRES/VIS
  IF(T.LE.TG) DV=0.0
ENDPROCEDURE
V=INTGRL(V0,DV)
VM=V*0.6
DTIM=1.0/V
TIM=INTGRL(0.0,DTIM)

```

```

D=SQRT(4.0*W/RHO/PI/V)
DM=D*10000.0
AR=PI*D*D/4.
H=C1*((RHO*V*V/W)**C2)*((1.+(8.*VY/VM)**2.))**C3)
RATE1=(C9*D*H*(TA-T))/CP
RATE2=DELH*DTH/V/CP
DT=RATE1+RATE2
T=INTGRL(TO,DT)
PROCED DTH,THE,CONST,B1,DTHE,RATE=G(TE,V,FA,TO,T)
    IF(T.GE.TM.AND.TE.LE.0.0) GO TO 10
    IF(T.LE.TG) GO TO 10
    IF(TO.GE.THI) GO TO 10
    TE=1.0
    IF(T.GT.TM-1.0) GO TO 10
    CONST=C8*FA*FA/(TM-T)
    B1=C5*(T-TMAX)*(T-TMAX)/DO/DO
    B2=B1+CONST
    IF(B2.GT.174.) B2=174.
    RATE=RMAX*EXP(B2)
    DTHE=RATE/V
    SUM=INTGRL(0,DTHE)
    DTH=THI*N*RATE*(SUM**(N-1.0))/EXP(SUM**N)
    THE=THI*(1.0-1.0/EXP(SUM**N))
    TO=THE
    GO TO 20
10    DTH=0.0
    THE=TO
20    CONTINUE
ENDPROCEDURE
XC=THE*100.0
DBIA=COP*DV*MOD/V-BIA*MOD/VIS/V
BIA=INTGRL(BIA0,DBIA)
BIC=THE*C6
BIT=(1.0-THE)*BIA + BIC
FA=BIA/DNA0
SDR=V/V0
DENI=W*900000.0/V
PRINT T,RATE
*PRINT VM,T,DM,BIT,FRHEO
*RANGE VM,DV,DM,FRHEO,FINER,FDRAG,FGRAV,STRES,REN,CD,BETA,ZETA,T,DT,...
*    NUL,H,RATE1,RATE2,THE,DTH,RATE,BIA,DBIA,BIC,BIT,FA,MOD,VIS,...
*    CP,RHO,TIM,DENI,TENA,ELONG,SDR
*PRINT VM,DV,DM,FRHEO,FINER,FDRAG,FGRAV,STRES,REN,CD,BETA,ZETA,T,DT,...
*    NUL,H,RATE1,RATE2,THE,DTH,RATE,BIA,DBIA,BIC,BIT,FA,MOD,VIS,...
*    CP,RHO,TIM,DENI,TENA,ELONG,SDR
*PRTPLT THE,FA,STRES
*PRTPLT VM,DM,T
METHOD STIFF
NOSORT
TIMER FINTIM=200.0,DELMIN=1.0E-12
END
STOP

```

VITA

Jayendra Hiralal Bheda was born in India on August 8, 1952. He earned a Bachelor of Science degree in Physics, Chemistry and Math from R.L.T. College of Science, Akola (Nagpur University, India) in 1971. In 1974, he earned a Bachelor of Science and Technology degree in Plastics Technology from Bombay University Department of Chemical Technology, Bombay, India. He then worked for about seven years in various areas of polymer processing including about two years in Houston, Texas.

He entered The University of Tennessee, Knoxville, in 1982 and received a Master of Science in Polymer Engineering in 1984. He continued his education in Polymer Engineering at The University of Tennessee and received a Doctor of Philosophy degree in 1987.

He is a member of Society of Plastics Engineers and the secretary of India Student Association since 1982. He is married to former Hansa Punshi Hariya and they have two daughters Poonam and Purvi.